

HOST-GUEST INTERACTIONS IN POROUS ORGANIC POLYMERS

A Dissertation

Presented to the Faculty of the Graduate School

of Cornell University

In Partial Fulfillment of the Requirements for the Degree of

Doctor of Philosophy

by

Jennifer Lynn Novotney

August 2016

© 2016 Jennifer Novotney

HOST-GUEST INTERACTIONS IN POROUS ORGANIC POLYMERS

Jennifer Novotney, Ph. D.

Cornell University 2016

This dissertation explores the host-guest interactions within two classes of porous organic polymers: amorphous porous organic polymers (POPs), and covalent organic frameworks (COFs). In both systems, processing conditions are explored which can greatly improve their surface area, as well as functionality as sensors. Guest molecules can range from trinitrotoluene (TNT) vapor to nanoparticles, but in each situation, these interactions are studied and modified to explore the functionality of the host-guest system.

BIOGRAPHICAL SKETCH

Jennifer Novotney was born in Tacoma, WA and spent the first two years of her life living and traveling with her family in Southeast Asia. They moved to Alaska soon after that where Jennifer spent her time playing soccer, competing on the math team, and pestering her older brothers. Jennifer moved to Spokane, WA where she graduated class valedictorian from Mead High School. She proceeded to receive a double major in mathematics and chemistry from Western Washington University where she was a presidential scholar and the president of the fencing team and Scottish country-dance club. Upon starting at Cornell University, Jennifer stayed very active in science outreach and communication, and she won the inaugural American Chemical Society Chemistry Champion Contest in 2014. Upon graduation, Jennifer is continuing her love of connection lay audiences with science.

I would like to dedicate my dissertation to my advisor Will, for guiding me these past five years, my family for all of their love and support, and my boyfriend Johan, who encouraged me every day to excel.

ACKNOWLEDGMENTS

Research for this manuscript was conducted with Government support under FA9550-11-C-0028 and awarded by the Department of Defense, Air Force Office of Scientific Research, National Defense Science and Engineering Graduate (NDSEG) Fellowship, 32 CFR 168a and the Cornell Integrative Graduate Education and Research Traineeship (IGERT) Program in the Nanoscale Control of Surfaces and Interfaces (NSF Award DGE-0654193).

TABLE OF CONTENTS

Biographical Sketch	iv
Acknowledgements	vi
List of Figures	vii
List of Tables	
List of Abbreviations	
List of Symbols	
Chapter One: Host-Guest Interactions for Sensing with Porous Organic Polymers	1
Chapter Two: Conjugated Porous Polymers for TNT Vapor Detection	21
Chapter Three: A 2D Covalent Organic Framework with 4.7 nm Pores and Insight into its Interlayer Stacking	57
Chapter Four: Exploring the Properties of HHTP-DPB COF	112
Chapter Five: Loading HHTP-DPB COF with CdSe Nanocrystals	136
Chapter Six: Hydrazone-Linked COF-43 Interactions with Li ⁺	165

LIST OF FIGURES

Figure 1.1: Common monomers used for PIM synthesis	1
Figure 1.2: Structure and BET surface area of typical porous organic polymers	4
Figure 1.3: Structures and BET surface areas of typical covalent organic frameworks	5
Figure 1.4: A) Single molecule fluorescence receptor quenching B) Conjugated porous polymer quenching response	7
Figure 1.5: A) Structure of polymer used for Yang, J.S; Swager, T.M; <i>J. Am. Chem. Soc.</i> , 1998 , <i>120</i> , (46), 11864 B) Diagram illustrating free space created by pentiptycene group	8
Figure 1.6: A) Modification to PIM which increases exciton lifetime B) Modification to pentiptycene group and addition of electron withdrawing groups makes this polymer able to detect biologically relevant material	9
Figure 1.7: A) Structure of TMBPT B) Selective uptake of Ag(I) ions from solution C) Images of TMBPT in various sulfur containing solutions	10
Figure 1.8: A) Structure of TFP B) Fluorescence quenching of TFP films exposed to RDX from solution C) Fluorescence quenching response of TFP films to vapors of various common household items	11
Figure 1.9: Structure of monomer and Py-Azine COF	13
Figure 1.10: A) Fluorescence emission of Py-Azine COF exposed to various concentrations of TNP B) Fluorescence quenching response of Py-Azine COF to various nitro compounds C) Structure of TNP	13
Figure 1.11: A) Synthesis and structure of the monomers and Tf-DBH and Tfp-DBH COFs	14
Figure 1.12: A) Fluorescence quenching response of exfoliated Tfp-DBH	15

COF in solution to TNP B) Fluorescence quenching response of exfoliated Tfp-DBP COF in solution to various nitroaromatics C) Images of exfoliated Tfp-DBH COF in solution before and after quenching	
D) Fluorescence emission of exfoliated Tfp-DBH COF films exposed to TNP in solution E) Fluorescence enhancement of exfoliated Tfp-DBH films exposed to various nitroaromatics	
Figure 2.1: Synthesis of CPP 3 and schematic of its fluorescence response to nitroaromatic quenchers	23
Figure 2.2: Representative N ₂ adsorption isotherms for the CPP powder samples as a function of growth solvent and activation method	26
Figure 2.3: A-D) Fluorescence emission of polymer films exposed to TNT vapor for times ranging from 0-60 min. E) Combined quenching curves of polymer films with exposure to TNT vapor	30
Figure A1.1: ¹ H NMR of Compound S2	38
Figure A1.2: ¹ H NMR of Compound S3	38
Figure A1.3: ¹ H NMR of Compound 1	39
Figure A1.4: ¹³ C CP-MAS NMR of polymer powders DMF-L, DMF-E, PhMe-L PhMe-E	40
Figure A1.5: FT-IR of polymer DMF-L	41
Figure A1.6: FT-IR of polymer DMF-E	41
Figure A1.7: FT-IR of polymer PhMe-L	42
Figure A1.8: FT-IR of polymer PhMe-E	42
Figure A1.9: UV-Vis of polymer DMF-L	43
Figure A1.10: UV-Vis of polymer DMF-E	43
Figure A1.11: UV-Vis of polymer PhMe-L	44
Figure A1.12: UV-Vis of polymer PhMe-E	44

Figure A1.13: Fluorescence emission of polymer DMF-L	45
Figure A1.14: Fluorescence emission of polymer DMF-E	45
Figure A1.15: Fluorescence emission of polymer PhMe-L	46
Figure A1.16: Fluorescence emission of polymer PhMe-E	46
Figure A1.17: A) Normalized UV-Vis absorbance of the films used to determine relative quantum yield. B) Fluorescence spectra used to determine relative quantum yield	47
Figure A1.18: TGA of polymer DMF-L	48
Figure A1.19: TGA of polymer DMF-E	48
Figure A1.20: TGA of polymer PhMe-L	49
Figure A1.21: TGA of polymer PhMe-E	49
Figure A1.22: BET plot of polymer DMF-L	50
Figure A1.23: BET plot of polymer DMF-E	51
Figure A1.24: BET plot of polymer PhMe-L	51
Figure A1.25: BET plot of polymer PhMe-E	52
Figure A1.26: Comparison of N ₂ adsorption isotherms of two DMF-L polymers	52
Figure A1.27: SEM of polymer DMF-L	53
Figure A1.28: SEM of polymer DMF-E	54
Figure A1.29: SEM of polymer PhMe-L	55
Figure A1.30: SEM of polymer PhMe-E	55
Figure 3.1: A) N ₂ adsorption (blue circles) and desorption (red squares) isotherms for HHTP-DPB COF. B) Scanning electron microscope (SEM) images of HHTP-DPB COF powder	61
Figure 3.2: Experimental (blue) and Pawley refined (red) vs. predicted (green) PXRD patterns of HHTP-DPB COF and difference plot (experimental – refined: black). Major observed reflections are labeled.	64

Figure 3.3: Potential energy surface generated from the semi-empirical MM3 potential.	67
Figure 3.4: Expansion of region A from Figure 3.3 calculated with density functional theory. B) Expansion of a subset of region B in Figure 3.3 calculated with density functional theory and atomic representation of the two-layer staggered structure.	68
Figure 3.5: A) Grazing incidence X-ray diffraction (GID) of HHTTP-DPB COF thin film on SLG (growth time: 24 h). B) Projection of A) near $Q = 0$ C) Cross – sectional SEM image of the film.	72
Figure 3.6: A) Transmission absorption (red) and normalized emission (blue) Spectra of HHTTP-DPB COF thin film and B) Photographs of fluorescent COF film on SiO ₂ (left) and powder (right) under 365 nm illumination	74
Figure A2.1: ¹ H-NMR of ester 5	85
Figure A2.2: ¹³ C-NMR of ester 5	85
Figure A2.3: ¹ H-NMR of acid 1	86
Figure A2.4: ¹³ C-NMR of acid 1	86
Figure A2.5: MALDI-MS of ester 5	87
Figure A2.6: MALDI-MS of acid 1	87
Figure A2.7: CP/MAS ¹³ C-NMR of HHTTP-DPB COF	88
Figure A2.8: CP/MAS ¹³ C-NMR of HHTTP-DPB COF after activation	89
Figure A2.9: SS ¹¹ B-NMR of HHTTP-DPB COF	90
Figure A2.10: FTIR of ester 5 and acid 1	91
Figure A2.11: FTIR of HHTTP-DPB COF before and after activation	91
Figure A2.12: UV-Vis absorption of ester 5 and acid 1 in DMF	92
Figure A2.13: UV-Vis absorption of HHTTP 2 in DMF	92
Figure A2.14: Emission spectra of acid 1, ester 5, and HHTTP 2 in DMF	93

Figure A2.15: PXRD of HHTTP-DPB COF	94
Figure A2.16: Precursor structure used for initial modeling of COF structure	96
Figure A2.17: COF crystal model in bnn configuration	97
Figure A2.18: Observed vs Pawley-refined PXRD profiles for HHTTP-DPB COF	97
Figure A2.19: Model of HHTTP-DPB COF in gra packing and simulated PXRD	99
Figure A2.20: TGA trace of HHTTP-DPB COF	100
Figure A2.21: Langmuir and BET surface area of HHTTP-DPB COF	101
Figure A2.22: Simulated N ₂ adsorption of HHTTP-DPB COF	103
Figure A2.23: BET plot of simulated N ₂ adsorption of HHTTP-DPB COF	103
Figure A2.24: A-D) Structures used for MM3 models of HHTTP-DPB COF	108
Figure A2.25: GID of HHTTP-DPB COF thin film	109
Figure A2.26: GID at large Q of HHTTP-DPB COF thin film	109
Figure A2.27: SEM of HHTTP-DPB COF think film	110
Figure 4.1: TEM images of HHTTP-DPB COF at 10, 20, 30 and 40 minutes	114
Figure 4.2: TEM images of HHTTP-DPB COF on A) Lacey carbon grid B) ultra-thin carbon grid. Each sample was grown for 30 minutes	115
Figure 4.3: TEM images of HHTTP-DPB COF on ultra-thin carbon grid after 30 minutes growth A) False color image demonstrating different crystallographic grains B) Grain boundary with pentagons, hexagons, and heptagons added to highlight growth pattern	116
Figure 4.4: A) Picture of heterogeneous COF-5 growth B) picture of homogenous COF-5 growth C) Turbidity measurement of homogenous COF-5 growth.	118
Figure 4.5: A) COF powder formation of four different boronate ester linked COFs from homogenous conditions B) Activation energies for the COFs tested	119
Figure 4.6: A) Nitrogen adsorption isotherm at 77K comparing literature conditions to homogenous growth conditions with supercritical activation B) Summary of	

synthesis methods, activation methods, and resulting BET surface area of HHTP-DPB COF	121
Figure A3.1: ¹ H NMR of Compound S1	129
Figure A3.2: ¹ H NMR of Compound 1	129
Figure A3.3: CP/MAS ¹³ C NMR of HHTP-DPB COF	130
Figure A3.4: FTIR of HHTP-DPB COF before and after activation	131
Figure A3.5: A) PXRD of HHTP-DPB COF synthesized under literature conditions (blue), and predicted pattern (red). B) PXRD of HHTP-DPB COF synthesized under homogenous conditions with super critical activation	132
Figure A3.6: TEM images of HHPT-DPB COF grown on ultra-thin carbon grid for 40 minutes	133
Figure A3.7: TEM image of HHTP-DPB COF grown on ultra-thin carbon grid for 40 minutes. This image shows the grain boundary with superimposed heptagons and pentagons	133
Figure A3.8: TEM image of HHTP-DPB COF grown on a lacey carbon grid for 30 minutes	134
Figure A3.9: Turbidity measurement of COF-5, COF-10, TP-COF, and HHTP-DPB COF with the addition of 700 equivalents of water relative to HHTP	135
Figure 5.1: Illustration of a 3 nm CdSe nanoparticle with oleic acid ligands and the structures and pore sizes of HHTP-DPB COF and COF-5	138
Figure 5.2: A) Absorbance of CdSe nanocrystals over time in the presence of HHTP-DPB COF (red), COF-5 (orange), HHTP monomer (green), DPB monomer (blue) B) Photo of CdSe nanocrystals in solution (left), and after being exposed to HHTP-DPB COF for 12 h (right)	140
Figure 5.3: Nitrogen adsorption isotherm at 77 K. Adsorption (filled circles) and desorption (open circles) of A) HHTP-DPB COF with and without 3 nm CdSe	

nanocrystals B) COF-5 with and without 3 nm CdSe nanocrystals	141
Figure 5.4: Quantitative elemental analysis of maximally loaded COF-5 (orange) and HHTTP-DPB COF (red) of Cd+Se loaded in A) original batch of COFs used for surface area analysis B) new batches of COFs and nanocrystals. Error bars represent 95% confidence interval	142
Figure 5.5: Nitrogen adsorption isotherm at 77K for HHTTP-DPB COF (blue) loaded with two different batches of 3 nm CdSe nanocrystals (orange and red)	143
Figure 5.6: Quantitative elemental analysis of maximally loaded COF-5 and HHTTP-DPB COF with 3 nm CdSe, 4.5 nm CdSe, and 6 nm PbS nanocrystals	145
Figure 5.7: TEM images of A) HHTTP-DPB COF powder maximally loaded with 3 nm CdSe nanocrystals B) Cross section of HHTTP-DPB COF film loaded with 3 nm CdSe nanocrystals	146
Figure A4.1: ¹ H NMR of Compound S1	153
Figure A4.2: ¹ H NMR of Compound 1	153
Figure A4.3: Image of HHTTP-DPB COF and COF-5 with and without 3 nm CdSe nanocrystal loading	154
Figure A4.4: FTIR spectra of HHTTP-DPB COF loaded with CdSe nanocrystals	155
Figure A4.5: FTIR spectra of COF-5 loaded with CdSe nanocrystals	155
Figure A4.6: UV-Vis spectra of HHTTP-DPB COF and COF-5 powders with and without CdSe nanocrystals	156
Figure A4.6: Fluorescence emission spectra of HHTTP-DPB COF and COF-5 powders with and without CdSe nanocrystals	157
Figure A4.7: A) PXRD of HHTTP-DPB COF powder with and without CdSe nanocrystals B) PXRD of maximally loaded HHTTP-DPB COF with CdSe showing the diffraction of the CdSe nanocrystals	158
Figure A4.8: PXRD of HHTTP-DPB COF with and without CdSe nanocrystals showing	

different activation methods after CdSe loading	158
Figure A4.9: PXRD of COF-5 powder with and without CdSe nanocrystals	159
Figure A4.10: Cross section of 2D GID of HHTP-DPB COF film exposed to CdSe nanocrystals	160
Figure A4.11: TEM images of HHTP-DPB COF powder loaded with CdSe nanocrystals	161
Figure A4.12: Nitrogen isotherm at 77K of pristine HHTP-DPB COF with and without 2 different batches of 3 nm CdSe nanocrystals	162
Figure A4.13: BET plot for pristine HHTP-DPB COF from Fig. A4.12	162
Figure A4.14: BET plot for HHTP-DPB COF with CdSe (orange trace from figure A4.12)	163
Figure A4.15: BET plot for HHTP-DPB COF with CdSe (red trace from figure A4.12)	163
Figure A4.16: BET plot for pristine HHTP-DPB COF from Fig. 5.3A	164
Figure A4.17: BET plot for pristine COF-5 from Fig. 5.3B	164
Figure 6.1: Solvothermal synthesis of COF-43 from tri-aldehyde (blue) and dihydrazide (green).	167
Figure 6.2: A) Photograph of COF-43 grown under literature conditions (left) and in the presence of SDS (right). B) Fluorescence emission of COF-43 under various growth conditions.	167
Figure 6.3: A) Photograph of COF-43 exposed to saturated solutions of SDS in THF which were allowed to age for 0, 1, 2, or 3 days. B) Photograph of COF-43 exposed to different peroxides in solution	168
Figure 6.4: Plot of maximum fluorescence emission versus the equivalents of TCA added to COF-43.	169
Figure 6.5: FTIR of COF-43 exposed to different equivalents of TCA	171

Figure 6.6: Change in maximum fluorescence emission of COF-43 exposed to excess additives	171
Figure 6.7: Change in maximum fluorescence emission of COF-43 exposed the excess lithium additives	172
Figure 6.8: Maximum fluorescence emission of COF-43 exposed to different equivalents of LiCl	173
Figure 6.9: Plot of maximum fluorescence emission of COF-43 after exposing to solutions where the concentrations of Li ⁺ is maintained and the concentration of Na ⁺ changes (blue), or where the concentration of Na ⁺ is maintained and the concentration of Li ⁺ varies	174
Figure 6.10: Top: Structure of model compound used for solution measurements. A) Fluorescence emission of model compound in solution with 0 to 14 equivalents of LiCl. B) Solid state fluorescence of samples in Fig. 6.10A with solution removed	175
Figure 6.11: Fluorescence emission of COF-43 exfoliated in solution of THF (left) or dioxane (right) with 0 to 8 equivalents of Li ⁺ in solution	176
Figure 6.12: Fluorescence emission of dried samples from Fig. 6.11	177
Figure A5.1: ¹ H NMR of Compound S1	184
Figure A5.2: ¹ H NMR of Compound 1	184
Figure A5.3: ¹ H NMR of Compound 2	185
Figure A5.4: ⁹ Li SSNMR of Li@COF-43	185
Figure A5.5: FTIR spectra of Li@COF-43	186
Figure A5.6: SSUV-Vis of Li@COF-43	187
Figure A5.7: SSUV-Vis of H@COF-43	187
Figure A5.8: UV-Vis of Li@Exfoliated COF-43	188
Figure A5.9: SSUV-Vis of dried Li@Exfoliated COF-43	188

Figure A5.10: SSUV-Vis of Li@Exfoliated COF-43	189
Figure A5.11: UV-Vis of Li@Model Compound	189
Figure A5.12: SSUV-Vis of Li@ Model Compound	190
Figure A5.13: Solid State Fluorescence spectra of Li@COF-43	191
Figure A5.14: Solid State Fluorescence spectra of H@COF-43	191
Figure A5.15: Solid State Fluorescence spectra of Li@Exfoliated COF-43	192
Figure A5.16: PXRD of Li@COF-43	193
Figure A5.17: TEM images of Li@Exfoliated COF-43 (THF)	194
Figure A5.18: TEM images of Li@Exfoliated COF-43 (Dioxane)	194
Figure A5.19: Formation of benzanulated product comparing Cu@COF-43 with the homogenous catalyst Cu(CF ₃ SO ₃) ₂ .	196
Figure A5.20: Recyclability of Cu@COF-43 looking at the amount of benzanulated product formed after 1 h of reaction	196
Figure A5.21: Formation of alkyne coupled product comparing Pd@COF-43 and the homogenous catalyst Pd(PPh ₃) ₂ Cl ₂ .	198
Figure A5.22: Recyclability of Pd@COF-43 looking at the amount of alkyne coupled product formed after 1 h of reaction	198

LIST OF TABLES

Table 1.1: BET surface areas of polymers synthesized from monomers in Figure 1.1	2
Table 2.1: Relative fluorescence quantum yields of polymer 3 as a function of growth solvent and activation method	28
Table A2.1: Fractional atomic coordinates for the unit cell of HHTP-DPB COF	98
Table A2.2: Accessible surface areas obtained from Connolly surfaces	104

LIST OF SCHEMES

Scheme 3.1: Synthesis of HHTP-DPB CO from bis(boronic acid) linker and HHTP and model of the idealized bnn topology	60
Scheme A2.1: Synthesis of boronic acid 1	83
Scheme A3.1: Synthesis of DPB monomer 1	127
Scheme A4.1: Synthesis of DPB monomer 1	151
Scheme A5.1: Synthesis of linear dihydrazide 1	182
Scheme A5.2: Benzanulation reaction	195
Scheme A5.3: Sonogashira reaction	197

LIST OF ABBREVIATIONS

PIM – Polymer of Intrinsic Microporosity
POP- Porous Organic Polymer
COF – Covalent Organic Framework
POF – Porous Organic Framework
CPP – Conjugated Porous Polymer
CMP – Conjugated Microporous Polymer
PPF – Porous Polymer Framework
MOP- Microporous Organic Polymer
TNT - Trinitrotoluene
TMBPT – Porous Triazine Network
TFP – Tris(polyphenylene)vinylene
RDX – Royal Demolition Explosive
UV – Ultraviolet
Py – Pyrene
TNP – Trinitrophenol
DNP – Dinitrophenol
DNT- Dinitrotoluene
TNP – Trinitrophenol
IPA - Isopropyl alcohol
DBH- Dibenzohydroquinone
PETN – Pentaerythritol tetranitrate
MOF- Metal Organic Framework
N₂ – Nitrogen
CP – Cross Polarizing
MAS – Magic Angle Spinning
¹³C – Carbon with 7 neutrons
NMR – Nuclear Magnetic Resonance
FTIR – Fourier Transform – Infrared Radiation Spectroscopy
DMF – Dimethylformamide
PhMe- Toluene
HHTP- 2,3,6,7,10,11-hexahydroxytriphenylene
DPB- 2,4'-diphenylbutadienebis(boronic acid)
2D – Two Dimensional
3D – Three Dimensional
PXRD – Powder X-Ray Diffraction
DFT – Density Functional Theory
SEM – Scanning Electron Microscope
PES – Potential Energy Surface
GID – Grazing Incidence X-Ray Diffraction
SLG – Single Layer Graphene
TMEDA – tetramethylethylenediamine
1H – Proton with 1 neutron

CDCl₃ – Deuterated chloroform
DMSO – Dimethyl sulfoxide
MALDI – Matrix Assisted Laser Desorption/Ionization
MS – Mass Spectroscopy
TGA – Thermogravimetric Analysis
STP – Standard Temperature and Pressure
TEM – Transmission Electron Microscopy
CdSe – Cadmium Selenide
nm - nanometers
ICP-OES – Inductivity Coupled Plasma optical emission spectrometry
PbS – Lead Sulfide
UV-Vis - Ultra Violet and Visible Light (spectrometry)
SDS – Sodium Dodecyl Sulfate
THF – Tetrahydrofuran
TCA – Trichloroacetic acid

CHAPTER 1
HOST-GUEST INTERACTIONS FOR SENSING WITH POROUS ORGANIC
POLYMERS

In this introductory chapter, three different classes of porous polymers, including polymers of intrinsic microporosity (PIMs), porous organic polymers (POPs), and covalent organic frameworks (COFs), and their applications, with a focus on sensing, will be discussed.

Polymers of Intrinsic Microporosity (PIMs) are linear polymers formed with shape persistent monomers which induce frustrated packing of the polymer system. These polymers typically are solution processable, with facile methods to create thin films. PIM thin films are often not characterized by their surface area (because thin-film surface area measurements are difficult), but it is strongly believe that the shape persistent monomers create small voids in the material for analyte to interact with more of the polymer film. Precipitated powders of these polymers do have significant BET surface areas, likely due to the inefficient packing of the polymer chains induced by the monomers. Figure 1.1 shows the structure of many typical shape persistent monomers used for PIM synthesis¹. In most reported cases, PIMs are synthesized through a double-aromatic nucleophilic substitution mechanism to form the dibenzodioxin linkage¹⁻⁵, but can also be created through other coupling chemistries⁶.

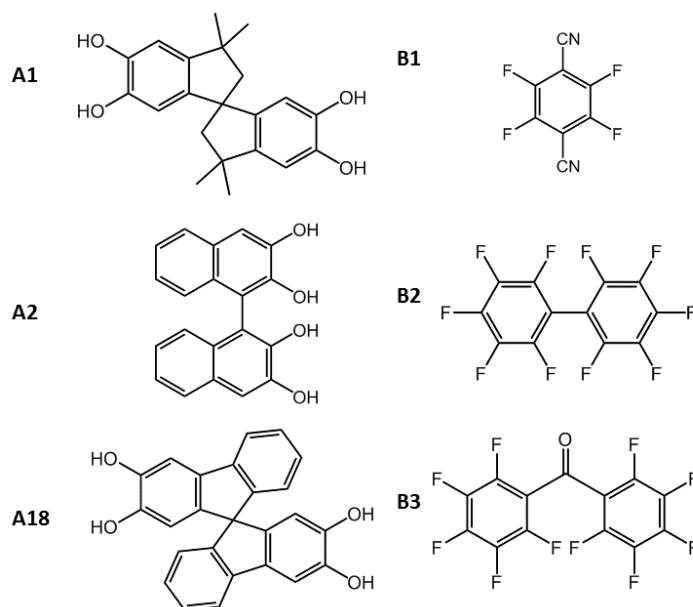


Figure 1.1: Common monomers used for PIM Synthesis. Figures from references 1,3,5.

Polymer	Surface Area (BET; m^2g^{-1})	Reference
A1+B1	850	3
A1+B2	600	3
A1+B3	560	3
A2+B1	440	3
A2+B2	540	3
A18+B1	803	5

Table 1.1: Table of BET surface areas for polymers made from the monomers in Figure 1.1

The microporous structure of PIMs make them excellent candidates for gas separation and storage⁷⁻¹³, chemosensors¹⁴⁻¹⁷, and heterogeneous catalysis^{18,19}.

Porous Organic Polymers (POPs) are amorphous two or three dimensional polymers whose porosity is induced by the shape-persistent geometry of at least one of the linkers²⁰. In the literature POPs can go by many names including porous organic frameworks (POFs), conjugated porous polymers (CPPs), conjugated microporous polymers (CMPs), porous polymer frameworks (PPFs) and microporous organic polymers (MOPs), but for the purpose of this chapter, all of them will go under the heading of POPs. POPs typically are isolated as an insoluble powder formed from irreversible reactions with surface area greater than 50 m²g⁻¹, but sometimes are grown as thin films. The porosity of a POP depends on the degree of interpenetration, synthesis solvent, activation procedure, monomer side chains, just to name a few. Of all classes of porous polymers discussed, POPs have the widest range of possible monomers and functionalization available. They can be synthesized by many different cross coupling reactions including Sonogashira²⁰⁻²², Suzuki, Yamamoto²³, and even oxidative polymerization²⁴. In figure 1.2, some of the POP morphologies are displayed^{2,22,25}. The high surface areas, in coordination with the large variety of chemical and electrical properties drives the study of utilizing POPs for sensing²⁶⁻³², gas storage³³⁻³⁷, gas separation^{38,39}, and catalysis applications⁴⁰⁻⁴².

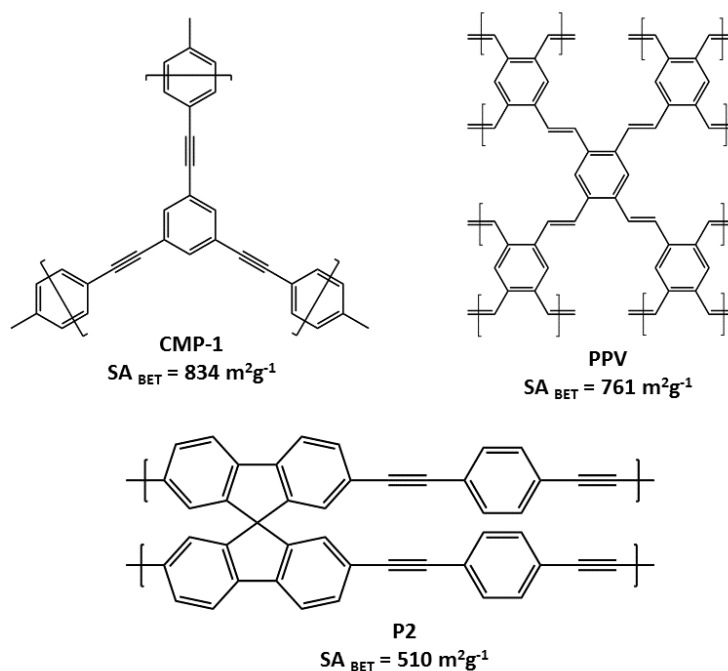


Figure 1.2: Structures and BET surface areas of some typical porous organic polymers. CMP-1, PPV, P2 are from references 22, 25, 2 respectively.

Covalent Organic Frameworks (COFs) are crystalline two or three dimensional polymers whose unit cell is determined by the monomer geometry^{43,44}. These crystalline materials can be isolated as a powder from reversible bond forming reactions with surface areas over $3000 \text{ m}^2\text{g}^{-1}$ ⁴⁴, or as a crystalline oriented thin film⁴⁵. The chemistries behind these polymers can also produce amorphous POPs, but COFs are valued for their high surface areas, and the monodispersity of their pore structures, and some COFs are displayed in Figure 1.3⁴⁶⁻⁴⁸. COFs are currently a field with limited number of bonding chemistries, but the field is growing since the first COFs were reported in 2005⁴⁹.

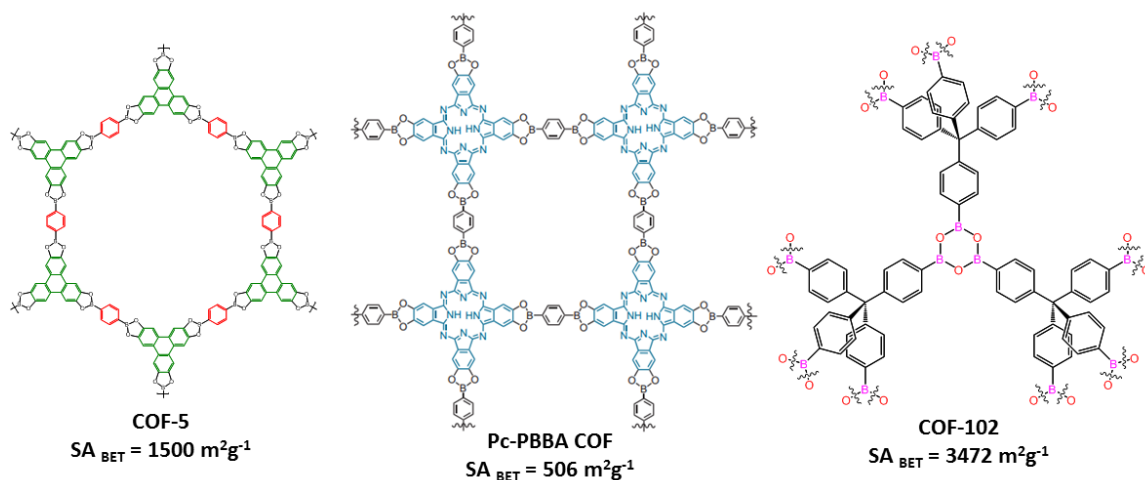


Figure 1.3: Structures and BET surface areas of some covalent organic frameworks. COF-5, Pc-PBBA COF, and COF-102 are from references 46, 47, 48 respectively.

As the ability to create more chemically stable materials with a high degree of tunability for the pore size, pore functionality, and electric characteristics, the applications for COFs has dramatically grown^{50–55,47,56}. These high surface area materials have been explored for the applications in gas storage^{57,58}, heterogeneous catalysis^{59,60}, optoelectronics^{61,62,55,47}, and energy storage devices^{63,64}.

Sensing: Within the past 20 years there has been a huge push in chemical research to create novel materials with the ability to identify analytes of choice from both the vapor and liquid phase. Porous polymers offer many advantages in the sensing field deriving both from the tunable chemistry of the monomers and the inherent surface area. The pores allow the analytes to diffuse into the polymers, giving more chances for sensing interactions to occur. These polymers can act as sensors in many ways including fluorescence quenching, fluorescence inducing, color changing, and electrochemical responses.

PIMS for Sensing: PIMs have been studied for sensing applications for the past 20 years, with some even being incorporated into commercial devices. Some PIMs rely on adsorbed dyes to display sensing effects¹⁵, others rely on changes in refractive index to produce color changes^{14,16}. There are even a few instances of using PIMs as concentrators for traditional sensors, which allow the PIM to take-up increased amounts of the analyte of interest, and then heating the PIM to release the analyte to a traditional sensor whose sensitivity is too low at the current conditions⁶⁵. There are many great reviews that highlight the developments and applications of polymer sensors, but most of the polymers used for sensing applications are not inherently porous⁶⁶⁻⁶⁹. Instead, these non-porous polymers typically rely on signal amplification for enhanced sensitivity^{68,70}.

Signal amplification is one way to achieve greater sensitivity for an analyte of interest, and is illustrated in Figure 1.5. For a single receptor to act as a turn-off sensor, it takes one molecule of analyte to turn off the fluorescence of that one receptor. In order to achieve good signal to noise, there needs to be a reasonable concentration of analyte to receptor. However, if these receptors are covalently linked into a conjugated polymer chain, a single molecule of analyte quenches the emission of an excimer, which is able to delocalize over a larger region of the polymer chain. This quenching phenomenon is very similar to how a single defective light-bulb turns off a strand of Christmas lights wired in series.

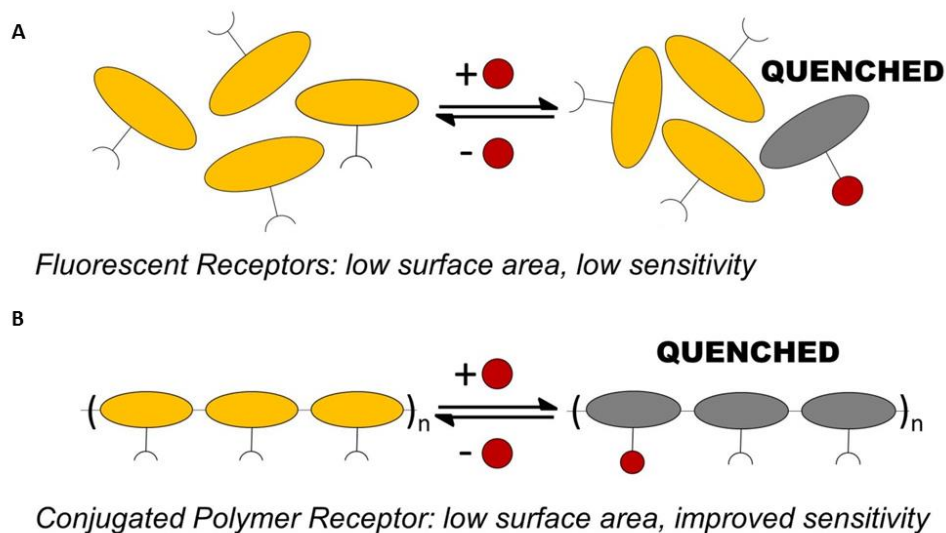


Figure 1.4: A) single molecule fluorescence receptor quenches in a 1 to 1 ratio with analyte B) conjugated porous polymer displays signal amplification through exciton quenching.

One of the first PIMs used for fluorescence sensing was developed by the Swagger group in 1998^{71,72}, and since then, many modifications to this original design have been developed to enhance sensitivity. The conjugated backbone seen in Figure 1.5, allows for excitons to diffuse along the polymer backbone, which is the basis for signal amplification. The large pentyptycene groups prevent the chains from stacking together which creates a two-fold advantage for this sensing system. By preventing the polymer chains from stacking, interlayer excitation quenching is reduced, meaning most of the quenching seen in the system comes from interaction with analytes. The second advantage is that the pentyptycene creates voids, making the polymer film slightly porous. These pores allow the TNT vapor to diffuse into the film, which allows TNT to interact with more of the polymer chains.

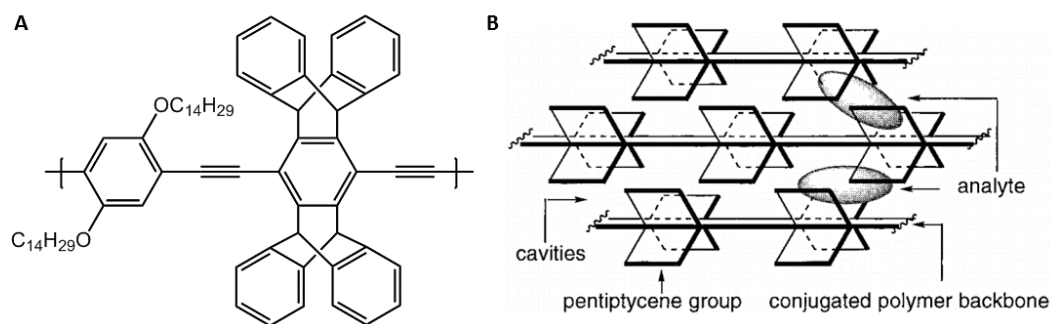


Figure 1.5: A) Structure of polymer used in reference 71, 71 for TNT sensing B) Diagram illustrating free space created by pentiptycene groups (from reference 72).

By modifying the polymer, through the addition of different sidechains, or creating other conjugated co-monomers, the Swager group is able to utilize this signal amplification method to detect biologically relevant molecules like tryptophan, or cytochrome *c*^{73,74}, TNT at lower concentrations^{75–77}, and methyl viologen in solution⁷⁸ (Figure 1.6). The diversity of sensing analytes targeted by this method shows both the compatibility of this method to different chemistries, and the effectiveness of signal amplification. Despite the success of these PIMs for sensing, there has not been significant research by other groups to include these intrinsically porous monomers into their system.

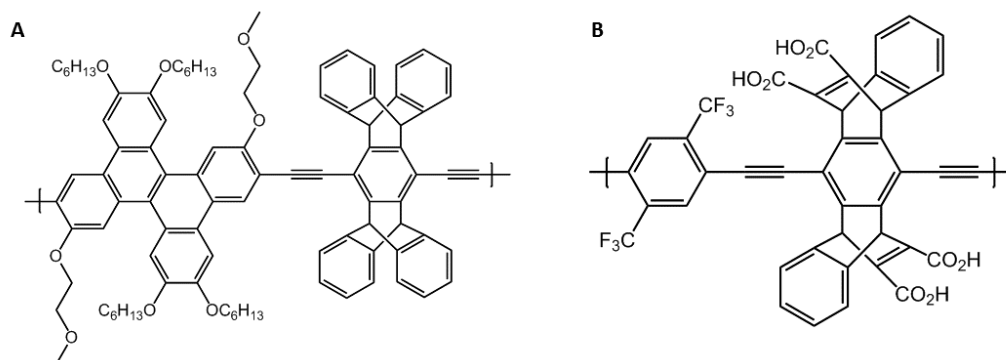


Figure 1.6: A) The addition of the dibenzo[g,p]chrysenes increases the exciton lifetime enhancing TNT sensing (reference 76) B) Modifications to the pentiptycene group and addition of electron withdrawing groups makes this polymer able to detect biologically relevant material (reference 74)

POPs for Sensing: Utilizing POPs for sensing was a natural progression to explore methods to enhance the sensitivity of PIMs. Since the chemistry of POPs is adaptable, POPs used for sensing applications drew from the chemistry of PIMs as a starting place, in the hopes of taking advantage of similar signal amplification properties. Also, the higher surface area of the materials opens the opportunity for better signal to noise in the responses allowing for lower limits of detection.

Many POPs are developed for heterogeneous catalysis applications, but the incorporation of Lewis bases into the POP framework also enable the binding of metal cations for sensing applications. The Xu group reports developing a porous triazine network (TMBPT) with a modest surface area, $355 \text{ m}^2\text{g}^{-1}$, that is able to selectively bind Ag(I) from solutions with other basic cations (Figure 1.7)⁷⁹. About 80% of the bound silver can be removed from the polymer, and the resulting partially loaded Ag-TMBPT can detect H_2S in solution. This colorimetric change does not occur with biologically relevant sulfur containing molecules like glutathione and cysteine. This

would allow for the monitoring of industrial waste without the concern of false positives from other sources of sulfur.

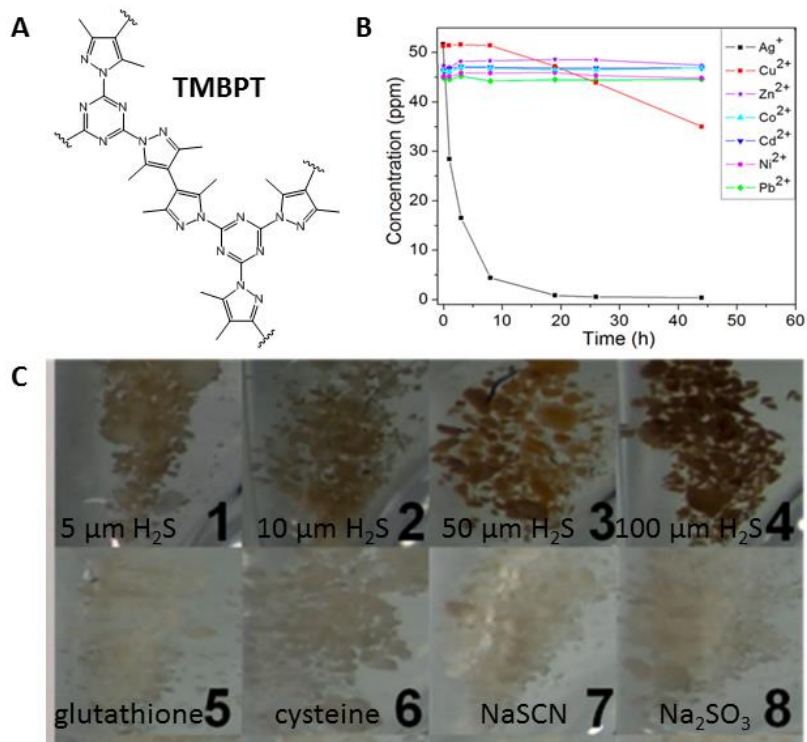


Figure 1.7: A) Structure of TMBPT B) Selective uptake of Ag(I) ions from solution containing other cations C) Images of TMBPT in various sulfur containing solutions. Modified from reference 79

Porous organic polymers have also been demonstrated for the detection of low volatility explosives, in particular RDX. The Dichtel group designed a tris(polyphenylene)vinylene (TFP) polymer, which can be grown as a thin film, which detects 1,3,5-trinitro-1,3,5-triazine (RDX) at the attogram scale from both solution and vapor phase^{26,27}. The performance of the films depends highly on the degree of conjugation, which can be monitored by UV-Vis spectroscopy. These thin films display signal amplification for the fluorescence quenching that is commonly utilized in PIMs. The TFP polymer also does not quench in the presence of other common

items travelers might have with them including lipstick, ethanol, and sunscreen, allowing for this material to be used in common screening situations, like airports (Figure 1.8).

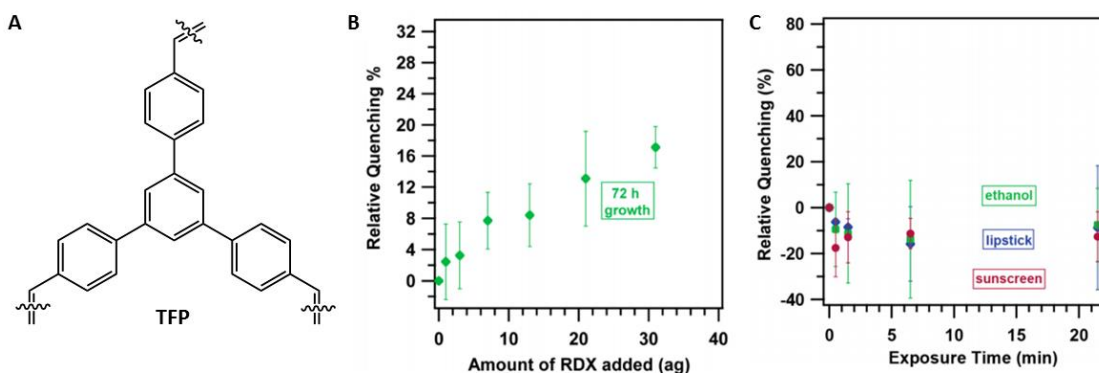


Figure 1.8: A) Structure of TFP B) Fluorescence quenching response of TFP film to RDX added from solution C) Fluorescence quenching response of TFP film to vapors of various common household items. Modified from reference 26

While these are just a few examples, POPs can be used for the detection of explosives^{29,30,80}, metal ions⁷⁹, volatile organic compounds⁸¹, just to name a few. These polymers utilize high surface areas to improve the signal-to-noise of their responses along with unique chemistries to be analyte specific. POPs have started to be grown as thin films and isolated on filter paper, which allows for facile incorporation into sensing devices.

COFs for Sensing: COFs have recently entered the field for sensing applications, mostly due to the limited chemistries known for COF formation. Currently there are only three examples of COF used for chemosensing^{82–84}. However, as the field is growing, there are many opportunities to utilize the chemistry of successful PIM and POP sensors. COFs have the advantage of high surface areas, which allow for facile

diffusion of analytes through the polymer, and regular moieties decorating the COF walls which allow for regular chemical recognition sites. Recent work has been on increasing the diversity of the chemical moieties within the COF framework, so soon COFs will be able to include analyte specific side chains like in PIMs.

Despite the high surface area of the material, so far all of the reports of COF sensing have been in solution. One of the first reports synthesizes an azine linked COF (Py-Azine COF) (Figure 1.9) which shows fluorescence quenching when exposed to nitroaromatics, in particular 1,3,5-trinitrophenol (TNP), better known as picric acid⁸³. The formation of the COF is strongly driven by the aromatic stacking of the pyrene unit, which contribute to the quenching sensitivity due to the ability for excitons to delocalize through the pyrene stacks. Furthermore, this synthesis places electron rich nitrogens along the pore wall, which can then hydrogen bond to the electron deficient nitroaromatic explosives. This material is especially sensitive to TNP because TNP is also the most acidic explosive tested. Through a Stern-Volmer analysis, this lead to a quenching constant for TNP to be $8 \times 10^4 \text{ M}^{-1}$, which is 37 and 86 times higher than those of DNP ($2.1 \times 10^3 \text{ M}^{-1}$) and DNT ($9.1 \times 10^2 \text{ M}^{-1}$), respectively (Figure 1.10).

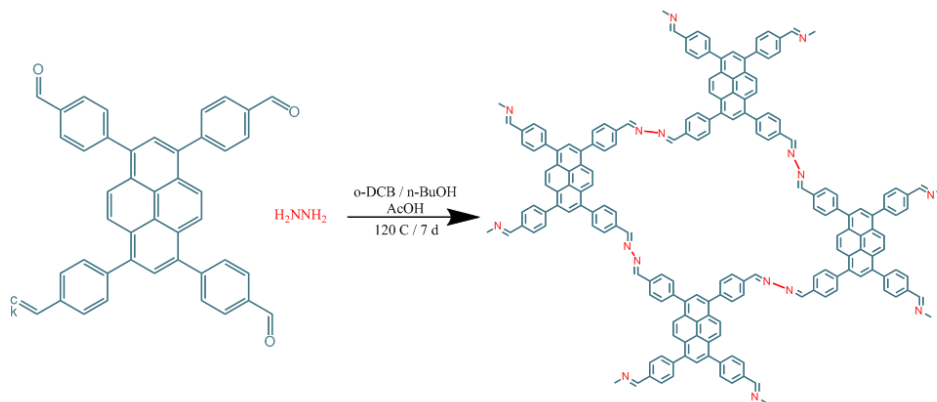


Figure 1.9: Structure of monomer and Py-Azine COF from reference 83

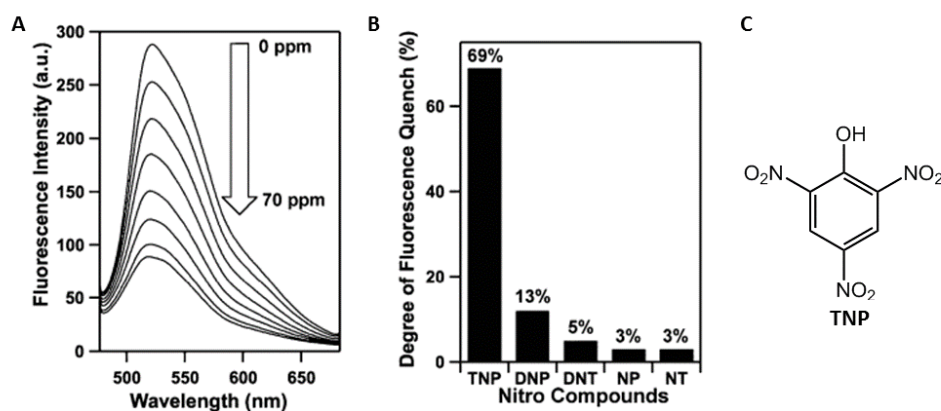


Figure 1.10: A) Fluorescence emission of Py-Azine COF exposed to various concentrations of TNP B) Fluorescence quenching response of Py-Azine COF to various nitro compounds. C) Structure of TNP. Modified from reference 83

Two years later, another group developed a new COF, again containing nitrogen decorating the pore walls which showed enhanced sensitivity to TNP. In this report⁸⁴, the Banerjee group synthesizes two new imide-based COFs (Figure 1.11), through traditional solvothermal conditions. Surprisingly, in these COFs, the sensing response to TNP is hindered by exciton delocalization through the stacks in the bulk

powder, so exfoliated nanosheets are used for sensing applications. Exfoliated sheets are isolated by sonicating the powder in IPA for nearly an hour and then isolating the soluble material. These exfoliated sheets are on average 5-15 layer thick, which minimizes the electron delocalization between sheets, thus creating an electron rich layer, which enhances the sensing interaction. Tp-DBH COF does not exhibit strong responses to nitroaromatics because the β -keto tautomerization which occurs during COF formation actually disrupts the conjugation enough to prevent strong signal amplification.

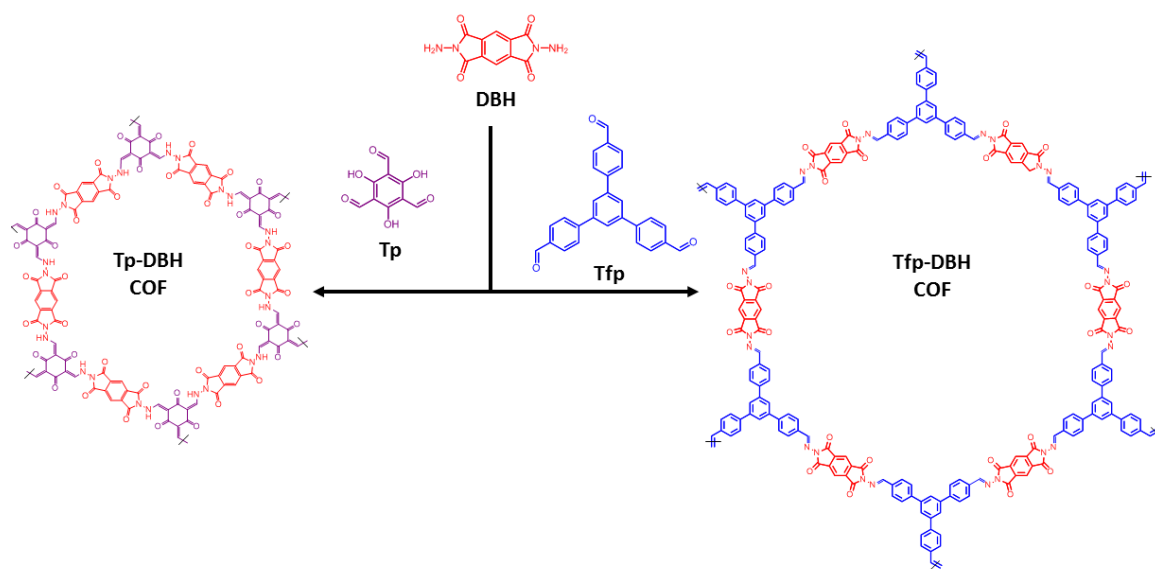


Figure 1.11: A) Synthesis and structure of the monomers and Tf-DBH and Tfp-DBH COFs. Modified from reference 84

In the Banerjee studies, their experiments display two different sensing responses depending on if their exfoliated Tfp-DBH COF sheets are dispersed in

solution or if they are dried on filter paper. The dispersed COF displayed fluorescence quenching in the presence of TNP, with quenching constant of $2.6 \times 10^4 \text{ M}^{-1}$.

However, when the exfoliated Tfp-DBH was dried on filter paper, when TNP in IP was added, the fluorescence emission shifted red and was enhanced, likely through an acid-base reaction with the acidic TNP and the basic imine on the COF walls. This interaction is reversible. Trimethylamine vapor is able to regenerate the original exfoliated COF fluorescence, and this process can be repeated multiple times.

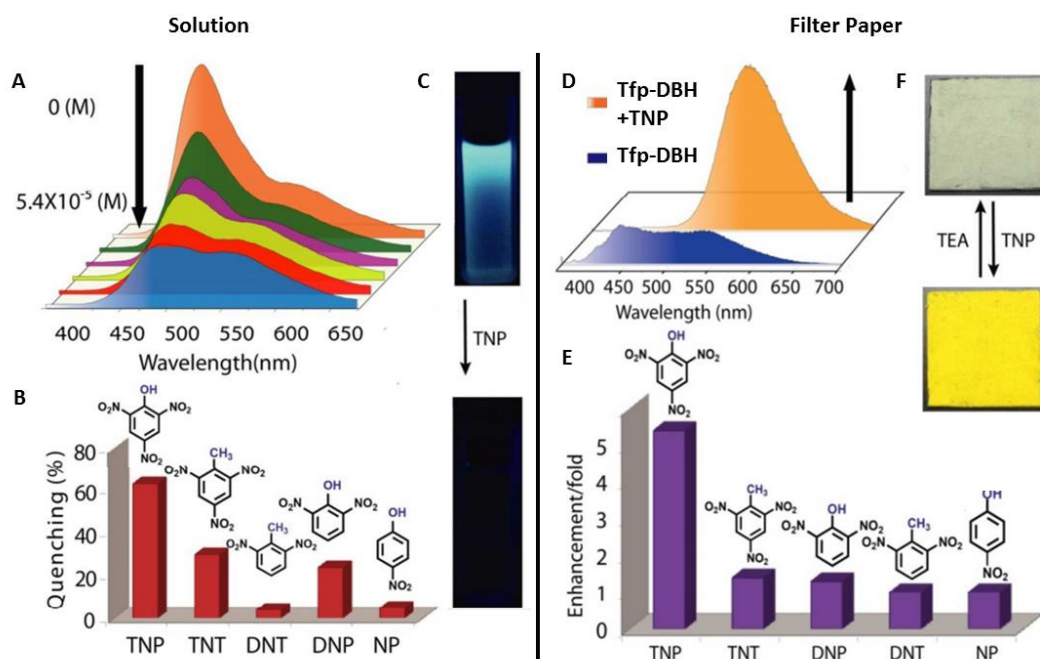


Figure 1.12: A) Fluorescence quenching response of exfoliated Tfp-DBH COF in solution to TNP B) Fluorescence quenching response of exfoliated Tfp-DBH in solution to various nitroaromatics C) Images of exfoliated Tfp-DBH COF in solution before (top) and after (bottom) addition of TNP D) Fluorescence enhancement of exfoliated Tfp-DBH COF films exposed to TNP in solution. E) Fluorescence enhancement of exfoliated Tfp-DBH COF films exposed to various nitroaromatics in solution F) Image of exfoliated Tfp-DBH COF film before (top) and after (bottom) addition of TNP Modified from reference 84

COFs have many advantages as chemosensors through their high surface areas, regular pore chemistries, the ability to modulate interlayer stacking, and the ability to tune the monomers that make up the COF. Until recently, many COFs were not stable under chemosensing conditions, but with the new developments in this field, it is very likely to more developments in the field COF sensing in the future.

Outlook: The utilization of porous materials for sensing has yielded large gains in sensitivity in many different fields. As more is understood about the host-guest interactions of these materials with different analytes, further selectivity and enhanced responses will be achieved. These materials often are easy to make which them desirable for incorporation into devices. By continuing to develop new chemistry, these high surface area materials will become more robust and will be applied to new applications.

REFERENCES

- (1) McKeown, N. B. *Int. Sch. Res. Not.* **2012**, 2012, e513986.
- (2) Weber, J.; Thomas, A. *J. Am. Chem. Soc.* **2008**, 130 (20), 6334–6335.
- (3) Budd, P. M.; Ghanem, B. S.; Makhseed, S.; McKeown, N. B.; Msayib, K. J.; Tattershall, C. E. *Chem. Commun.* **2004**, No. 2, 230–231.
- (4) McKeown, N. B.; Budd, P. M. *Macromolecules* **2010**, 43 (12), 5163–5176.
- (5) Bezzu, C. G.; Carta, M.; Tonkins, A.; Jansen, J. C.; Bernardo, P.; Bazzarelli, F.; McKeown, N. B. *Adv. Mater.* **2012**, 24 (44), 5930–5933.
- (6) Yang, J.-S.; Swager, T. M. *J. Am. Chem. Soc.* **1998**, 120 (21), 5321–5322.
- (7) McDonald, T. O.; Akhtar, R.; Lau, C. H.; Ratvijitvech, T.; Cheng, G.; Clowes, R.; Adams, D. J.; Hasell, T.; Cooper, A. I. *J. Mater. Chem. A* **2015**, 3 (9), 4855–4864.
- (8) McKeown, N. B.; Gahnem, B.; Msayib, K. J.; Budd, P. M.; Tattershall, C. E.; Mahmood, K.; Tan, S.; Book, D.; Langmi, H. W.; Walton, A. *Angew. Chem. Int. Ed.* **2006**, 45 (11), 1804–1807.
- (9) Budd, P. M.; McKeown, N. B.; Fritsch, D. *Macromol. Symp.* **2006**, 245-246 (1), 403–405.
- (10) McKeown, N. B. *Int. Sch. Res. Not.* **2012**, 2012, e513986.
- (11) Wang, Z.; Wang, D.; Jin, J. *Macromolecules* **2014**, 47 (21), 7477–7483.
- (12) Budd, P. M.; Msayib, K. J.; Tattershall, C. E.; Ghanem, B. S.; Reynolds, K. J.; McKeown, N. B.; Fritsch, D. *J. Membr. Sci.* **2005**, 251 (1–2), 263–269.
- (13) Jeon, Y.-W.; Lee, D.-H. *Environ. Eng. Sci.* **2015**, 32 (2), 71–85.
- (14) Rakow, N. A.; Wendland, M. S.; Trend, J. E.; Poirier, R. J.; Paolucci, D. M.; Maki, S. P.; Lyons, C. S.; Swierczek, M. J. *Langmuir* **2010**, 26 (6), 3767–3770.
- (15) Carturan, S.; Antonaci, A.; Maggioni, G.; Quaranta, A.; Tonezzer, M.; Milan, R.; Mea, G. D. In *Sensors and Microsystems*; Malcovati, P., Baschirotto, A., d'Amico, A., Natale, C., Eds.; Lecture Notes in Electrical Engineering; Springer Netherlands, 2010; pp 55–58.
- (16) Thomas, J. C.; Trend, J. E.; Rakow, N. A.; Wendland, M. S.; Poirier, R. J.; Paolucci, D. M. *Sensors* **2011**, 11 (3), 3267–3280.
- (17) Wang, Y.; McKeown, N. B.; Msayib, K. J.; Turnbull, G. A.; Samuel, I. D. W. *Sensors* **2011**, 11 (3), 2478–2487.
- (18) McKeown, N. B.; Budd, P. M. *Chem. Soc. Rev.* **2006**, 35 (8), 675–683.
- (19) Du, X.; Sun, Y.; Tan, B.; Teng, Q.; Yao, X.; Su, C.; Wang, W. *Chem Commun* **2010**, 46 (6), 970–972.
- (20) Cooper, A. I. *Adv. Mater.* **2009**, 21 (12), 1291–1295.
- (21) Jiang, J.-X.; Trewin, A.; Su, F.; Wood, C. D.; Niu, H.; Jones, J. T. A.; Khimyak, Y. Z.; Cooper, A. I. *Macromolecules* **2009**, 42 (7), 2658–2666.
- (22) Jiang, J.-X.; Su, F.; Trewin, A.; Wood, C. D.; Campbell, N. L.; Niu, H.; Dickinson, C.; Ganin, A. Y.; Rosseinsky, M. J.; Khimyak, Y. Z.; Cooper, A. I. *Angew. Chem. Int. Ed.* **2007**, 46 (45), 8574–8578.
- (23) Schmidt, J.; Werner, M.; Thomas, A. *Macromolecules* **2009**, 42 (13), 4426–4429.

- (24) Schmidt, J.; Weber, J.; Epping, J. D.; Antonietti, M.; Thomas, A. *Adv. Mater.* **2009**, *21* (6), 702–705.
- (25) Dawson, R.; Su, F.; Niu, H.; Wood, C. D.; Jones, J. T. A.; Khimyak, Y. Z.; Cooper, A. I. *Macromolecules* **2008**, *41* (5), 1591–1593.
- (26) Gopalakrishnan, D.; Dichtel, W. R. *J. Am. Chem. Soc.* **2013**, *135* (22), 8357–8362.
- (27) Gopalakrishnan, D.; Dichtel, W. R. *Chem. Mater.* **2015**.
- (28) Liu, X.; Xu, Y.; Jiang, D. *J. Am. Chem. Soc.* **2012**, *134* (21), 8738–8741.
- (29) Novotney, J. L.; Dichtel, W. R. *ACS Macro Lett.* **2013**, *2* (5), 423–426.
- (30) Naddo, T.; Che, Y.; Zhang, W.; Balakrishnan, K.; Yang, X.; Yen, M.; Zhao, J.; Moore, J. S.; Zang, L. *J. Am. Chem. Soc.* **2007**, *129* (22), 6978–6979.
- (31) Li, J.; Kendig, C. E.; Nesterov, E. E. *J. Am. Chem. Soc.* **2007**, *129* (51), 15911–15918.
- (32) Liu, X.; Xu, Y.; Jiang, D. *J. Am. Chem. Soc.* **2012**, *134* (21), 8738–8741.
- (33) Lee, J.-Y.; Wood, C. D.; Bradshaw, D.; Rosseinsky, M. J.; Cooper, A. I. *Chem. Commun.* **2006**, No. 25, 2670–2672.
- (34) Lu, W.; Yuan, D.; Zhao, D.; Schilling, C. I.; Plietzsch, O.; Muller, T.; Bräse, S.; Guenther, J.; Blümel, J.; Krishna, R.; Li, Z.; Zhou, H.-C. *Chem. Mater.* **2010**, *22* (21), 5964–5972.
- (35) McKeown, N. B.; Gahnem, B.; Msayib, K. J.; Budd, P. M.; Tattershall, C. E.; Mahmood, K.; Tan, S.; Book, D.; Langmi, H. W.; Walton, A. *Angew. Chem. Int. Ed.* **2006**, *45* (11), 1804–1807.
- (36) Wood, C. D.; Tan, B.; Trewin, A.; Niu, H.; Bradshaw, D.; Rosseinsky, M. J.; Khimyak, Y. Z.; Campbell, N. L.; Kirk, R.; Stöckel, E.; Cooper, A. I. *Chem. Mater.* **2007**, *19* (8), 2034–2048.
- (37) Wood, C. D.; Tan, B.; Trewin, A.; Su, F.; Rosseinsky, M. J.; Bradshaw, D.; Sun, Y.; Zhou, L.; Cooper, A. I. *Adv. Mater.* **2008**, *20* (10), 1916–1921.
- (38) McKeown, N. B.; Budd, P. M.; Msayib, K. J.; Ghanem, B. S.; Kingston, H. J.; Tattershall, C. E.; Makhseed, S.; Reynolds, K. J.; Fritsch, D. *Chem. – Eur. J.* **2005**, *11* (9), 2610–2620.
- (39) Park, H. B.; Jung, C. H.; Lee, Y. M.; Hill, A. J.; Pas, S. J.; Mudie, S. T.; Wagner, E. V.; Freeman, B. D.; Cookson, D. J. *Science* **2007**, *318* (5848), 254–258.
- (40) Dawson, R.; Laybourn, A.; Clowes, R.; Khimyak, Y. Z.; Adams, D. J.; Cooper, A. I. *Macromolecules* **2009**, *42* (22), 8809–8816.
- (41) Mackintosh, H. J.; Budd, P. M.; McKeown, N. B. *J. Mater. Chem.* **2008**, *18* (5), 573–578.
- (42) Kaur, P.; Hupp, J. T.; Nguyen, S. T. *ACS Catal.* **2011**, *1* (7), 819–835.
- (43) Côté, A. P.; Benin, A. I.; Ockwig, N. W.; O’Keeffe, M.; Matzger, A. J.; Yaghi, O. M. *Science* **2005**, *310* (5751), 1166–1170.
- (44) El-Kaderi, H. M.; Hunt, J. R.; Mendoza-Cortés, J. L.; Côté, A. P.; Taylor, R. E.; O’Keeffe, M.; Yaghi, O. M. *Science* **2007**, *316* (5822), 268–272.
- (45) Colson, J. W.; Woll, A. R.; Mukherjee, A.; Levendorf, M. P.; Spitler, E. L.; Shields, V. B.; Spencer, M. G.; Park, J.; Dichtel, W. R. *Science* **2011**, *332* (6026), 228–231.

- (46) Côté, A. P.; Benin, A. I.; Ockwig, N. W.; O’Keeffe, M.; Matzger, A. J.; Yaghi, O. M. *Science* **2005**, *310* (5751), 1166–1170.
- (47) Spitler, E. L.; Dichtel, W. R. *Nat. Chem.* **2010**, *2* (8), 672–677.
- (48) El-Kaderi, H. M.; Hunt, J. R.; Mendoza-Cortés, J. L.; Côté, A. P.; Taylor, R. E.; O’Keeffe, M.; Yaghi, O. M. *Science* **2007**, *316* (5822), 268–272.
- (49) Côté, A. P.; Benin, A. I.; Ockwig, N. W.; O’Keeffe, M.; Matzger, A. J.; Yaghi, O. M. *Science* **2005**, *310* (5751), 1166–1170.
- (50) Colson, J. W.; Dichtel, W. R. *Nat. Chem.* **2013**, *5* (6), 453–465.
- (51) Côté, A. P.; El-Kaderi, H. M.; Furukawa, H.; Hunt, J. R.; Yaghi, O. M. *J. Am. Chem. Soc.* **2007**, *129* (43), 12914–12915.
- (52) Ding, X.; Chen, L.; Honsho, Y.; Feng, X.; Saengsawang, O.; Guo, J.; Saeki, A.; Seki, S.; Irle, S.; Nagase, S.; Parasuk, V.; Jiang, D. *J. Am. Chem. Soc.* **2011**, *133* (37), 14510–14513.
- (53) Feng, X.; Ding, X.; Jiang, D. *Chem. Soc. Rev.* **2012**, *41* (18), 6010–6022.
- (54) Kandambeth, S.; Mallick, A.; Lukose, B.; Mane, M. V.; Heine, T.; Banerjee, R. *J. Am. Chem. Soc.* **2012**, *134* (48), 19524–19527.
- (55) Spitler, E. L.; Colson, J. W.; Uribe-Romo, F. J.; Woll, A. R.; Giovino, M. R.; Saldivar, A.; Dichtel, W. R. *Angew. Chem. Int. Ed.* **2012**, *51* (11), 2623–2627.
- (56) Uribe-Romo, F. J.; Doonan, C. J.; Furukawa, H.; Oisaki, K.; Yaghi, O. M. *J. Am. Chem. Soc.* **2011**, *133* (30), 11478–11481.
- (57) Doonan, C. J.; Tranchemontagne, D. J.; Glover, T. G.; Hunt, J. R.; Yaghi, O. M. *Nat. Chem.* **2010**, *2* (3), 235–238.
- (58) Furukawa, H.; Yaghi, O. M. *J. Am. Chem. Soc.* **2009**, *131* (25), 8875–8883.
- (59) Ding, X.; Guo, J.; Feng, X.; Honsho, Y.; Guo, J.; Seki, S.; Maitarad, P.; Saeki, A.; Nagase, S.; Jiang, D. *Angew. Chem. Int. Ed.* **2011**, *50* (6), 1289–1293.
- (60) Ding, S.-Y.; Gao, J.; Wang, Q.; Zhang, Y.; Song, W.-G.; Su, C.-Y.; Wang, W. *J. Am. Chem. Soc.* **2011**, *133* (49), 19816–19822.
- (61) Yang, L.-M.; Ganz, E.; Wang, S.; Li, X.-J.; Frauenheim, T. *J. Mater. Chem. C* **2015**, *3* (10), 2244–2254.
- (62) Ding, X.; Chen, L.; Honsho, Y.; Feng, X.; Saengsawang, O.; Guo, J.; Saeki, A.; Seki, S.; Irle, S.; Nagase, S.; Parasuk, V.; Jiang, D. *J. Am. Chem. Soc.* **2011**, *133* (37), 14510–14513.
- (63) DeBlase, C. R.; Silberstein, K. E.; Truong, T.-T.; Abruña, H. D.; Dichtel, W. R. *J. Am. Chem. Soc.* **2013**, *135* (45), 16821–16824.
- (64) DeBlase, C. R.; Hernández-Burgos, K.; Silberstein, K. E.; Rodríguez-Calero, G. G.; Bisbey, R. P.; Abruña, H. D.; Dichtel, W. R. *ACS Nano* **2015**, *9* (3), 3178–3183.
- (65) Hobson, S. T.; Cemalovic, S.; Patel, S. V. *The Analyst* **2012**, *137* (5), 1284–1289.
- (66) Adhikari, B.; Majumdar, S. *Prog. Polym. Sci.* **2004**, *29* (7), 699–766.
- (67) McQuade, D. T.; Pullen, A. E.; Swager, T. M. *Chem. Rev.* **2000**, *100* (7), 2537–2574.
- (68) Swager, T. M. *Acc. Chem. Res.* **1998**, *31* (5), 201–207.
- (69) Toal, S. J.; Trogler, W. C. *J. Mater. Chem.* **2006**, *16* (28), 2871–2883.

- (70) Thomas, S. W.; Joly, G. D.; Swager, T. M. *Chem. Rev.* **2007**, *107* (4), 1339–1386.
- (71) Yang, J.-S.; Swager, T. M. *J. Am. Chem. Soc.* **1998**, *120* (46), 11864–11873.
- (72) Yang, J.-S.; Swager, T. M. *J. Am. Chem. Soc.* **1998**, *120* (21), 5321–5322.
- (73) Kim, T.-H.; Swager, T. M. *Angew. Chem. Int. Ed.* **2003**, *42* (39), 4803–4806.
- (74) Kim, Y.; Swager, T. M. *Macromolecules* **2006**, *39* (16), 5177–5179.
- (75) Rose, A.; Lugmair, C. G.; Swager, T. M. *J. Am. Chem. Soc.* **2001**, *123* (45), 11298–11299.
- (76) Yamaguchi, S.; Swager, T. M. *J. Am. Chem. Soc.* **2001**, *123* (48), 12087–12088.
- (77) Zahn, S.; Swager, T. M. *Angew. Chem. Int. Ed.* **2002**, *41* (22), 4225–4230.
- (78) Joly, G. D.; Geiger, L.; Kooi, S. E.; Swager, T. M. *Macromolecules* **2006**, *39* (21), 7175–7177.
- (79) Liu, J.; Yee, K.-K.; Lo, K. K.-W.; Zhang, K. Y.; To, W.-P.; Che, C.-M.; Xu, Z. *J. Am. Chem. Soc.* **2014**, *136* (7), 2818–2824.
- (80) Andrew, T. L.; Swager, T. M. *J. Am. Chem. Soc.* **2007**, *129* (23), 7254–7255.
- (81) Liu, X.; Xu, Y.; Jiang, D. *J. Am. Chem. Soc.* **2012**, *134* (21), 8738–8741.
- (82) Yuan, Y.; Ren, H.; Sun, F.; Jing, X.; Cai, K.; Zhao, X.; Wang, Y.; Wei, Y.; Zhu, G. *J. Mater. Chem.* **2012**, *22* (47), 24558–24562.
- (83) Dalapati, S.; Jin, S.; Gao, J.; Xu, Y.; Nagai, A.; Jiang, D. *J. Am. Chem. Soc.* **2013**, *135* (46), 17310–17313.
- (84) Banerjee, R.; Das, G.; Biswal, B.; K, S. G.; Venkatesh, V.; Addicoat, M.; Heine, T.; Kaur, G.; Verma, S. *Chem. Sci.* **2015**.

CHAPTER 2

CONJUGATED POROUS POLYMERS FOR TNT VAPOR DETECTION

*ABSTRACT: A conjugated porous polymer (CPP) that exhibits fluorescence quenching when exposed to TNT vapor was synthesized via a Sonogashira cross-coupling reaction. Two polymerization solvents, DMF and PhMe, and two activation procedures, evacuation and lyophilization, were evaluated to optimize the response of the CPP to TNT vapor. Key differences in surface area and absorption were seen as a function of polymerization solvent and activation procedure. The polymer synthesized in DMF and activated by lyophilization had the highest surface area and the strongest response to TNT vapor. This paper demonstrates the importance of growth and activation conditions in optimizing the porosity and sensing performance of CPPs. This paper was originally published as [Novotney, J. L.; Dichtel, W. R.; *ACS Macro Lett.* **2013**, 2 (5), 423]*

PAPER: Explosive compounds, such as 2,4,6-trinitrotoluene (TNT), 1,3,5-trinitrotriazinane (RDX), and pentaerythritol tetranitrate (PETN), pose a large threat to public safety and military security. Detecting explosive devices or individuals contaminated by these compounds, which have low vapor pressures, represents a significant and important challenge.¹⁻⁴ Contemporary approaches include itemizers commonly used in aviation security, trained canines, colorimetric spot tests,^{5,6} and chemoresistive devices,⁷⁻⁹ many of which are equipment intensive, expensive, or do not allow for stand-off, remote detection. Fluorescence quenching of conjugated polymers offers an attractive alternative, as TNT and its common contaminant, 2,4-dinitrotoluene (DNT), provide a highly sensitive “turn-off” response by nonradiatively

deactivating their mobile excitons.² The most sensitive conjugated polymers readily detect TNT vapors and have achieved commercial and military adoption.¹⁰

Introducing free volume into conjugated polymer films was identified as an important design strategy for ultrasensitive TNT detection more than a decade ago, which was first accomplished by introducing large, shape persistent monomers within the polymer backbone.^{11,12} Several alternative strategies to impart permanent porosity and high-surface area to organic and organometallic materials have since emerged. These new materials classes include crystalline metal-organic and covalent organic frameworks (MOFs and COFs),¹³⁻¹⁷ amorphous polymers of intrinsic microporosity (PIMs)¹⁸⁻²⁰ and conjugated porous polymers (CPPs),^{21,22} and porous molecular cages.²³⁻²⁵ The high surface areas and tunable structures of many of these materials classes make them interesting candidates for detecting explosives, potentially enabling simultaneous concentration and detection of analytes of interest. Significant progress towards this goal was reported by Li and coworkers, who observed rapid and reversible fluorescence quenching of pillared Zn-paddlewheel MOFs by DNT and the explosive taggant 2,3-dimethyl-2,3-dinitrobutane.²⁶ Jiang and coworkers also reported a diindolinocarbazole-based CPP capable of detecting vapors of DNT and other more volatile nitroaromatic compounds.²⁷ Zang and Moore described carbazole-containing macrocycles that assemble into porous fibers that respond to TNT vapor, which is nearly 20 times less volatile than DNT.²⁸⁻³⁰ Here we report a CPP that responds to TNT vapor and evaluate important synthetic and processing parameters that impact its sensing performance. These considerations are particularly important for inherently insoluble materials, such as MOFs and CPPs, in order to evaluate their performance

relative to other fluorescent materials and incorporate them into relevant sensing devices.

The CPP **3** (Figure 2.1) was synthesized from dialkyne monomer **1** and 1,3,5-tribromobenzene **2** under typical Sonogashira cross-coupling conditions (0.02 eq Pd(PPh₃)₄; 0.02 eq CuI; excess NEt₃). The π -electron rich monomer **1** was employed because of its electronic complementarity to TNT and the use of 1,4-dialkoxybenzene subunits in highly sensitive linear conjugated polymers.^{12,31} These linear polymers commonly incorporate larger alkyl chains as solubilizing groups. Since CPP **3** is inherently insoluble, methoxy groups were used instead to maximize the free pore volumes of the CPP. A similar polymer network lacking methoxy groups (denoted CMP-4) was reported by Cooper and coworkers with a BET surface area of 744 m²/g.³² We prepared CPP-4 under similar conditions used to prepare **3** and obtained a BET surface area of 767 m²/g (Figure A1.26), which is approximately double that we obtained for a sample of **3** prepared in parallel (408 m²/g, see below). These differences may reflect a combination of the added size of monomer **1** and changes in the solubility and aggregation behavior of its growing polymer networks.

We prepared samples of **3** in two different solvents: DMF and PhMe, which provide polymers of similar chemical composition but significantly different porosity and TNT sensitivity (see below). For each solvent, **3** was isolated and characterized as an amorphous, insoluble powder. For optical characterization, we formed thin films of **3** by including a fused SiO₂ substrate in the growth solution. Powder samples of **3** were characterized by solid-state cross polarization magic angle spinning (CP-MAS) ¹³C NMR spectroscopy, FT-IR, UV-Vis absorption, fluorescence emission, thermal

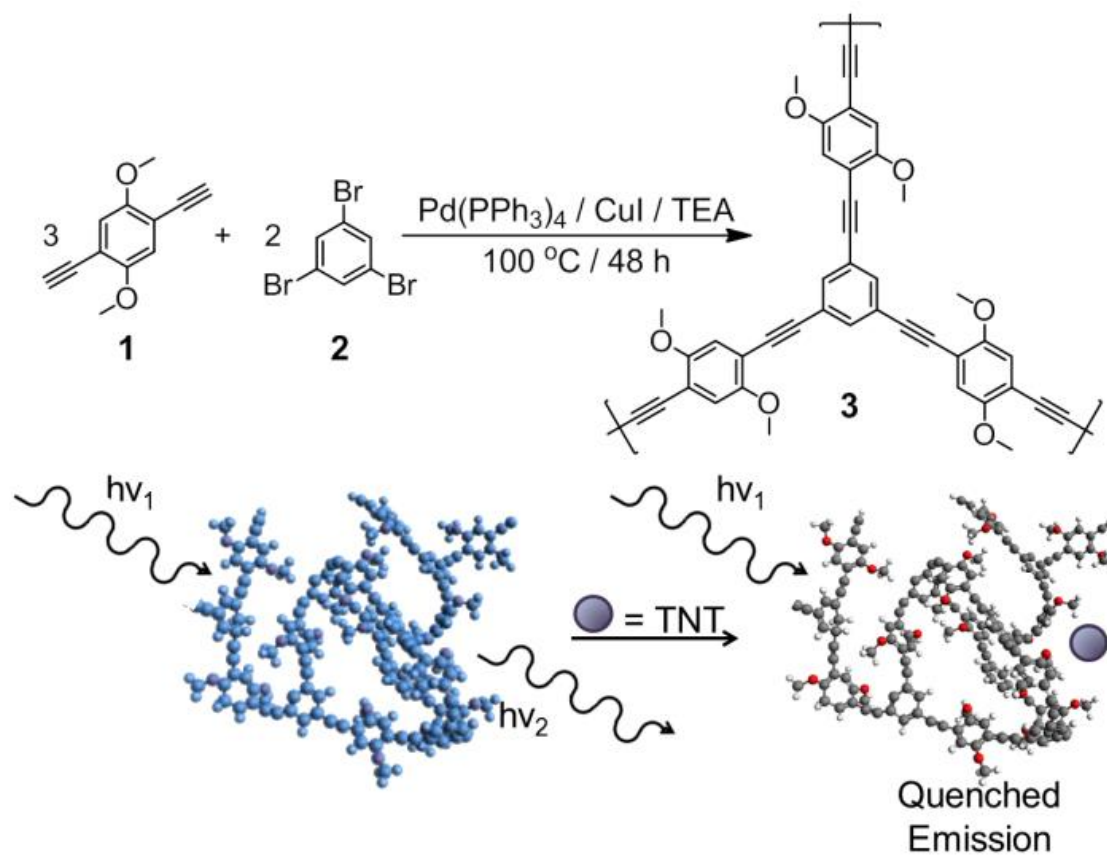


Figure 2.1. Synthesis of CPP 3 and schematic of its fluorescence response to nitroaromatic quenchers

gravimetric analysis, and N₂ adsorption measurements. The solid-state CP-MAS ¹³C NMR spectra were virtually identical for all powder samples (Supporting Information Figure A1.4), with resolved resonances at δ 148 ppm and 53 ppm, corresponding to the aryloxy and methoxy carbons, respectively. The spectra also exhibit broad peaks from 100-140 ppm, corresponding to the other aromatic carbons, and the alkyne carbons resonate at 80-100 ppm. The FT-IR spectra of each powder sample were also identical (Supporting Information Figures A1.5-A1.8), with absorbances at 1205 and 2210 cm⁻¹ that are characteristic of the methoxy and asymmetric alkyne stretches, respectively. Finally, all powders displayed high thermal stability associated with porous organic polymers and covalent organic frameworks (Supporting Information Figures A1.18-A1.21). These complementary analyses indicate that the expected arylene-ethynylene linked network structure is formed in each growth solvent.

In spite of their similar chemical structures, the polymer samples show dramatic differences in accessible surface area, as measured by their N₂ adsorption behavior. Independent of their polymerization solvent, CPP powders that were activated by evacuation under high vacuum (DMF-E or PhMe-E) showed low N₂ uptake and were essentially nonporous (Figure 2.2). In contrast, we found that freezing the polymers in 1,4-dioxane and removing the solvent by lyophilization provided higher surface area materials that demonstrated type II isotherms associated with microporous materials. A lyophilized polymer synthesized in DMF (DMF-L) showed the highest N₂ uptake, with an average BET surface area of 259 m²/g obtained over five samples. A lyophilized polymer synthesized in PhMe (PhMe-L) exhibited reduced N₂ uptake and BET surface area of 53 m²/g. These data indicate that evacuation

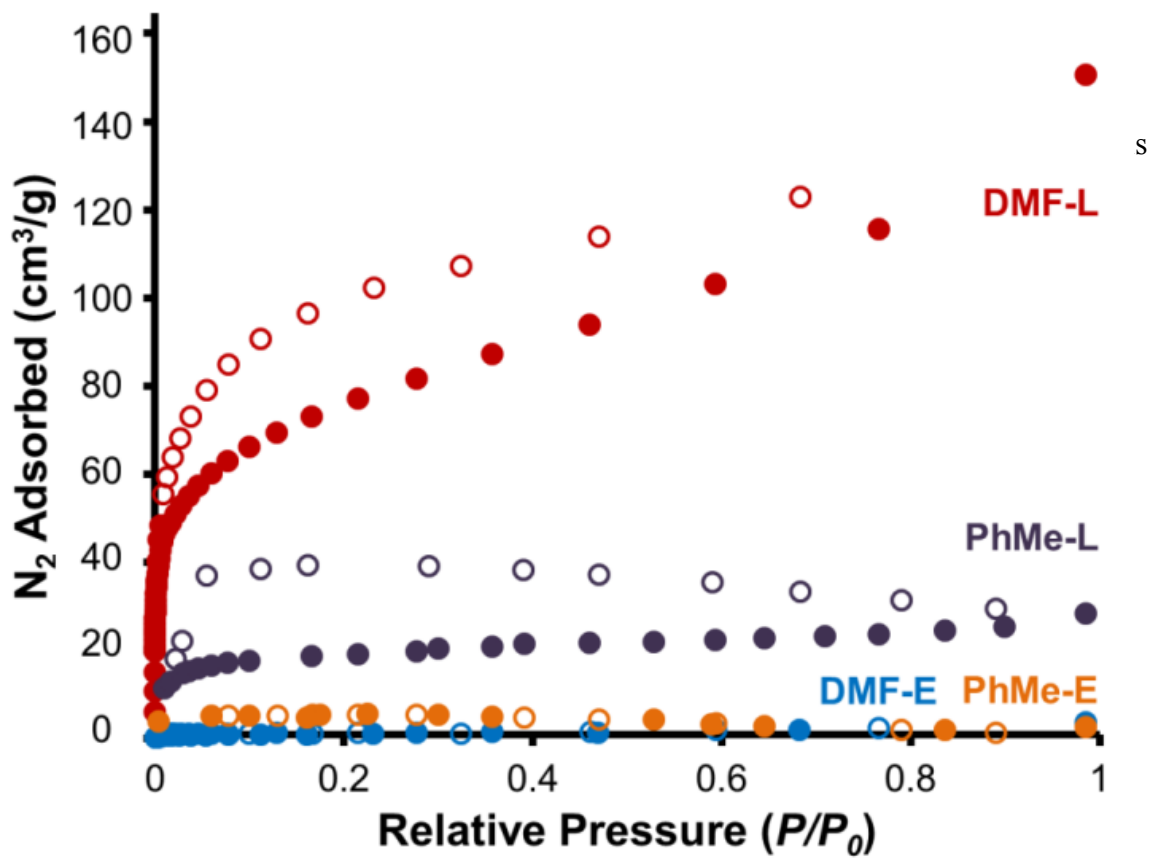


Figure 2.2. Representative N₂ adsorption isotherms for the CPP powder samples as a function of growth solvent and activation method.

higher surface areas than PhMe, which is expected to influence their sensing performance. Although the choice of reaction solvent must be optimized empirically for each new CPP, Cooper et al also noted superior surface areas for similar CPPs synthesized in DMF.³³

The absorbance properties of the CPP films show subtle but reproducible differences as a function of the polymerization solvent (Figure 2.3). Each film absorbs strongly out to ~450 nm, as expected for a m-polyphenyleneethynylene network. Local λ_{\max} are observed at 325 and 380 nm for DMF growths and 300 and 370 nm for PhMe growths, which could indicate an increased degree of conjugation in the DMF polymers consistent with their increased TNT sensitivity (see below). Although the normalized fluorescence spectra of polymers activated through each method are similar, their fluorescence quantum yields differ significantly. DMF-L films are the most emissive ($\Phi_{\text{rel}} = 1$), while the other activation methods provide less emissive films (see Table 2.1 and Figure A1.17). These differences in emission efficiency may arise from variable degrees of chromophore aggregation obtained from the growth and activation protocols.

The sensitivity of polymer fluorescence to TNT vapor (approx. 5 ppb equilibrium concentration) was evaluated using films of each growth and processing method. The initial fluorescence of a film was measured, after which it was stored in a sealed desiccator containing an open sample of TNT adsorbed onto sand, which are commonly used to train bomb-sniffing dogs. The film was removed from the desiccator at various time intervals and its fluorescence spectrum was recorded. The

Polymer	Relative Fluorescence Quantum Yield (Φ_{rel})
DMF-L	1.00
DMF-E	0.13
PhMe-L	0.45
PhMe-E	0.41

Table 2.1: Relative fluorescence quantum yields of **3** as a function of growth solvent and activation method.

DMF-L, PhMe-L, DMF-E, and PhMe-E films each showed decreased emission in response to TNT vapor over the course of 1 h (Figure 2.4 A-D). The magnitude of this effect depended strongly on the synthesis and processing methods. Figure 2.4E indicates the average relative fluorescence quenching for 7-12 samples of each type of film as a function of TNT exposure time. Independent of activation method, polymer films synthesized in DMF show increased TNT response as compared to films synthesized in PhMe. We attribute this difference to longer excitation diffusion lengths in the DMF films, as suggested by the differences in their absorbance spectra. These differences might arise from increased conversion of the Sonogashira polymerization or from differences in chromophore aggregation. Furthermore, DMF-L films show both faster and more complete quenching than those activated through evacuation. This trend is consistent with the surface area analysis of the corresponding powder samples, in which DMF-L samples showed the highest porosity. Interestingly, PhMe-L and PhMe-E films showed similar quenching responses, indicating either that they are inherently insensitive to TNT or that the only modest surface areas of the PhMe-L samples do not confer additional sensitivity. These results indicate the importance of optimizing sensing performance of conjugated porous polymers by varying both the growth solvent and activation protocols.

In conclusion, we report a CPP that detects TNT vapor. Through this study we have shown how growth and activation procedures strongly influence analyte response and introduce lyophilization as a gentle and convenient activation method that requires no specialized equipment. With this preliminary study, we have demonstrated that this class of polymers shows promise for detecting low-volatility explosives, but further

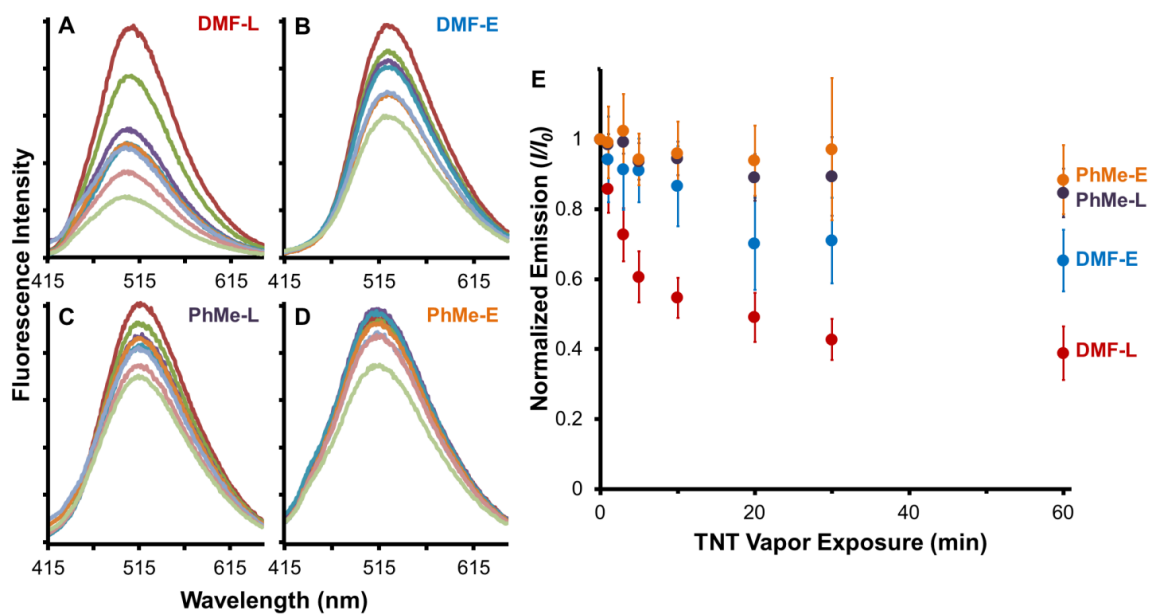


Figure 2.4. A-D: Fluorescence emission ($\lambda_{\text{ex}} = 396 \text{ nm}$) of polymer films exposed to TNT vapor for times ranging from 0-60 min. E: Combined quenching curves of polymer films (7-12 films of each type) with exposure to TNT vapor.

work is required to achieve the rapid and reversible response seen in other electron-rich polymer systems. Future work will involve optimizing the CPP chemical structure and synthetic and processing conditions to address this challenge. Controlled methods for forming CPP films and characterizing their structure will be of great future value.

REFERENCES

- (1) McQuade, D. T.; Pullen, A. E.; Swager, T. M. *Chem. Rev.* **2000**, *100* (7), 2537–2574.
- (2) Thomas, S. W.; Joly, G. D.; Swager, T. M. *Chem. Rev.* **2007**, *107* (4), 1339–1386.
- (3) Toal, S. J.; Trogler, W. C. *J. Mater. Chem.* **2006**, *16* (28), 2871–2883.
- (4) Singh, S. *J. Hazard. Mater.* **2007**, *144* (1–2), 15–28.
- (5) Germain, M. E.; Knapp, M. J. *Chem. Soc. Rev.* **2009**, *38* (9), 2543–2555.
- (6) Salinas, Y.; Martínez-Mañez, R.; Marcos, M. D.; Sancenón, F.; Costero, A. M.; Parra, M.; Gil, S. *Chem Soc Rev* **2012**, *41* (3), 1261–1296.
- (7) Li, J.; Lu, Y.; Ye, Q.; Cinke, M.; Han, J.; Meyyappan, M. *Nano Lett.* **2003**, *3* (7), 929–933.
- (8) Chen, P.-C.; Sukcharoenchoke, S.; Ryu, K.; Gomez de Arco, L.; Badmaev, A.; Wang, C.; Zhou, C. *Adv. Mater.* **2010**, *22* (17), 1900–1904.
- (9) Engel, Y.; Elnathan, R.; Pevzner, A.; Davidi, G.; Flaxer, E.; Patolsky, F. *Angew. Chem. Int. Ed.* **2010**, *49* (38), 6830–6835.
- (10) Cumming, C. J.; Aker, C.; Fisher, M.; Fok, M.; la Grone, M. J.; Reust, D.; Rockley, M. G.; Swager, T. M.; Towers, E.; Williams, V. *IEEE Trans. Geosci. Remote Sens.* **2001**, *39* (6), 1119–1128.
- (11) Yang, J.-S.; Swager, T. M. *J. Am. Chem. Soc.* **1998**, *120* (46), 11864–11873.
- (12) Yang, J.-S.; Swager, T. M. *J. Am. Chem. Soc.* **1998**, *120* (21), 5321–5322.
- (13) Long, J. R.; Yaghi, O. M. *Chem. Soc. Rev.* **2009**, *38* (5), 1213–1214.
- (14) Cote, A. P. *Science* **2005**, *310* (5751), 1166–1170.
- (15) Tilford, R. W.; Gemmill, W. R.; zur Loye, H.-C.; Lavigne, J. J. *Chem. Mater.* **2006**, *18* (22), 5296–5301.
- (16) Wan, S.; Guo, J.; Kim, J.; Ihee, H.; Jiang, D. *Angew. Chem. Int. Ed.* **2008**, *47* (46), 8826–8830.
- (17) Spitler, E. L.; Dichtel, W. R. *Nat. Chem.* **2010**, *2* (8), 672–677.
- (18) Budd, P. M.; McKeown, N. B.; Fritsch, D. *J. Mater. Chem.* **2005**, *15* (20), 1977–1986.
- (19) Budd, P. M.; Ghanem, B. S.; Makhseed, S.; McKeown, N. B.; Msayib, K. J.; Tattershall, C. E. *Chem. Commun.* **2004**, No. 2, 230–231.
- (20) McKeown, N. B.; Budd, P. M. *Macromolecules* **2010**, *43* (12), 5163–5176.
- (21) Dawson, R.; Laybourn, A.; Clowes, R.; Khimiyak, Y. Z.; Adams, D. J.; Cooper, A. I. *Macromolecules* **2009**, *42* (22), 8809–8816.
- (22) Dawson, R.; Laybourn, A.; Khimiyak, Y. Z.; Adams, D. J.; Cooper, A. I. *Macromolecules* **2010**, *43* (20), 8524–8530.
- (23) Tozawa, T.; Jones, J. T. A.; Swamy, S. I.; Jiang, S.; Adams, D. J.; Shakespeare, S.; Clowes, R.; Bradshaw, D.; Hasell, T.; Chong, S. Y.; Tang, C.; Thompson, S.; Parker, J.; Trewin, A.; Bacsá, J.; Slawin, A. M. Z.; Steiner, A.; Cooper, A. I. *Nat. Mater.* **2009**, *8* (12), 973–978.
- (24) Mastalerz, M. *Angew. Chem. Int. Ed.* **2010**, *49* (30), 5042–5053.
- (25) Cooper, A. I. *Angew. Chem. Int. Ed.* **2011**, *50* (5), 996–998.

- (26) Lan, A.; Li, K.; Wu, H.; Olson, D. H.; Emge, T. J.; Ki, W.; Hong, M.; Li, J. *Angew. Chem. Int. Ed.* **2009**, *48* (13), 2334–2338.
- (27) Liu, X.; Xu, Y.; Jiang, D. *J. Am. Chem. Soc.* **2012**, *134* (21), 8738–8741.
- (28) Naddo, T.; Che, Y.; Zhang, W.; Balakrishnan, K.; Yang, X.; Yen, M.; Zhao, J.; Moore, J. S.; Zang, L. *J. Am. Chem. Soc.* **2007**, *129* (22), 6978–6979.
- (29) Zhang, C.; Che, Y.; Yang, X.; Bunes, B. R.; Zang, L. *Chem. Commun.* **2010**, *46* (30), 5560–5562.
- (30) Che, Y.; Gross, D. E.; Huang, H.; Yang, D.; Yang, X.; Discekici, E.; Xue, Z.; Zhao, H.; Moore, J. S.; Zang, L. *J. Am. Chem. Soc.* **2012**, *134* (10), 4978–4982.
- (31) Li, J.; Kendig, C. E.; Nesterov, E. E. *J. Am. Chem. Soc.* **2007**, *129* (51), 15911–15918.
- (32) Jiang, J.-X.; Su, F.; Trewin, A.; Wood, C. D.; Campbell, N. L.; Niu, H.; Dickinson, C.; Ganin, A. Y.; Rosseinsky, M. J.; Khimyak, Y. Z.; Cooper, A. I. *Angew. Chem. Int. Ed.* **2007**, *46* (45), 8574–8578.
- (33) Dawson, R.; Cooper, A. I.; Adams, D. J. *Prog. Polym. Sci.* **2012**, *37* (4), 530–563.

APPENDIX 1

A. Materials. All reagents were purchased from commercial sources and used without further purification. Other solvents were purchased from commercial sources and purified using a custom-built alumina-column based solvent purification system.

Instrumentation.

Infrared spectra were recorded on a Thermo Nicolet iS10 with a diamond ATR attachment and are uncorrected.

UV/Vis absorbance spectra were recorded on a Cary 5000 UV-Vis-NIR spectrophotometer with a mercury lamp either as thin films on fused silica using a solid sample holder or as solids using a praying mantis diffuse reflectance accessory. Emission spectra were recorded on a Horiba Jobin Yvon Fluorolog-3 fluorescence spectrophotometer equipped with a 450 W Xe lamp, double excitation and double emission monochromators, a digital photon-counting photomultiplier and a secondary InGaAs detector for the NIR range. Correction for variations in lamp intensity over time and wavelength was achieved with a solid-state silicon photodiode as the reference. The spectra were further corrected for variations in photomultiplier response over wavelength and for the path difference between the sample and the reference by multiplication with emission correction curves generated on the instrument. The fused silica substrates were mounted on a solid sample holder, and emission was observed using a front face detection accessory.

Thermogravimetric analysis from 20-600 °C was carried out on a TA Instruments Q500 Thermogravimetric Analyzer in nitrogen atmosphere using a 10 °C/min ramp without equilibration delay.

Surface area measurements were conducted on a Micromeritics ASAP 2020 Accelerated Surface Area and Porosimetry Analyzer using ca. 20 mg samples degassed at 60 °C for 12 hours. Ar isotherms were generated by incremental exposure to ultra high purity argon up to ca. 1 atm over 48-hour periods in a liquid Ar (87K) bath, and surface area parameters were determined using BET adsorption models included in the instrument software (Micromeritics ASAP 2020 V1.05).

NMR spectra of solutions were recorded on a Varian INOVA-400 MHz spectrometer using a standard AWX probe at ambient temperature with a 20 Hz sample spin rate. Solid-state NMR spectra were recorded at ambient temperature on a Varian INOVA-400 spectrometer using an external Kalmus ¹H linear pulse amplifier blanked using a spare line.

Samples were packed into 7 mm outside diameter silicon nitride rotors and inserted into a Varian HX magic angle spinning (MAS) probe. ^{13}C data was acquired using linearly ramped cross-polarization with MAS (CP/MAS) at 100.5 MHz. The ^1H and ^{13}C had ninety-degree pulse widths of 5 μs , and the CP contact time was 1 ms. Two-pulse phase modulation (TPPM) ^1H decoupling was applied during data acquisition with a decoupling frequency of 78 kHz. The recycle delays between scans were 2 s. The MAS spin rate varied between 6–7 kHz, as labeled in the spectra. ^{13}C chemical shifts were assigned relative to tetramethylsilane at 0.0 ppm and were calibrated using the methyl carbon signal of hexamethylbenzene assigned at 16.9 ppm.

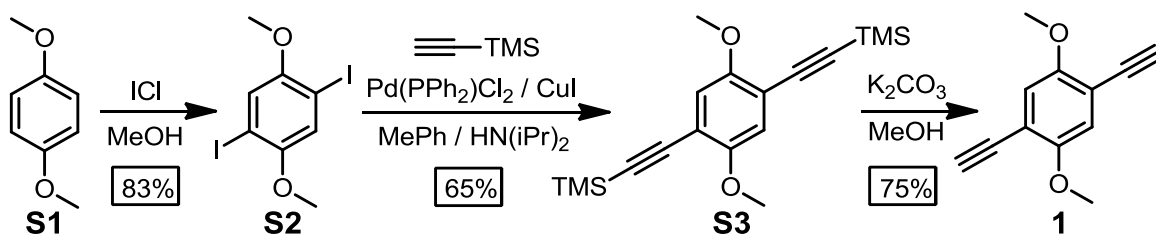
B. Methods and Synthetic Procedures.

General polymerization procedure and growth of polymer films. 1,4-diethynyl-2,5-dimethoxybenzene (200 mg, 1.07 mmol), 1,3,5-tribromobenzene (226 mg, 0.716 mmol), CuI (4 mg, 0.02 mmol), and Pd(PPh₃)₄ (12 mg, 0.0010 mmol) were added to a 100 mL round bottom flask containing six fused SiO₂ substrates (1 cm x 2 cm) under a N₂ atmosphere. Anhydrous DMF (32 mL) and anhydrous NEt₃ (4 mL) were added and the solution was stirred and heated to 100 °C for 48 h under nitrogen. The mixture was cooled to rt and the resulting bulk polymer was isolated as an orange gel by filtration. The polymer and films were washed with CHCl₃/MeOH (1:1 v/v) in a Soxhlet extractor for 24 h and then subjected to one of the following processing procedures:

A. Evacuation: The sample was activated under dynamic vacuum at rt for 24 h.

B. Lyophilization: The sample was washed with 1,4-dioxane in a Soxhlet extractor for 24 h, after which the polymer or fused silica substrate was submerged in fresh dioxane, frozen in a liquid N₂ bath, and lyophilized under dynamic vacuum for 24 h.

Scheme A.2.1. Synthesis of 1,4-diethynyl-2,5-dimethoxybenzene (**1**).



Preparation of 1,4-diiodo-2,5-dimethoxybenzene (S2): **S2** was synthesized using the procedure described by Inagaki. Analysis matched the previous report¹.

Preparation of S3: A 100 mL round bottom flask was charged with **S2** (5.00 g, 12.8 mmol), Pd(PPh₃)₂Cl₂ (0.180 g, 0.257 mmol), and CuI (0.098 g, 0.51 mmol), and placed under N₂. The solids were dissolved in anhydrous PhMe:HN(iPr)₂ (2:1 v/v, 55 mL) and stirred for 5 min, after which degassed trimethylsilacetylene (3.895 g, 39.65 mmol) was added. The mixture was stirred at rt for 48 h. The reaction mixture was filtered through celite using excess Et₂O (300 mL). The filtrate was washed with aqueous NH₄Cl (saturated, 3 x 200 mL), after which it was dried (MgSO₄), filtered, and solvent removed to yield **S3** as a dark yellow solid. The solid was dried under high vacuum, yielding 2.77 g (65%) of **S3** as a white powder.. Analysis of **S3** matched a previous report².

Preparation of 1: **S3** (1.750 g, 5.262 mmol) was dissolved in CH₂Cl₂ (10 mL) in a 250 mL round bottom flask. Anhydrous K₂CO₃ (5.730 g, 41.46 mmol) and MeOH (100 mL) were added, and the mixture stirred at 45 °C for 48 h. The reaction mixture was cooled to rt and filtered through silica gel using Et₂O (300 mL). The filtrate was washed with H₂O (3 x 200 mL). The organic layer was dried (MgSO₄), filtered, and solvent removed to give **1** (0.740 g, 75% yield) as a yellow powder. Analysis of **1** matched a previous report³.

C. NMR Spectra

Figure A1.1: ^1H NMR of Compound S2

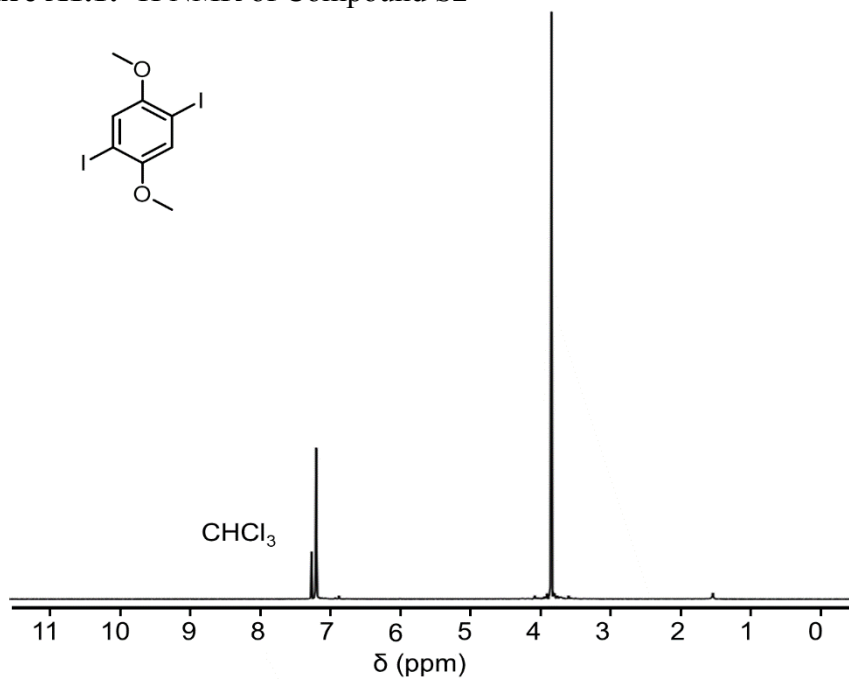


Figure A1.2: ^1H NMR of Compound S3

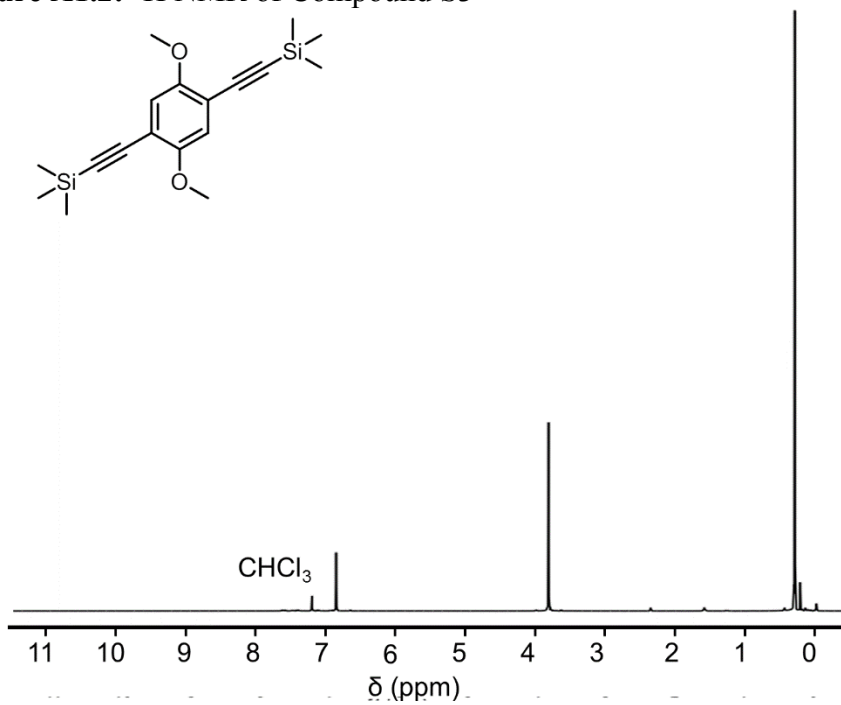


Figure A1.3: ^1H NMR of Compound 1

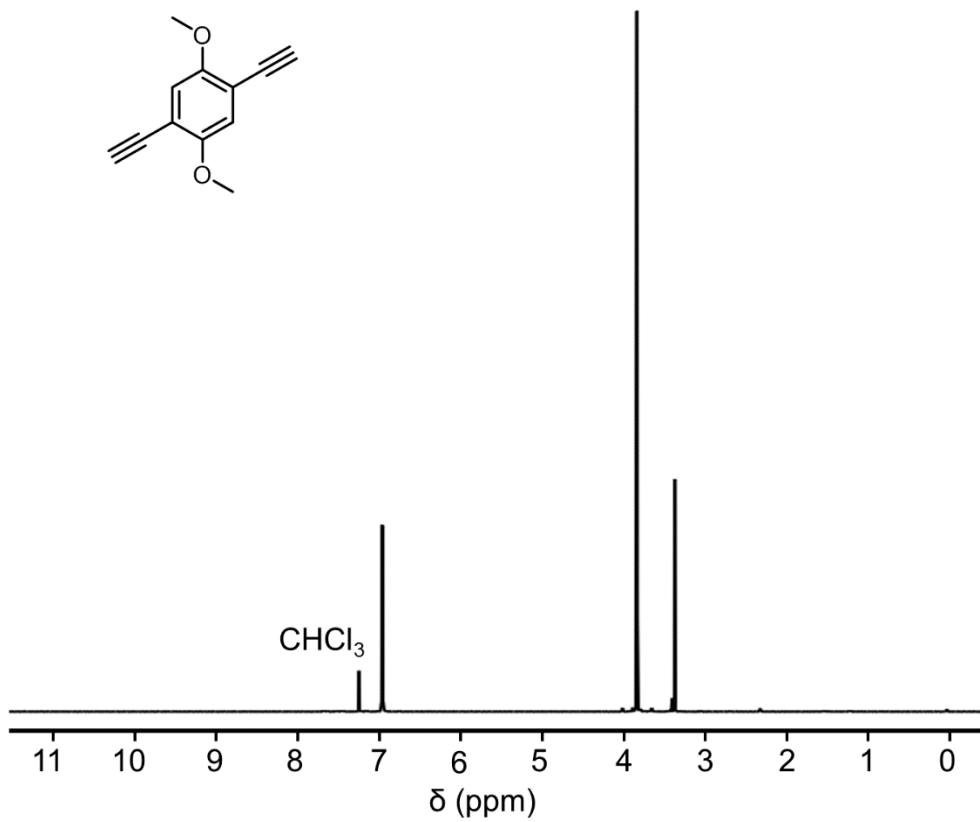
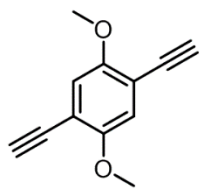
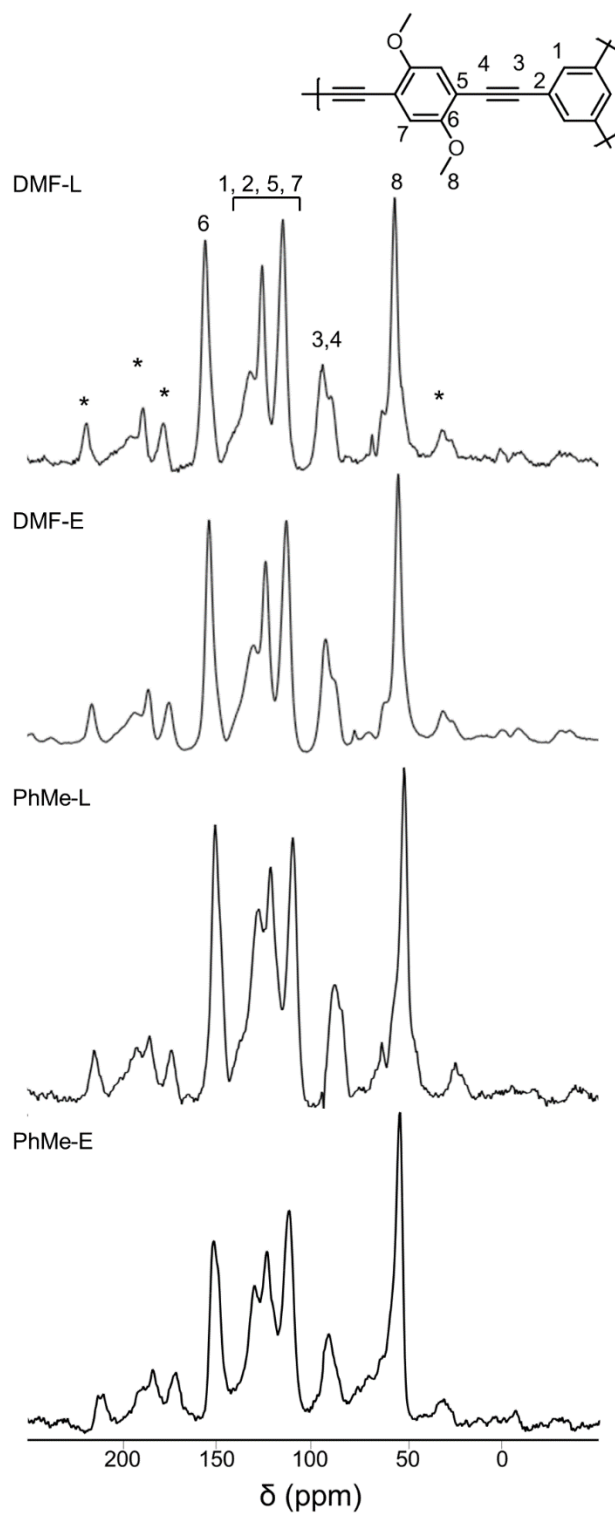


Figure A1.4: ^{13}C solid state cross polarization magic angle spinning (CP-MAS) NMR of polymer powders, spin rate = 6.2 kHz. Chemical shifts assigned by comparison to starting materials. Asterisks denote spinning side bands



D. FT-IR of Polymer

Figure A1.5: FT-IR of Polymer prepared in DMF and activated by lyophilization.

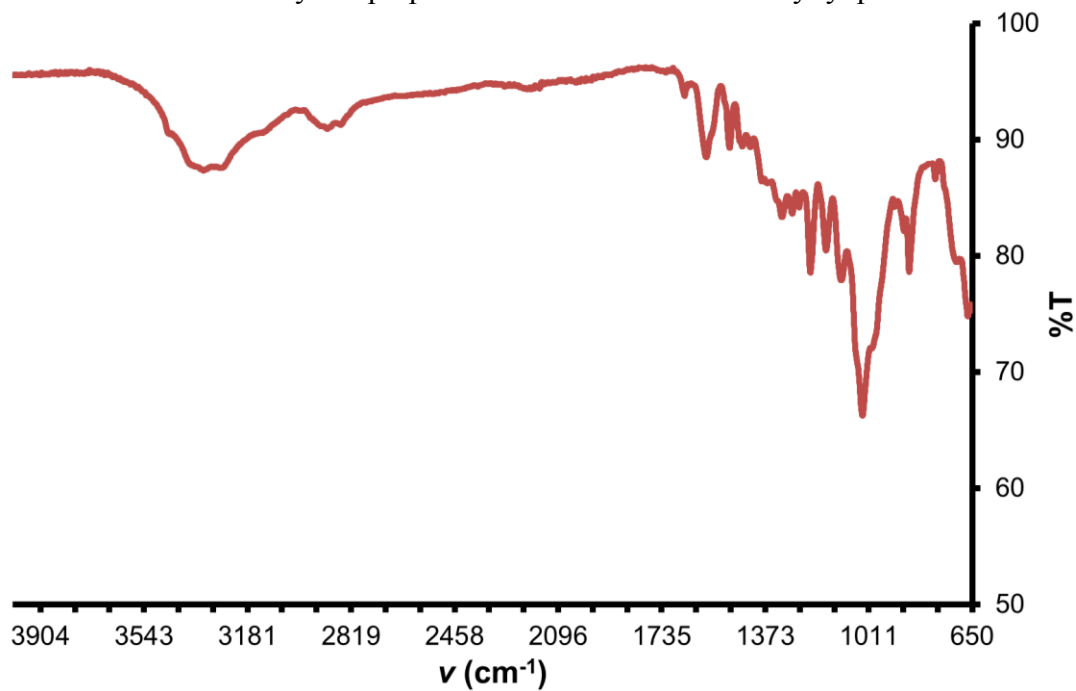


Figure A1.6: FT-IR of Polymer prepared in DMF and activated by evacuation.

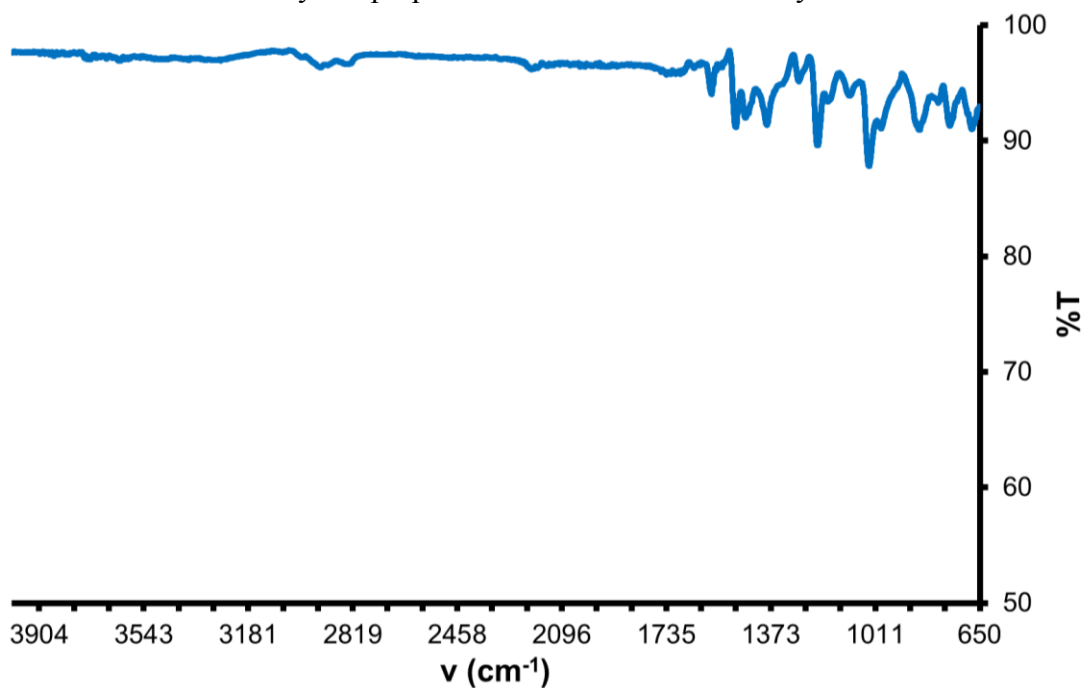


Figure A1.7: FT-IR of Polymer prepared in PhMe and activated by lyophilization.

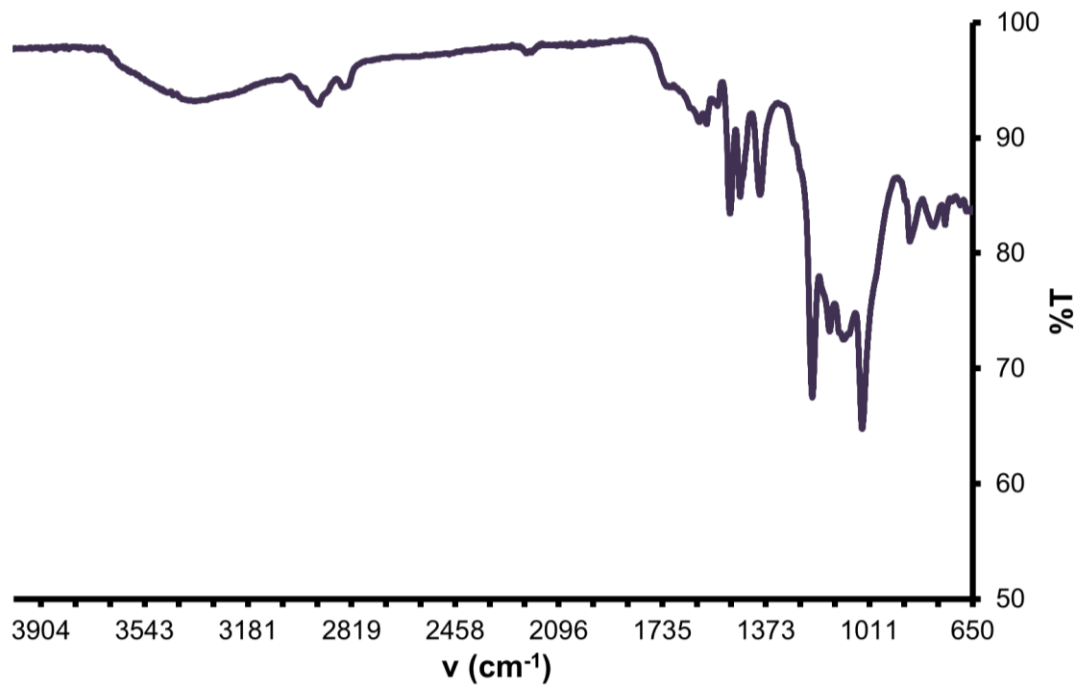
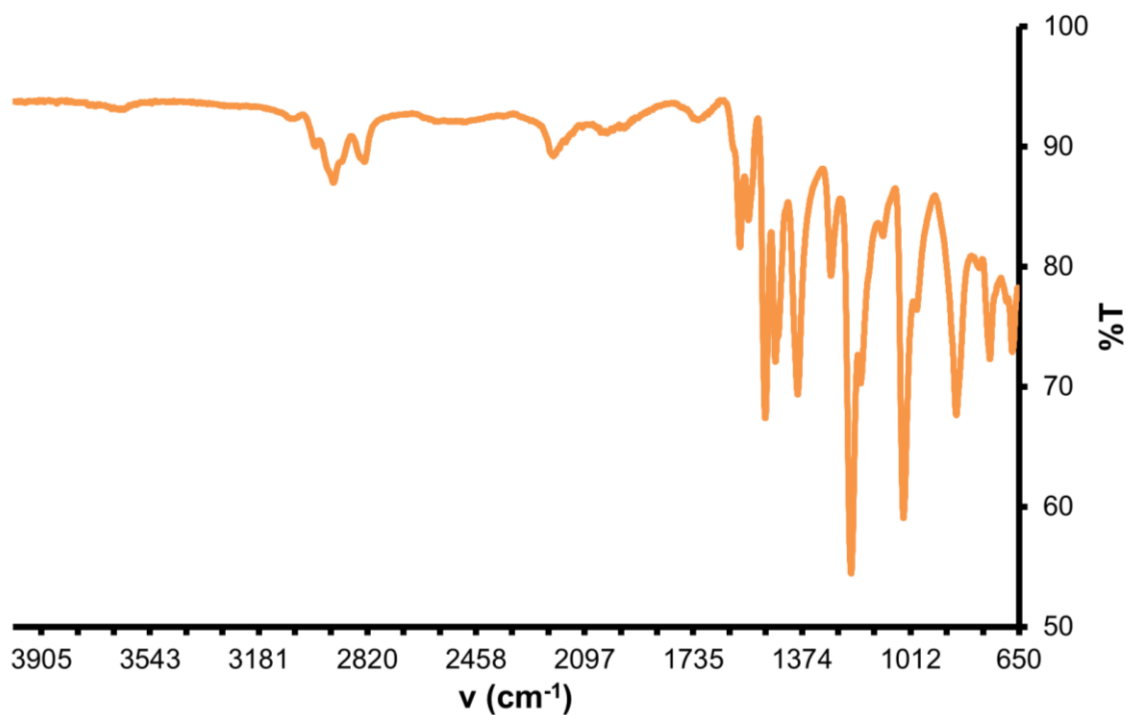


Figure A1.8: FT-IR of Polymer prepared in PhMe and activated by evacuation.



E. Diffuse Reflectance UV-Vis of polymer powders

Figure A1.9: Absorbance of lyophilized polymer from DMF growth.

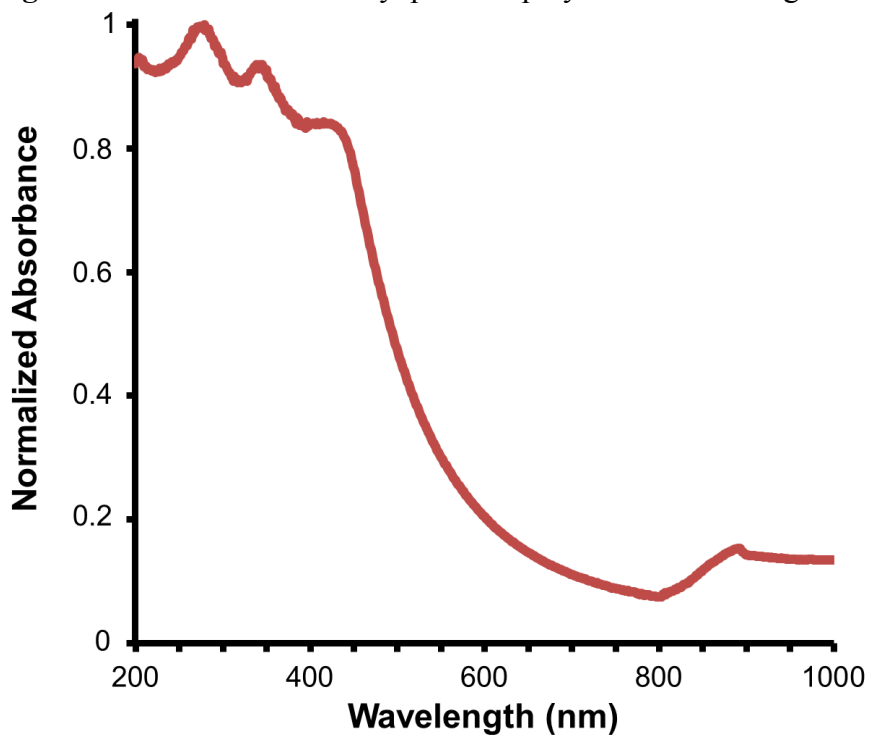


Figure A1.10: Absorbance of evacuated polymer from DMF growth

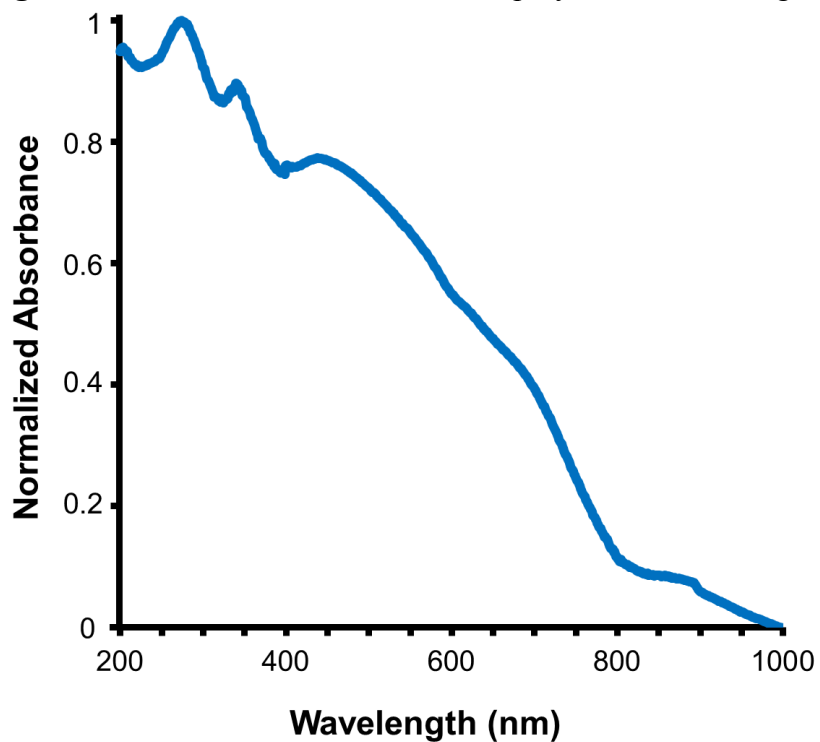


Figure A1.11: Absorbance of polymer prepared by lyophilization from PhMe growth

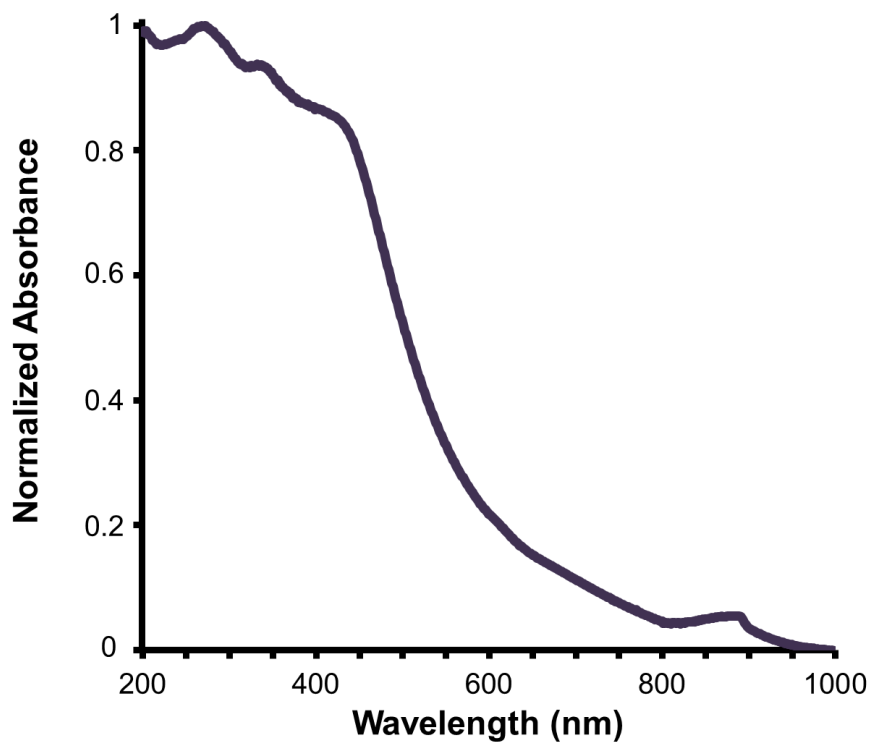
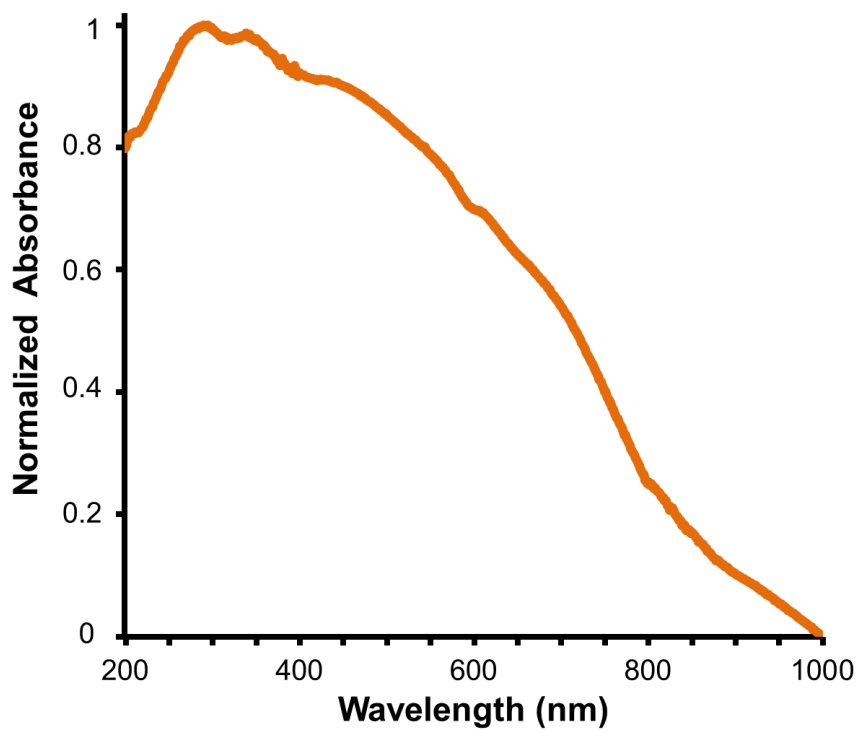


Figure A1.12: Absorbance of polymer prepared by evacuation from PhMe growth



F. Fluorescence Emission of Powders and Relative Quantum Yield of Films

Figure A1.13: Photoemission ($\lambda_{\text{ex}} = 396 \text{ nm}$) of the polymer grown in DMF and activated by lyophilization.

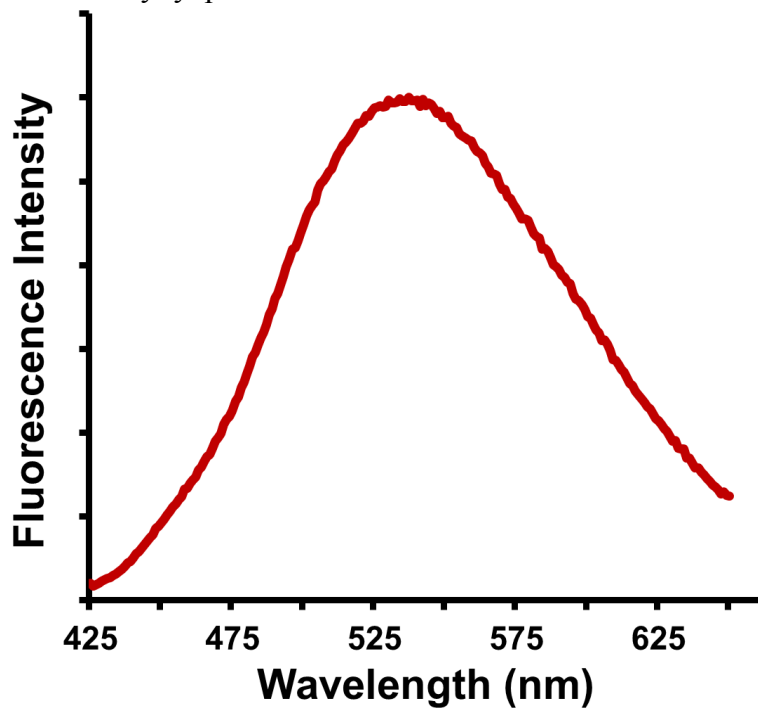


Figure A1.14: Photoemission ($\lambda_{\text{ex}} = 396 \text{ nm}$) of the polymer grown in DMF and activated by evacuation.

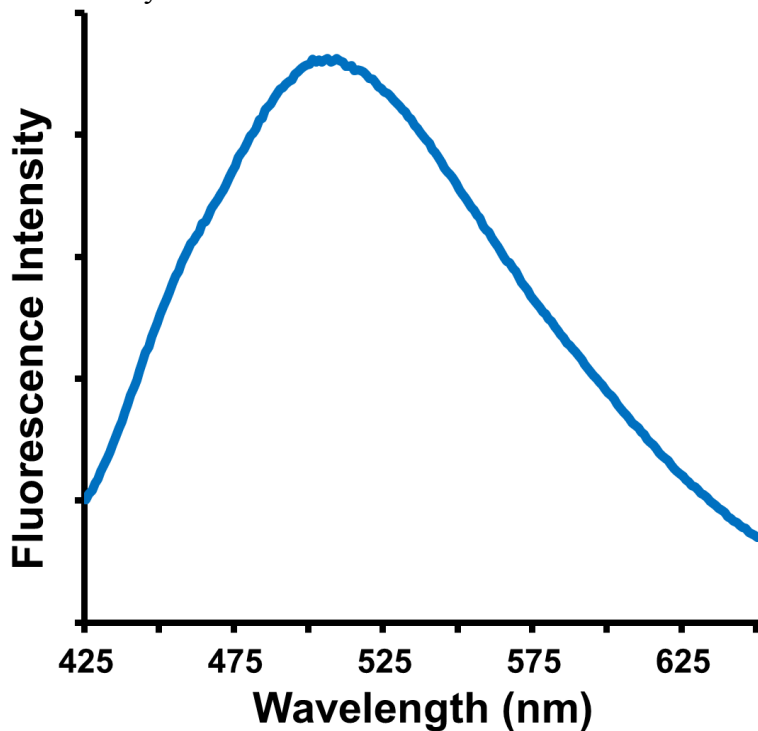


Figure A1.15: Photoemission ($\lambda_{\text{ex}} = 396 \text{ nm}$) of the polymer grown in PhMe and activated by lyophilization.

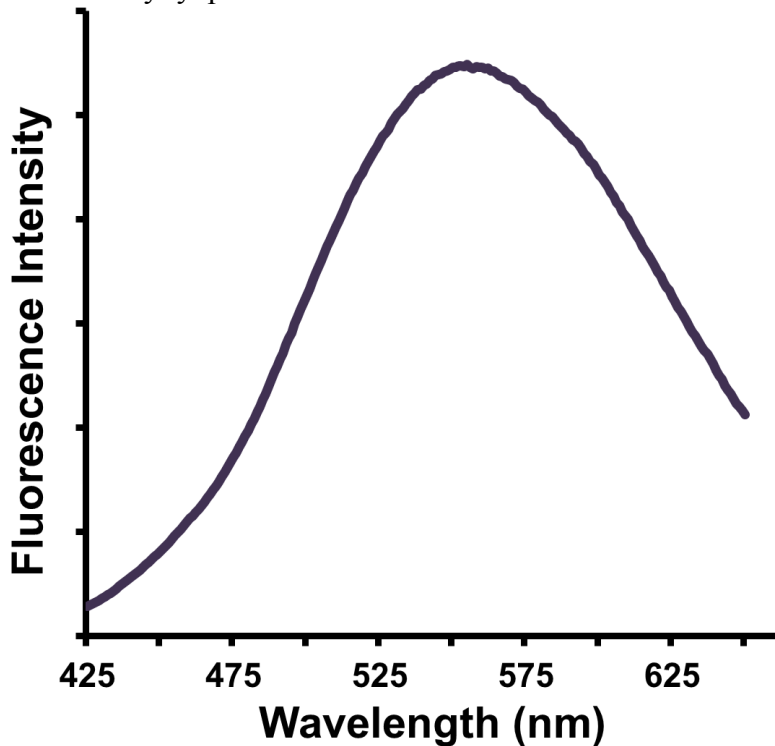


Figure A1.16: Photoemission ($\lambda_{\text{ex}} = 396 \text{ nm}$) of the polymer grown in PhMe and activated by evacuation.

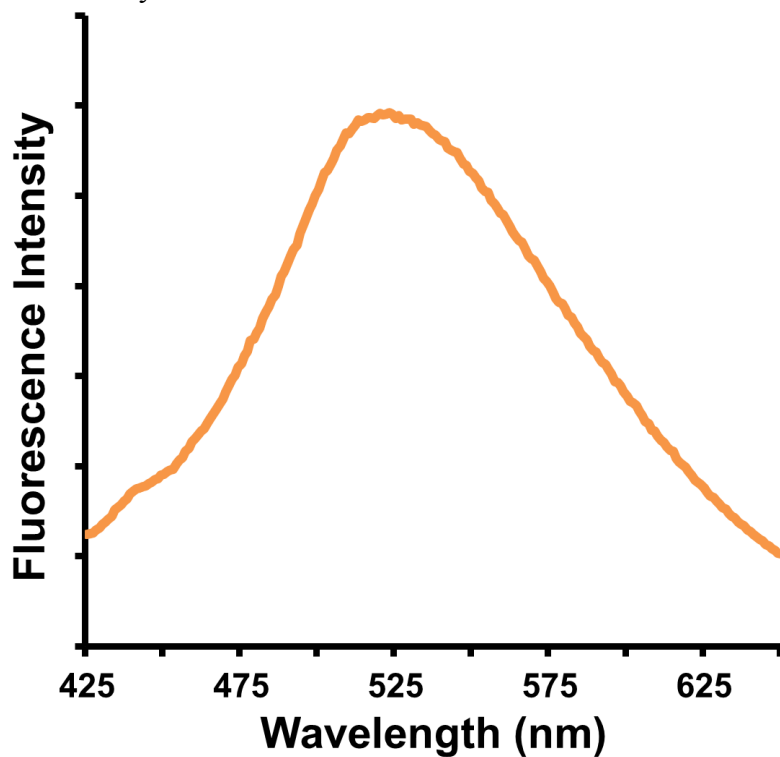
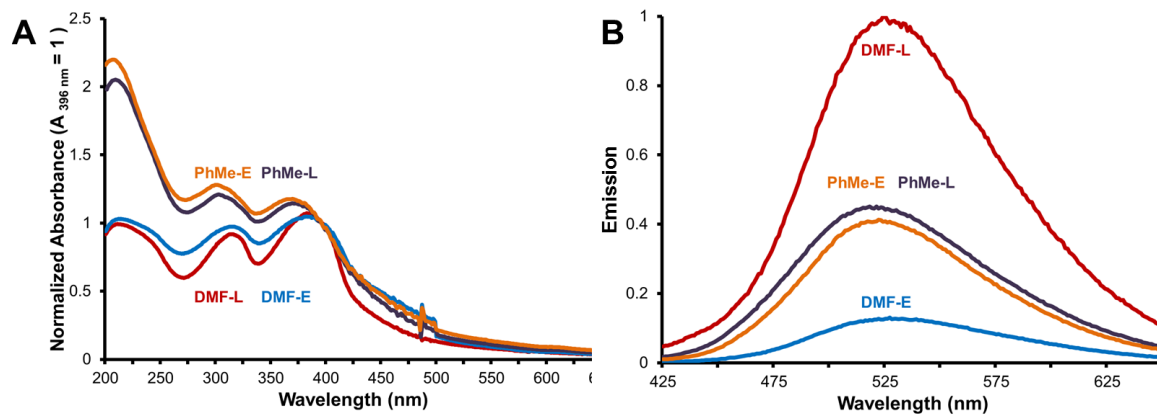


Figure A1.17: **A)** Normalized UV-Vis absorbance ($\lambda = 396$ nm) of the films used to determine relative fluorescence quantum yield. **B)** Fluorescence spectra ($\lambda_{\text{ex}} = 396$ nm) used to determine Φ_{rel} , assigning DMF-L as $\Phi_{\text{rel}} = 1$.



G. Thermogravimetric Analysis TGA trace of the polymer was obtained using a linear 10 °C/min ramp method.

Figure A1.18: Powder prepared by lyophilization with growth from DMF

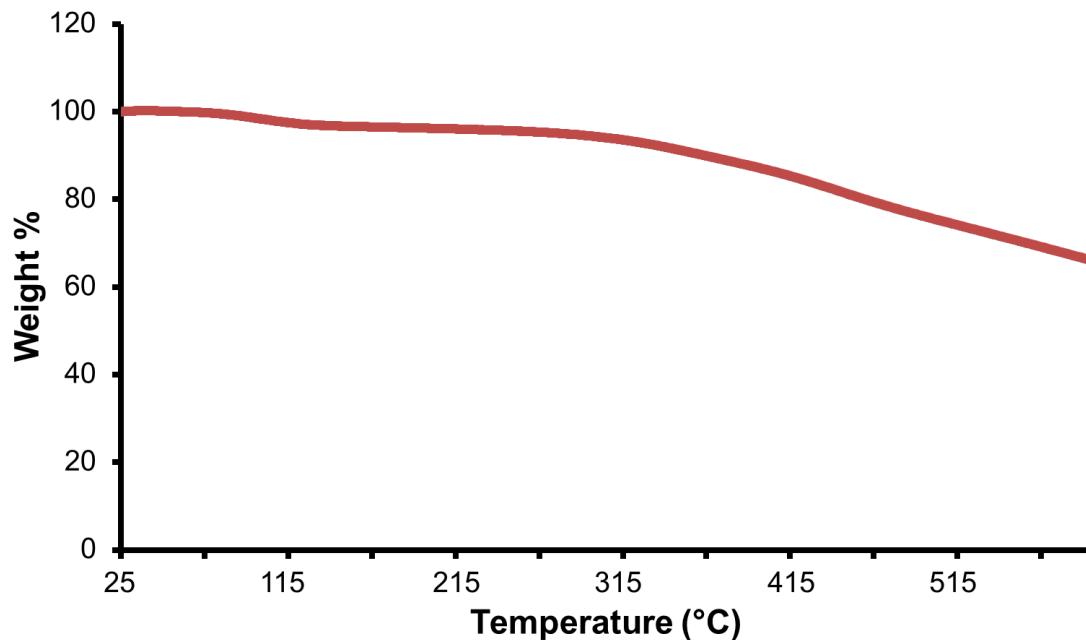


Figure A1.19: Powder prepared by evacuation with growth from DMF

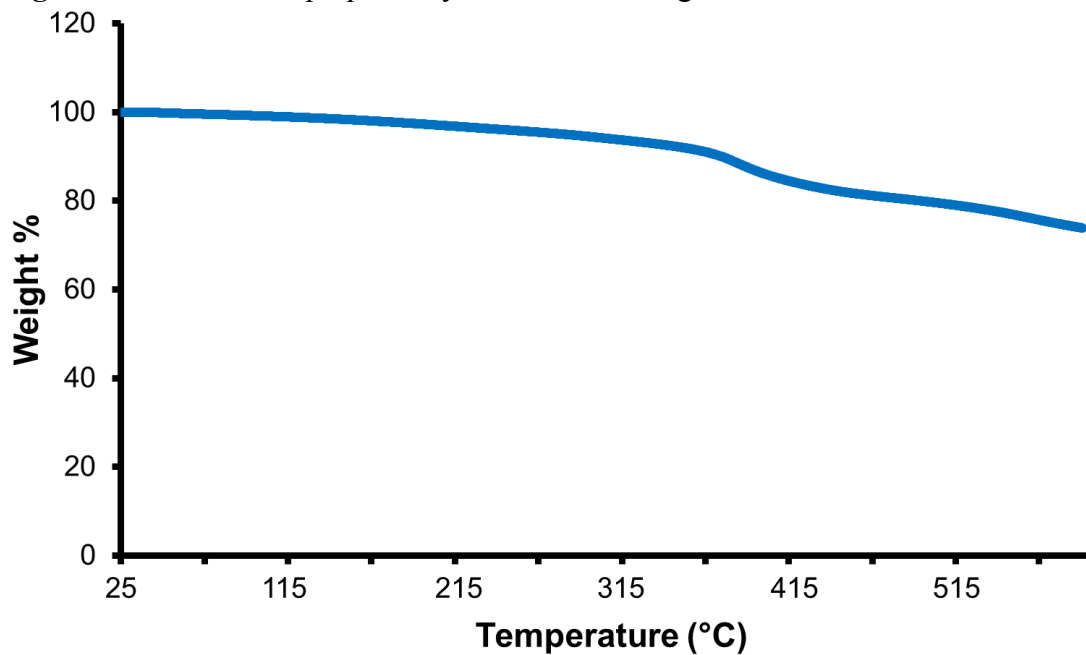


Figure A1.20: Powder prepared by lyophilization with growth from PhMe

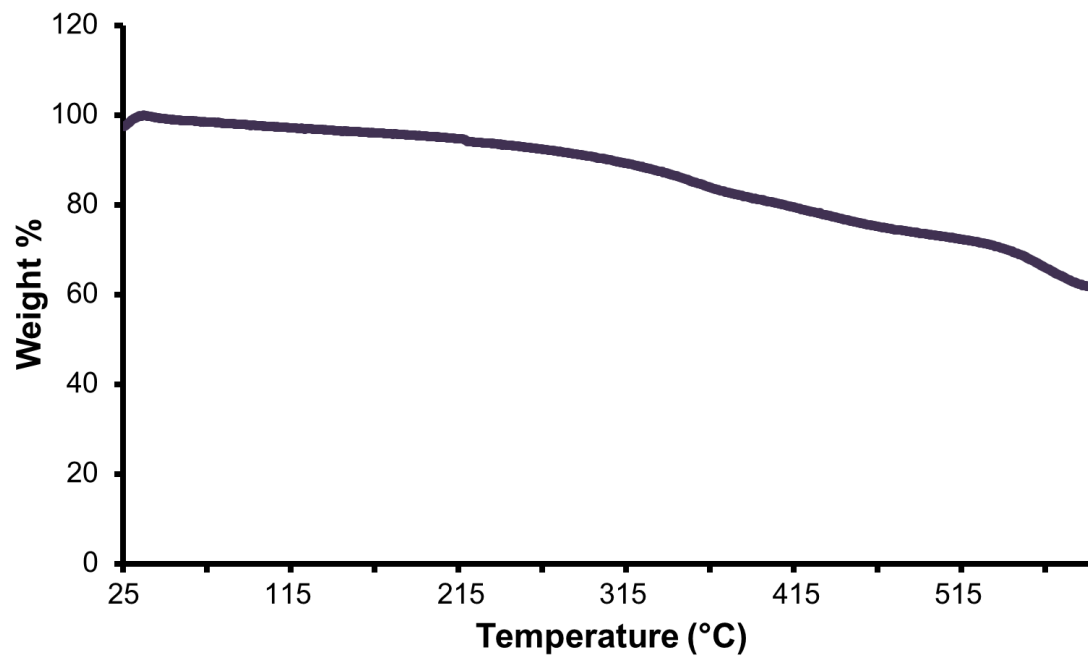
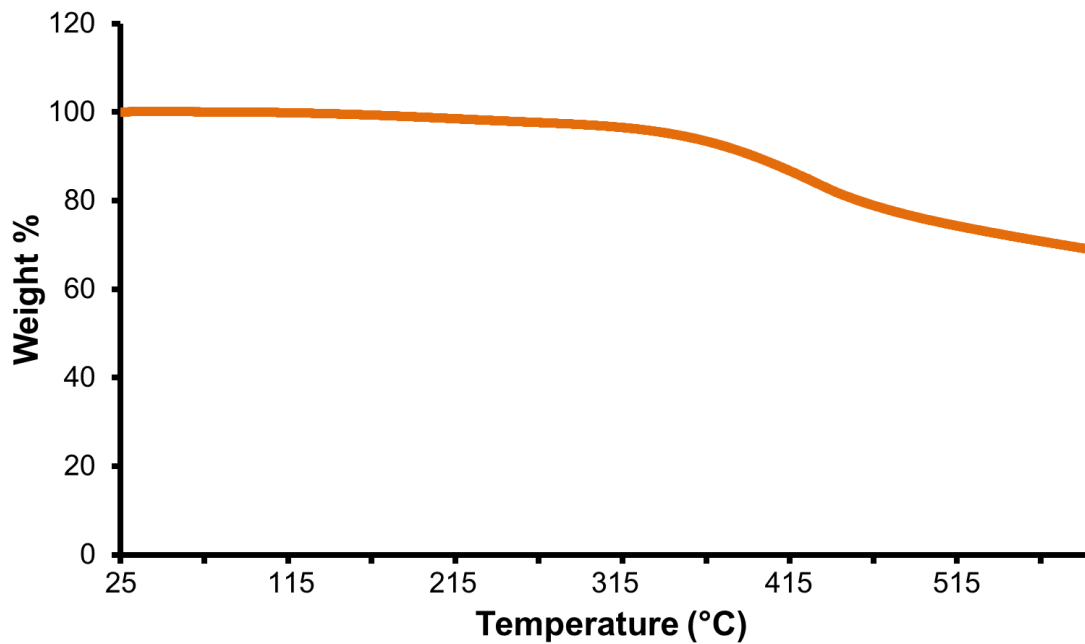


Figure A1.21: Powder prepared by evacuation with growth from PhMe



H. Surface Area Determinations

Figure A1.22: BET Plot for the solid polymer synthesized in DMF and activated by lyophilization.

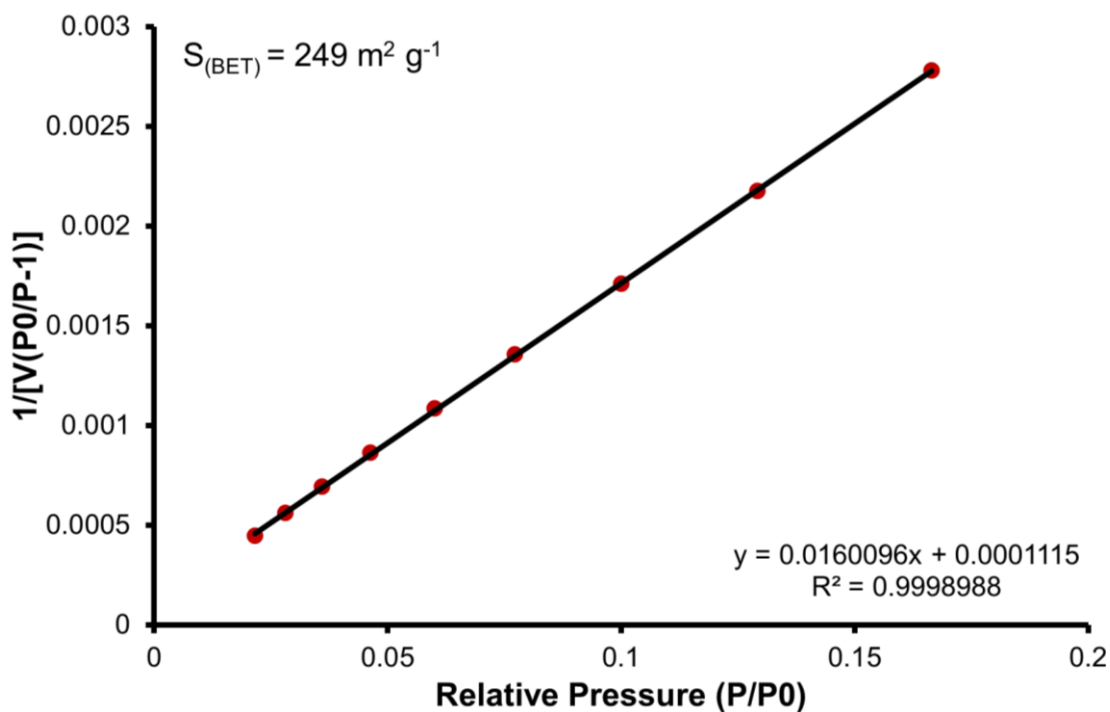


Figure A1.23: BET Plot for the solid polymer synthesized in DMF and activated by evacuation.

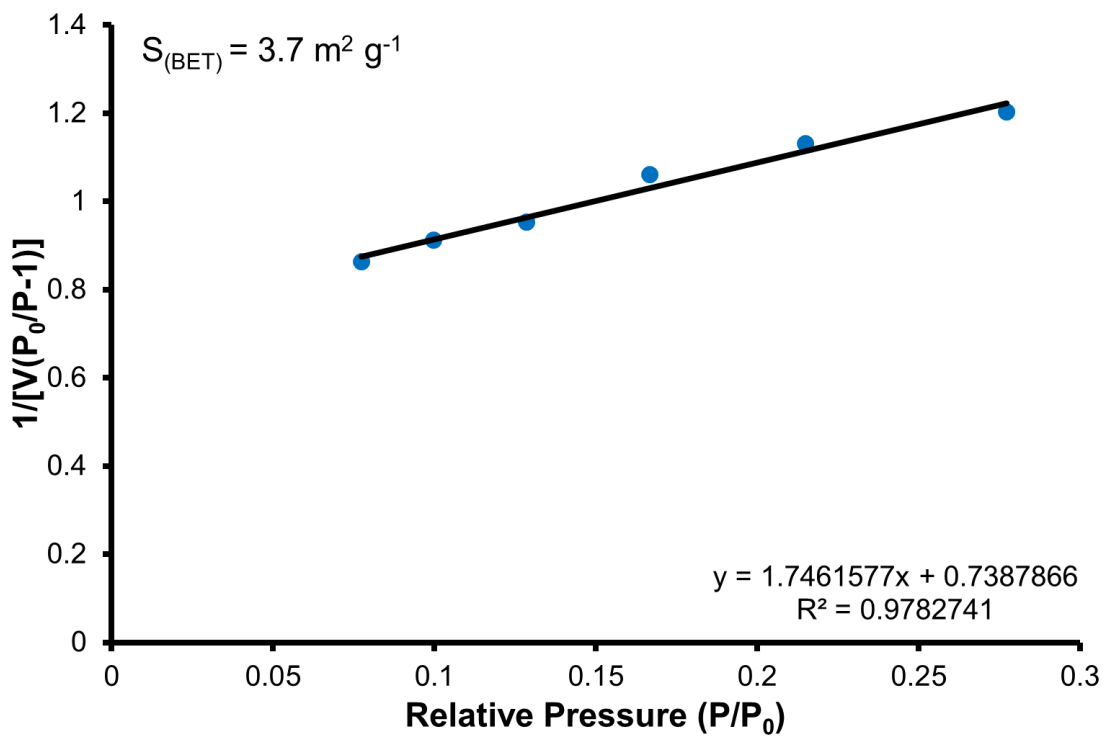


Figure A1.24: BET Plot for the solid polymer synthesized in PhMe and activated by lyophilization.

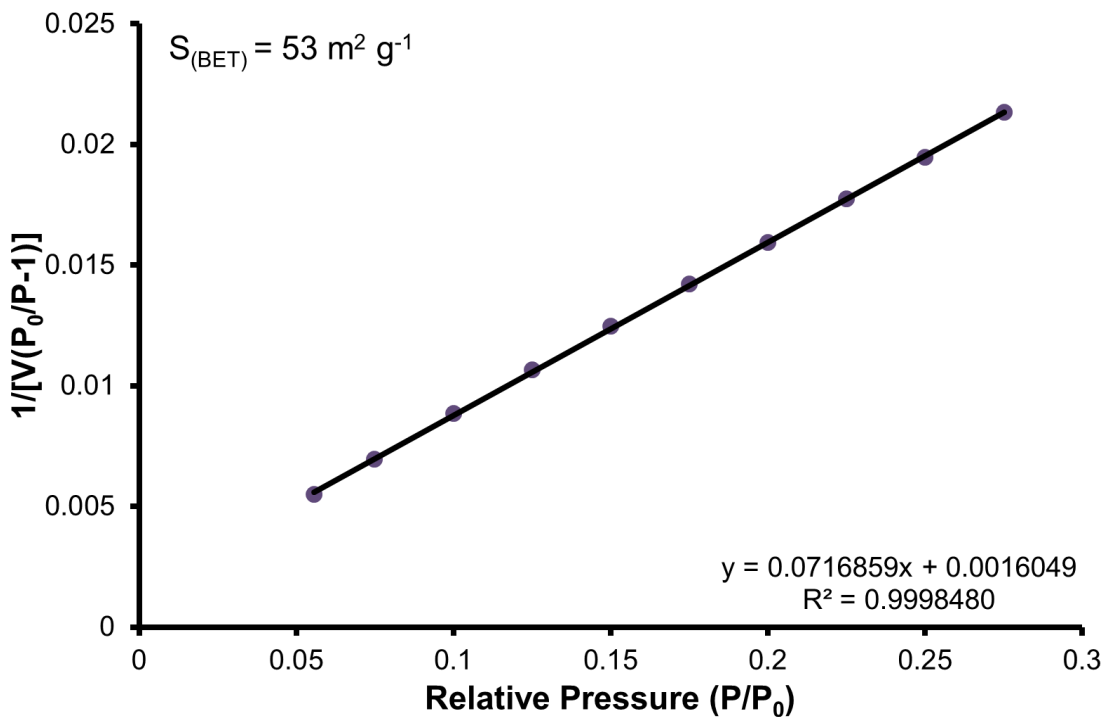


Figure A1.25: BET Plot for the solid polymer synthesized in PhMe and activated by evacuation.

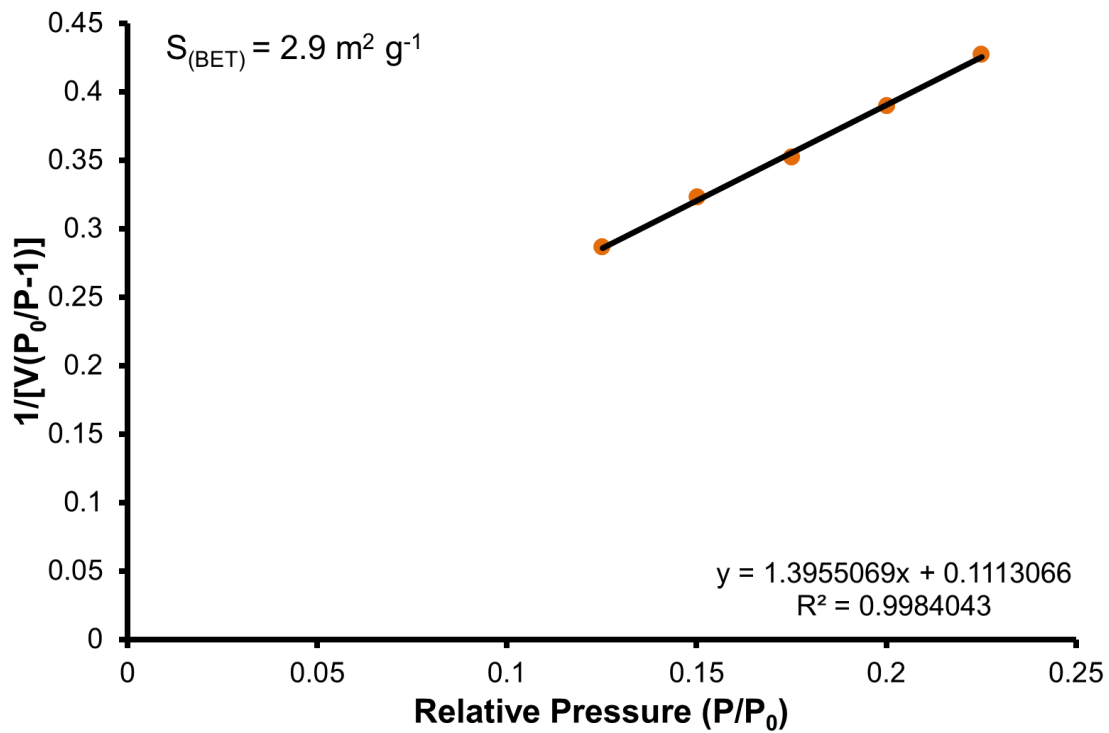
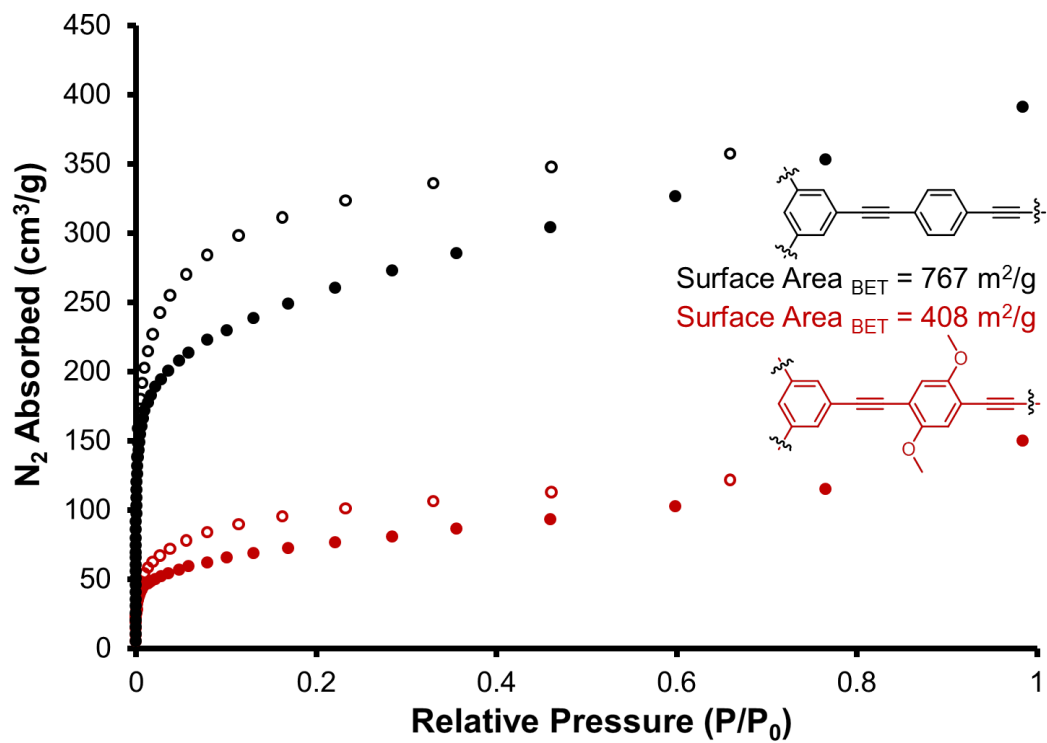


Figure A1.26: Comparison of N₂ adsorption isotherms for the polymers synthesized in DMF and activated by lyophilization.



I. Scanning Electron Micrographs

Figure A1.27: SEM of polymer synthesized in DMF and activated by lyophilization.

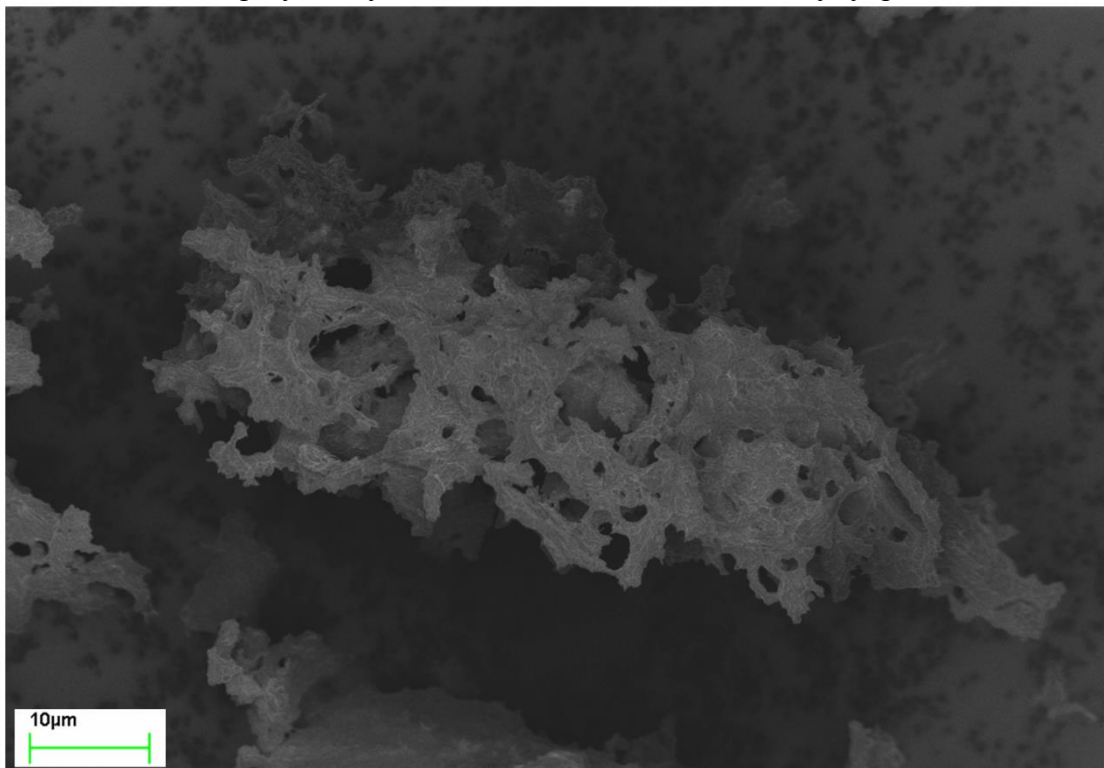


Figure A1.28: SEM of polymer synthesized in DMF and activated by evacuation

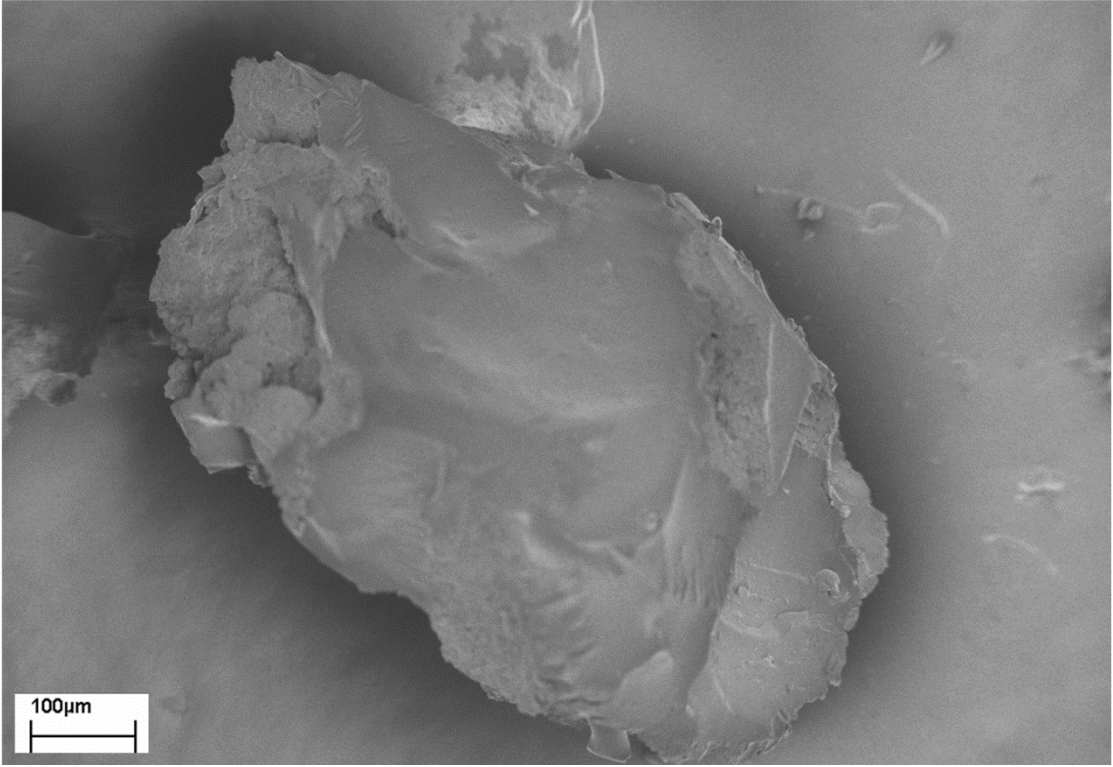


Figure A1.29: SEM of polymer synthesized in PhMe and activated by lyophilization

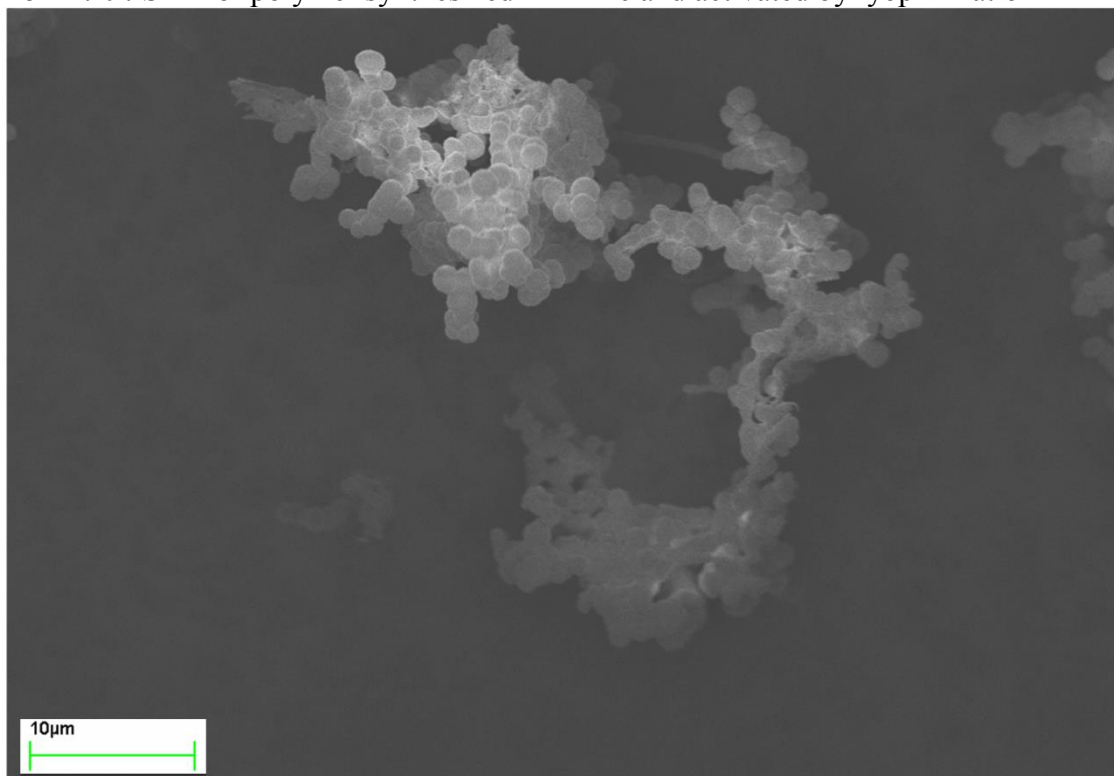
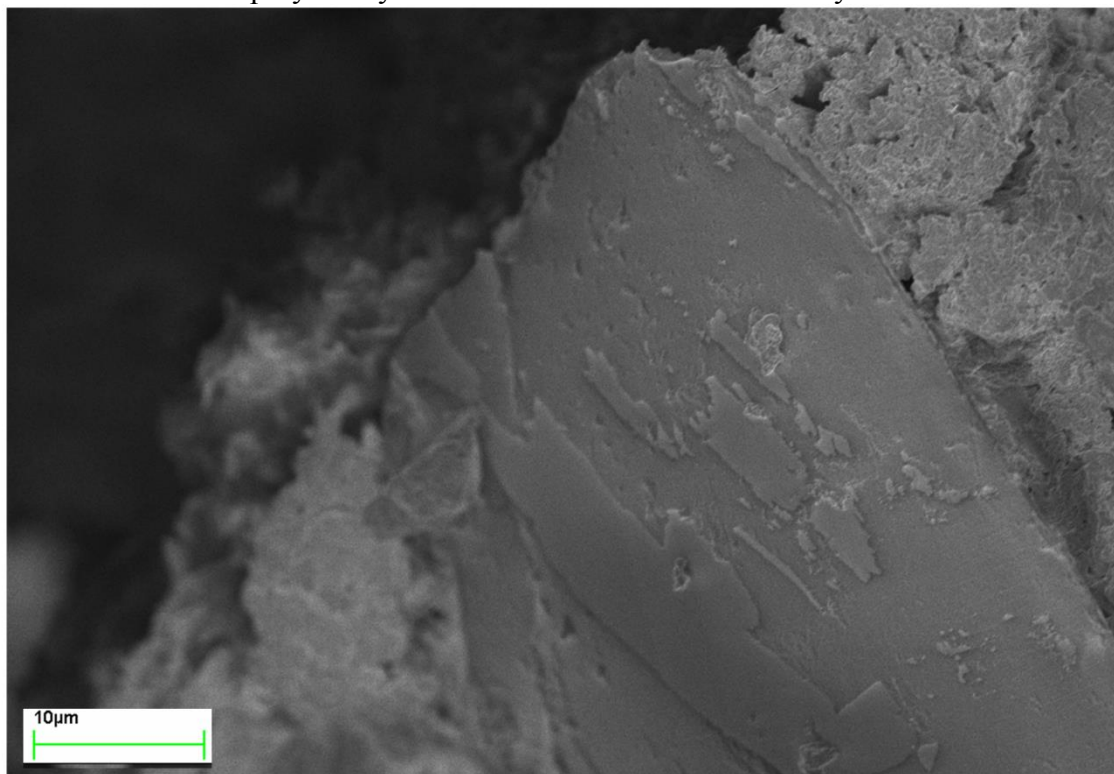


Figure A1.30: SEM of polymer synthesized in PhMe and activated by evacuation



J. References

1. Wariishi, K.; Morishima, S.; Inagaki, Y.; *Org. Process Res. Dev.*, **2003**, *7*, 98-100
2. Yi, C.; Blum, C.; Lehmann, M.; Seller, S.; Liu, S.X.; Grei, G.; Neels, A.; Hauser, J.; Schürch, S.; Decurtins, S.; *J. Org. Chem.* **2010**, *75*, 3350-3357
3. Zhao, Y.-L.; Liu, L.; Zhang, W.; Sue, C.H.; Li, Q.; Miljanic, O. S.; Yaghi, O. M.; Stoddart, J. F.; *Chem. Eur. J.* **2009**, *15*, 13356-13380

CHAPTER 3

A 2D COVALENT ORGANIC FRAMEWORK WITH 4.7 NM PORES AND INSIGHT INTO ITS INTERLAYER STACKING

ABSTRACT *Two-dimensional layered covalent organic frameworks (2D COFs) organize π -electron systems into ordered structures ideal for exciton and charge transport and exhibit permanent porosity available for subsequent functionalization. A 2D COF with the largest pores reported to date was synthesized by condensing 2,3,6,7,10,11-hexahydroxytriphenylene (HHTP) and 4,4'-diphenylbutadiynebis(boronic acid) (DPB). The COF was prepared as both a high surface area microcrystalline powder as well as a vertically oriented thin film on a transparent single-layer graphene / fused silica substrate. Complementary molecular dynamics and density functional theory calculations provide insight into the interlayer spacing of the COF and suggest that adjacent layers are horizontally offset by 1.7–1.8 Å, in contrast to the eclipsed AA stacking typically proposed for these materials. This paper was originally published as [Spitler, E. L.; Koo, B. T.; Novotney, J. L.; Colson, J. W.; Uribe-Romo, F. J.; Gutierrez, G. D.; Clancy, P.; Dichtel, W. R.; *J. Am. Chem. Soc.* **2011**, 133 (48), 19416].*

Introduction:

Covalent organic frameworks (COFs) organize molecular building blocks into layered two-dimensional (2D)^{34–43} or three-dimensional (3D)^{44,45} periodic crystalline networks that feature high surface areas, excellent thermal stability, and extremely low densities. The layered 2D variants stack functional π -electron systems in van der Waals contact with maximal π -orbital overlap ideal for charge or exciton transport^{38–40,46–48} and exhibit open

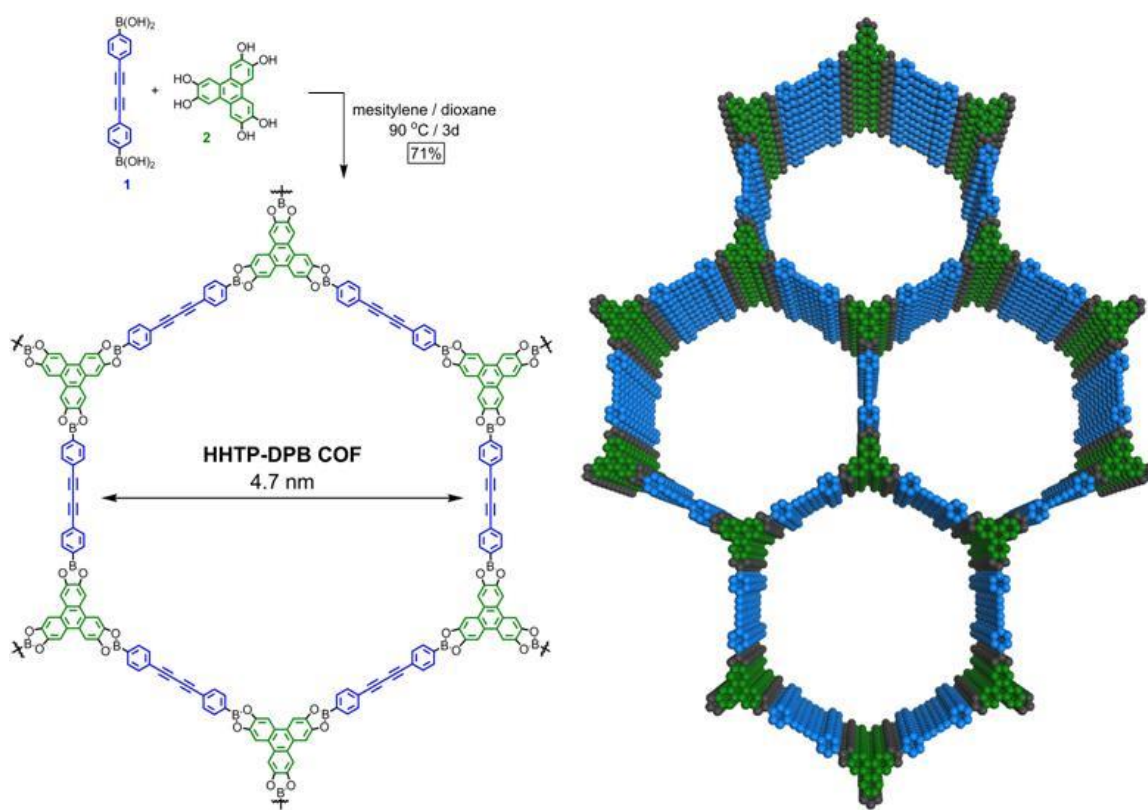
porous channels that run parallel to the direction of stacking. These properties, in addition to the predictable nature of COF design, have attracted great interest as structurally precise optoelectronic materials. COFs are usually isolated as insoluble and unprocessable powders, but we recently reported the first oriented, crystalline COF films on transparent conductive substrates.⁴⁹ Oriented thin film morphologies broaden the potential applications of COFs significantly, as they might template the formation of other nanomaterials or enable nanometer-scale patterning;⁵⁰ however, these applications require larger pores than the typical 2-3 nm size range.^{41,51} Here we describe a 2D COF (**HHTP-DPB COF**) with 4.7 nm-wide hexagonal pores, the largest yet reported, which we synthesized as both an insoluble powder and as a vertically oriented thin film.

Nearly all 2D layered COFs have been described as fully eclipsed structures based on their powder X-ray diffraction (PXRD) patterns, but the relatively broad peaks do not rule out small horizontal offsets between layers.⁵² We have performed a detailed molecular mechanics and density functional theory (DFT) modeling analysis of the interlayer potential energies of various stacking conformations of **HHTP-DPB COF**. These studies suggest that adjacent layers of **HHTP-DPB COF** are slightly offset (1.7–1.8 Å) from the true AA eclipsed packing structure previously proposed for these materials. Though these offsets are relatively small relative to the size of the COF unit cell, similar changes in packing dramatically affect the charge mobility of discotic liquid crystals.^{53,54} Thus, our simulations are critical for optimizing future 2D layered COFs for efficient vertical charge transport.⁵⁵ Given the similarity of the **HHTP-DPB COF** to other 2D layered COF structures, we believe these offsets are likely to be found across the entire class of these materials.

Results and Discussion

2.1 COF Powder Synthesis and Characterization. The solvothermal condensation of 4,4'-diphenylbutadiynebis(boronic acid) (**1**, **DPB**) with 2,3,6,7,10,11-hexahydroxytriphenylene (**2**, **HHTP**) in a 1:1 mixture of mesitylene:dioxane provided the **HHTP-DPB COF** as a microcrystalline powder (Scheme 2.1). **1** is an intriguing COF building block because of its linear structure, extended conjugation, and minimal steric conflicts associated with achieving a planar conformation. The **HHTP-DPB COF** powders were isolated from the reaction mixture by filtration and purified by washing with toluene and drying under vacuum. Fourier transform infrared spectroscopy (FTIR) indicated boronate ester formation, as evidenced by a sharp B-O stretch located at 1354 cm^{-1} not found in either of the reactants. The spectrum also showed strongly attenuated hydroxyl stretches. Spectra taken prior to activating the pores show intense $-\text{CH}_3$ stretches of toluene or mesitylene, which disappear upon heating the COF at 90 °C under vacuum for 72 h. In contrast, we have successfully removed these solvents from other 2D layered COFs containing HHTP at room temperature under vacuum. ^1H - ^{13}C CP/MAS NMR of **HHTP-DPB COF** confirmed the formation of the expected structure, and its ^{11}B NMR spectrum consisted of a single resonance consistent with the formation of a single type of boronate ester linkage (see Supporting Information).

The gas adsorption properties of **HHTP-DPB COF** were evaluated by N_2 gas adsorption at 77 K (Figure 3.1A). The material exhibits a reversible isotherm typical of mesoporous materials most resembling Type IV, in which gas adsorption by the pores occurs in two steps at $P/P_0 < 0.10$ and $0.20 < P/P_0 = 0.40$ pressures.⁵⁶ Analysis of the



Scheme 3.1. Synthesis of **HHTP-DPB COF** from bis(boronic acid) linker **1** and HHTP **2** (left) and model of the idealized **bnn** topology (right).

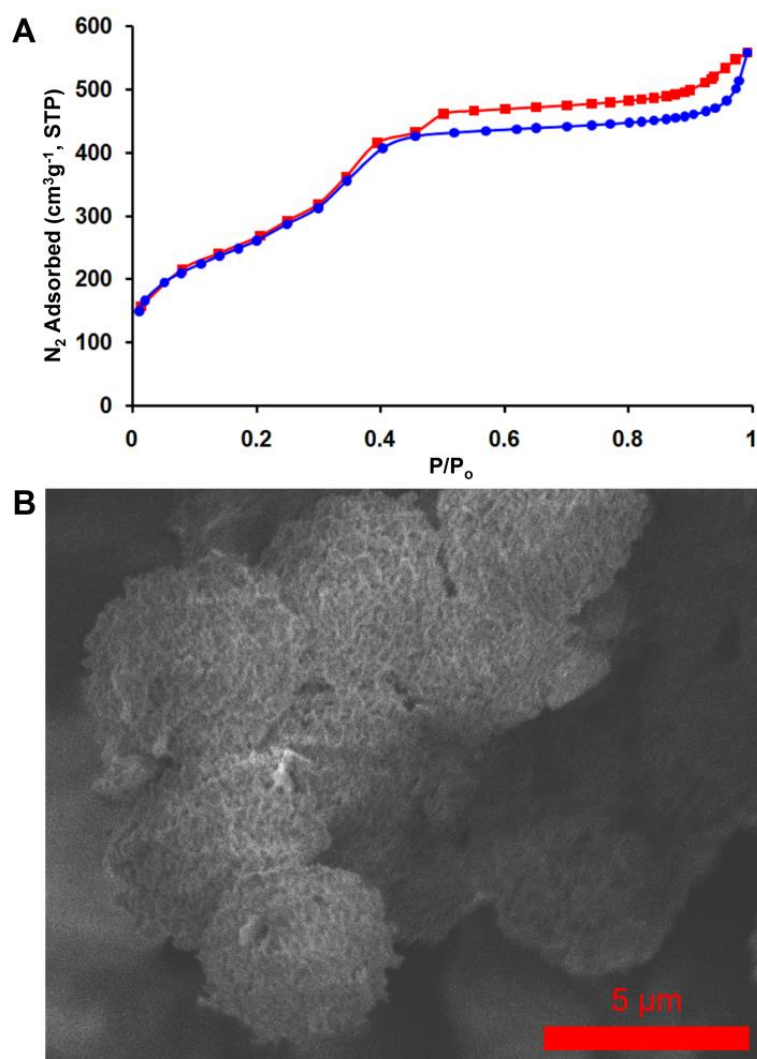


Figure 3.1. (A) N₂ adsorption (blue circles) and desorption (red squares) isotherms for **HHTP-DPB COF**. (B) Scanning electron microscope (SEM) images of **HHTP-DPB COF** powder

low-pressure region ($0.05 < P/P_0 < 0.20$) of the isotherm provides a Langmuir surface area of $1290 \text{ m}^2 \text{ g}^{-1}$ and BET surface area of $930 \text{ m}^2 \text{ g}^{-1}$ (see Supporting Information, Figure A2.21).⁵⁷ In order to compare the measured gas adsorption capacity of the prepared COF with its maximum uptakes, we simulated an isotherm using Monte Carlo simulations using the Metropolis method in Materials Studio (Figure A2.22), from which a maximum BET surface area of $2640 \text{ m}^2 \text{ g}^{-1}$ was calculated. This value is quite similar to the calculated Connolly surface area of $2670 \text{ m}^2 \text{ g}^{-1}$ for the eclipsed **HHTP-DPB COF** structure and consistent with that observed in other frameworks. These calculations suggest that the measured COF has been activated to approximately 40% of its maximum uptake, and further optimization is ongoing. The hysteresis observed during desorption is typical of interparticle adsorption and has been observed in other COFs. These particles were uniform spheres with $4 \mu\text{m}$ diameters, as observed by scanning electron microscopy (SEM, Figure 3.1B). **HHTP-DPB COF** retained 92% of its mass up to $350 \text{ }^\circ\text{C}$ by thermal gravimetric analysis (Figure A2.20).

The crystallinity and unit cell parameters of the **HHTP-DPB COF** were determined by PXRD (CuK α line, Figure 3.2). The PXRD patterns of **HHTP-DPB COF** showed poor crystallinity prior to activation (Figure A2.15), which improved dramatically after activating the COF under vacuum at $100 \text{ }^\circ\text{C}$ for 12 h. The diffraction pattern of the activated material shows peaks at 2.17° , 3.79° , 5.90° , 7.93° , and 8.02° , which correspond to the (100), (110), (210), (220), and (310) Bragg peaks of a primitive hexagonal lattice. The crystal structure was simulated using the Materials Studio suite of programs⁵⁸ by assembling eclipsed triphenylenes into a **bnn** net ($P6/mmm$).⁵⁹ The experimental PXRD displayed a diffraction pattern in agreement with one simulated from this model, allowing

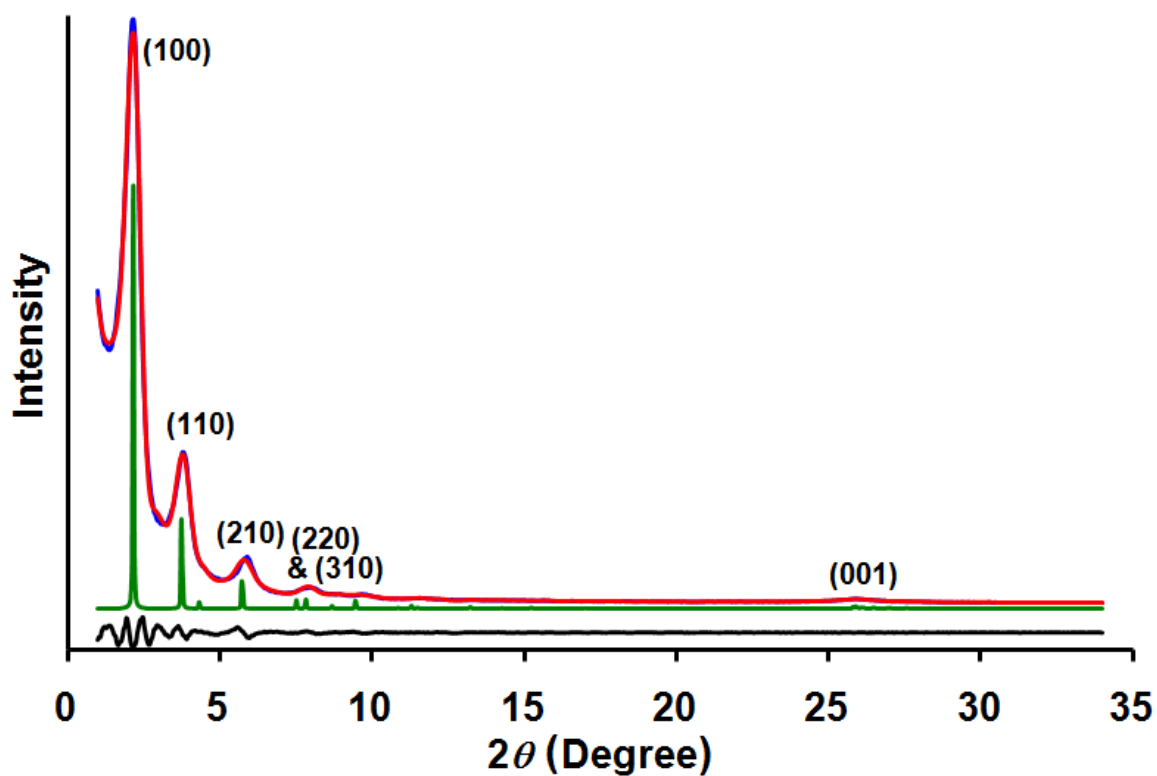


Figure 3.2. Experimental (blue) and Pawley refined (red) vs. predicted (green) PXRD patterns of **HHTP-DPB COF** and difference plot (experimental – refined; black). Major observed reflections are labeled.

facile indexing of the diffraction peaks. Pawley refinement (Figure A2.18) of the pattern gave unit cell parameters $a = b = 46.9 \text{ \AA}$. The broad (001) diffraction peak at 25.8° corresponds to a vertical spacing between stacked sheets of 3.37 \AA , indicating that adjacent layers are in van der Waals contact. The relative positions of the butadiyne groups in the COF lattice lack the appropriate spacing and angular offset necessary to undergo topochemical polymerization,^{60–62} and we saw no evidence for this process by differential scanning calorimetry or by heating the COF powders. We also considered an alternate structure wherein adjacent sheets are not co-facially stacked, but offset by half of the unit cell distance in the horizontal a and b planes, thus creating a **gra** net ($P6_3/mmc$; Figure A2.19). The simulated PXRD pattern of these structures did not match the experimental data.

2.2 Simulation of HHTP-DPB COF Interlayer Packing. It is important to note that almost all other 2D COFs have been described as eclipsed layered structures, but the X-ray diffraction peaks of these materials are too broad to preclude slight interlayer offsets. We performed complementary simulations to understand the 2D stacking of **HHTP-DPB COF** beyond the information available from the PXRD data. Two levels of theory were used to model the intermolecular interactions between COF layers: molecular mechanics, using the MM3 force field, which describes hydrocarbon and ringed aromatic systems reliably,^{63,64} and DFT, a more accurate quantum mechanical treatment that accounts for electronic interactions.⁶⁵ Molecular Dynamics simulations are orders of magnitude faster than static DFT calculations and can explore a far broader set of configurations. Therefore, we used molecular mechanics to broadly define the potential energy surface (PES) associated with

offsetting two layers of the **HHTP-DPB COF** and subsequently refined this model in regions of interest using DFT.

The MM3-derived PES (Figure 3.3) was generated by varying the x - and y -translational offsets of two adjacent COF layers and recalculating the interlayer spacing at each point to minimize the interaction energy. The PES contains three regions (labeled A-C) of relatively flat ‘terrain’ bounded by steep gradients. Region A exhibits significantly more stabilizing interaction energies (-2.8 eV) than Regions B and C (-0.8 and -0.4 eV, respectively) and corresponds to structures that are eclipsed or nearly eclipsed. The interlayer spacing that minimizes the interaction energy in this region is 3.45 Å, which is within 0.1 Å of the experimental value. In the MM3 calculations, the potential energy of the fully eclipsed structure is only 0.13 eV higher than the minimum energy calculated in Region A, which occurs at offsets that define a ring of radius 1.6 Å around the origin. This result indicates almost no preference for nearly eclipsed structures, but repulsive electrostatic forces that occur at the origin are likely to be underestimated at the MM3 level of theory.

Regions B and C of the PES correspond to offsets that reduce the van der Waals contact between layers, each of which is higher in energy than Region A. The flatter regions at the corners of the PES form Region B, which correspond to **gra** layers (see Figure 3.4B). The potential energy in this region varies from a peak of about -0.7 eV to a valley of about -0.9 eV. The average binding energy of this region is less than a third of the binding energy of near-eclipsed structures in Region A. The energy difference between Regions A and B is about 2.0 eV, which is a very significant potential energy increase from the bottom of the potential energy well in Region A. There are no

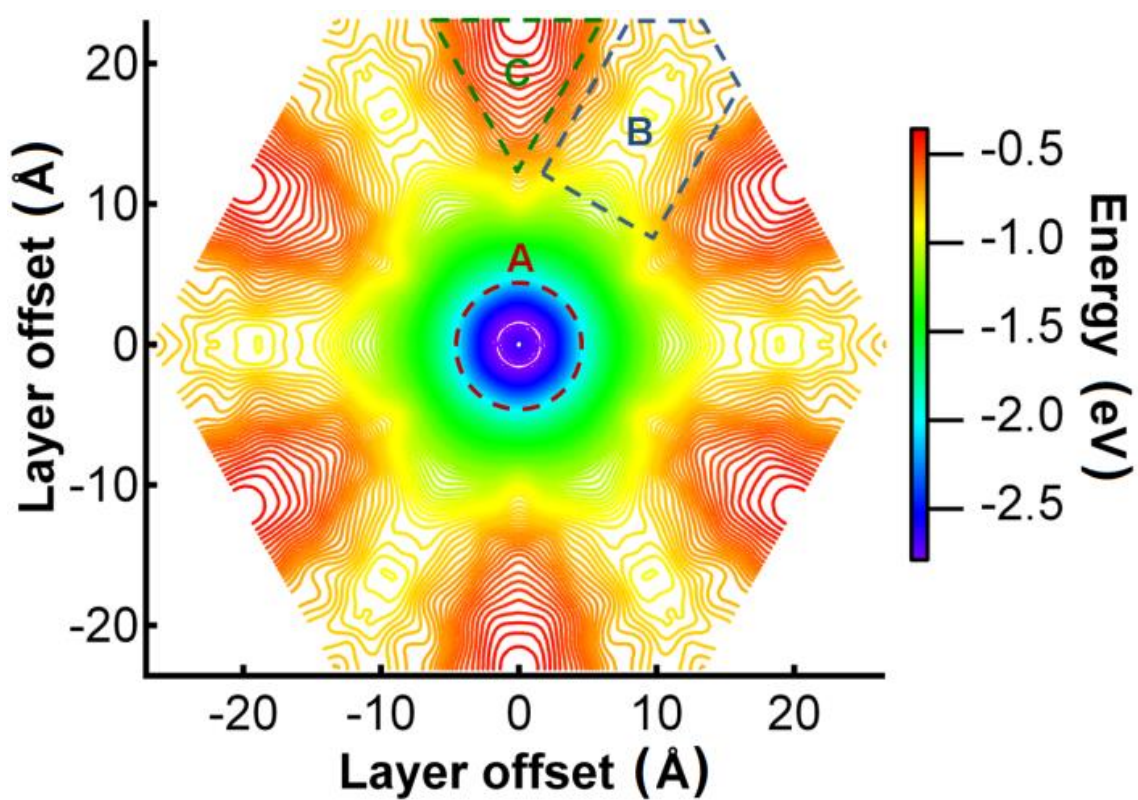


Figure 3.3. Potential energy surface generated from the semi-empirical MM3 potential. The surface can be divided into three regions with distinct energetic properties: A, Low energy region containing eclipsed and near-eclipsed two-layer structures; B, Region containing all staggered structures, shown schematically in Figure 3.4A; C, High-energy region containing the structures shown in Figure 3.4B.

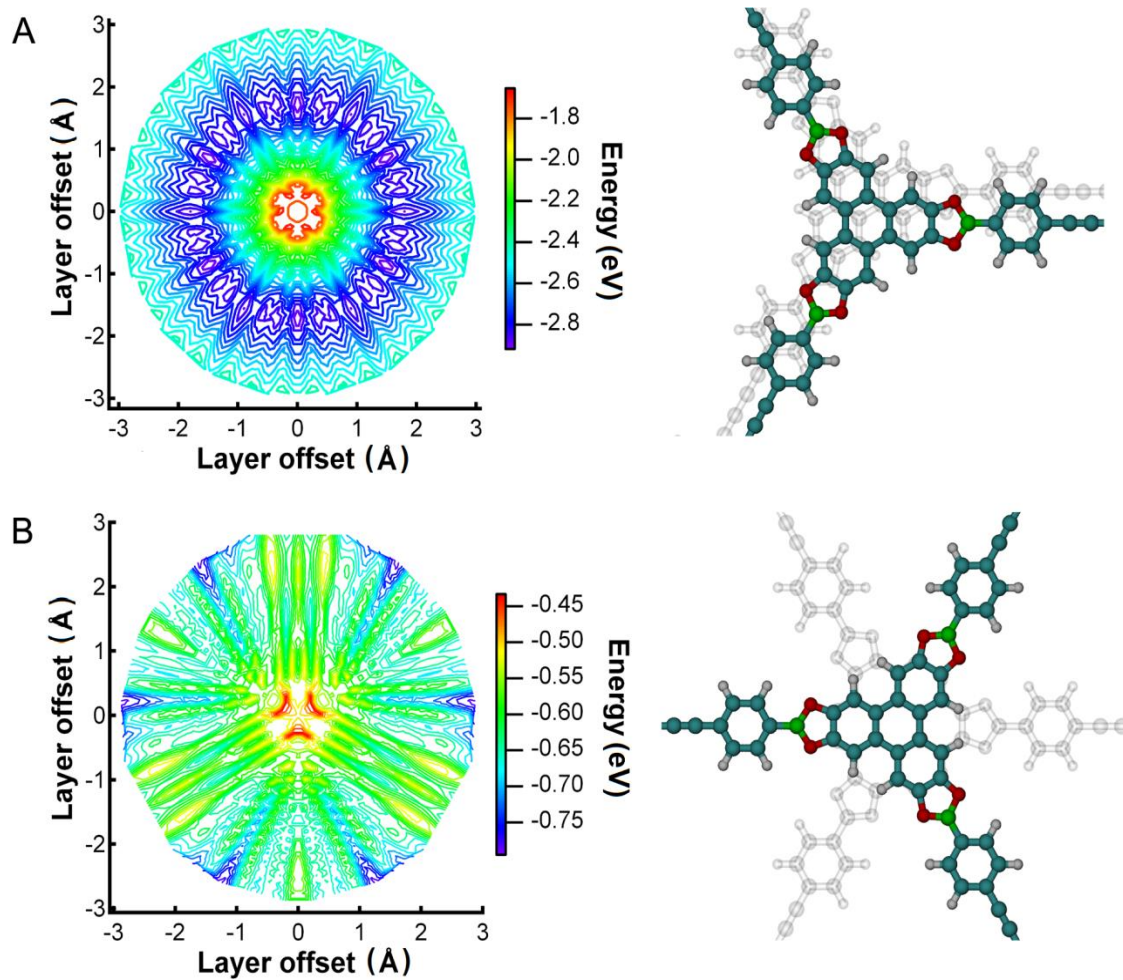


Figure 3.4. (A) Expansion of region “A” in Figure 3.3 calculated with density functional theory. (B) Expansion of a subset of region “B” in Figure 3.3 calculated with density functional theory and atomic representation of the two-layer staggered structure.

significant potential energy barriers that might prevent reorganization of COF layers from Region B to Region A, suggesting that forming these structures is unlikely. As shown in Fig. 3.4, there is less overlap in this configuration than in a more eclipsed configuration, which lowers the contribution of the van der Waals component to the intermolecular energy. However, monopoles in adjacent layers are staggered by 60 degrees so that the repulsive interaction between them is less than in the eclipsed case. The potential energy gradient near staggered configurations is less steep than the gradient near eclipsed configurations because near-staggered configurations balance the decrease in HHTP overlap with an increase in linker overlap. Configurations of layers with the highest potential energy are the triangle-shaped protrusions near the edges of the PES, labeled as Region C in Fig. 3.3. The energy of arrangements in this region is approximately -0.4 eV, which is 0.4 eV higher than the energies in Region B, and 2.4 eV higher than arrangements in region A. The gradient between Regions B and C attains a maximum value of 0.1 eV/Å. Since there is a constant negative gradient in Region C, these structures are also unstable and unlikely to form. These are the most energetically unfavorable configurations because the structures have no molecular overlap between HHTP units and only minimal overlap of linkers in adjacent layers. This reduces the van der Waals component of the intermolecular energy to the smallest value possible and significantly raises the potential energy of structures in this region. Based on these findings, we did not perform further calculations on structures in Region C

We next generated a new PES (Figure 3.4) for Regions A and B using more accurate DFT calculations as expressed in Gaussian09 using the M06 exchange correlation functional.⁶⁵⁻⁶⁷ The overall potential energy surface is qualitatively similar to that

generated from the MM3 potential, but with more finely corrugated surface features. Configurations with the lowest energy, of about -2.9 eV, are found 1.7-1.8 Å from the origin with an interlayer spacing of 3.42 Å, which is close to the experimental value and matches that of other 2D COFs. DFT calculations for structures in Region B confirm that staggered structures remain significantly higher in energy (2.4 eV) than the eclipsed structures of Region A. Thus the MM3 model can give a reasonably accurate result for COF structures in a fraction of the time needed for *ab initio* calculations.

Despite the qualitative agreement between the MM3 and DFT calculations, there are important differences between the two approaches. The DFT PES suggests that fully eclipsed structures are unlikely, because they show a potential energy maximum -1.8 eV, significantly higher (1.1 eV) than the more stable structures just 1.7-1.8 Å away. These differences arise from DFT's more precise treatment of electrostatic forces. The variation in potential energy around the ring is 0.1 eV, compared with the insignificant 3×10^{-3} eV variations predicted by MM3. The net result is that, while MM3-generated results suggest perfectly eclipsed structures are accessible, DFT calculations predict this is much less likely. Because this offset has no preferred direction, the average representation of the 3D structure of the COF cannot be reduced to a simple monoclinic unit cell. It is unlikely that there will be a prevalence of patterns, such as staircase, zigzag, or helical arrangements of layers that would be observable by X-ray diffraction. Instead, adjacent layers are more likely to stack in random arrangements around a preferred offset from the origin, similar to turbostratic disorder commonly observed in layered materials. These random offsets are difficult to observe in low resolution powder diffraction data, as they would generally affect only the relative intensity and width of certain diffraction peaks, while affecting peak

positions only at small d -spacings (neither of which has not yet been observed experimentally). We also compared the accessible surface area from the Connolly surfaces for eclipsed **HHTP-DPB COF** with that for 1.0 Å and 1.7 Å interlayer offsets. No significant differences were found, as each of these structures had accessible surface areas close to 2700 m² g⁻¹ (Supporting Information Table A2.2). Thus, most methods used for COF characterization are unable to distinguish between eclipsed and slightly offset structures. In COFs designed for optoelectronic applications, small changes in these offsets will strongly affect charge mobilities through the stacked aromatic systems,⁵⁴ and the computational methods described above will be important to understand their performance and design optimal new materials.

2.3 Synthesis and Characterization of Vertically Oriented HHTP-DPB COF Films on Single Layer Graphene. Despite their intriguing structures, it remains difficult to perform advanced spectroscopy on COF powders or incorporate them into devices. We overcame this limitation recently by growing COF thin films on single-layer graphene (SLG) functionalized substrates.⁴⁹ We prepared crystalline, vertically oriented **HHTP-DPB COF** thin films by condensing **1** and **2** under solvothermal conditions in the presence of SLG on a transparent fused SiO₂ substrate (SLG/SiO₂). Grazing incidence x-ray diffraction (GID, Figure 1.5A) indicates scattering intensity at 0.156 Å⁻¹, 0.271 Å⁻¹, 0.311 Å⁻¹, 0.411 Å⁻¹, 0.543 Å⁻¹, and 0.568 Å⁻¹, corresponding to the same (100), (110), (200), (210), (220) and (310) peaks observed in the powder samples. The intensity of these diffractions is concentrated near $Q_{\infty} = 0$, indicating that the c -axis of the COF is oriented normal to the substrate surface. The (001) Bragg peak that appears at $Q_{\parallel} = 1.83$ Å⁻¹ in powder samples is not observed in the GID experiment (Figure A2.25), again

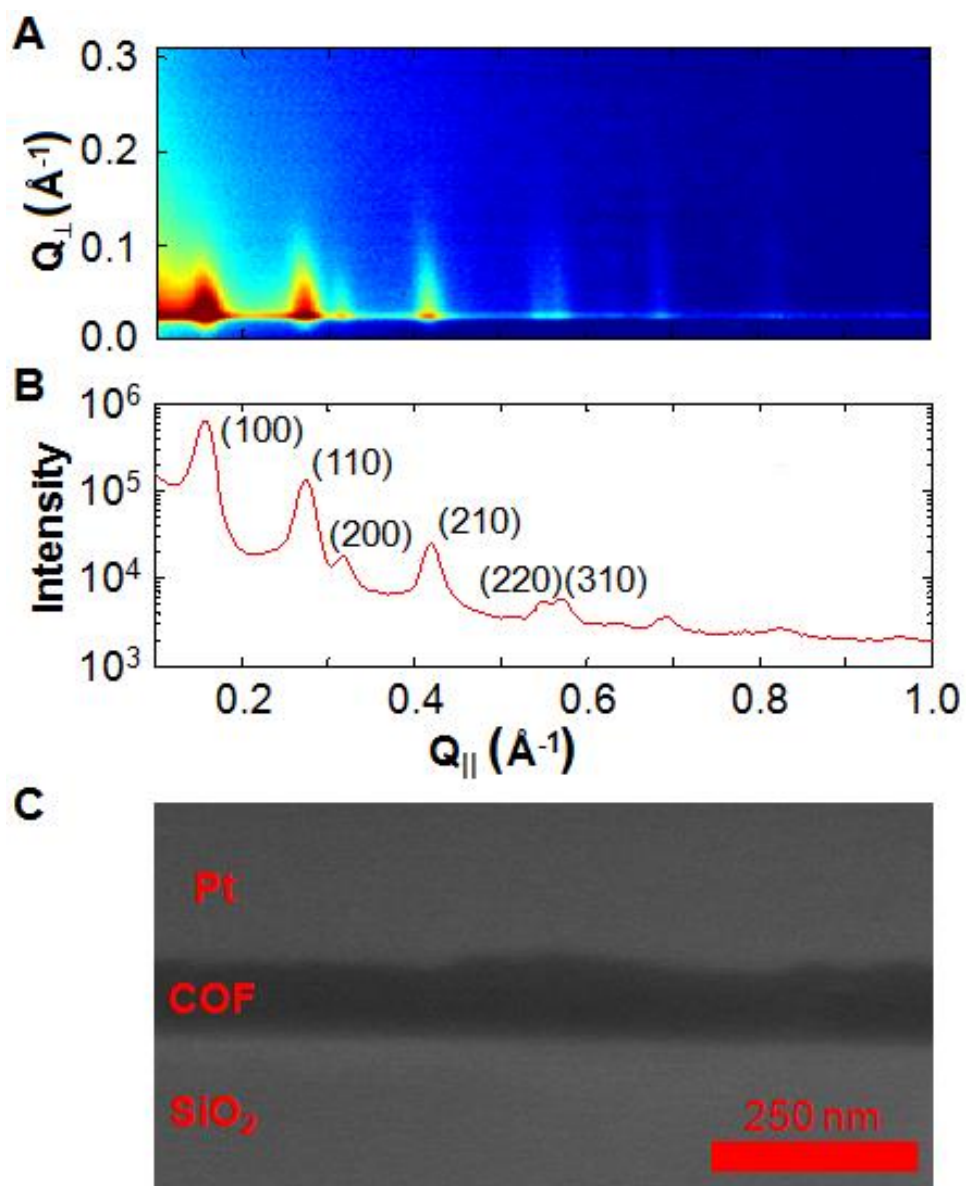


Figure 3.5. (A) Grazing incidence X-ray diffraction (GID) of **HHTP-DPB COF** thin film on SLG (growth time: 24 h). (B) Projection of (A) near $Q_{\infty} = 0$. (C) Cross-sectional SEM image of the film.

indicating that the *c*-axis is specifically oriented normal to the substrate. Instead, the (001) peak is observed at $Q_{\infty} = 1.85 \text{ \AA}^{-1}$ in measurements performed at large out-of-plane diffraction angles (Figure A2.26). Top-down SEM images indicate that the films are featureless over large areas and have only occasional bulk crystallites distributed across the surface (Figure A2.27). Cross-sectional micrographs obtained by milling the sample using a Ga^+ focused ion beam indicate that the films are continuous across the substrate with thickness $132 \pm 18 \text{ nm}$ (Figure 3.5C). The large pore size obtained in the thin film morphology may also serve as a useful template for nanopatterning, as features in the 2–5 nm region are difficult to obtain using either standard lithographic techniques or block copolymer lithography.⁶⁸

The **HHTP-DPB COF** powders and films are strongly photoluminescent (Figure 3.6), which we attribute to the co-facially packed diphenylbutadiyne subunits, as other HHTP-containing COFs do not fluoresce strongly. UV/Vis spectra of the films obtained through the transparent SLG/ SiO_2 substrate are consistent with the presence of the triphenylene and diphenylbutadiyne chromophores and show only moderate tailing at longer wavelengths associated with scattering. Photoemission spectra of the films show a λ_{max} of 457 nm ($\lambda_{\text{exc}} = 357 \text{ nm}$) that is red-shifted by 55 nm relative to that of **1** dissolved in DMF. Several aspects of the COF structure impact the fluorescence of the diphenylbutadiyne chromophores. First, catechol boronate ester linkages have shown evidence of extended conjugation in linear polymers.⁶⁹ Though the conjugation efficiency of these groups is not as high as other linkages, this effect should be maximized in a COF given the coplanar relationship among the chromophores. Similarly, diphenylbutadiynes capable of free rotation of each phenyl group generally have very low fluorescence

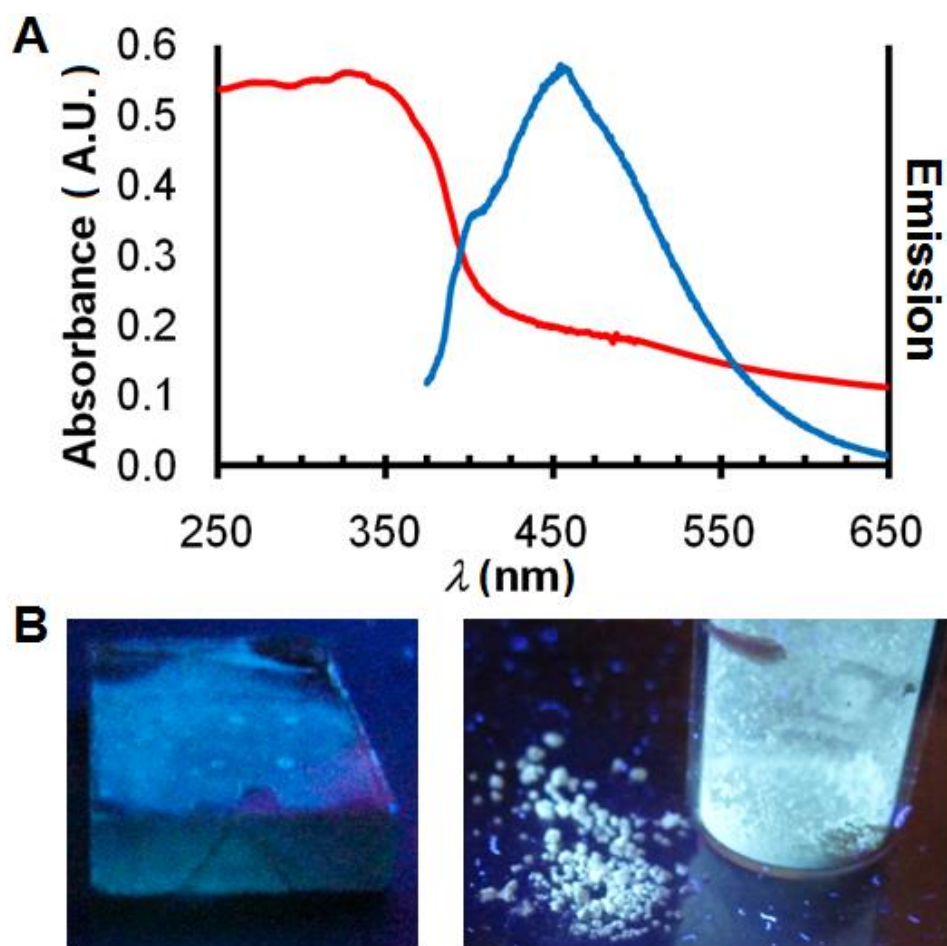


Figure 3.6. (A) Transmission absorption (red) and normalized emission (blue) spectra of **HHTP-DPB COF** thin film ($\lambda_{\text{exc}} = 357$ nm) and (B) photographs of fluorescent COF film on SiO₂ (left) and powder (right) under 365 nm illumination.

quantum yields, which increase dramatically when the phenyl rings are fixed into a coplanar arrangement.^{70,71} Finally, vertical stacking of the diphenylbutadiynes can also lead to a red-shifted emission.⁷²⁻⁷⁴

Conclusions

We have demonstrated that the pore sizes of oriented 2D layered COF films can be pushed well into the mesoporous regime, which significantly expands the range of complementary molecular, polymeric, or inorganic guests that might be co-organized with these unique materials. Our computational studies strongly suggest that 2D layered COFs do not adopt true eclipsed structures usually reported for these materials, but that the layers are slightly offset from one another. These calculations are easily generalized to other 2D layered COFs and will be critical for understanding interlayer exciton and charge transport, two processes of fundamental importance for COF-based optoelectronic devices. Highly luminescent COF films are of interest for fluorescent sensors,^{75,76} for which structural precision, tunable composition, and high surface areas will prove extremely useful.

REFERENCES

- (34) Cote, A. P.; Benin, A. I.; Ockwig, N. W.; O’Keeffe, M.; Matzger, A. J.; Yaghi, O. M. *Science* **2006**, *310*, 1166–1170.
- (35) Tilford, R. W.; Gemmill, W. R.; zur Loye, H.-C.; Lavigne, J. J. *Chem. Mater.* **2006**, *18* (22), 5296–5301.
- (36) Côté, A. P.; El-Kaderi, H. M.; Furukawa, H.; Hunt, J. R.; Yaghi, O. M. *J. Am. Chem. Soc.* **2007**, *129* (43), 12914–12915.
- (37) Tilford, R. W.; Mugavero, S. J.; Pellechia, P. J.; Lavigne, J. J. *Adv. Mater.* **2008**, *20* (14), 2741–2746.
- (38) Wan, S.; Guo, J.; Kim, J.; Ihee, H.; Jiang, D. *Angew. Chem. Int. Ed.* **2008**, *47* (46), 8826–8830.
- (39) Wan, S.; Guo, J.; Kim, J.; Ihee, H.; Jiang, D. *Angew. Chem. Int. Ed.* **2009**, *48* (30), 5439–5442.
- (40) Spitler, E. L.; Dichtel, W. R. *Nat. Chem.* **2010**, *2* (8), 672–677.
- (41) Dogru, M.; Sonnauer, A.; Gavryushin, A.; Knochel, P.; Bein, T. *Chem. Commun.* **2011**, *47* (6), 1707–1709.
- (42) Spitler, E. L.; Giovino, M. R.; White, S. L.; Dichtel, W. R. *Chem. Sci.* **2011**, *2* (8), 1588–1593.
- (43) Feng, X.; Chen, L.; Dong, Y.; Jiang, D. *Chem. Commun.* **2011**, *47* (7), 1979–1981.
- (44) El-Kaderi, H. M.; Hunt, J. R.; Mendoza-Cortés, J. L.; Côté, A. P.; Taylor, R. E.; O’Keeffe, M.; Yaghi, O. M. *Science* **2007**, *316* (5822), 268–272.
- (45) Uribe-Romo, F. J.; Hunt, J. R.; Furukawa, H.; Klöck, C.; O’Keeffe, M.; Yaghi, O. M. *J. Am. Chem. Soc.* **2009**, *131* (13), 4570–4571.
- (46) Ding, X.; Guo, J.; Feng, X.; Honsho, Y.; Guo, J.; Seki, S.; Maitarad, P.; Saeki, A.; Nagase, S.; Jiang, D. *Angew. Chem. Int. Ed.* **2011**, *50* (6), 1289–1293.
- (47) Ding, X.; Chen, L.; Honsho, Y.; Feng, X.; Saengsawang, O.; Guo, J.; Saeki, A.; Seki, S.; Irle, S.; Nagase, S.; Parasuk, V.; Jiang, D. *J. Am. Chem. Soc.* **2011**, *133* (37), 14510–14513.
- (48) Wan, S.; Gándara, F.; Asano, A.; Furukawa, H.; Saeki, A.; Dey, S. K.; Liao, L.; Ambrogio, M. W.; Botros, Y. Y.; Duan, X.; Seki, S.; Stoddart, J. F.; Yaghi, O. M. *Chem. Mater.* **2011**, *23* (18), 4094–4097.
- (49) Colson, J. W.; Woll, A. R.; Mukherjee, A.; Levendorf, M. P.; Spitler, E. L.; Shields, V. B.; Spencer, M. G.; Park, J.; Dichtel, W. R. *Science* **2011**, *332* (6026), 228–231.
- (50) Berlanga, I.; Ruiz-González, M. L.; González-Calbet, J. M.; Fierro, J. L. G.; Mas-Ballesté, R.; Zamora, F. *Small* **2011**, *7* (9), 1207–1211.
- (51) Dogru, M.; Bein, T. *Nat. Nanotechnol.* **2011**, *6* (6), 333–335.
- (52) Lukose, B.; Kuc, A.; Heine, T. *Chem. – Eur. J.* **2011**, *17* (8), 2388–2392.
- (53) Cornil, J.; Lemaire, V.; Calbert, J.-P.; Brédas, J.-L. *Adv. Mater.* **2002**, *14* (10), 726–729.

- (54) Coropceanu, V.; Cornil, J.; da Silva Filho, D. A.; Olivier, Y.; Silbey, R.; Brédas, J.-L. *Chem. Rev.* **2007**, *107* (4), 926–952.
- (55) Patwardhan, S.; Kocherzhenko, A. A.; Grozema, F. C.; Siebbeles, L. D. A. *J. Phys. Chem. C* **2011**, *115* (23), 11768–11772.
- (56) Sing, K. S. W. *Pure Appl. Chem.* **1985**, *57* (4), 603–619.
- (57) Walton, K. S.; Snurr, R. Q. *J. Am. Chem. Soc.* **2007**, *129* (27), 8552–8556.
- (58) *Accelrys*; Accelrys Software: San Diego, 2008.
- (59) O’Keeffe, M.; Peskov, M. A.; Ramsden, S. J.; Yaghi, O. M. *Acc. Chem. Res.* **2008**, *41* (12), 1782–1789.
- (60) Coates, G. W.; Dunn, A. R.; Henling, L. M.; Dougherty, D. A.; Grubbs, R. H. *Angew. Chem. Int. Ed. Engl.* **1997**, *36* (3), 248–251.
- (61) Li, Z.; Fowler, F. W.; Lauher, J. W. *J. Am. Chem. Soc.* **2009**, *131* (2), 634–643.
- (62) Deschamps, J.; Balog, M.; Boury, B.; Ben Yahia, M.; Filhol, J.-S.; van der Lee, A.; Al Choueiry, A.; Barisien, T.; Legrand, L.; Schott, M.; Dutremez, S. G. *Chem. Mater.* **2010**, *22*, 3961–3982.
- (63) Allinger, N. L.; Yuh, Y. H.; Lii, J. H. *J. Am. Chem. Soc.* **1989**, *111* (23), 8551–8566.
- (64) Cantrell, R.; Clancy, P. *Surf. Sci.* **2008**, *602* (22), 3499–3505.
- (65) Jacquemin, D.; Perpète, E. A.; Ciofini, I.; Adamo, C.; Valero, R.; Zhao, Y.; Truhlar, D. G. *J. Chem. Theory Comput.* **2010**, *6* (7), 2071–2085.
- (66) Zhao, Y.; Truhlar, D. G. *Theor. Chem. Acc.* **2007**, *120* (1-3), 215–241.
- (67) Zhao, Y.; Truhlar, D. G. *J. Chem. Phys.* **2009**, *130* (7), 074103.
- (68) Tang, C.; Lennon, E. M.; Fredrickson, G. H.; Kramer, E. J.; Hawker, C. J. *Science* **2008**, *322* (5900), 429–432.
- (69) Niu, W.; Smith, M. D.; Lavigne, J. J. *J. Am. Chem. Soc.* **2006**, *128* (51), 16466–16467.
- (70) Mizobe, Y.; Ito, H.; Hisaki, I.; Miyata, M.; Hasegawa, Y.; Tohnai, N. *Chem. Commun.* **2006**, No. 20, 2126–2128.
- (71) Shanks, D.; Preus, S.; Qvortrup, K.; Hassenkam, T.; Nielsen, M. B.; Kilså, K. *New J. Chem.* **2009**, *33* (3), 507–516.
- (72) Egbe, D. A. M.; Ulbricht, C.; Orgis, T.; Carbonnier, B.; Kietzke, T.; Peip, M.; Metzner, M.; Gericke, M.; Birckner, E.; Pakula, T.; Neher, D.; Grummt, U.-W. *Chem. Mater.* **2005**, *17* (24), 6022–6032.
- (73) Egbe, D. A. M.; Birckner, E.; Klemm, E. *J. Polym. Sci. Part Polym. Chem.* **2002**, *40* (15), 2670–2679.
- (74) Goichi, M.; Miyahara, H.; Toyota, S. *Chem. Lett.* **2006**, *35* (8), 920–921.
- (75) Thomas, S. W.; Joly, G. D.; Swager, T. M. *Chem. Rev.* **2007**, *107* (4), 1339–1386.
- (76) Allendorf, M. D.; Bauer, C. A.; Bhakta, R. K.; Houk, R. J. T. *Chem. Soc. Rev.* **2009**, *38* (5), 1330–1352.

APPENDIX II

A. Materials. All reagents were purchased from commercial sources and used without further purification. Mesitylene and dioxane were purchased from commercial sources and used without further purification. Other solvents were purchased from commercial sources and purified using a custom-built alumina-column based solvent purification system.

Instrumentation.

Infrared spectra were recorded on a Thermo Nicolet iS10 with a diamond ATR attachment and are uncorrected.

UV/Vis absorbance spectra were recorded on a Cary 5000 UV-Vis-NIR spectrophotometer with a mercury lamp in either dichloromethane solution or as solids using a praying mantis diffuse reflectance accessory. Emission and excitation spectra were recorded on a Horiba Jobin Yvon Fluorolog-3 fluorescence spectrophotometer equipped with a 450 W Xe lamp, double excitation and double emission monochromators, a digital photon-counting photomultiplier and a secondary InGaAs detector for the NIR range. Correction for variations in lamp intensity over time and wavelength was achieved with a solid-state silicon photodiode as the reference. The spectra were further corrected for variations in photomultiplier response over wavelength and for the path difference between the sample and the reference by multiplication with emission correction curves generated on the instrument. Solid samples were mounted between quartz slides and mounted on a solid sample holder, and emission was observed using a front face detection accessory.

X-ray diffraction patterns were recorded on a Rigaku Smartlab Powder X-Ray Diffractometer in 2θ medium resolution parallel beam/PSA mode employing Cu K α line focused radiation at 40 kV, 44 mA power and equipped with a Ge crystal detector fitted with a 1.0 mm radiation entrance slit. Samples were mounted on zero background sample holders by dropping powders from a wide-blade spatula and then leveling the sample surface with a glass microscope slide. No sample grinding or sieving was used prior to analysis. Samples were observed using a 0.045° 2θ step scan from $1.0 - 34^\circ$ ($\Omega = 1.0^\circ$) with an exposure time of 0.4 s per step. No peaks could be resolved from the baseline for $2\theta > 34^\circ$ data and was therefore not considered for further analysis.

Thermogravimetric analysis from 20-600 °C was carried out on a TA Instruments Q500 Thermogravimetric Analyzer in nitrogen atmosphere using a 10 °C/min ramp without equilibration delay.

Scanning electron microscopy (SEM) was performed on a FEI Strata 400 FE-SEM. Materials were deposited onto a sticky carbon surface on a flat aluminum platform sample holder. No metal sputtering of the sample was necessary. Focused ion beam (FIB) patterning and milling was performed using a FEI Strata 400 FIB Ga⁺ LIM system. A 2x10 µm Pt strip (~1000 nm thickness) was deposited using the electron gun onto COF films grown on SLG/SiO₂ substrates prior to exposing the sample to the FIB. The sample was then milled with the FIB using a cleaning cross-section. After milling, the samples were imaged at 2 keV using the electron gun. Cross-sectional images were obtained using a stage tilt angle of 52°; thickness measurements made at this angle were corrected by multiplying by 1.26. SLG/SiO₂ substrates were grounded to the sample holder using sticky carbon prior to imaging to minimize charging.

Mass spectra were obtained on a Waters MALDI micro MX MALDI-TOF mass spectrometer using positive ionization and a reflectron detector. MALDI samples were prepared by wet deposition of a saturated analyte/dithranol matrix solution onto a metallic sample plate and air dried before loading into the instrument.

Surface area measurements were conducted on a Micromeritics ASAP 2020 Accelerated Surface Area and Porosimetry Analyzer using ca. 20 mg samples degassed at 180 °C for 12 hours. Nitrogen isotherms were generated by incremental exposure to ultra high purity nitrogen up to ca. 1 atm over 28-hour periods in a liquid nitrogen (77K) bath, and surface parameters were determined using Langmuir, BET and BJH adsorption models included in the instrument software (Micromeritics ASAP 2020 V1.05).

NMR spectra were recorded on a Bruker ARX 300 MHz spectrometer using a standard ¹H/X Z-PFG probe at ambient temperature with a 20 Hz sample spin rate.

Solid-state NMR spectra were recorded at ambient temperature on a Varian INOVA-400 spectrometer using an external Kalmus ¹H linear pulse amplifier blanked

using a spare line. Samples were packed into 7 mm outside diameter silicon nitride rotors and inserted into a Varian HX magic angle spinning (MAS) probe. ^{13}C data was acquired using linearly ramped cross-polarization with MAS (CP/MAS) at 100.5 MHz. The ^1H and ^{13}C had ninety-degree pulse widths of 5 μs , and the CP contact time was 1 ms. Two-pulse phase modulation (TPPM) ^1H decoupling was applied during data acquisition with a decoupling frequency of 78 kHz. The recycle delays between scans were 2 s. The MAS spin rate varied between 5–7 kHz, as labeled in the spectra. ^{13}C chemical shifts were assigned relative to tetramethylsilane at 0.0 ppm and were calibrated using the methyl carbon signal of hexamethylbenzene assigned at 16.9 ppm as a secondary reference. Direct observation of the ^{11}B nucleus was used to acquire the ^{11}B data at 128.3 MHz. using a pulse width of 1.5 μs , corresponding to a 27° response from the ^{11}B . TPPM decoupling was applied during data acquisition with a decoupling frequency of 78 kHz. A recycle time of 0.6 s was used. The MAS spinning rate varied between 5-7 kHz, as labeled in the spectra. The ^{11}B chemical shifts are assigned relative to $\text{BF}_3 \cdot \text{OEt}_2$ at 0.0 ppm and were calibrated using aqueous boric acid at pH = 4.4 assigned at 19.6 ppm as a secondary reference.

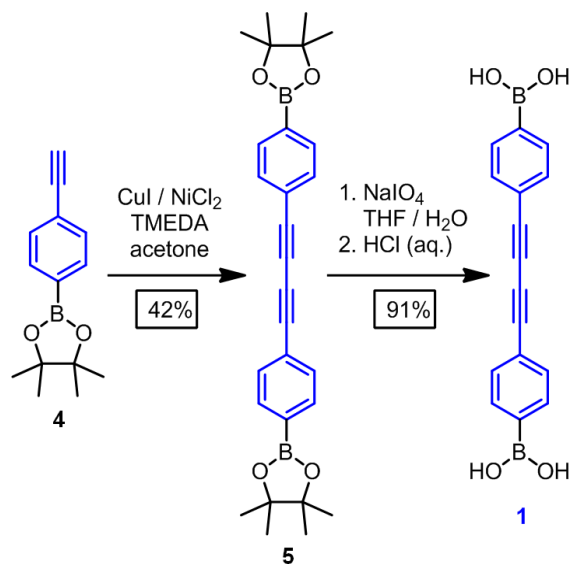
Grazing incidence X-ray diffraction (GID) was performed at the G2 station at Cornell High Energy Synchrotron Source (CHESS) using a beam energy of 8.78 ± 0.01 keV ($\lambda = 0.1414$ nm), selected using a single-crystal Be crystal monochromator. Motorized slits were used to define a 0.2×2 (V \times H) mm^2 beam, with a typical flux of 2×10^{10} photons/s. The data were collected using a 640-element 1D diode-array, of which each element incorporates its own pulse counting electronics capable of count rates of $\sim 10^5$ photons/s. A set of 0.1° Soller slits were used on the detector arm to define the in-plane resolution. The scattering geometry is described in detail elsewhere.¹ Each data set was collected by scanning the detector with the sample stationary. The incidence angle α between the beam and sample surface was 0.175° . Axes labels Q_∞ and Q_\parallel are defined using the GISAXS convention $Q_\infty = 4\pi/\lambda \sin(\delta/2)$ and $Q_\parallel = 4\pi/\lambda \sin(\nu/2)$, where δ and ν are the vertical and horizontal scattering angles, respectively.² At $\alpha = \delta = 0$, hQ_\parallel and hQ_∞ (where h is Planck's constant) are the components of momentum transfer parallel and perpendicular to the sample surface, respectively.

B. Methods and Synthetic Procedures.

Graphene Growth. Single-layer graphene was grown on 25 μm -thick copper foil using previously reported chemical vapor deposition methods.³ A layer of PMMA (50 nm) was spin-coated on top of the graphene and the copper was etched using aq. FeCl_3 . The graphene was then transferred to fused SiO_2 and the PMMA removed by washing first with chloroform then isopropyl alcohol. The SLG/ SiO_2 was finally calcined at 300 $^\circ\text{C}$ for 2.5 h.

General procedure HHTP-DPB film growth on SLG. HHTP **2** (16 mg, 0.049 mmol) and diboronic acid **1** (43 mg, 0.15 mmol) were added to a 15 mL cylindrical pressure vessel and suspended in a mixture of mesitylene and 1,4-dioxane (v/v 1:1; 1.0 mL). After capping, the mixture was sonicated for 30 minutes and a graphene-containing substrate was added. The sealed vessel was heated in a 90 $^\circ\text{C}$ oven for 24 h. The vessel was cooled to room temperature and the resulting gray powder was recovered by filtration and dried under vacuum. The graphene-containing substrate was submerged in anhydrous toluene and sonicated for 5 seconds, and finally dried under vacuum.

Scheme A2.1. Synthesis of boronic acid **1**.



Diboronate ester **5**: TMEDA (0.459 g, 3.946 mmol), CuI (0.188 g, 0.986 mmol), and NiCl₂•6H₂O (0.234 g, 0.986 mmol) were dissolved or suspended in (CH₃)₂CO (13 mL) under an atmosphere of air. The mixture became dark green after 10 min. 4-Ethynylbenzeneboronic acid pinacol ester (**4**, 4.50 g, 19.7 mmol) was added, and the mixture was stirred for 12 h. The solvent was evaporated and the resulting yellow-green residue was washed with H₂O (50 mL) and recrystallized from CH₃CN, providing the dialkyne ester **5** (1.90 g, 42%) as a white solid. ¹H-NMR (CDCl₃, 300 MHz, 298 K) δ 7.65 (d, *J* = 9.0 Hz, 4H); 7.52 (d, *J* = 9.0 Hz, 4H); 1.34 (s, 24H). ¹³C-NMR (CDCl₃, 300 MHz) δ 135, 132, 125, 83, 75, 25. MALDI-MS *m/z* (%) 453.0 (45, M⁺); 453.9 (100, M⁺+1); 454.9 (38, M⁺+2). IR (powder, ATR) 2981, 2936, 1604, 1542, 1510, 1398, 1355, 1323, 1274, 1261, 1217, 1168, 1141, 1085, 1017, 963, 857, 836, 826, 758, 738 cm⁻¹. UV-Vis [*λ* /nm (log *ε* / M⁻¹ cm⁻¹), 4.4 μM in DMF] 343 (4.64), 321 (4.75), 300 (4.74), 279(sh) (4.86). Em (*λ*/nm in DMF) 371, 344. Anal. Calcd for (C₂₈H₃₂B₂O₄): C, 74.05; H, 7.10. Found: C, 73.93; H, 6.94.

Diboronic acid **1**: A 20 mL scintillation vial was charged with the diboronate ester **5** (400 mg, 0.88 mmol) and NaIO₄ (400 mg, 2.0 mmol). The solids were dissolved in a THF:H₂O mixture (4:1, 6 mL) and stirred at rt for 2 h. 1M HCl (2 mL) was then added via micropipette to the white suspension, which was stirred for another 12 h. The pale

yellow-white suspension was diluted with H₂O (20 mL), and the solids recovered by filtration. The recovered solid was washed with an additional H₂O (20 mL) followed by hexanes (10 mL). The white solid was dried under vacuum to yield 233 mg (91%) of boronic acid **1**. ¹H-NMR (DMSO-d₆, 300 MHz) δ 8.26 (s, 4H); 7.82 (d, *J* = 7.5 Hz, 4H); 7.57 (d, *J* = 7.5 Hz, 4H). ¹³C-NMR (DMSO-d₆, 300 MHz) δ 136, 134, 131, 122, 82, 74. MALDI-MS *m/z* (%) 289.1 (21, M⁺); 290.1 (100, M⁺+1); 291.1 (2, M⁺+2). IR (powder, ATR) 3391, 3315, 1604, 1545, 1509, 1399, 1337, 1263, 1215, 1162, 1121, 1084, 1027, 1012, 972, 859, 834, 809, 757, 738 cm⁻¹. UV-Vis [λ /nm (log ϵ / M⁻¹ cm⁻¹), 7.6 μ M in DMF] 341 (4.77), 319 (4.85), 299 (4.76), 277(sh) (4.77). Em (λ /nm in DMF, λ_{ex} = 350 nm) 372, 390, 402. Anal. Calcd for (C₁₆H₁₂B₂O₄): C, 66.29; H, 4.17. Found: C, 66.08; H, 4.03.

HHTP-DPB COF: Boronic acid **1** (20 mg, 0.069 mmol) and HHTP **2** (7 mg, 0.022 mmol) were combined in a mixture of dioxane and mesitylene (1:1, 4 mL) and sonicated for 10 min. The light gray suspension was transferred to a 10 mL pre-scored long-necked glass ampoule, flash-frozen in a liquid nitrogen bath, and flame-sealed. The ampoule was placed in a 90 °C gravity convection oven for 72 h, and the resulting free-flowing tan powder was collected by filtration on a Hirsch funnel, washed with 1 mL anhydrous toluene and air-dried. The crude **HHTP-DPB COF** was characterized by PXRD and IR before and after heating at 100 °C under vacuum. Isolated yield 10 mg (71%). IR (powder, ATR) 1606, 1493, 1452, 1355, 1326, 1243, 1161, 1065, 1018, 832, 734 cm⁻¹. PXRD [2θ (relative intensity)] 2.17 (100), 3.29 (26), 5.90 (8.0), 8.02 (2.7), 9.68 (1.60), 11.66 (0.86), 25.84 (0.74). UV-Vis (powder, praying mantis DRA) 1069, 989, 615 (sh), 369. Em (λ /nm, λ_{ex} = 350 nm) 463. Anal. Calcd for (C₄₂H₁₈B₃O₆)_n: C, 77.49; H, 2.79. Found: C, 72.57; H, 3.04. It has been noted^{4,5} that elemental analysis of boronate COFs typically give lowered carbon values from the formation of non-combustible boron carbide byproducts. The presence of boron was confirmed by a characteristic B 1s peak in the XPS with a binding energy of 190.6 eV.

C. NMR Spectra.

Figure A2.1. ^1H -NMR spectrum of ester **5** (CDCl_3 , 500 MHz, 298K).

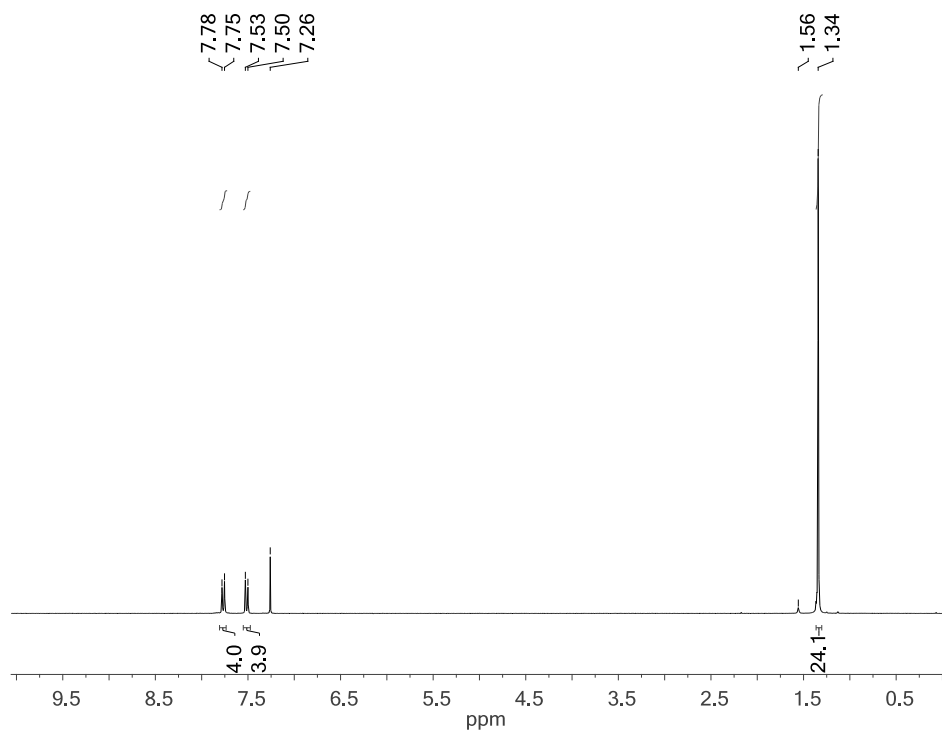


Figure A2.2. ^{13}C -NMR spectrum of ester **5** (CDCl_3 , 500 MHz, 298K).

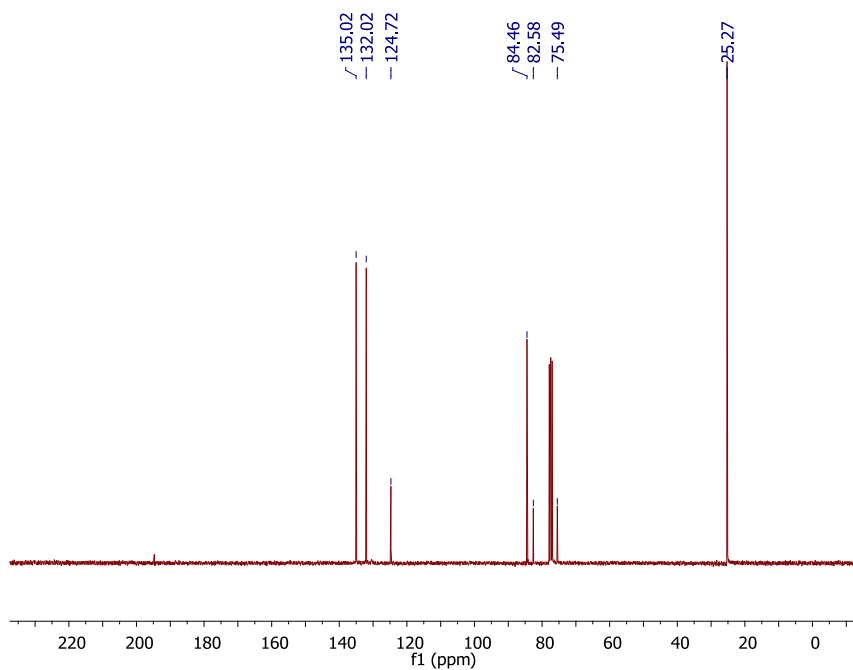


Figure A2.3. ^1H -NMR spectrum of acid **1** (DMSO- d_6 , 500 MHz, 298K).

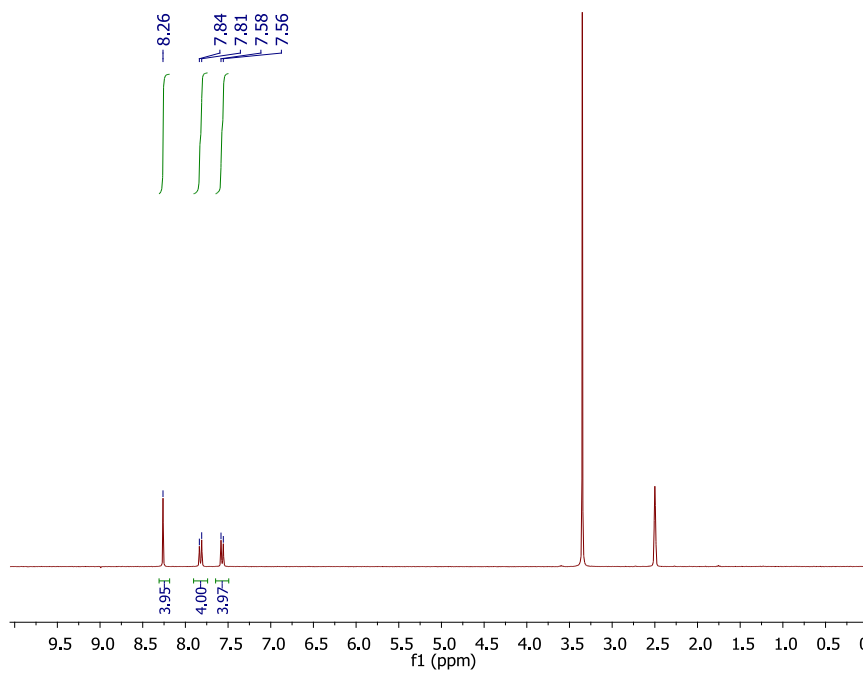
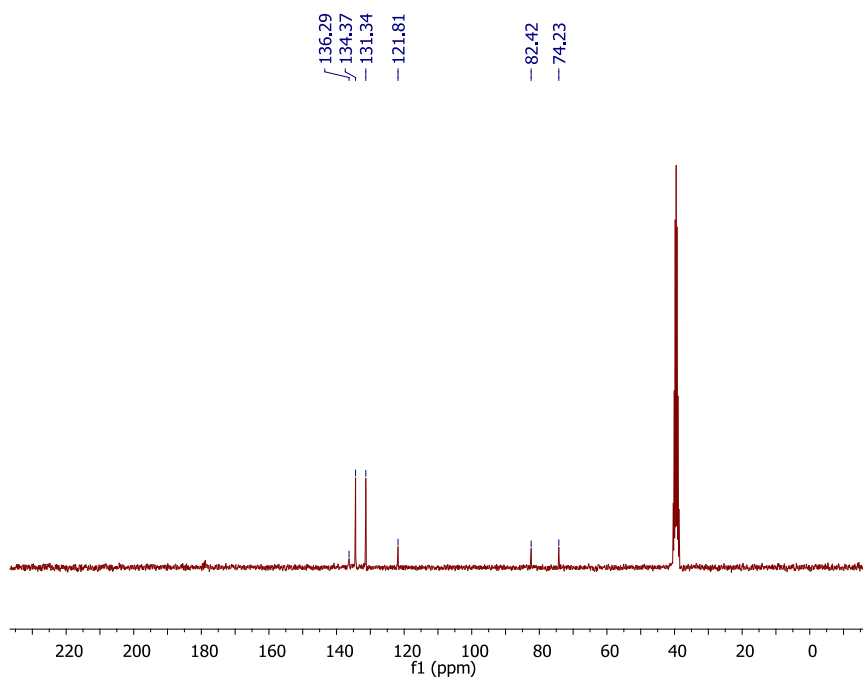


Figure A2.4. ^{13}C -NMR spectrum of acid **1** (DMSO- d_6 , 500 MHz, 298K).



D. MALDI-TOF MS of COF Precursors

Figure A2.5. MALDI-MS spectrum of ester **5**.

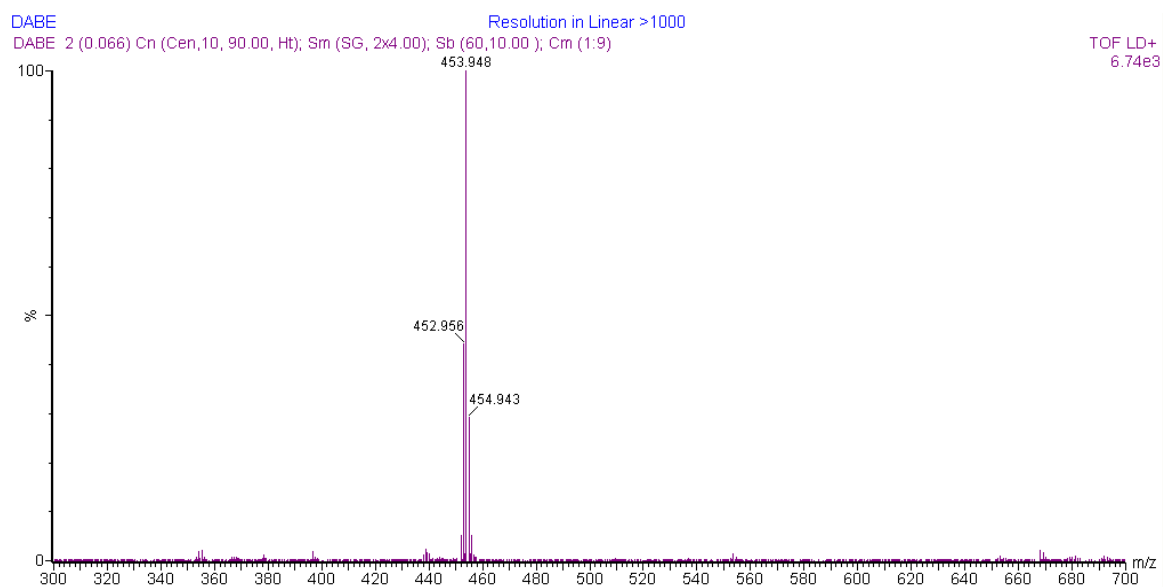
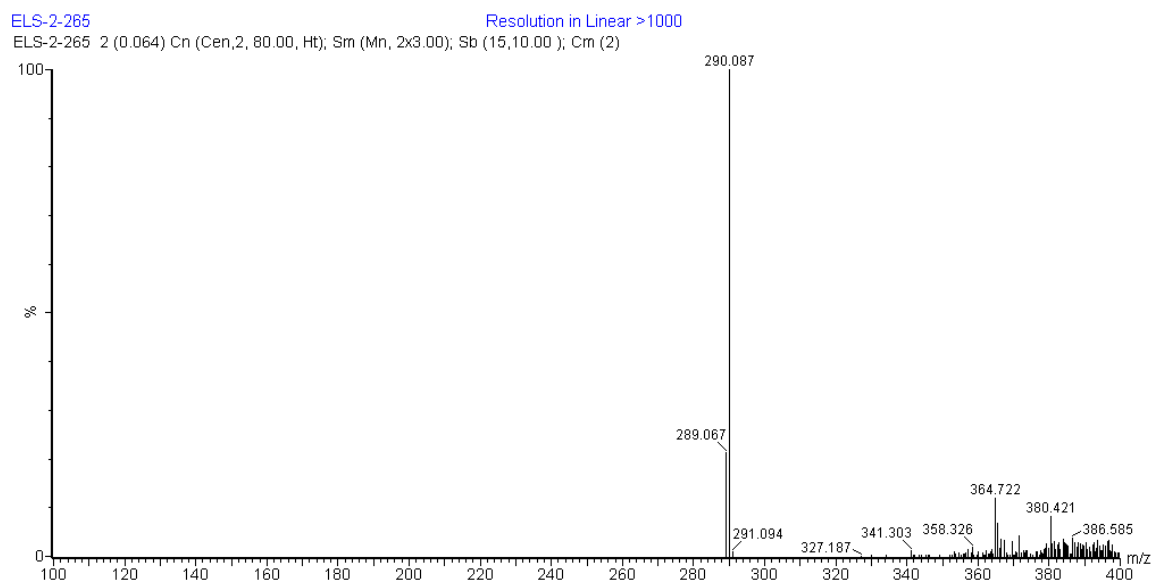


Figure A2.6. MALDI-MS spectrum of acid **1**.



E. Solid-state CP/MAS ^{13}C and ^{11}B NMR of HHTP-DPB COF

Figure A2.7. CP/MAS ^{13}C NMR spectra of **HHTP-DPB COF** prior to activation (note presence of mesitylene). The spectra were acquired at two different spinning rates to assign spinning side bands (*).

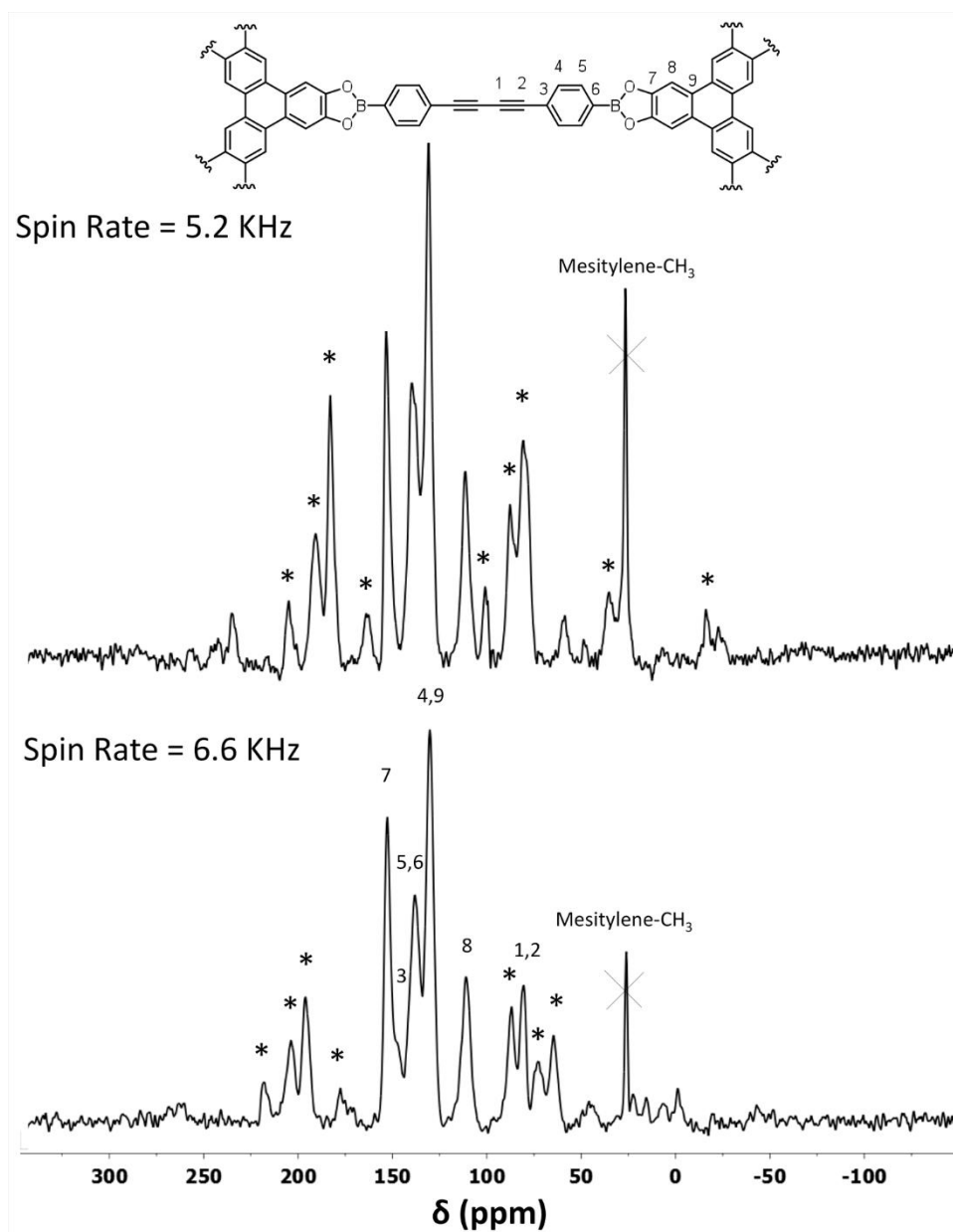


Figure S8. CP/MAS ^{13}C NMR spectra of **HHTP-DPB COF** after activation. The spectra were acquired at two different spinning rates to assign spinning side bands (*).

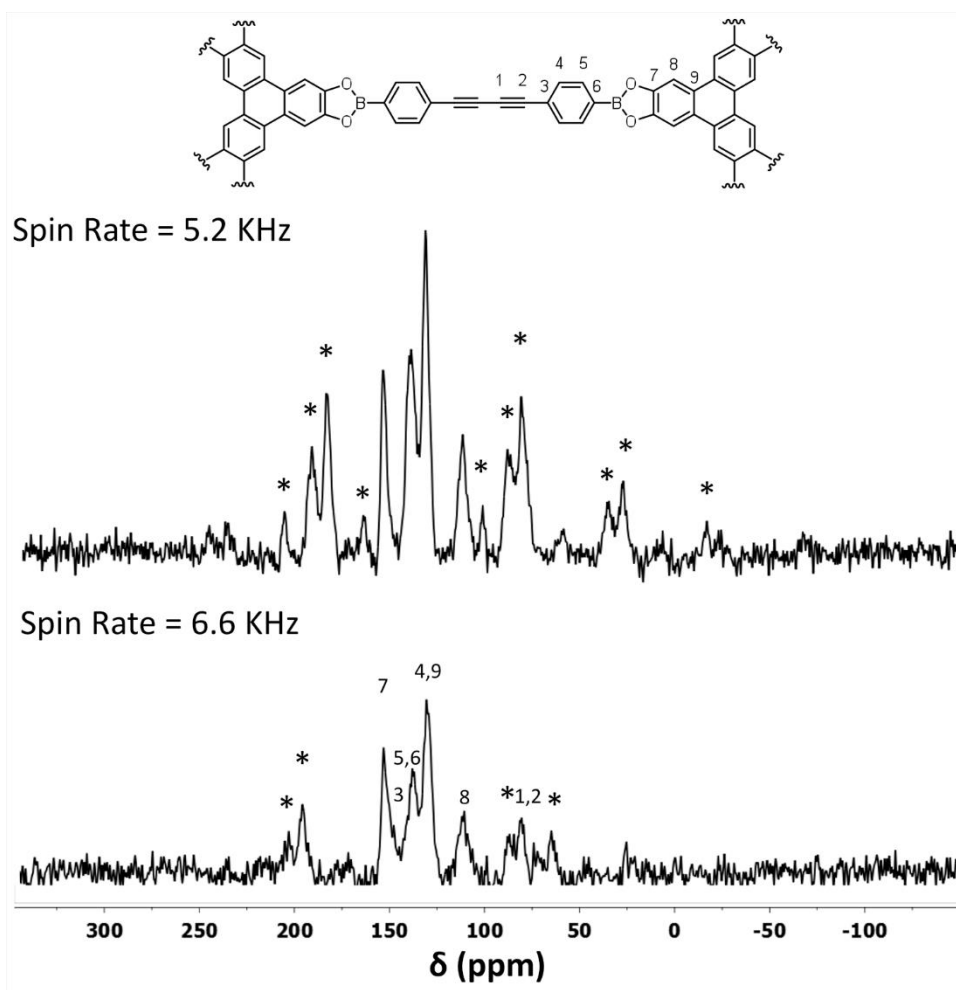
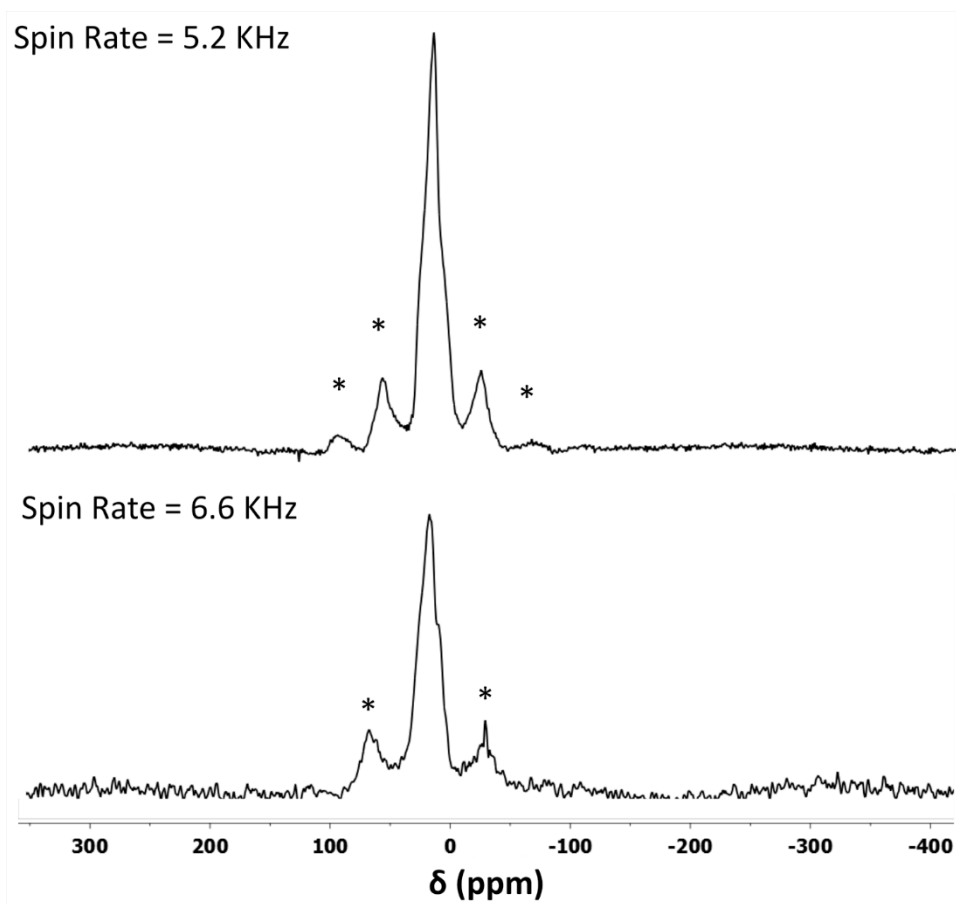


Figure A2.9. Solid-state ^{11}B NMR spectra of **HHTP-DPB COF** prior to activation. The spectra were acquired at two different spinning rates to assign spinning side bands (*).



F. FTIR Spectra.

Figure A2.10. FTIR spectra of diboronate ester **5** (blue) and acid **1** (red).

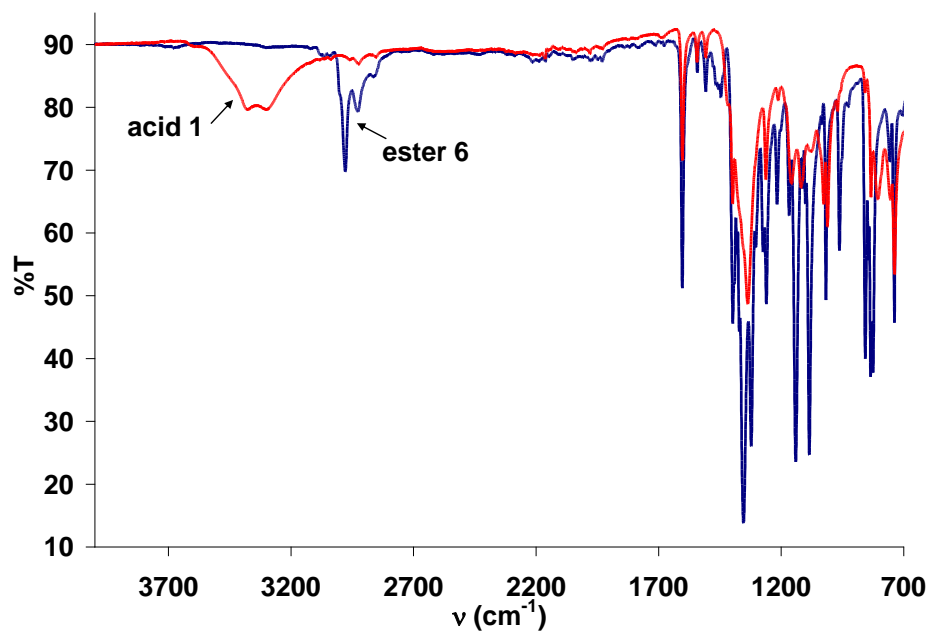
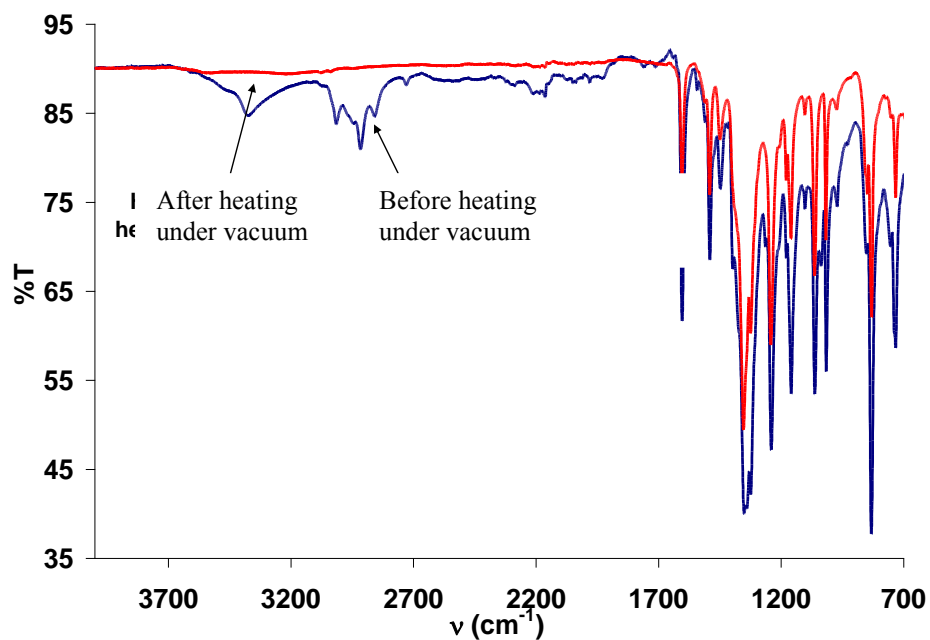


Figure A2.11. FTIR spectra of **HHTP-DPB COF** before (blue) and after (red) pore activation by heating under vacuum.



G. UV-Vis-NIR Characterization

Figure A2.12. Absorption spectra of ester **5** (blue) and acid **1** (red) in DMF.

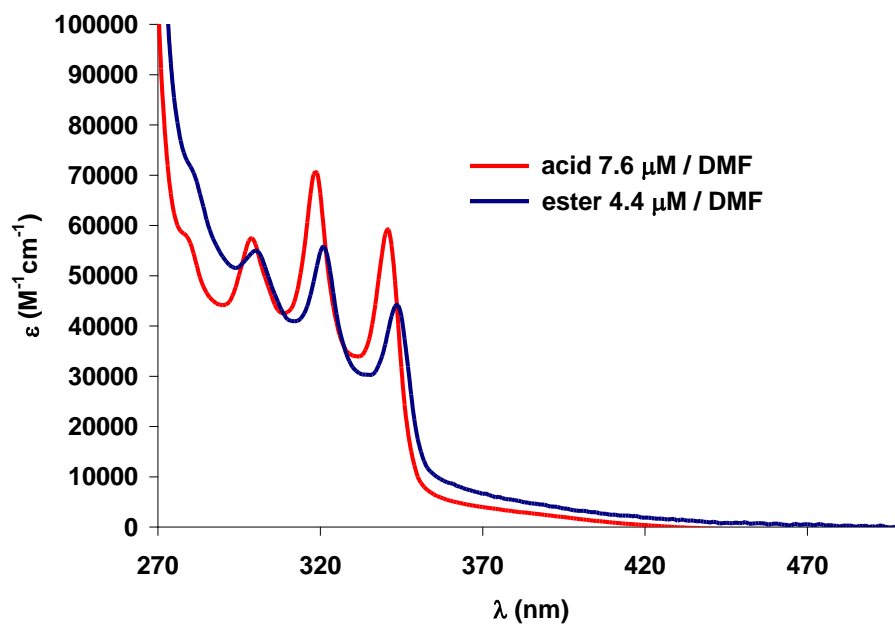
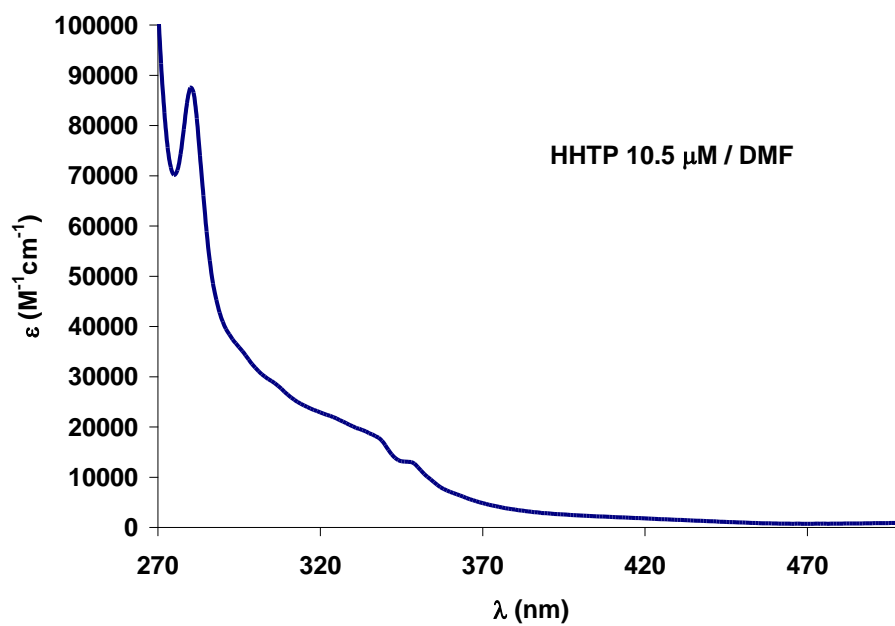
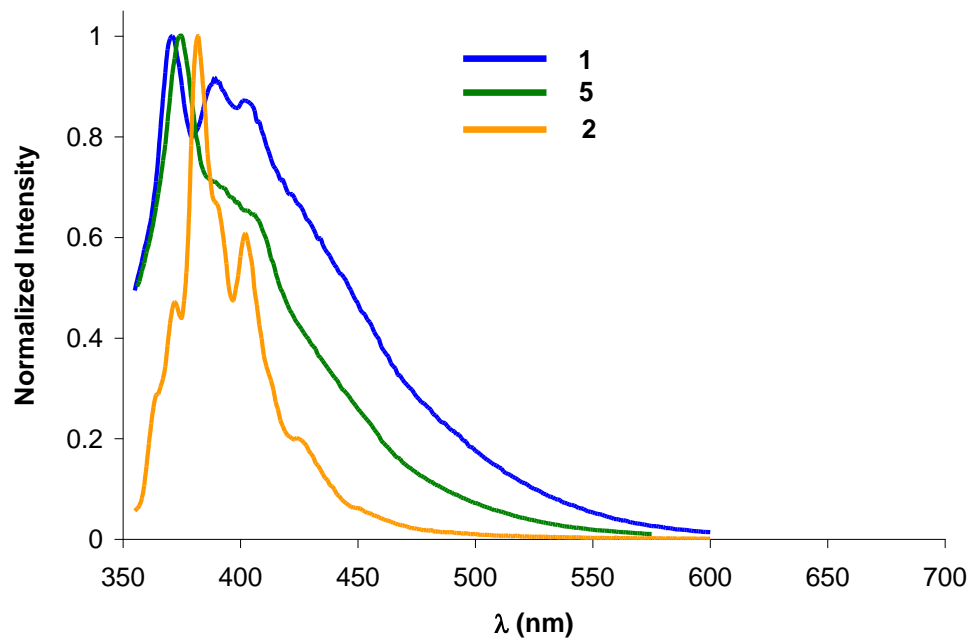


Figure A2.13. Absorption spectrum of HHTP **2** in DMF.



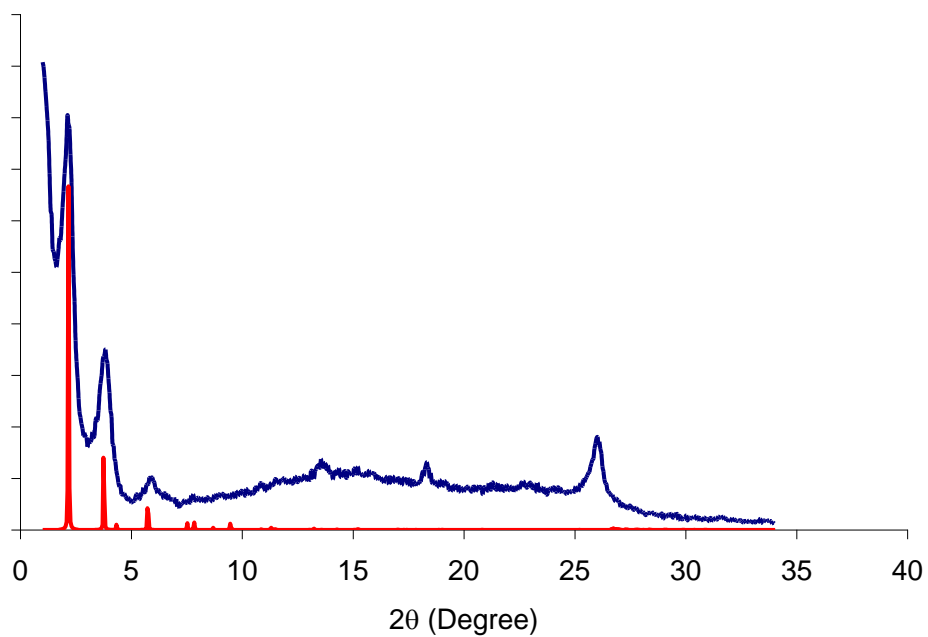
H. Emission Spectra.

Figure A2.14. Emission spectra ($\lambda_{\text{exc}} = 350 \text{ nm}$) of acid **1** (blue), ester **5** (green), and HHTP **2** (gold) in DMF.



I. Powder X-Ray Diffraction Data.

Figure A2.15. PXRD pattern of initially isolated **HHTP-DPB COF** material before pore activation (blue) vs simulated pattern (red). Note significant amount of amorphous material and impurities.



J. Simulation of the COF Structures from X-ray Diffraction Data. Molecular modeling of the COF was carried out using the Materials Studio (ver.5.0) suite of programs by Accelrys.⁶ The unit cell precursor was defined as the model structures shown in Figure S22a. The initial structures (**bnn**) were constructed piecewise starting with a primitive hexagonal unit cell with space group $P6/mmm$. The a cell parameter was estimated according to the distance between the center of the vertices for each COF as shown in Figure S13, and c parameter was arbitrarily chosen as 3.35 Å. The structures were optimized using the Geometry Optimization routine including energy minimization with cell parameters optimization, using the parameters from the Universal Force Field.⁸ Modeling of the staggered structures (**gra**) was performed in a similar manner but starting with the space group $P6_3/mmc$, and $c = 6.70$ Å. The MS Reflex Plus module was then used to calculate the expected PXRD patterns, which matched the experimentally observed pattern closely in peak position and intensity (line broadening from crystallite size was not calculated). The observed diffraction pattern was subjected to Pawley refinement wherein peak profile and line shape parameters were refined using the Pseudo-Voigt peak shape function and asymmetry was corrected using the Berar-Baldinozzi function.^{4,7} The refinement was applied to the calculated lattice, producing the refined PXRD profile.

Figure A2.16. Precursor structure used for initial modeling of the COF structure.

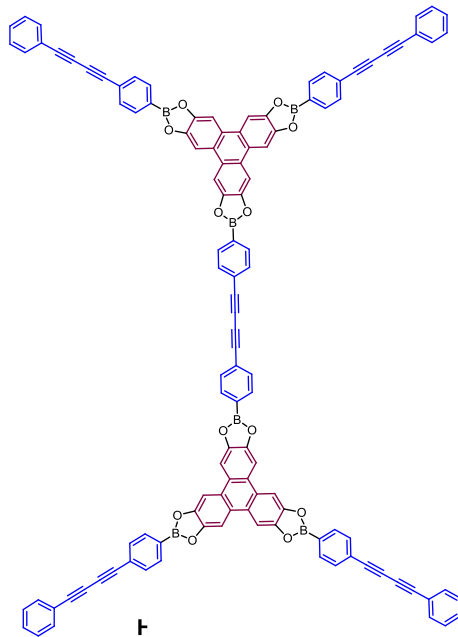


Figure A2.17. COF crystal model in **bnn** configuration.

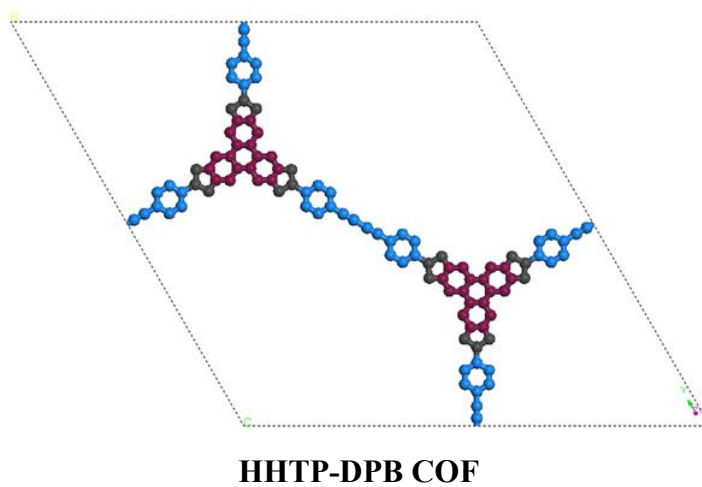


Figure A2.18. Observed (blue) versus Pawley-refined (red) PXRD pattern profiles for **HHTP-DPB COF**.

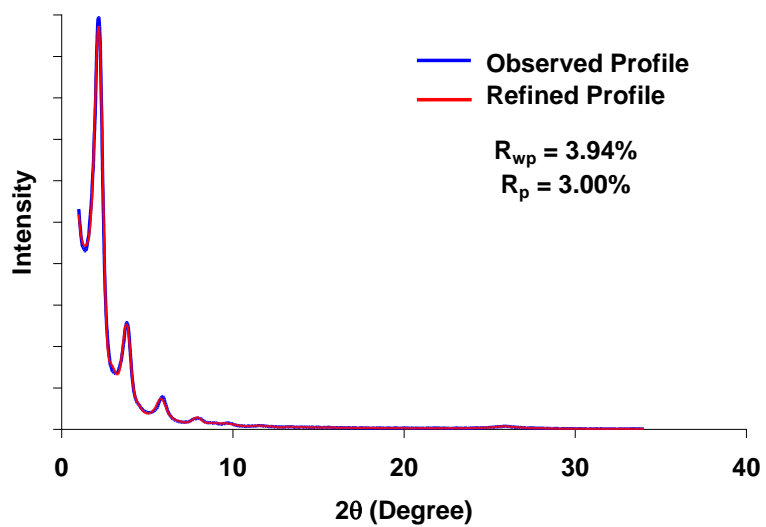
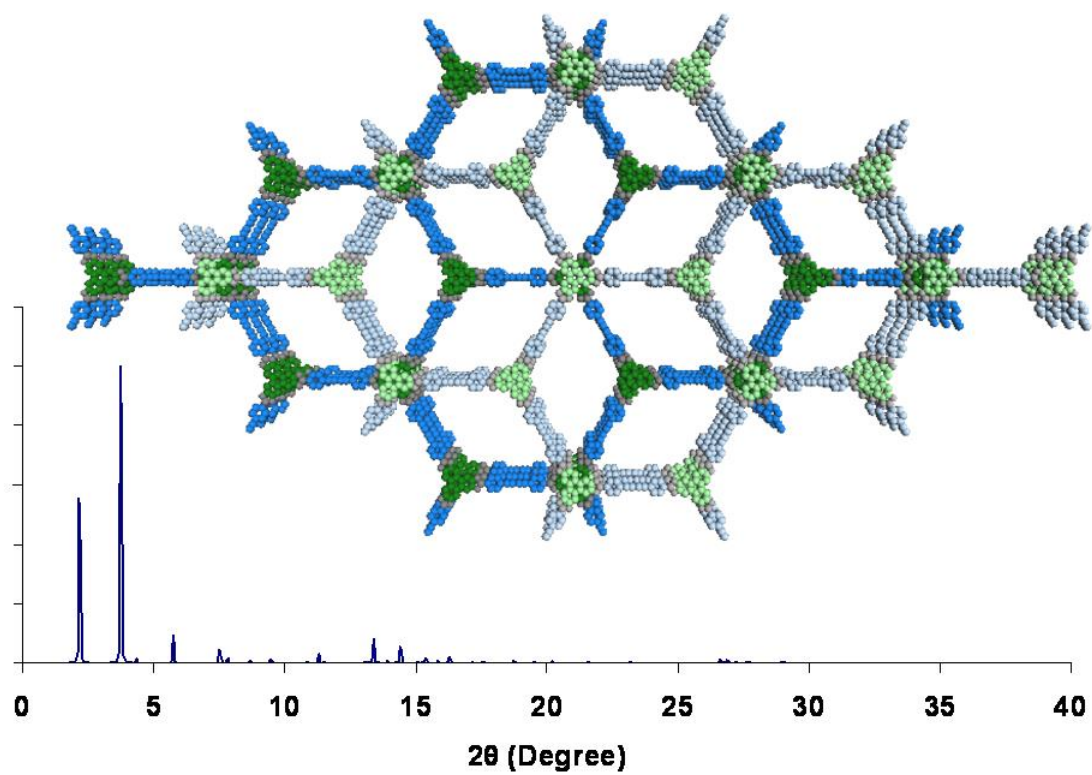


Table A2.1. Fractional atomic coordinates for unit cell of **HHTP-DPB COF** calculated using the Materials Studio ver. 5.0 modeling program.

bnn
(P6/mmm)
 $a = b = 46.909 \text{ \AA}$, $c = 3.369 \text{ \AA}$

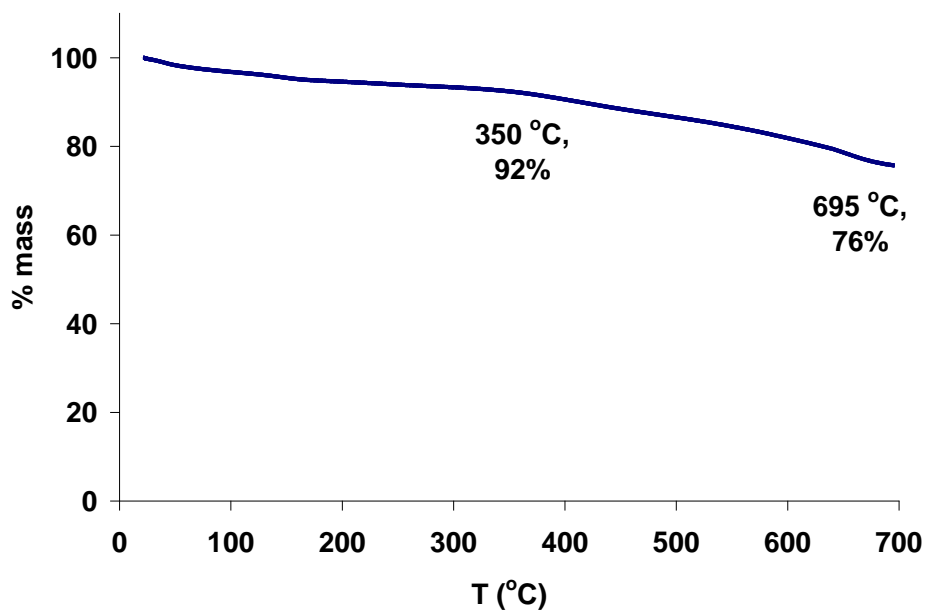
atom	x	y	z
C1	0.980992	0.490590	0.50000
C2	0.950829	0.475552	0.50000
C3	0.914652	0.457440	0.50000
C4	0.896801	0.474121	0.50000
C5	0.862091	0.456695	0.50000
C6	0.844338	0.422146	0.50000
C7	0.755507	0.391306	0.50000
C8	0.726037	0.392127	0.50000
C9	0.695359	0.362223	0.50000
B1	0.804937	0.402202	0.50000
O1	0.785010	0.366023	0.50000

Figure A2.19. Model (top) of HHTP-DPB COF in a *gra* packing and corresponding simulated PXRD pattern (bottom).



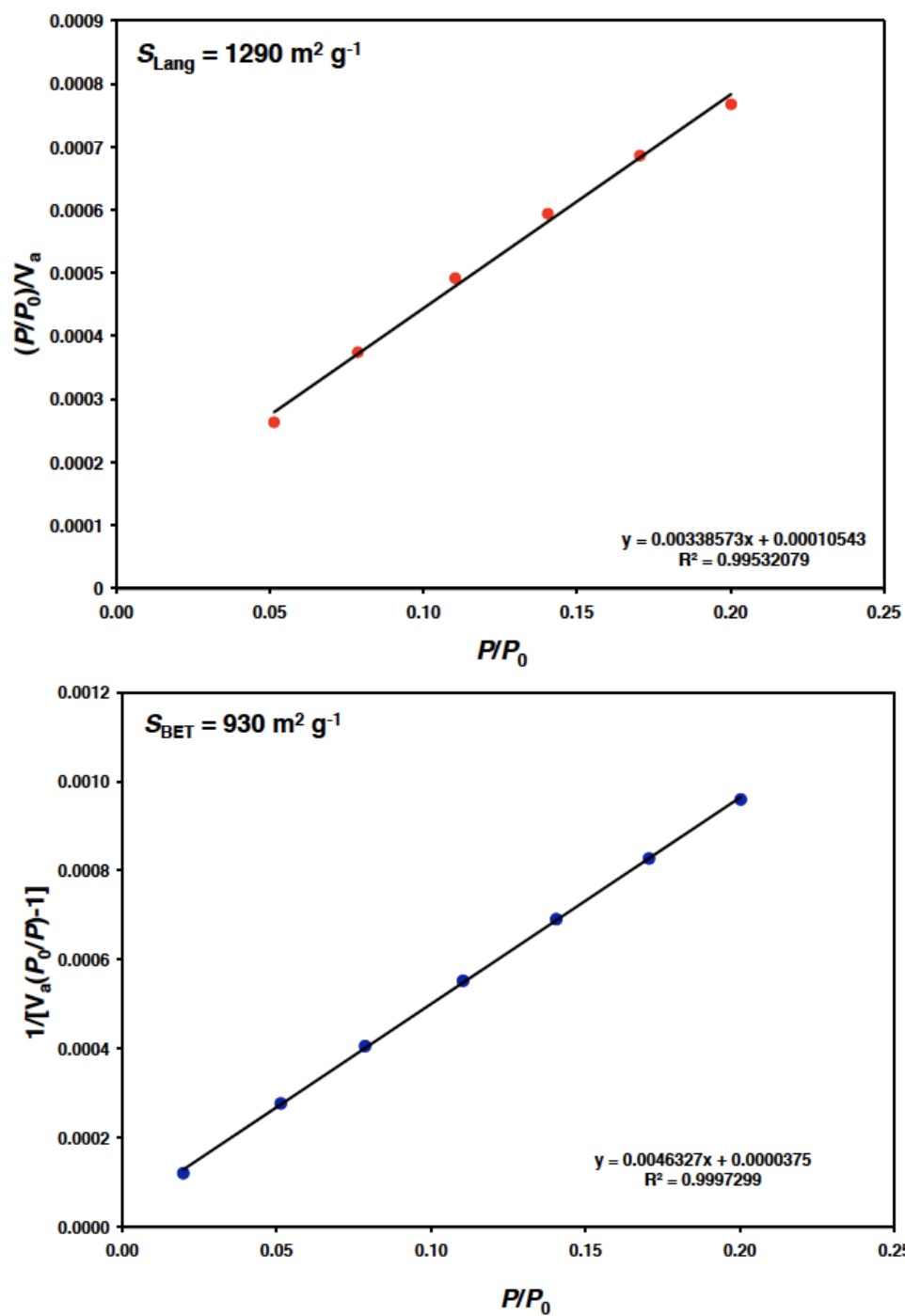
K. Thermogravimetric Analysis. TGA trace of the COF was obtained up to 700 °C using a linear 10 °C/min ramp method.

Figure A2.20. Thermogravimetric trace of **HHTP-DPB COF**.



L. Surface Area Measurements and Simulations.

Figure A2.21. Langmuir and BET surface area plot for **HHTP-DPB COF** calculated from adsorption data.



Simulations of the N₂ Isotherm of HHTP-DPB COF

Simulations of the N₂ adsorption isotherm was performed using Monte Carlo Metropolis method⁹ using the Sorption Module in Materials Studio. 100 adsorption steps in logarithmic scale were simulated using 10⁵ equilibration steps and 10⁶ production steps at 77 K for N₂. The relaxed structures obtained from crystal modeling and dinitrogen adsorbate were used as inputs for the simulation using the parameters in the universal force field (UFF).⁸ For the final isotherms, the fugacity was transformed into P/P_0 units and loading per cell was transformed into cm³ (STP) g⁻¹ units. The Brunauer-Emmett-Teller (BET) model was used over the obtained isotherms in the $0.05 < P/P_0 < 0.30$ ranges to obtain the BET surface area.

The accessible surface area was calculated in Materials Studio by determining the Connolly surface of the crystal models using a probe with a radius of 1.6 Å. In addition to the fully eclipsed $P6/mmm$ (**bnn**) structure, accessible surfaces of crystal models were calculated of the fully staggered structure $P6_3/mmc$ (**gra**) and the eclipsed structure after reducing the symmetry of a super cell ($a' = a$, and $c' = 2c$) to $P1$ and inducing offsets between the two independent layers present.

Figure A2.22. Simulated N₂ adsorption isotherm of HHTP-DPB-COF.

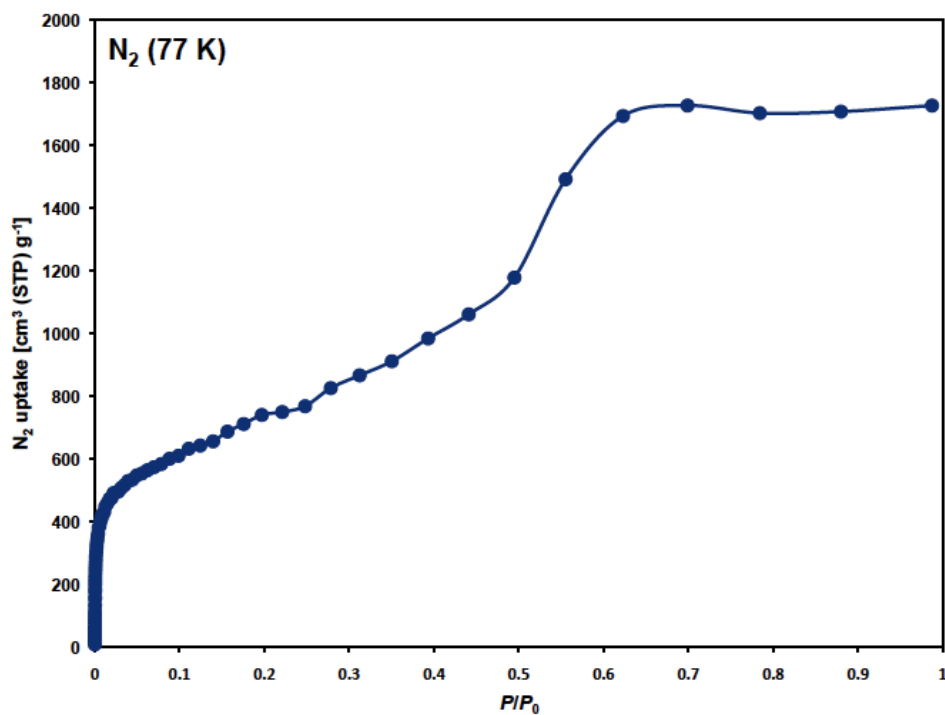


Figure A2.23. BET plot of the simulated N₂ adsorption isotherm of HHTP-DPB-COF. Surface area and linear equation inset.

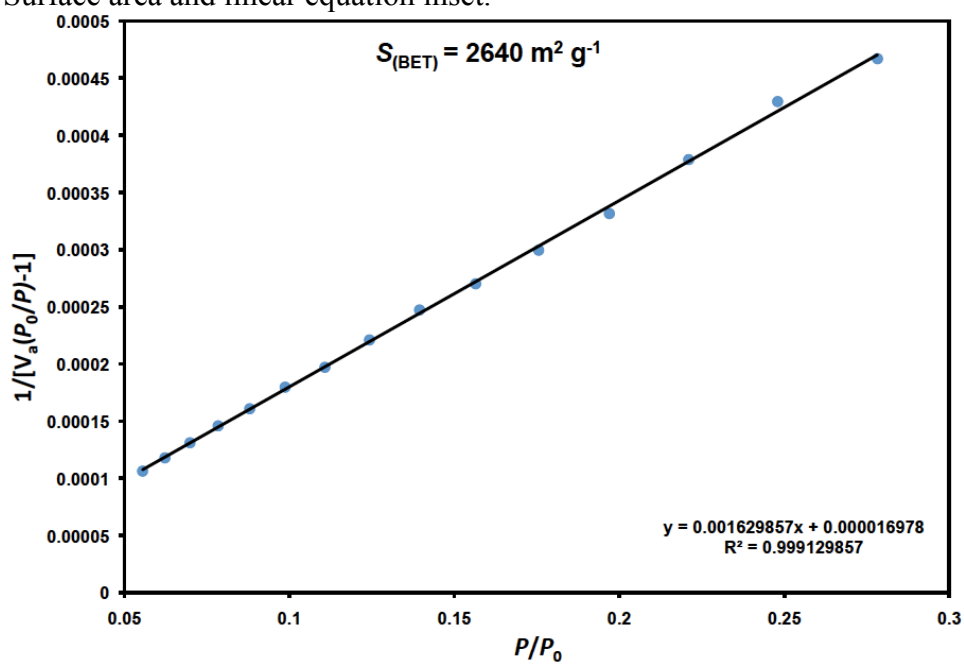


Table A2.2. Accessible surface areas obtained from the Connolly surfaces of the crystal models.

Structure	Accessible Surface Area (m ² g ⁻¹)
<i>P6/mmm</i> (bnn)	2669.5
<i>P6₃/mmc</i> (gra)	9206.7
<i>P1</i> (eclipsed w/offset by 1 Å <i>a</i> + 1 Å <i>b</i>)	2689.4
<i>P1</i> (eclipsed w/offset by 1.7 Å to center of pore)	2709.6

M. Computational Methods

We computed the potential energy surface (PES) describing the offset of **HHTP-DPB COF** layers with two independent approaches: density functional theory (DFT) and molecular mechanics (MM). Preceding the PES calculations, the geometry of a single HHTP-DPB layer was optimized in Gaussian09¹² with DFT using the M06¹³ exchange correlation functional and the 6-31G(d,p) basis set. M06 is a meta-hybrid generalized gradient approximation functional that has been designed to accurately model non-covalent interactions and has been used in prior studies to model molecular systems with π - π stacking.¹² Therefore, in addition to the modeling of intramolecular interactions, the M06 functional was used to model the intermolecular interactions between layers, given the highly aromatic structure of **HHTP-DPB COF**. To generate the PES with molecular mechanics methods, we implemented the intermolecular portion of the semi-empirical Molecular Mechanics 3 (MM3) force field¹³ in the LAMMPS software package.¹⁴ The MM3 force field was chosen based on our prior experience applying it to hydrocarbon and aromatic systems, where results were comparable to *ab initio* MP2-derived intermolecular energies.¹⁵ The two intermolecular interactions described in MM3 are van der Waals and bond dipole interactions, which are implemented as a Buckingham potential and a dipole-dipole term from the series expansion of the electrostatic potential, respectively. We modified the force field by replacing the bond dipole interaction terms with relatively stronger atomic monopole interactions derived from CHelpG¹⁶ partial charges to more accurately model the electrostatic interactions. The CHelpG partial charges were computed at the level of B3LYP/6-31G(d,p). The MM3 force field provides a complete, though phenomenological, description of the intermolecular interactions for all common covalent organic framework atoms, such as boron, carbon, hydrogen, and oxygen.

To determine the structure of the **HHTP-DPB COF** layer using DFT, we combined the individually optimized geometries of a diphenylbutadiyne linker and a HHTP/phenylene COF (COF-5) as shown in Fig. A2.19A by replacing the phenylene “linker” in COF-5 with the longer diphenylbutadiyne linker and increasing the size of the unit cell accordingly. The geometry of the composite **HHTP-DPB COF** structure

is shown in Fig. A2.19B. The C-C bond lengths of the two aromatic rings of the diphenylbutadiyne linker differ from the C-C bond lengths of the phenylene linker by no more than 0.01 Å, so we are confident that the composite **HHTP-DPB COF** structure is an accurate representation of the structure obtained by a geometry optimization of the full **HHTP-DPB COF**. Also, the composite **HHTP-DPB COF** structure produces a pore size of 46 Å, which is similar to the experimentally obtained pore size.

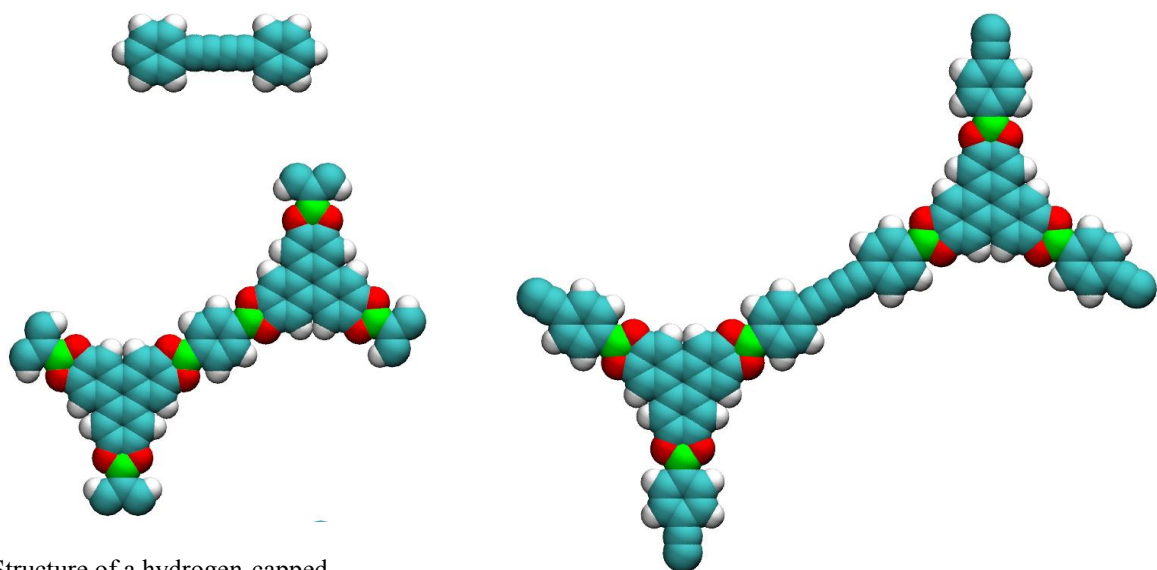
The two-layer configurations on which the semi-empirical MM calculations were performed consisted of 276 atoms, with 138 atoms per layer adopting the geometry obtained from DFT. Each layer was represented with a monoclinic unit cell with a lattice parameter of 46.3 Å along the *a* and *b* crystallographic axes and a γ of 60°. The system was slab-like with vacuum above and below to limit the intermolecular interactions to first and second layer interactions. In each intermolecular potential energy calculation, the layers were assumed to retain their exact geometry, so further geometry relaxations were not performed.

To generate the PES, atoms in the bottom layer of the stacked system were held rigidly in place while the top layer was translated over the surface of the other in increments of 0.1 Å along both *a* and *b* axes. At each *a* and *b* offset, the layer spacing (*c*-axis) was shifted from 2.50 Å to 4.00 Å in increments of 0.01 Å, and the intermolecular potential energies were computed. The lowest energy configurations along the *c*-axis were projected onto the *ab* plane to be able to visualize the 3-dimensional data in two dimensions. The range of layer spacing probed was wide enough to include all minimum energy structures. The layer spacing was continuous across the PES and ranged from 3.2 to 3.5 Å. Layer rotations were not considered while constructing the PES because the resulting loss of order would be computationally intractable to model. After analysis of the PES corresponding to only translational offsets, we concluded that the disruption in symmetry from layer rotations would also result in less overlap between the layers leading to a smaller and more unfavorable van der Waals interaction. As a further assumption, we hypothesized that the intermolecular interactions between non-adjacent layers would not contribute significantly to the PES since a doubling of the layer spacing reduces the intermolecular energy to less than 10%

of its original value, which allows us to use just two layers in the simulation of layer-layer stacking.

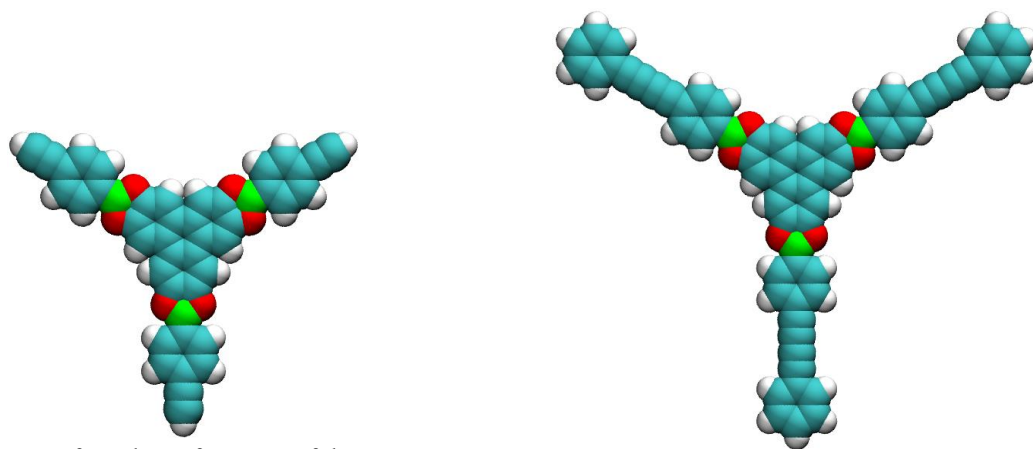
Eclipsed (**bnn**) and staggered (**gra**) structures were explored in greater detail with DFT by calculating the potential energy of representative fragments of a two-layer system. We fashioned dimers out of small fragments taken from the full COF layer, consisting of one HHTP unit and either three half-sized hydrogen-capped linkers (for eclipsed calculations) or three full-sized hydrogen-capped linkers (for staggered calculations), as shown in Fig. S19C and S19D, respectively. We used layer fragments instead of complete layers to probe the PES since it constrained the number of atoms to a more computationally tractable size; given the symmetry in the COF structure, and the rigidity of the overall COF, we believe that this approach of considering only part of the COF is an acceptable compromise. For calculations of eclipsed dimers, the potential energy was doubled to match the energy obtained from the larger system size in the molecular mechanics simulations. For calculations of staggered dimers, the potential energy of dimers was not doubled, since the number of HHTP-HHTP interactions matched that of the molecular mechanics simulations. The same procedure followed for the MM3 model was used to generate the PES from the **HHTP-DPB COF** layer fragments. Dimers with translational offsets within a 3 Å radius of the center of the PES were tested with a resolution of $0.1 \times 0.1 \text{ \AA}^2$, and the dimer spacing was shifted in increments of 0.01 Å, after which the lowest energy configurations were projected onto the x-y plane. The PES for the staggered layer configurations was generated by testing translational offsets within a 3 Å radius of a perfectly staggered structure.

Figure A2.24.



A. Structure of a hydrogen-capped diphenylbutadiyne linker and an HHTP-phenylene (COF-5) covalent organic framework used to build the unit cell structure of the **HHTP-DPB COF**.

B. Structure of one unit cell of the **HHTP-DPB COF** used in the molecular mechanics simulations.



C. Structure of one layer fragment of the **HHTP-DPB COF** with half-sized hydrogen capped linkers used in the ab initio simulation of eclipsed layers.

D. Structure of one layer fragment of the **HHTP-DPB COF** with full-sized hydrogen capped linkers used in the ab initio simulation of staggered layers.

N. Film Characterization

Figure A2.25. GID of HHTP-DPB COF thin film (growth time: 24 h).

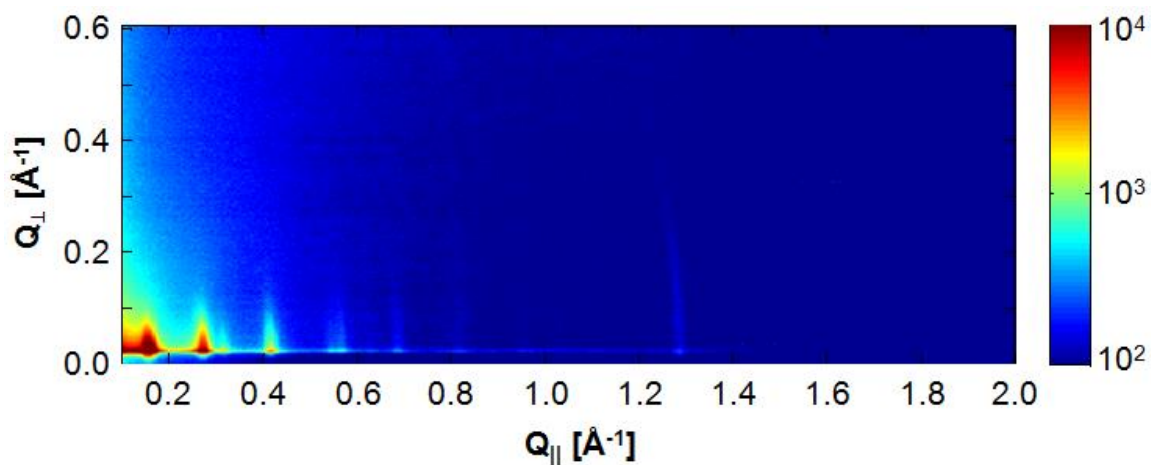


Figure A2.26. GID data obtained at large Q_{∞} , showing the off-specular projection of the HHTP-DPB COF film (001) Bragg peak (growth time: 24 h).

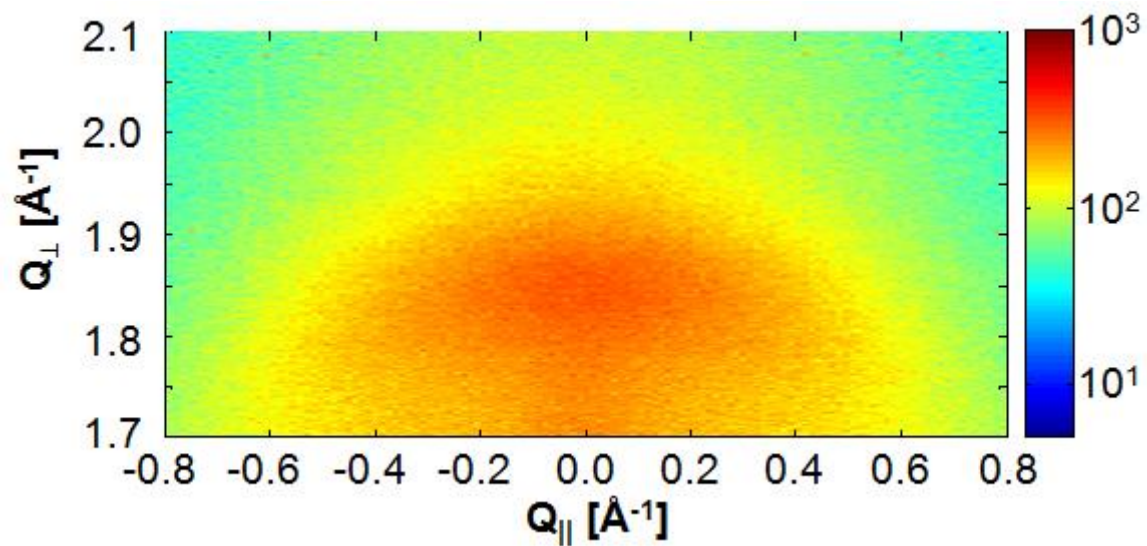
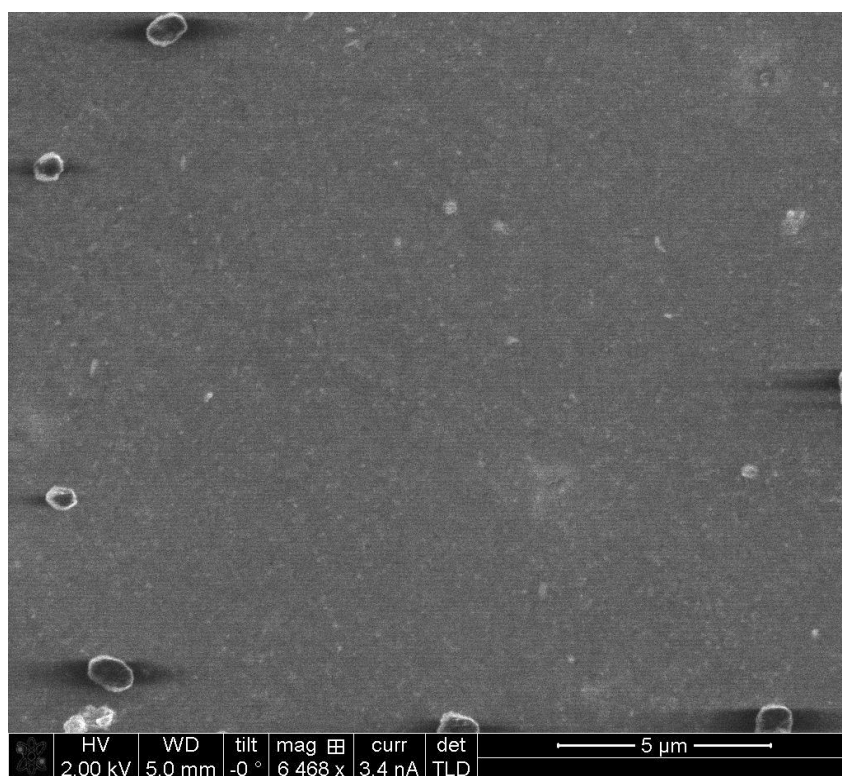
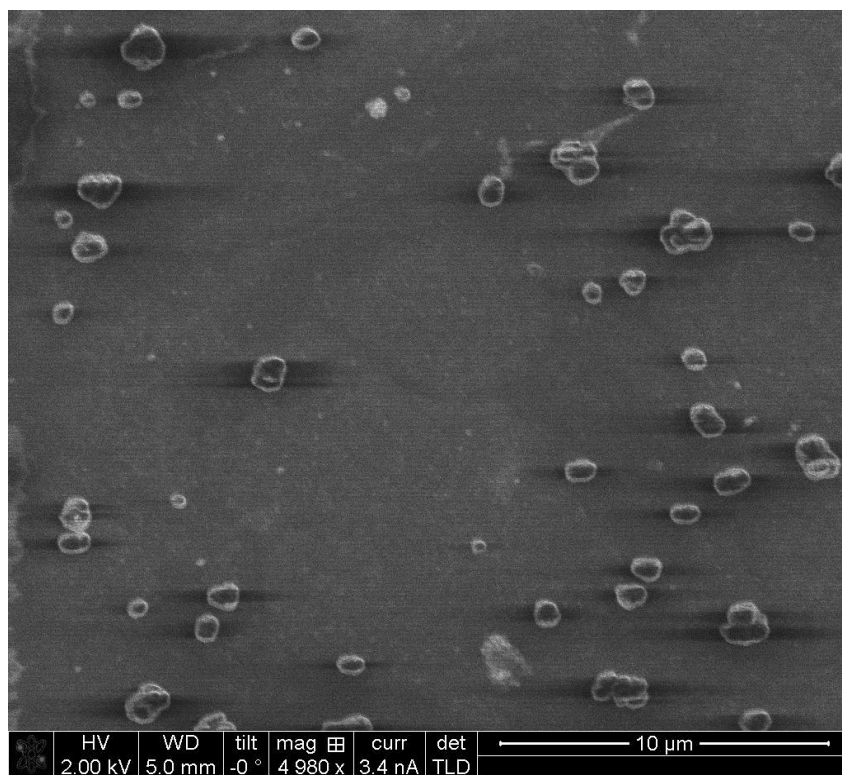


Figure A2.27. Top down SEM of **HHTP-DPB COF** thin film on SLG (growth time: 24 h).



O. References.

- [1] D. M. Smilgies, D. R. Blasini, S. Hotta, H. Yanagi, *J. Synchrotron Rad.* **2005**, *12*, 807.
- [2] D. M. Smilgies, D. R. Blasini, *J. Appl. Crystallogr.* **2007**, *40*, 716.
- [3] a) X. S. Li, W. W. Cai, J. H. An, S. Kim, J. Nah, D. X. Yang, R. Piner, A. Velamakanni, I. Jung, E. Tutuc, S. K. Banerjee, L. Colombo, R. S. Ruoff, *Science* **2009**, *324*, 1312; b) M. P. Levendorf, C. S. Ruiz-Vargas, S. Garg, J. Park, *Nano Lett.* **2009**, *9*, 4479.
- [4] E. L. Spitler, W. R. Dichtel, *Nat. Chem.* **2010**, *2*, 672.
- [5] A. P. Côté, A. I. Benin, N. W. Ockwig, M. O'Keeffe, A. J. Matzger, O. M. Yaghi, *Science* **2005**, *310*, 1166.
- [6] Accelrys, 4.4 ed., Accelrys Software, San Diego, **2008**.
- [7] S. Wan, J. Guo, J. Kim, H. Ihee, D. L. Jiang, *Angew. Chem. Int. Ed.* **2008**, *47*.
- [8] Metropolis, N., Rosenbluth, A. W., Rosenbluth, M. N., Telle, A. H., Teller, E. *J. Chem. Phys.* **1953**, *21*, 1087.
- [9] Rappe, A. K., Casewit, C. J., Colwell, K. S., Goddard-III, W. A., Skiff, W. M. *J. Am. Chem. Soc.* **1992**, *114*, 10024.
- [10] Gaussian 09, Revision A.02, M. J. Frisch, G. W. Trucks, H. B. Schlegel, G. E. Scuseria, M. A. Robb, J. R. Cheeseman, G. Scalmani, V. Barone, B. Mennucci, G. A. Petersson, H. Nakatsuji, M. Caricato, X. Li, H. P. Hratchian, A. F. Izmaylov, J. Bloino, G. Zheng, J. L. Sonnenberg, M. Hada, M. Ehara, K. Toyota, R. Fukuda, J. Hasegawa, M. Ishida, T. Nakajima, Y. Honda, O. Kitao, H. Nakai, T. Vreven, J. A. Montgomery, Jr., J. E. Peralta, F. Ogliaro, M. Bearpark, J. J. Heyd, E. Brothers, K. N. Kudin, V. N. Staroverov, R. Kobayashi, J. Normand, K. Raghavachari, A. Rendell, J. C. Burant, S. S. Iyengar, J. Tomasi, M. Cossi, N. Rega, J. M. Millam, M. Klene, J. E. Knox, J. B. Cross, V. Bakken, C. Adamo, J. Jaramillo, R. Gomperts, R. E. Stratmann, O. Yazyev, A. J. Austin, R. Cammi, C. Pomelli, J. W. Ochterski, R. L. Martin, K. Morokuma, V. G. Zakrzewski, G. A. Voth, P. Salvador, J. J. Dannenberg, S. Dapprich, A. D. Daniels, Ö. Farkas, J. B. Foresman, J. V. Ortiz, J. Cioslowski, and D. J. Fox, Gaussian, Inc., Wallingford CT, 2009.
- [11] a) D. Jacquemin, E. A. Perpète, I. Ciofini, C. Adamo, R. Valero, Y. Zhao, D. G. Truhlar, *J. Chem. Theory Comput.* **2010**, *6*, 2071; b) Y. Zhao, D. G. Truhlar, *Theor. Chem. Acc.* **2008**, *120*, 215; c) Y. Zhao, D. G. Truhlar, *J. Chem. Phys.* **2009**, *130*, 074103.
- [12] a) J. Vura-Weis, M. A. Ratner, M. R. Wasielewski, *J. Am. Chem. Soc.* **2010**, *132*, 1738; b) N. Marom, A. Tkatchenko, M. Scheffler, L. Kronik, *J. Chem. Theory Comput.* **2010**, *6*, 81.
- [13] N. L. Allinger, Y. H. Yuh, J. H. Lii, *J. Am. Chem. Soc.* **1989**, *111*, 8551.
- [14] S. Plimpton, *J. Comp. Phys.* **1995**, *117*, 1.
- [15] R. Cantrell, P. Clancy, *Surf. Sci.* **2008**, *602*, 3499.
- [16] M. M. Francl, C. Carey, L. E. Chirlian, D. M. Gange, *J. Comput. Chem.* **1996**, *17*, 367.

CHAPTER 4

EXPLORING THE PROPERTIES OF HHTP-DPB COF

Abstract: *Thin films of HHTP-DPB COF with 4.7 nm pores were grown on TEM grids and imaged at various stages of film growth. Regular hexagonal domains are visible after 20 minutes, with larger domains and better defined boundaries visible at later times. These images are some of the first of their type showing the formation of COF thin films. Modifying the growth conditions of HHTP-DPB COF to form from a fully homogenous starting mixture allowed the study of HHTP-DPB COF powder formation using turbidity measurements. This growth method followed by activation using supercritical CO₂ increased the surface area from 910 m² g⁻¹ to 2500 m² g⁻¹, approaching the Connolly surface area.*

Introduction: Since the first report of boronate ester COFs in 2005¹, there has been a flurry of activity to explore new COF chemistries including hydrazones², azines³⁻⁵, β -ketoenamines^{6,7}, and to find ways to exploit the well-defined nanoporous structures for functional applications. However, during the past 10 years very little insight has been shed on the mechanism of growth for these crystalline powders and oriented thin films until recently^{8,9}. By understanding the mechanism, we can rationally optimize methods of COF synthesis to improve the quality of the grown COF and develop methods to rapidly screen material quality.

Recent work on COF mechanisms has been limited to the formation of nanocrystalline powders of boronate ester linked COFs. While this class is the largest class of 2-D COFs, preliminary results show that 3-D boronate ester COFs do not grow by the same mechanism. This result highlights that it is likely that each COF

chemistry and whether powder or films are formed had a different growth mechanism. COF films create a platform for utilizing insoluble COF powders for functional materials like capacitors⁷, solar cells^{10,11}, and for other uses¹².

COF powders have been investigated for a variety of applications due to their high surface area and regular crystalline structure. These applications include sensing, gas storage¹³, charge storage⁷ and catalysis¹⁴⁻¹⁶, all based upon the high surface area of the ordered, porous material. When a COF exhibits a BET surface area that is close to its theoretical surface area (which is calculated assuming a single crystal morphology) the COF is assumed to be of high quality. This is because it is less likely for the powder to have a high surface area if it is comprised of a minimal crystalline phase within an amorphous phase, or if the pore are clogged by unreacted monomer. Despite the high significance and impact on utility, most reported COF surface areas fall far below the theoretical maximum, and very few studies have explored new methods to enhance the surface area of COF powders.

Discussion: HHTP-DPB COF held the record for many years as the COF with the largest pore size, a diameter of 4.7 nm¹⁷. This large pore opens many opportunities to characterize the formation of COF films, especially in utilizing transmission electron microscopy (TEM). These sized features of HHTP-DPB COF are within the sensitivity of common TEMs. To study HHTP-DPB COF, thin films were grown by including a TEM grid in the literature¹⁷ growth conditions and removed the grid after a given time. This method offers snapshots of the film morphology at each time point chosen. The grids are covered in bulk powder as well as thin film growth. Figure 4.1 shows the growth of COF domains over time. After 10 minutes of growth there are

very few discernable hexagons, but from 20 minutes on, hexagonal arrays start to form. These hexagons possess the same diameter as the pores of HHTP-DPB COF. However, they do not produce a noticeable diffraction pattern. This is likely due to the fact that crystals with smaller unit cells (like graphene) produce visible electron beam diffraction in the TEM, but the diffraction pattern gets closer to the beam as the unit cell increases. HHT-DPBs unit cell is great than 10 times the size of graphenes, so the COFs diffraction pattern small enough that was blocked by the electron beam. At 30 minutes of growth, well-defined domains are formed and at 40 min the grain boundaries are more intense and better defined. It is promising to see hexagonal domains form after 20 minutes, considering literature conditions for crystalline HHTP-DPB COF propose heating the sample for 3 days at 90 ° C. This is more consistent with the recent kinetic studies showing COF formation within minutes from homogenous conditions (discussed further in this chapter).

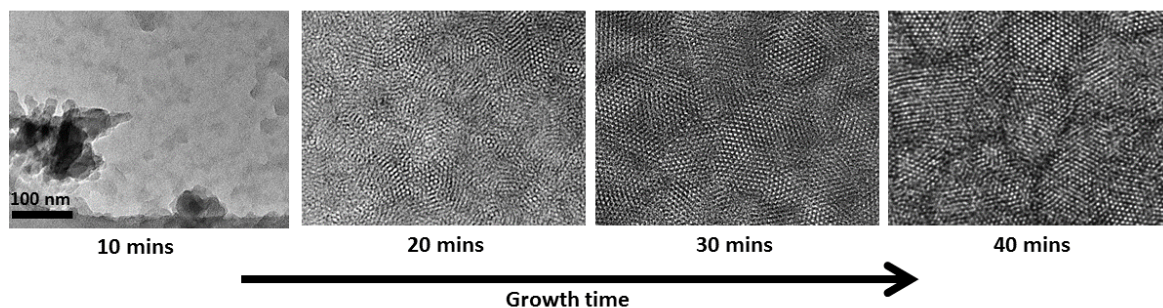


Figure 4.1: TEM images of HHTP-DPB COF at different growth times. All of the images are scaled to the 100 nm scale bar on the 10 minute growth image.

HHTP-DPB COF has been reported to grow as crystalline, oriented films with pores aligned perpendicular to a variety of substrates, including graphene, fused silica, and gold¹⁷. Depending on the type of TEM grid used, we manipulate the apparent

orientation of the COF growth. Seen in Figure 4.2A, long rows of COF growing parallel to the surface form within the pores of a lacey carbon grid. The long lines seen grown with increasing growth times and are spaced close to the interlayer stacking of HHTP-DPB COF. Using a copper grid coated with ultrathin carbon, the COF grew with its pores perpendicular to the surface, similar to most other substrates, including graphene. This allows for us to image down the pores and see the larger hexagonal domains of the COF. The size of these large hexagonal domains seen in Figure 4.3A are larger than the average crystallite size determined from applying the Scherrer equation to powder x-ray diffraction (PXRD) (Figure A3.5), with some domains appearing to have in plain crystallinity as large as 100 nm, compared to the 20 nm determined for the powder measurements. Part of the underestimate from the PXRD measurement comes from the nature of the measurement which is performed on a bulk sample and the value is an average. These images can illustrate domains of the COF and explore the ways these domains are stitched together, which is impossible using bulk measurements.

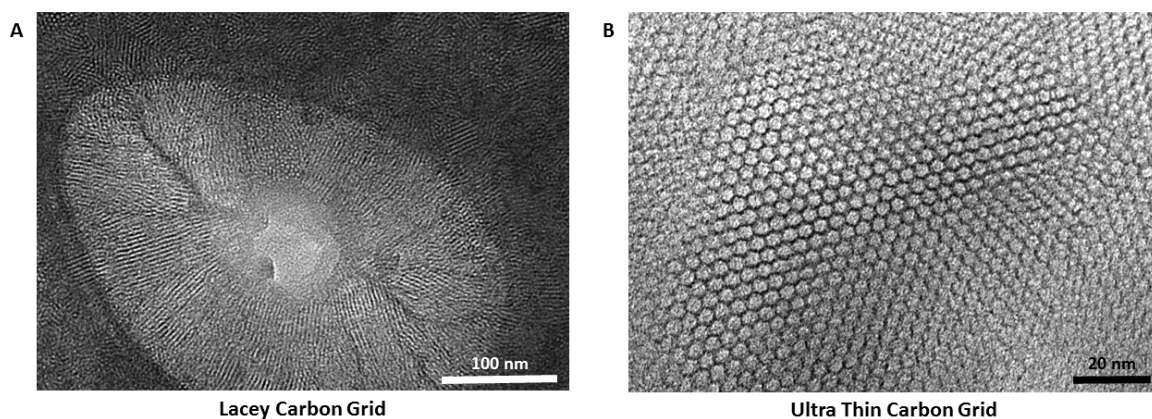


Figure 4.2: TEM images of HHTP-DPB COF on A) Lacey carbon grid B) Ultra-thin carbon grid. Both samples were allowed to grow for 30 min before removing the grid

In Figure 4.3B, the well-defined grain boundary displays both 5 and 7 member, suggesting fusion of discrete sheets that the surface. This is similar to graphene grain boundaries, and suggests that there is limited reversibility under these conditions to correct the linkage defects. It also suggests that the energy difference between a 6-member ring and a 5 or 7 member ring is low under these conditions. Overall, insights into 2D COF properties suggest a high degree of similarity with graphene monolayer systems.

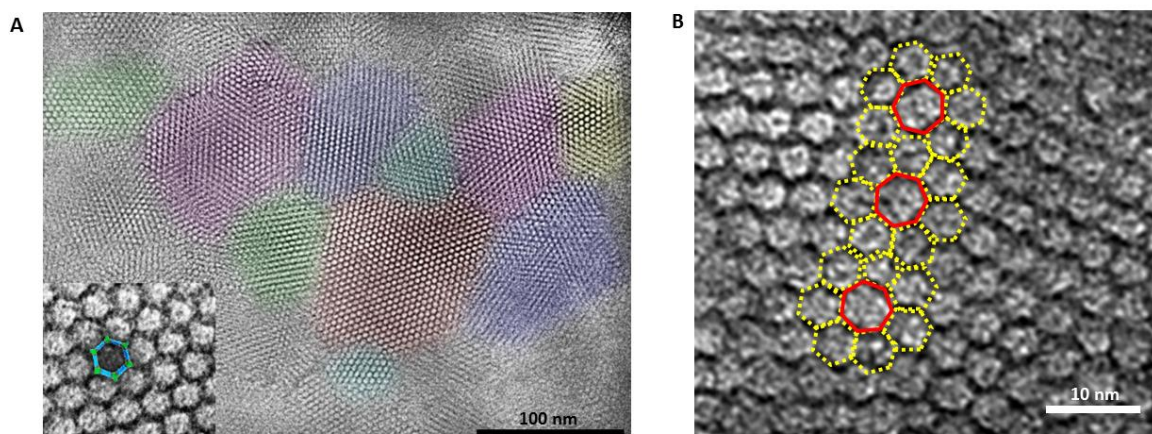


Figure 4.3: TEM images of HHTP-DPB COF ultra-thin carbon grid after 30 min growth. A) False color image demonstrating different crystallographic grains B) Grain boundary with pentagons, hexagons, and heptagons added to highlight growth pattern.

The initial TEM characterization of COF thin films inspired further studies into the kinetics and mechanisms of boronate ester COF growth^{8,9}. Prior to this, crystalline COF synthesis was dependent on solely empirical observations leading to presumptions such as the necessity of COF from heterogeneous starting conditions where the monomers are not fully soluble in the growth medium. It was believed that

heterogeneous conditions allowed for slow solvation of the COF monomers, leading to controlled COF formation. In this system, it is very difficult to spectroscopically characterize the growth of crystalline powder from the insoluble monomers, as illustrated in Figure 4.4A. By adjusting the solvent ratio and adding methanol, boronate ester linked COFs were grown from fully soluble starting conditions. Using the turbidity of the solution as a proxy for the formation of COF powder, the rate of COF powder formation can be determined, by choosing the linear region outlined in Figure 4.4C. This method correlates with the rate of boronate ester formation, probed by NMR analysis, and identifies the induction period of growth. Surprisingly, for each boronate ester COF examined, crystalline powder can be recovered within five minutes of growth. This is in stark contrast to the published literature conditions for these materials which originally called for 3 days of growth, but it is more consistent with the TEM images showing hexagonal domains occurring a shorter growth times. As seen in Figure 4.5, the HHTP-DPB COF is the slowest COF to form, likely due to a combination of having the most flexible linker and the lowest interlayer interactions. Perhaps interlayer interactions between HHTP-DPB COF and the carbon layer on the TEM grids helped create such large COF domains. COF-5¹ and COF-10¹⁸ grow at similar rates, despite the differences in linker size. The growth for TP-COF¹⁹ is accelerated compared to COF-10, which is the same length, due to the increased interlayer stacking of the pyrene moieties. This stacking advantage for the TP-COF is also seen in the very low activation energy for this COF formation, 13 kcal mol⁻¹, nearly half the activation energy for COF-5 and COF-10.

The hydrolytic digestion of COFs with water was also monitored by turbidity experiments. It is important to note that the rate of COF digestion with the introduction of water shows a similar trend where the HHTP-DPB COF is digested the fastest, and the TP-COF is the most water stable (Figure A3.9). These experiments show that it is the interlayer stacking that drives COF powder formation and not boronate ester bond formation. Prior experiments also found that the in-plane crystallite size in COF-5 could be nearly doubled to 40 nm by the controlled addition of water. Collectively, these observations establish a rational approach to both controlling COF growth and designing next generation COF materials.

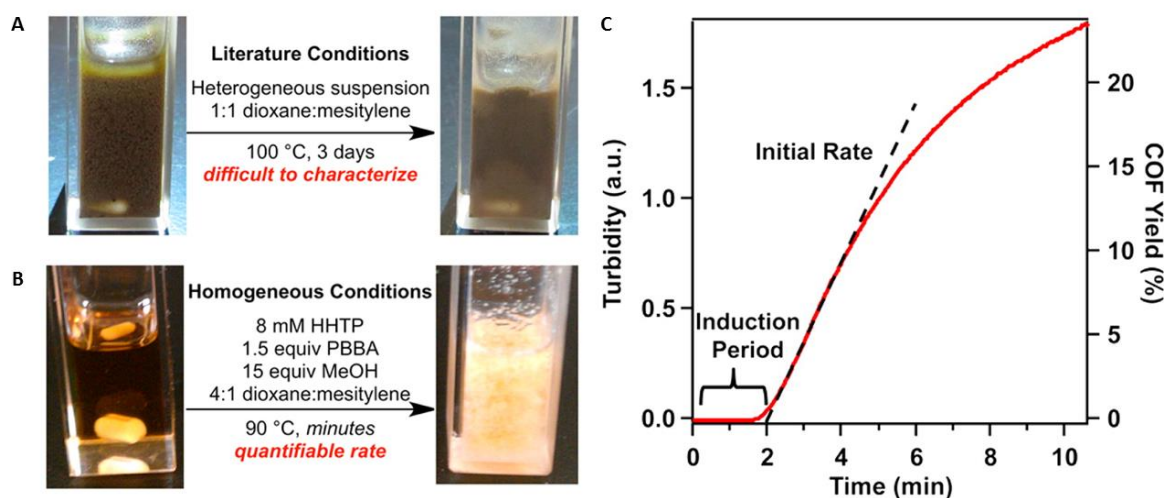


Figure 4.4: A) Picture of heterogenous COF-5 growth B) Picture of homogenous COF-5 growth C) Turbidity measurement of homogenous COF-5 growth. These figures were originally published in reference 8.

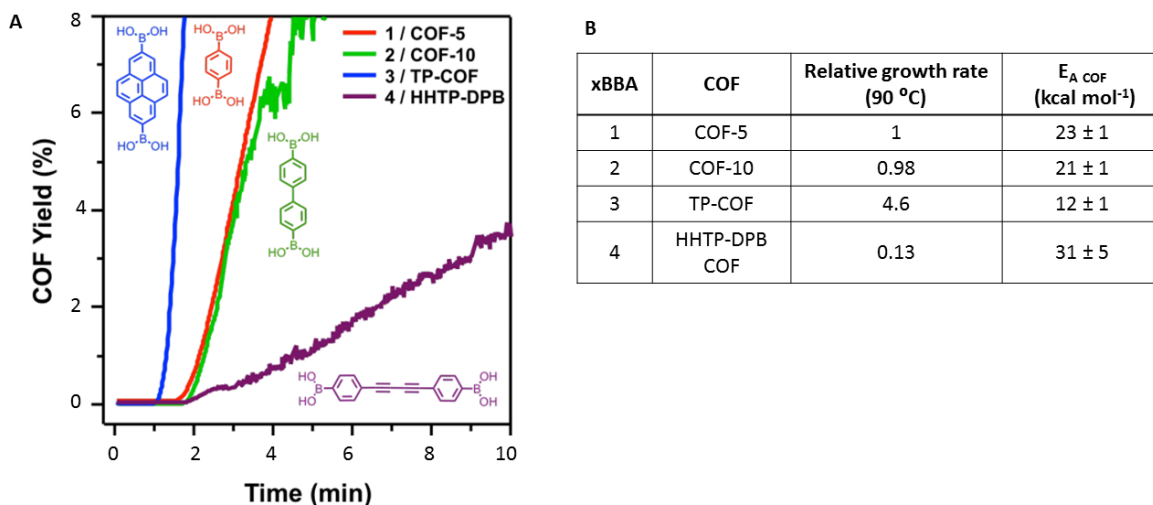


Figure 4.5: A) COF powder formation of four different boronate ester linked COFs from homogeneous conditions. Blue – TP-COF (3), Red – COF-5 (1), Green – COF-10 (2), Purple –HHTP-DPB COF (4) B) Activation energies for the four boronate ester COFs tested. These figures were originally published in reference 9.

In addition to developing the ability to monitor growth of COF powder formation, the homogenous conditions offer other benefits to the quality of the COF formed in all boronate ester linked COFs test. One of the challenges of creating a high quality COF sample is maximizing the material surface area, generally by fully removing trapped, unreacted monomers from the COF pores. These trapped monomers reduce the surface area of the COF, thus reducing the quality of the material. Utilizing the homogenous growth conditions, since all of the monomers are fully soluble, it is significantly easier to wash them from the COF pores, improving the quality of the final product. Simply by switching to homogenous growth conditions, the surface area of COF-5 was improved from the originally reported 1590 m²g⁻¹ to 2000 m²g⁻¹. When originally published from heterogeneous conditions, the maximum surface area achieved for HHTP-DPB COF was 910 m²g⁻¹, which is only a

third of its theoretical surface area of $2650 \text{ m}^2\text{g}^{-1}$. Synthesis from homogenous conditions yields HHTP-DPB COF with a surface area *ca.* $1000 \text{ m}^2\text{g}^{-1}$ when activated by heat and vacuum (Figure 4.6B). Improving the surface area of HHTP-DPB COF required an additional activation step to prevent the pores from collapsing (Figures A3.3,3.4). The homogenous growth conditions aided in removing the trapped monomers from the pores, but to address the challenges during activation, supercritical CO_2 was used to fully activate the material (Figure A3.5). Rinsing with liquid CO_2 removes solvents from the material while maintaining the overall structure. By heating under pressure, a supercritical phase change was induced, slowly releasing the CO_2 and minimizing pore collapse, since supercritical fluids do not have appreciable surface tension. By removing the surface tension pulling on the COF pores during activation, the large pores comprised of the flexible DPB monomer were less susceptible to collapsing and maintain overall structure. Using the homogenous growth conditions and activation using supercritical CO_2 , surface area of the COF increases nearly 3 fold, to $2470 \text{ m}^2\text{g}^{-1}$. This higher surface area is approaching the theoretical surface area of $2650 \text{ m}^2\text{g}^{-1}$, which is unique since many COF systems report surface areas far below their theoretical maximum. While supercritical CO_2 has been used to activate other porous materials like metal organic frameworks²⁰ and porous organic polymers²¹, this is the first example within a COF system. When applied to other COFs, the increases in surface area were more modest, but in most cases the sharpness of the PXRD peaks increased after supercritical activation.

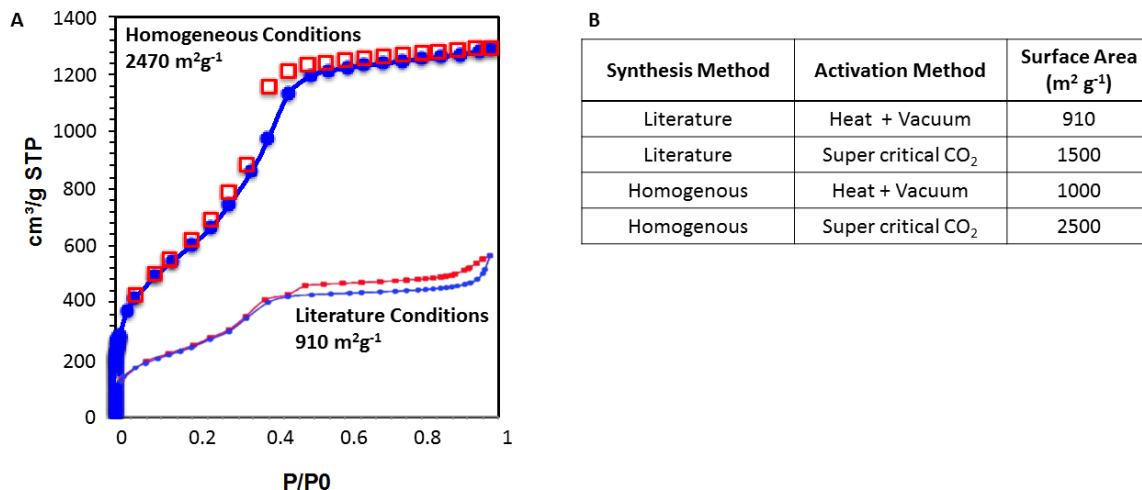


Figure 4.6: A) Nitrogen adsorption isotherm at 77 K. Blue circles -adsorption, red squares -desorption. Comparing literature conditions to homogenous growth with supercritical activation B) Summary of synthesis methods, activation methods, and resulting BET surface area of HHTP-DPB COF

Conclusion: These methods of studying HHTP-DPB COF film and powder growth offer insight into the formation of this high surface area material. In thin films, hexagonal arrays form within the first 20 minutes, and the grain boundaries show 5 and 7 member ring defects, similar to graphene monolayers. Homogenous growth conditions illustrate the challenges of controlling COF synthesis, and the strong dependence on interlayer stacking. The surface area can be dramatically improved by utilizing the homogenous growth conditions and by taking special care to activate using supercritical CO₂. The lessons learned for this 2D boronate ester COF can applied to other systems to maximize surface area and improve the quality of the COF produced.

REFERENCES

- (1) Côté, A. P.; Benin, A. I.; Ockwig, N. W.; O’Keeffe, M.; Matzger, A. J.; Yaghi, O. M. *Science* **2005**, *310* (5751), 1166–1170.
- (2) Uribe-Romo, F. J.; Doonan, C. J.; Furukawa, H.; Oisaki, K.; Yaghi, O. M. *J. Am. Chem. Soc.* **2011**, *133* (30), 11478–11481.
- (3) Jackson, K. T.; Reich, T. E.; El-Kaderi, H. M. *Chem. Commun.* **2012**, *48* (70), 8823–8825.
- (4) Ren, S.; Bojdys, M. J.; Dawson, R.; Laybourn, A.; Khimyak, Y. Z.; Adams, D. J.; Cooper, A. I. *Adv. Mater.* **2012**, *24* (17), 2357–2361.
- (5) Dalapati, S.; Jin, S.; Gao, J.; Xu, Y.; Nagai, A.; Jiang, D. *J. Am. Chem. Soc.* **2013**, *135* (46), 17310–17313.
- (6) Biswal, B. P.; Chandra, S.; Kandambeth, S.; Lukose, B.; Heine, T.; Banerjee, R. *J. Am. Chem. Soc.* **2013**, *135* (14), 5328–5331.
- (7) DeBlase, C. R.; Silberstein, K. E.; Truong, T.-T.; Abruña, H. D.; Dichtel, W. R. *J. Am. Chem. Soc.* **2013**, *135* (45), 16821–16824.
- (8) Smith, B. J.; Dichtel, W. R. *J. Am. Chem. Soc.* **2014**, *136* (24), 8783–8789.
- (9) Smith, B. J.; Hwang, N.; Chavez, A. D.; Novotney, J. L.; Dichtel, W. R. *Chem. Commun.* **2015**, *51* (35), 7532–7535.
- (10) Dogru, M.; Handloser, M.; Auras, F.; Kunz, T.; Medina, D.; Hartschuh, A.; Knochel, P.; Bein, T. *Angew. Chem. Int. Ed.* **2013**, *52* (10), 2920–2924.
- (11) Wan, S.; Gándara, F.; Asano, A.; Furukawa, H.; Saeki, A.; Dey, S. K.; Liao, L.; Ambrogio, M. W.; Botros, Y. Y.; Duan, X.; Seki, S.; Stoddart, J. F.; Yaghi, O. M. *Chem. Mater.* **2011**, *23* (18), 4094–4097.
- (12) Colson, J. W.; Woll, A. R.; Mukherjee, A.; Levendorf, M. P.; Spitler, E. L.; Shields, V. B.; Spencer, M. G.; Park, J.; Dichtel, W. R. *Science* **2011**, *332* (6026), 228–231.
- (13) Doonan, C. J.; Tranchemontagne, D. J.; Glover, T. G.; Hunt, J. R.; Yaghi, O. M. *Nat. Chem.* **2010**, *2* (3), 235–238.
- (14) Ding, S.-Y.; Gao, J.; Wang, Q.; Zhang, Y.; Song, W.-G.; Su, C.-Y.; Wang, W. *J. Am. Chem. Soc.* **2011**, *133* (49), 19816–19822.
- (15) Xu, H.; Chen, X.; Gao, J.; Lin, J.; Addicoat, M.; Irle, S.; Jiang, D. *Chem. Commun.* **2014**, *50* (11), 1292–1294.
- (16) Fang, Q.; Gu, S.; Zheng, J.; Zhuang, Z.; Qiu, S.; Yan, Y. *Angew. Chem. Int. Ed.* **2014**, *53* (11), 2878–2882.
- (17) Spitler, E. L.; Koo, B. T.; Novotney, J. L.; Colson, J. W.; Uribe-Romo, F. J.; Gutierrez, G. D.; Clancy, P.; Dichtel, W. R. *J. Am. Chem. Soc.* **2011**, *133* (48), 19416–19421.
- (18) Côté, A. P.; El-Kaderi, H. M.; Furukawa, H.; Hunt, J. R.; Yaghi, O. M. *J. Am. Chem. Soc.* **2007**, *129* (43), 12914–12915.
- (19) Wan, S.; Guo, J.; Kim, J.; Ihee, H.; Jiang, D. *Angew. Chem. Int. Ed.* **2008**, *47* (46), 8826–8830.
- (20) Farha, O. K.; Hupp, J. T. *Acc. Chem. Res.* **2010**, *43* (8), 1166–1175.

- (21) Nelson, A. P.; Farha, O. K.; Mulfort, K. L.; Hupp, J. T. *J. Am. Chem. Soc.* **2009**, *131* (2), 458–460.

APPENDIX III

A. Materials. All reagents were purchased from commercial sources and used without further purification. CH₂Cl₂, PhMe, and MeOH were purchased from commercial sources and purified using a custom-built alumina-column based solvent purification system. Other solvents were purchased from commercial sources and used without further purification

Instrumentation. Infrared spectra were recorded on a Thermo Nicolet iS10 with a diamond ATR attachment and are uncorrected. Ultraviolet/visible/near infrared absorbance spectra were recorded on a Cary 5000 spectrophotometer with a Hg lamp.

Photoemission and excitation spectra were recorded on a Horiba Jobin Yvon Fluorolog-3 fluorescence spectrophotometer equipped with a 450 W Xe lamp, double excitation and double emission monochromators, a digital photon-counting photomultiplier and a secondary InGaAs detector for the NIR range. Correction for variations in lamp intensity over time and wavelength was achieved with a solid-state silicon photodiode as the reference. The spectra were further corrected for variations in photomultiplier response over wavelength and for the path difference between the sample and the reference by multiplication with emission correction curves generated on the instrument.

Surface area measurements were conducted on a Micromeritics ASAP 2020 Accelerated Surface Area and Porosimetry Analyzer using 75 mg samples degassed at 90 °C for 24 h and backfilled with N₂. N₂ isotherms were generated by incremental exposure to ultra high purity nitrogen up to 1 atm in a liquid nitrogen (77 K) bath and surface parameters were determined using BET adsorption models included in the instrument software (Micromeritics ASAP 2020 V4.00).

NMR spectra were recorded on a Varian 400 MHz, a Varian 500 MHz or a Bruker ARX 300 MHz spectrometer using a standard ¹H/X Z-PFG probe at ambient temperature with a 20 Hz sample spin rate.

Solid-state NMR spectra were recorded at ambient temperature on a Varian INOVA- 400 spectrometer using an external Kalmus 1 H linear pulse amplifier blanked using a spare line. Samples were packed into 7 mm outside diameter silicon nitride rotors and inserted into a Varian HX magic angle spinning (MAS) probe. ¹³C data was

acquired using linearly ramped cross-polarization with MAS (CP/MAS) at 100.5 MHz. The ^1H and S4 ^{13}C had ninety-degree pulse widths of 5 μs , and the CP contact time was 1 ms. Two-pulse phase modulation (TPPM) ^1H decoupling was applied during data acquisition with a decoupling frequency of 78 kHz. The recycle delays between scans were 2 s. The MAS spin rate varied between 5–7 kHz, as labeled in the spectra. ^{13}C chemical shifts were assigned relative to tetramethylsilane at 0.0 ppm and were calibrated using the methyl carbon signal of hexamethylbenzene assigned at 16.9 ppm as a secondary reference. The MAS spinning rate varied between 5-7 kHz as labeled in the spectra.

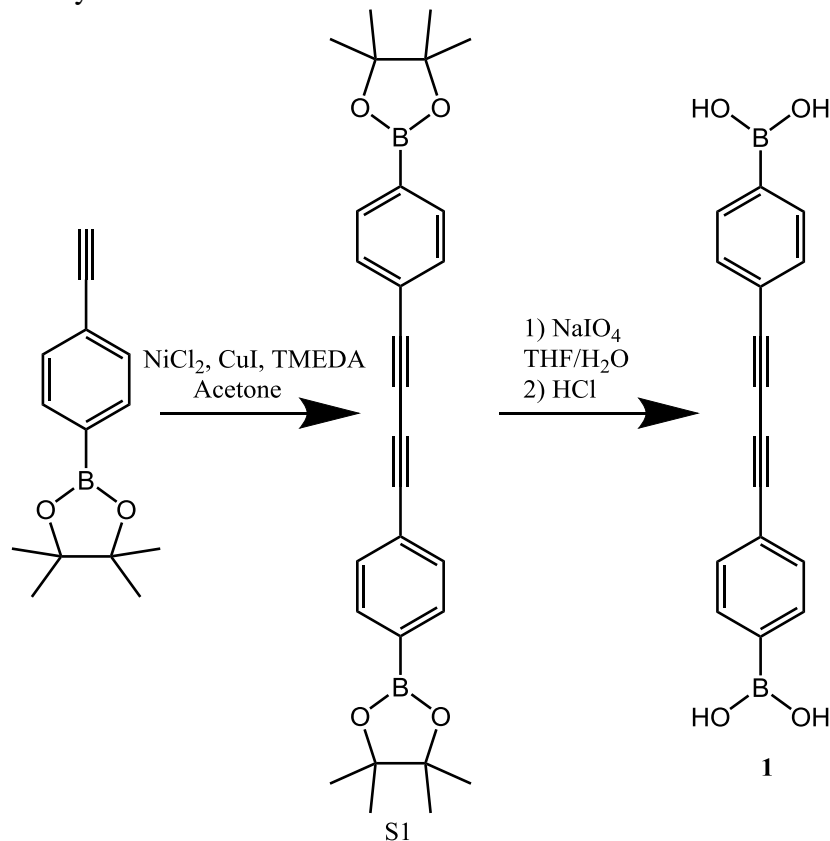
Powder X-ray diffraction (PXRD) patterns were obtained on a Scintag Theta-Theta Powder X-Ray Diffractometer in reflectance Bragg-Brentano geometry employing Cu $K\alpha$ line focused radiation at 2200 W (40 kV, 40 mA) power and equipped with a Ge crystal detector fitted with a 0.3 mm radiation entrance slit. Samples were mounted on zero background sample holders by dropping powders from a spatula and then leveling the sample surface with a glass microscope slide. No sample grinding or sieving was used prior to analysis. Crystallite size was determined by applying the Scherrer equation to the powder patterns using MDI JADE.

Supercritical CO_2 wash was performed with a Baltech critical point drier.

Transmission electron micrographs were obtained a FEI Technai T12 Spirit operating at 120 kV. Lacey carbon grids, and ultra-thin carbon grids (Ted Pella) were introduced into the COF growth solution prior to heating and removed at different times. The grids were isolated by vacuum filtration, rinsing with PhMe, and dried by blotting on a ChemWipe.

B. Synthetic Procedures

Scheme A3.1. Synthesis of DPB monomer 1.



Synthesis of S1: TMEDA (0.459 g, 3.946 mmol), CuI (0.188 g, 0.986 mmol), and NiCl_2 (0.234 g, 0.986 mmol) were dissolved or suspended in $(\text{CH}_3)_2\text{CO}$ (13 mL) under an atmosphere of air. The mixture became dark green after 10 min. 4-Ethynylbenzeneboronic acid pinacol ester (4.50 g, 19.7 mmol) was added, and the mixture was stirred rapidly for 2 h. The solvent was evaporated and the resulting yellow-green residue was washed with H_2O (50 mL), providing the yellow dialkyne ester S1 (1.90 g, 42%) as a white solid. $^1\text{H-NMR}$ (CDCl_3 , 300 MHz, 298 K) δ 7.65 (d, $J = 9.0$ Hz, 4H); 7.52 (d, $J = 9.0$ Hz, 4H); 1.34 (s, 24H). $^{13}\text{C-NMR}$ (CDCl_3 , 300 MHz) δ 135, 132, 125, 83, 75, 25. This spectrum matched that previously reported¹.

Synthesis of 1: A 20 mL scintillation vial was charged with the diboronate ester S1 (400 mg, 0.88 mmol) and NaIO_4 (400 mg, 2.0 mmol). The solids were dissolved in a THF:H₂O mixture (4:1, 6 mL) and stirred at rt for 12 h. 1M HCl (10 mL) was then added to the white suspension, which was stirred for another 12 h. The pale yellow-white suspension was diluted with H_2O (20 mL), and the solids recovered by filtration. The recovered solid was washed with an additional H_2O (20 mL) followed by hexanes (10 mL). The white solid was dried under vacuum to yield 233 mg (91%) of boronic acid 1. $^1\text{H-NMR}$ (DMSO-d_6 , 300 MHz) δ 8.26 (s, 4H); 7.82 (d, $J = 7.5$ Hz, 4H); 7.57 (d, $J = 7.5$ Hz, 4H). This spectrum matched that previously reported¹.

Synthesis of HHTP-DPB COF (Literature Conditions)¹: Boronic acid 1 (20 mg, 0.069 mmol) and HHTP (7 mg, 0.022 mmol) were combined in a mixture of dioxane and mesitylene (1:1, 4 mL) and sonicated for 10 min. The light gray suspension was heated to 90 °C in an aluminum block for 72 h, and the resulting free-flowing tan powder was collected by filtration on a Hirsch funnel, washed with 1 mL anhydrous toluene and air-dried. The crude HHTP-DPB COF isolated after drying under vacuum for 12 h. Isolated yield 10 mg (71%).

Synthesis of HHTP-DPB COF (Homogenous Conditions)²: Boronic acid 1 (13 mg, 0.046 mmol) and MeOH (0.012 mL, 0.463 mmol) was dissolved mixture of dioxane / mesitylene (4:1, 4 mL). HHTP (10 mg, 0.031 mmol) was added and sonicated for 10 min, or until the HHTP is fully dissolved. The solution was filtered (0.45 µm PTFE) to remove any trace residual particulate into a 20 mL scintillation vial. The vial was heated to 90 °C for 20 h. After cooling to rt, the COF solid was filtered into a chemwipe with dry toluene and active using supercritical CO₂. Isolated yield 7 mg (65%).

Supercritical Activation: Crude COF powder was isolated into a chemwipe tied shut with copper wire, and placed into the super critical activation chamber. The chamber was filled with liquid CO₂ and allowed to sit for 5 min, and then half of the volume released. This was repeated six times or until the evacuated CO₂ no longer smelled of toluene. The liquid CO₂ was then heated to 40 °C at a constant volume and then the gas was slowly released.

C. NMR Spectra

Figure A3.1: ¹H NMR of Compound S1

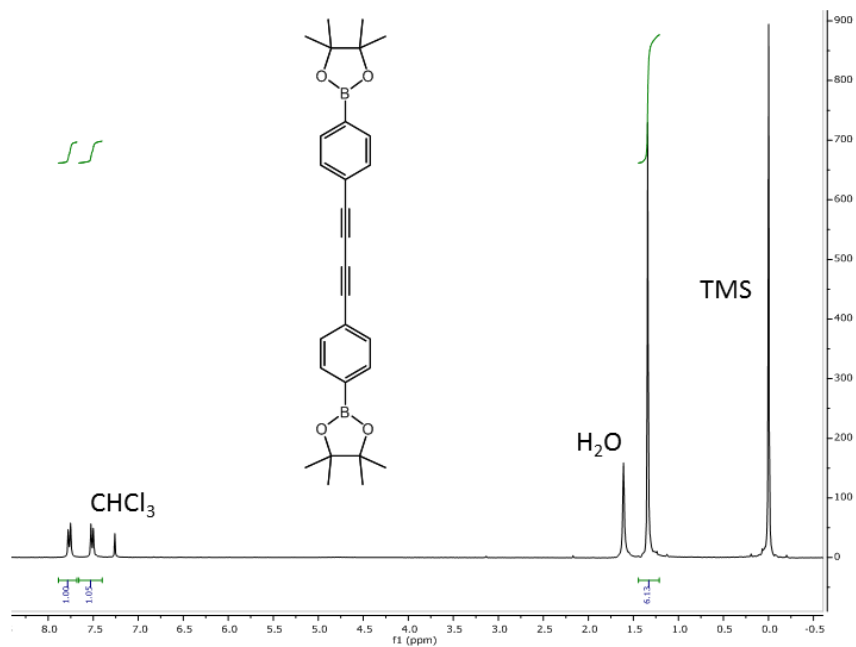
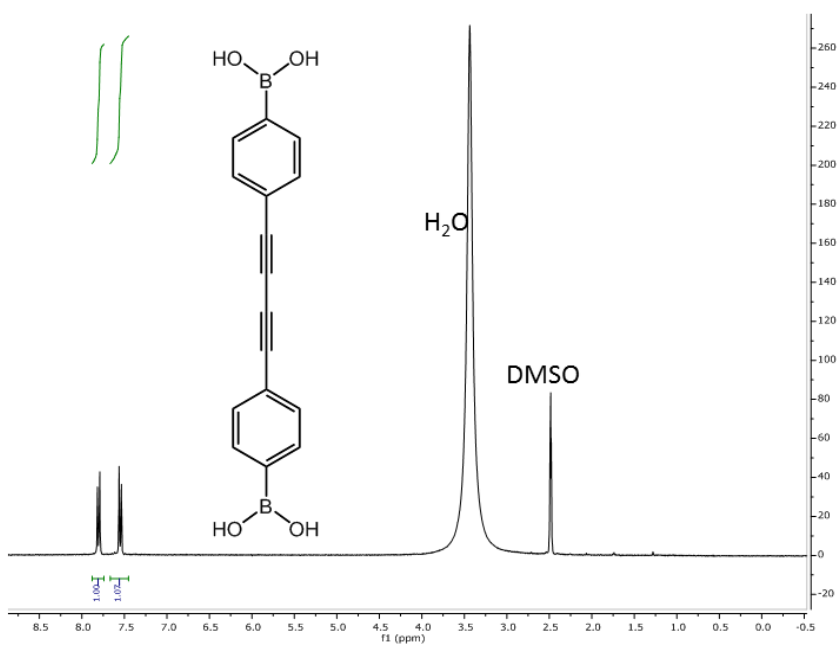
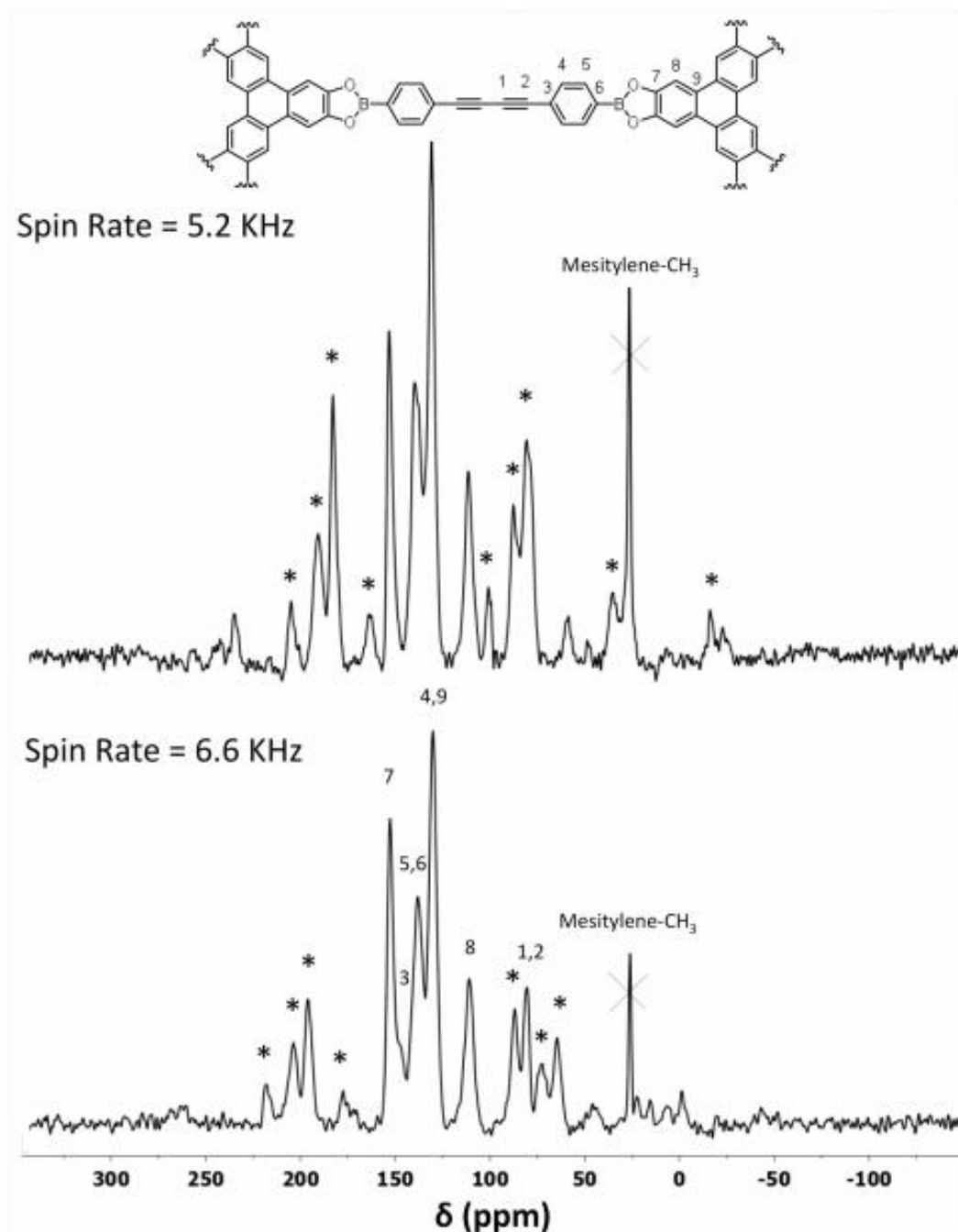


Figure A3.2: ¹H NMR of Compound 1



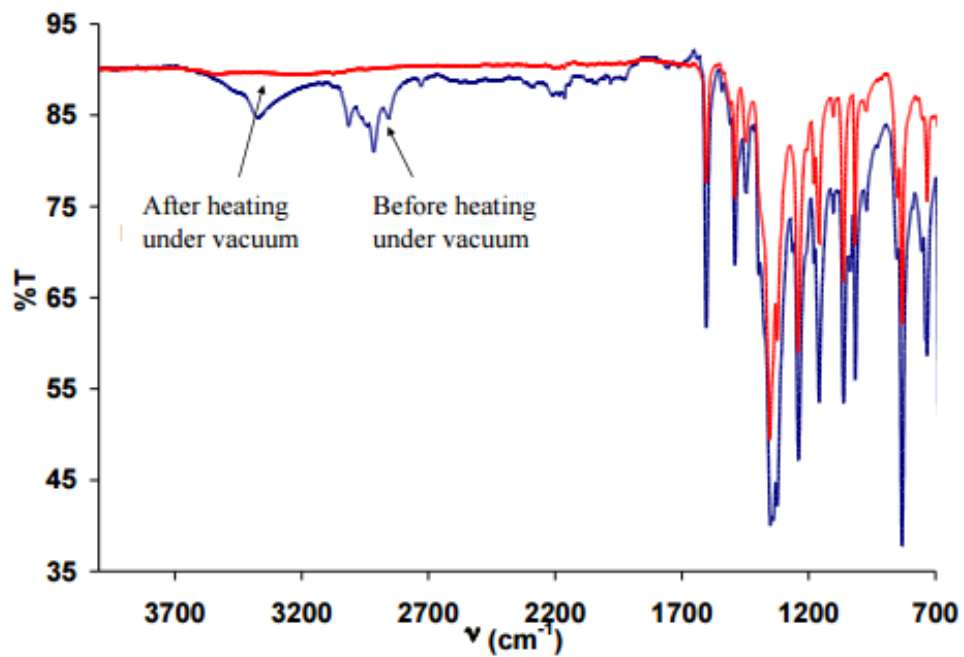
D. Solid State MAS ^{13}C NMR

Figure A3.3: CP/MAS ^{13}C NMR spectra of HHTP-DPB COF prior to activation (note presence of mesitylene). The spectra were acquired at two different spinning rates to assign spinning side bands (*). This supporting figure was originally published in 1.



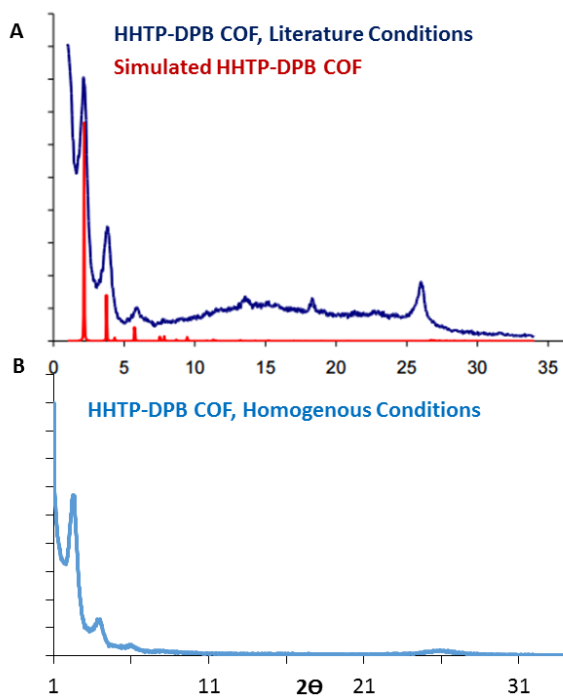
E. FTIR Spectra

Figure A3.4: FTIR of HHTP-DPB COF before and after activation. This supporting figure was originally published in 1.



F. XRD Spectra

Figure A3.5: A) PXRD Pattern of HHTP-DPB COF powder synthesized under literature conditions before activation (blue). Predicted diffraction pattern (red). B) PXRD of HHTP-DPB COF powder synthesized using homogenous conditions, activated using supercritical CO₂.



G. TEM Images

Figure A3.6: TEM image HHTP-DPB COF grown on an ultra-thin carbon grid for 40 min. This image shows the strong grain boundaries

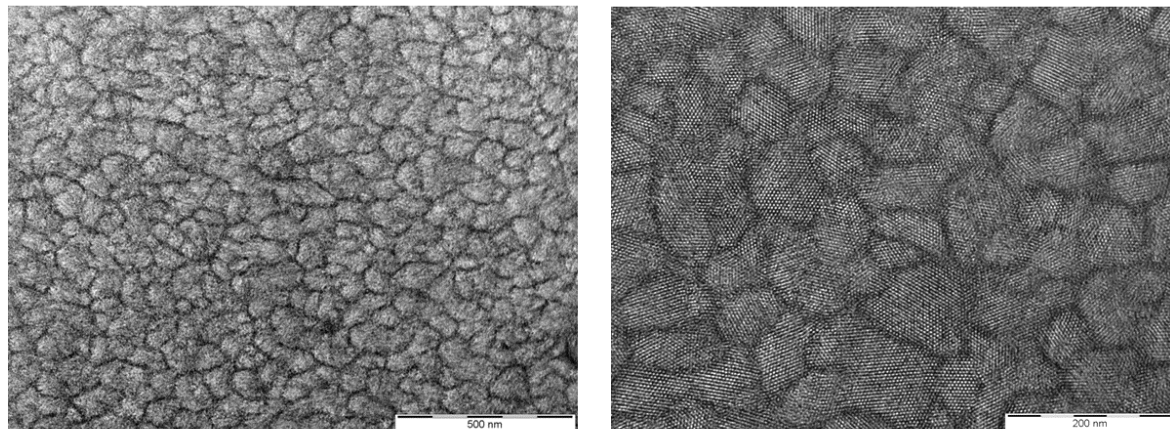


Figure A3.7: TEM image HHTP-DPB COF grown on an ultra-thin carbon grid for 40 min. This image shows the grain boundary with superimposed heptagons and pentagons

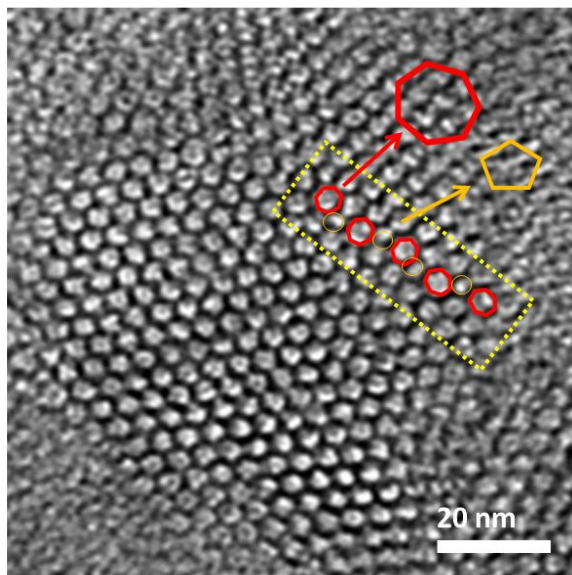
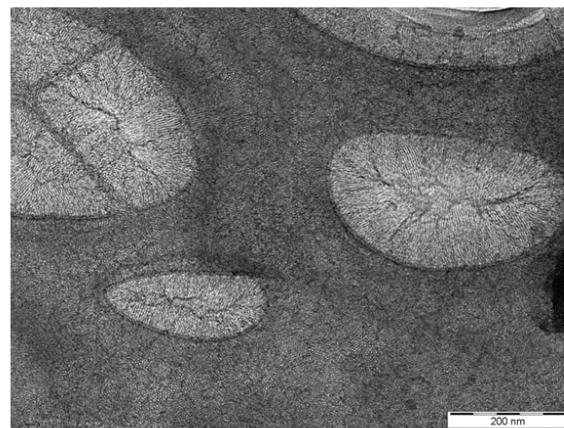
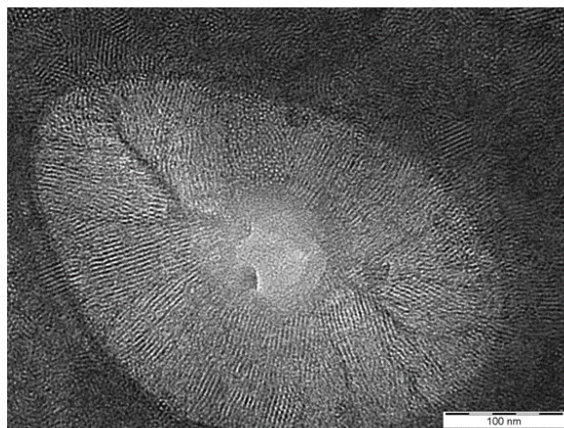
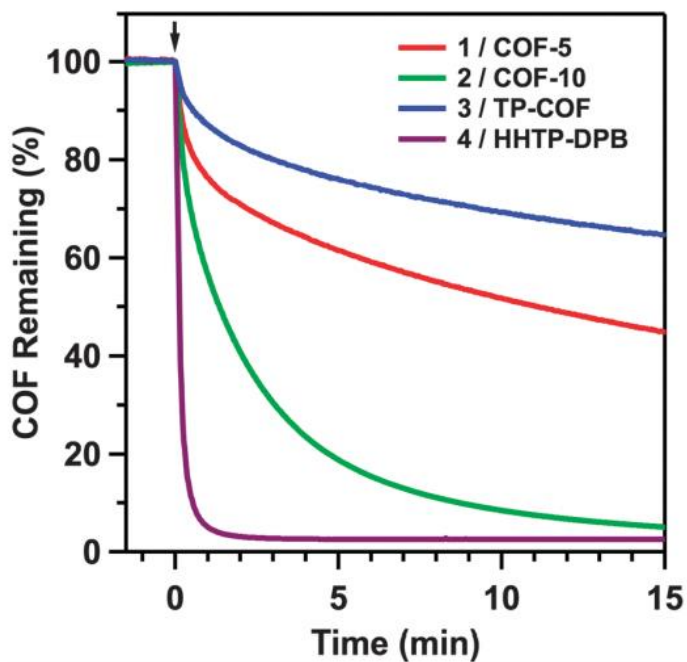


Figure A3.8: TEM image HHTP-DPB COF grown on a lacey carbon grid for 30 min.



H. Turbidity Measurements

Figure A3.9: Turbidity measurement of COF-5 (red/1), COF-10 (green/2), TP-COF (blue/3), and HHTTP-DPB COF (purple/4) with the addition of ~700 eq water relative to HHTTP. This figure was originally published in 2.



References:

- (1) Spitler, E. L.; Koo, B. T.; Novotney, J. L.; Colson, J. W.; Uribe-Romo, F. J.; Gutierrez, G. D.; Clancy, P.; Dichtel, W. R. *J. Am. Chem. Soc.* **2011**, *133* (48), 19416–19421.
- (2) Smith, B. J.; Hwang, N.; Chavez, A. D.; Novotney, J. L.; Dichtel, W. R. *Chem. Commun.* **2015**, *51* (35), 7532–7535.

CHAPTER 5

LOADING HHTP-DPB COF WITH CdSe NANOCRYSTALS

Abstract: *Different sized covalent organic frameworks (COFs) interact differently with 3 nm CdSe nanocrystals: HHTP-DPB COF with 4.7 nm pores spontaneously pulls 3 nm CdSe nanocrystals from dilute solutions, while COF-5 with 2.7 nm pores interacts with nanocrystals to a far smaller extent. The CdSe loaded COF samples show the characteristic absorbance of the 3 nm CdSe nanocrystals, but in both cases the fluorescence emission of the particles is quenched. The powders also demonstrates a decrease in surface area, implying an interaction between the nanocrystals and the COF pores. Tests with 6 nm PbS nanocrystals show similar responses for both COFs and behaves similarly as the 3 nm CdSe nanocrystals for COF-5, demonstrating the size sieving effect the COF pores has on the nanocrystals.*

Introduction: Nanoparticles exhibit unique optical, electronic, and magnetic properties that differ from the bulk material; at the nanoscale surface effects dominate over bulk effects¹⁻⁴. When nanoparticles assemble into ordered structures, either as superlattices or polymer-nanocomposites, novel properties emerge. These new assemblies differ from both their parent nanoparticles and the bulk materials in their abilities for light harvesting through absorption band engineering⁵⁻⁸, energy transfer^{9,10}, electronic effects¹¹, and magnetism¹². Current methods to create these systems are inherently flawed because the methods are not scalable to for production beyond the research laboratory. These assembly procedures depend on ligands to control orientation, evaporation conditions; both require monodisperse nanoparticles with limited final geometries based on the particle shape^{10,13,14}. Often, these systems

cannot produce structures larger than 100 nm and most structures do not have assembly control on features less than 10 nm¹⁵.

Understanding the current limitations in nanoparticle assembly, we aim to create a new patterning paradigm by utilizing crystalline, covalent organic frameworks (COFs) for nanoparticle organization. COFs can be isolated as thin films or free flowing powders through facile, scalable synthesis. They can also be designed with many different morphologies (both 2 and 3 dimensional) and have pore sizes up to 5.3 nm, which allows for variable patterning of nanoparticles into inorganic-organic hybrid materials^{16,17}. By using COFs as templates, particle shape would not control the final morphology (since it would be determined by the parent COF), and size-sieving effects due to the pore size of the COF would eliminate the need for monodisperse samples. By utilizing the tunable thickness (up to 300 nm) of the aligned COF array, the imbedded nanoparticles can also be turned and fused together to create a hybrid material with novel properties¹⁸.

Discussion: One of the characteristics of two-dimensional covalent organic frameworks (COFs) is the pore topology defined by the monomer. These pores can range in diameter from 1.9 nm up to 5.3 nm. HHTP-DPB COF held the record for many years as the largest pore sized COF, with a pore size of 4.7 nm, but recently lost the title to a COF with 5.3 nm pores^{17,19}.

The large pores can offer a defined channel for incorporating well-aligned guest molecules. Ordered metal nanoparticles create unique spectroscopic properties compared to the isolated nanoparticles. Recent developments from the Robinson group created a method for synthesizing small, crystalline, nanoparticles in large

batches, which will be referred to in this chapter as nanocrystals²⁰. These nanocrystals are highly absorbent in solution with the absorbance peaks correlating to the size of the metallic core of the nanocrystal. Large nanocrystals tend to absorb in the near IR, but the 3 nm cadmium selenide nanocrystals used for these experiments absorb around 550 nm and are bright pink in solution. These small nanocrystals have a crystalline cadmium selenide core with an average diameter of 3 nm and then passivated with oleic acid ligands. These ligands are about 1.9 nm long, but flexible, and allow the nanocrystals to be dispersed in non-polar solvents.

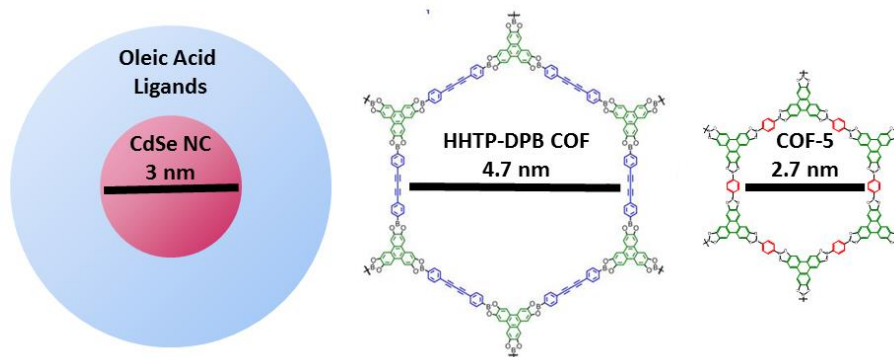


Figure 5.1: Illustration of a 3 nm CdSe nanoparticle with oleic acid ligands and the structures and pore sizes of HHTP-DPB COF and COF-5.

When HHTP-DPB COF powder is exposed to a dilute solution of 3 nm CdSe nanocrystals in toluene, the solution grows less absorbent over time, thus the concentration of free nanocrystals in solution is decreasing with time (Figure 5.2B). To better understand this phenomenon, COF powder was placed in the bottom of a cuvette and a nanoparticle solution was added on top. Over a span of 10 hours the absorbance at the top of the solution was monitored. By the last time-point nearly 80% of the absorbance was lost, implying that the nanocrystals are interacting with the

HHTTP-DPB COF powder and coming out of solution. In contrast, when the same experiment was performed with COF-5, with a smaller pore size of 2.7 nm, only 25% of the absorbance was lost. COF-5 is chemically similar to HHTTP-DPB COF: they both have HHTTP as a node and boronate ester linkages, therefore the key difference is their pore size. From the nanocrystal absorbance data, the large pore of the HHTTP-DPB COF appears to aid in its ability to remove the 3 nm CdSe nanocrystals from solution. It was also necessary to ensure that the affect was not from ligand exchange, since oleic acid ligands are labile in solution. Therefore, the same absorbance experiment was repeated with HHTTP and DPB monomers. For the monomer experiment, the absorbance did not change significantly after 10 hours. Visual inspection of the COFs loaded with CdSe nanocrystals showed a color change which corresponded to the color of the nanocrystals, and the absorbance of the loaded powder nearly matches the absorbance of nanocrystals dried from solution (Figure A4.6). Because the absorbance peak of the CdSe nanocrystal is strongly tied to the size of the nanocrystal core, since the peak shape and location did not change upon loading into a COF, it is important to note that the nanocrystal shape and size are not being significantly changed when they are introduced to the COF powders.

Another way to explore the loading properties of the CdSe nanocrystals into COFs, is to look at the surface area before and after loading. For this trial, HHTTP-DPB COF with a BET surface area of $588 \text{ m}^2\text{g}^{-1}$ was exposed to dilute CdSe nanocrystals with the solution refreshed daily until the concentration of nanocrystals (measured by absorbance) in solution stopped changing, meaning the COF was maximally loaded with nanocrystals. The resulting powder retained only 10% of its original surface area,

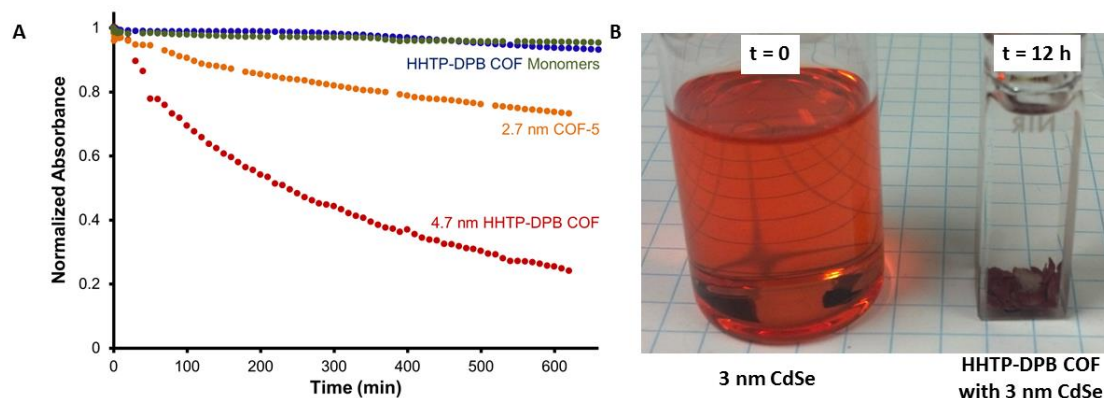


Figure 5.2: A) Absorbance of CdSe nanocrystals over time in the presence of HHTP-DPB COF (red), COF-5 (orange), HHTP monomer (green), DPB monomer (blue) B) Photo of CdSe nanoparticles in solution (left), and after being exposed to HHTP-DPB COF for 12 h (right)

giving a BET surface area of $63 \text{ m}^2\text{g}^{-1}$ (Figure 5.3A). This huge change in surface area could not correlate to strictly nanocrystals on the surface of the COF because the added weight of the nanocrystals (determined from ICP-OES, Figure 5.4) could not solely affect the surface area to this extent, and thus some of the nanocrystals must be interacting with the pores of the COF. In comparison to a maximally loaded COF-5, the surface area changed from $795 \text{ m}^2\text{g}^{-1}$ for pristine COF-5, down to $521 \text{ m}^2\text{g}^{-1}$ for loaded COF-5 (Figure 5.3B). This smaller change in surface area, coupled with the fact that the pores of COF-5 are smaller than most of the nanocrystals in solution, strongly suggests that the change in surface area for COF-5 comes both from the added weight of the nanocrystals and the possibility of pore blocking on the surface. It is important to note that the interaction of the nanocrystals with the two COFs is not strictly a surface area effect. COF-5 in this test has a greater surface area than HHTP-DPB COF, yet it appears to load fewer nanocrystals, likely from the size of the COF-5 pores excluding nanocrystals.

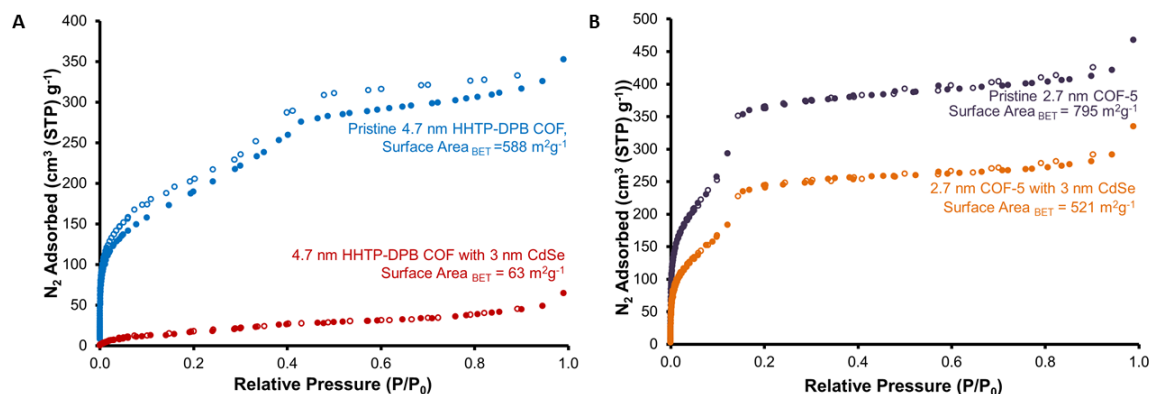


Figure 5.3: Nitrogen adsorption isotherm at 77 K. Absorption (filled circles), Desorption (open circles). A) HHTTP-DPB COF with and without 3 nm CdSe nanocrystals B) COF-5 with and without 3 nm CdSe nanocrystals

Quantitative elemental analysis by ICP-OES of the COF samples used for surface area analysis show very different CdSe loading by weight (Figure 5.4A). COF-5 only loaded 5% on average over 3 samples, while HHTTP-DPB COF loaded on average 28% nanocrystals by weight for 3 samples. The large change in surface area for the HHTTP-DPB COF with only 28% loading strongly suggests the nanocrystals are incorporating into the COF pores. However, the 5% weight loading into COF-5 causing a $200 \text{ m}^2 \text{ g}^{-1}$ difference in surface area, indicates there is some effect of the nanocrystals on the pores of the COF as well. The nanocrystals used are not strictly monodisperse, so a small fraction of the nanocrystals are smaller than 2.7 nm, which means they might be able to enter the COF pores. Also, the nanocrystals could cap the pores, leading to a reduction in surface area without actually penetrating the pores. Further tests to reproduce this result do not corroborate this phenomenon. Using new batches of each COF with similar surface areas, and new batches of the nanocrystal, the same experiment produced different weight percent loading. COF-5 loaded a

comparable amount, around 3 % nanocrystals by weight, while HHTP-DPB COF only loaded around 8 %, which is a dramatic decrease in loading performance (Figure 5.4B). The differences in nanocrystal loading between batches truly highlights the difficulty in characterizing this polycrystalline powders. By every metric, the batches of COF were comparable: they had similar surface area, crystallite size, and IRs matched. Yet, the loading values varied significantly, illustrating that these materials (both the COFs and the nanoparticles) are not completely uniform between batches.

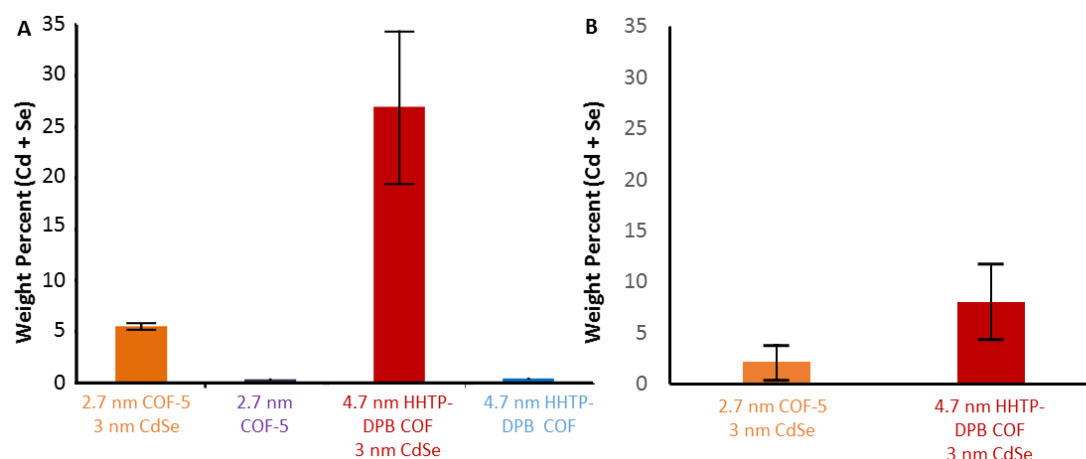


Figure 5.4: Quantitative elemental analysis of maximally loaded COF-5 (orange) and HHTP-DPB COF (red) of Cd + Se loaded A) Original batch of COFs used for surface area analysis B) New batches of COFs and nanocrystals. Errors bars represent 95% confidence interval

Although the above results were intriguing, complementary experiments could not unambiguously prove that the nanoparticles were in the HHTP-DPB COF pores and were impacted by batch to batch inconsistencies of both the COFs and nanoparticles. To further understand these effects, we performed similar maximally loading experiments on higher surface area HHTP-DPB COF that was grown under

homogenous starting conditions (discussed further in the prior chapter). Utilizing this growth method, we were able to achieve HHTP-DPB COF with a surface area of 2225 $\text{m}^2 \text{g}^{-1}$, which is far closer to its theoretical yield of 2650 $\text{m}^2 \text{g}^{-1}$. Loading this higher quality COF with two different batches of 3 nm CdSe nanoparticles still showed huge variations in the change in surface area seen in Figure 5.5. Loading with the original batch of nanoparticles used for the analysis is Figures 5.3 and 5.4, after maximally loading the sample, the surface area dropped to 490 $\text{m}^2 \text{g}^{-1}$, which is about a 73% decrease in surface area. This is not at dramatic, but when compared to a second batch of nanoparticles with the same high surface area HHTP-DPB COF only changes the surface area by about 50%, indicating strong variation in the nanocrystal batches.

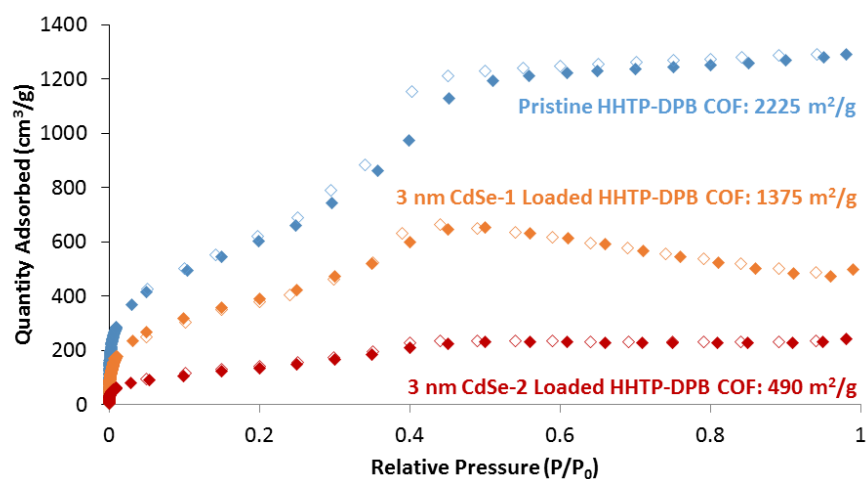


Figure 5.5: Nitrogen adsorption isotherm for HHTP-DPB COF (blue) loaded with two different batches of 3 nm CdSe nanocrystals (orange and red)

When COF-5 was exposed to the 3 nm CdSe nanoparticles, the weight percent loaded was around 5%. Since COF-5's pores are 2.7 nm, we expected the change in surface area, and the weight of CdSe loaded to come from two factors: polydispersity in the nanoparticle sample led to particles smaller than 2.7 nm, or the nanoparticles

capped the surface of the pores preventing nitrogen adsorption. To confirm these effects, we tested both COFs against larger nanoparticles: 4.5 nm Cdse, and 6 nm PbS. Compared to the 4.7 nm HHTP-DPB COF pore, it is expected that very little of either particle enters the COF pores when the surrounding ligands are taken into account. As seen in Figure 5.6, once larger nanoparticles are used, both COFs load similar weights of the metal, implying similar interaction mechanisms. Since more of the 4.5 nm CdSe nanocrystals load into the larger pore HHTP-DPB COF, it is likely that the polydispersity of the nanocrystals allows for some to be loaded into the pores, but since the very large 6 nm PbS nanocrystals still show noticeable loading, surface interactions must play a role in COF – nanocrystal interactions. Since the larger nanoparticles interact with both COFs similarly, it is likely that the very high loading of HHTP-DPB COF with 3 nm CdSe nanoparticles is due to nanoparticles loading into the COF pores. Also, in this series of experiments using high surface area HHTP-DPB COF, a high loading of 3 nm CdSe (65% is also seen), which again demonstrates the batch to batch variability of these methods.

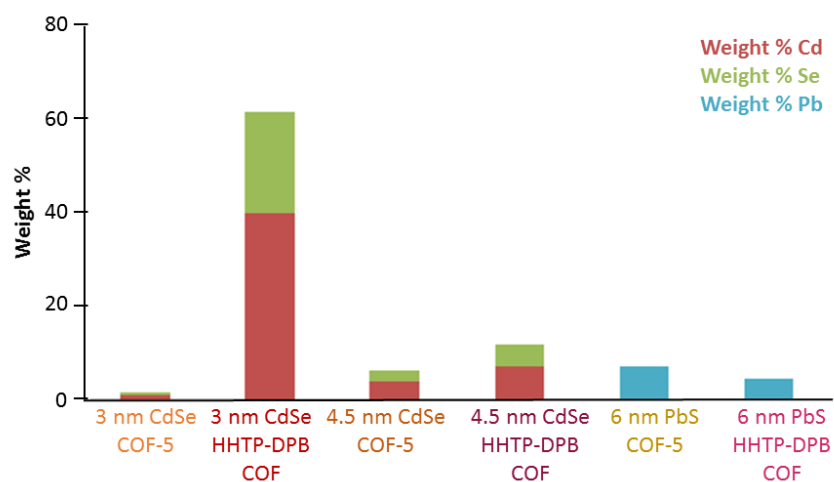


Figure 5.6: Quantitative elemental analysis of maximally loaded COF-5 and HHTP-DPB COF with 3 nm CdSe, 4.5 nm CdSe, and 6 nm PbS nanocrystals.

To explore this further, maximally loaded HHTP-DPB COF powders with 3 nm CdSe nanocrystals were embedded in epoxy and microtomed before placing on a TEM grid. TEM images of these powders shows nanoparticles and COF morphology, but it is difficult to discern the location of the nanoparticles with respect to the powder (Figure 6.7A). To further investigate, thin films of HHTP-DPB COF were grown on doped silica and then exposed to a dilute solution of 3 nm CdSe nanocrystals in toluene. After soaking for 12 hours, the films were dried and then cross sectioned using a focused ion beam. TEM images of this milled section (Figure 6.7B), show nanoparticles imbedded within the COF matrix, but they only exist as a small band, and not continuous throughout the film as expected. This finding seems to imply that the nanocrystals are penetrating into the HHTP-DPB COF film, but not creating the well-defined arrays as expected.

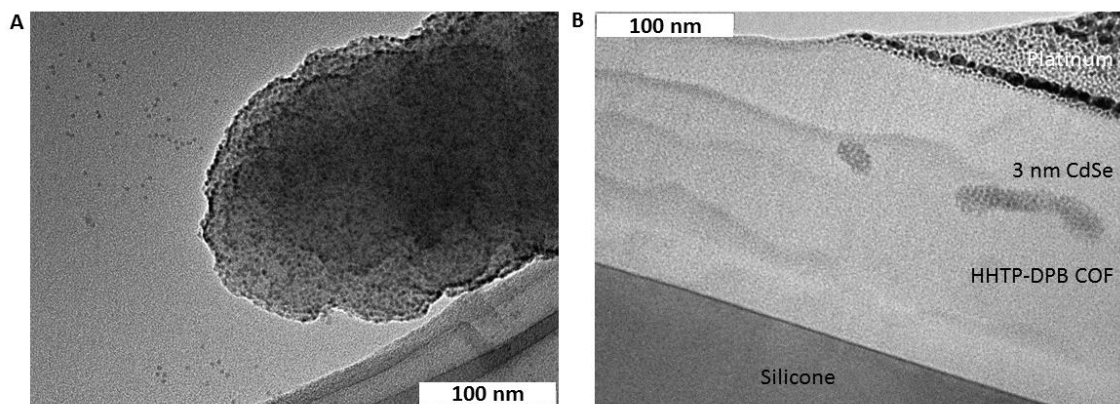


Figure 5.7. TEM images of A) HHTP-DPB COF powder maximally loaded with 3 nm CdSe nanocrystals B) Cross section of HHTP-DPB COF film loaded with 3 nm CdSe nanocrystals. Dark gray lower right corner is the silicone substrate with lighter gray HHTP-DPB COF on top of it (approx. 150 nm thick). About 100 nm above the silicone is a small band of 3 nm CdSe nanocrystals. The top visible layer is the sputtered platinum coating to protect the film from the ion beam during milling.

Conclusions: It is unambiguous that 2D boronate ester linked COFs can bind CdSe nanoparticles from dilute solution. This effect is not a function of COF monomers, but instead appears to be an effect that depends on the size of the nanoparticle and the size of the COF pore. These loaded nanoparticles maintain the characteristic absorbance of nanocrystals, and the COFs remain crystalline. Future work will focus on methods to empirically determine COF and nanoparticle quality. Once both of these materials can be thoroughly appraised, a better understanding of the nanoparticle – COF interactions can be understood.

REFERENCES

- (1) Murray, C. B.; Kagan, C. R.; Bawendi, M. G. *Annu. Rev. Mater. Sci.* **2000**, *30* (1), 545–610.
- (2) El-Sayed, M. A. *Acc. Chem. Res.* **2001**, *34* (4), 257–264.
- (3) Burda, C.; Chen, X.; Narayanan, R.; El-Sayed, M. A. *Chem. Rev.* **2005**, *105* (4), 1025–1102.
- (4) Lu, A.-H.; Salabas, E. L.; Schüth, F. *Angew. Chem. Int. Ed.* **2007**, *46* (8), 1222–1244.
- (5) Godovsky, D. Y. In *Biopolymers · PVA Hydrogels, Anionic Polymerisation Nanocomposites*; Advances in Polymer Science; Springer Berlin Heidelberg, 2000; pp 163–205.
- (6) Kelzenberg, M. D.; Boettcher, S. W.; Petykiewicz, J. A.; Turner-Evans, D. B.; Putnam, M. C.; Warren, E. L.; Spurgeon, J. M.; Briggs, R. M.; Lewis, N. S.; Atwater, H. A. *Nat. Mater.* **2010**, *9* (3), 239–244.
- (7) Labastide, J. A.; Baghgar, M.; Dujovne, I.; Yang, Y.; Dinsmore, A. D.; G. Sumpter, B.; Venkataraman, D.; Barnes, M. D. *J. Phys. Chem. Lett.* **2011**, *2* (24), 3085–3091.
- (8) Saunders, B. R.; Turner, M. L. *Adv. Colloid Interface Sci.* **2008**, *138* (1), 1–23.
- (9) Vossmeier, T.; Reck, G.; Katsikas, L.; Haupt, E. T. K.; Schulz, B.; Weller, H. *Science* **1995**, *267* (5203), 1476–1479.
- (10) Weller, H. *Angew. Chem. Int. Ed. Engl.* **1996**, *35* (10), 1079–1081.
- (11) Brust, M.; Kiely, C. J. *Colloids Surf. Physicochem. Eng. Asp.* **2002**, *202* (2–3), 175–186.
- (12) Sun, S. *Adv. Mater.* **2006**, *18* (4), 393–403.
- (13) Gao, Y.; Tang, Z. *Small* **2011**, *7* (15), 2133–2146.
- (14) Mazid, R. R.; Si, K. J.; Cheng, W. *Methods* **2014**, *67* (2), 215–226.
- (15) Mehdizadeh Taheri, S.; Fischer, S.; Förster, S. *Polymers* **2011**, *3* (2), 662–673.
- (16) Ding, S.-Y.; Wang, W. *Chem. Soc. Rev.* **2012**, *42* (2), 548–568.
- (17) Fang, Q.; Zhuang, Z.; Gu, S.; Kaspar, R. B.; Zheng, J.; Wang, J.; Qiu, S.; Yan, Y. *Nat. Commun.* **2014**, *5*, 4503.
- (18) Colson, J. W.; Woll, A. R.; Mukherjee, A.; Levendorf, M. P.; Spitler, E. L.; Shields, V. B.; Spencer, M. G.; Park, J.; Dichtel, W. R. *Science* **2011**, *332* (6026), 228–231.
- (19) Spitler, E. L.; Koo, B. T.; Novotney, J. L.; Colson, J. W.; Uribe-Romo, F. J.; Gutierrez, G. D.; Clancy, P.; Dichtel, W. R. *J. Am. Chem. Soc.* **2011**, *133* (48), 19416–19421.
- (20) Zhang, H.; Hyun, B.-R.; Wise, F. W.; Robinson, R. D. *Nano Lett.* **2012**, *12* (11), 5856–5860.

APPENDIX IV

A. Materials. All reagents were purchased from commercial sources and used without further purification. CH₂Cl₂, PhMe, and MeOH were purchased from commercial sources and purified using a custom-built alumina-column based solvent purification system. Other solvents were purchased from commercial sources and used without further purification

Instrumentation. Infrared spectra were recorded on a Thermo Nicolet iS10 with a diamond ATR attachment and are uncorrected. Ultraviolet/visible/near infrared absorbance spectra were recorded on a Cary 5000 spectrophotometer with a Hg lamp.

Photoemission and excitation spectra were recorded on a Horiba Jobin Yvon Fluorolog-3 fluorescence spectrophotometer equipped with a 450 W Xe lamp, double excitation and double emission monochromators, a digital photon-counting photomultiplier and a secondary InGaAs detector for the NIR range. Correction for variations in lamp intensity over time and wavelength was achieved with a solid-state silicon photodiode as the reference. The spectra were further corrected for variations in photomultiplier response over wavelength and for the path difference between the sample and the reference by multiplication with emission correction curves generated on the instrument.

Surface area measurements were conducted on a Micromeritics ASAP 2020 Accelerated Surface Area and Porosimetry Analyzer using 75 mg samples degassed at 90 °C for 24 h and backfilled with N₂. N₂ isotherms were generated by incremental exposure to ultra high purity nitrogen up to 1 atm in a liquid nitrogen (77 K) bath and surface parameters were determined using BET adsorption models included in the instrument software (Micromeritics ASAP 2020 V4.00).

NMR spectra were recorded on a Varian 400 MHz, a Varian 500 MHz or a Bruker ARX 300 MHz spectrometer using a standard ¹H/X Z-PFG probe at ambient temperature with a 20 Hz sample spin rate.

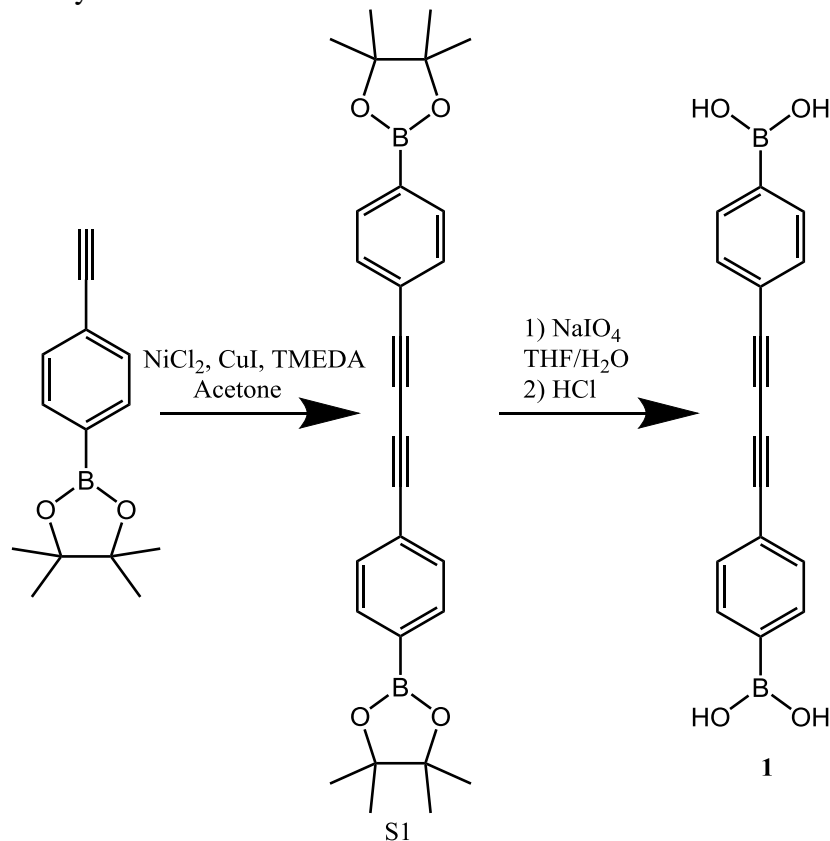
Solid-state NMR spectra were recorded at ambient temperature on a Varian INOVA- 400 spectrometer using an external Kalmus 1 H linear pulse amplifier blanked using a spare line. Samples were packed into 7 mm outside diameter silicon nitride rotors and inserted into a Varian HX magic angle spinning (MAS) probe. ¹³C data was

acquired using linearly ramped cross-polarization with MAS (CP/MAS) at 100.5 MHz. The ^1H and S4 ^{13}C had ninety-degree pulse widths of 5 μs , and the CP contact time was 1 ms. Two-pulse phase modulation (TPPM) ^1H decoupling was applied during data acquisition with a decoupling frequency of 78 kHz. The recycle delays between scans were 2 s. The MAS spin rate varied between 5–7 kHz, as labeled in the spectra. ^{13}C chemical shifts were assigned relative to tetramethylsilane at 0.0 ppm and were calibrated using the methyl carbon signal of hexamethylbenzene assigned at 16.9 ppm as a secondary reference. The MAS spinning rate varied between 5-7 kHz as labeled in the spectra.

Powder X-ray diffraction (PXRD) patterns were obtained on a Scintag Theta-Theta Powder X-Ray Diffractometer in reflectance Bragg-Brentano geometry employing Cu $K\alpha$ line focused radiation at 2200 W (40 kV, 40 mA) power and equipped with a Ge crystal detector fitted with a 0.3 mm radiation entrance slit. Samples were mounted on zero background sample holders by dropping powders from a spatula and then leveling the sample surface with a glass microscope slide. No sample grinding or sieving was used prior to analysis. Crystallite size was determined by applying the Scherrer equation to the powder patterns using MDI JADE.

B. Synthetic Procedures

Scheme A4.1. Synthesis of DPB monomer 1.



Synthesis of S1: TMEDA (0.459 g, 3.946 mmol), CuI (0.188 g, 0.986 mmol), and NiCl_2 (0.234 g, 0.986 mmol) were dissolved or suspended in $(\text{CH}_3)_2\text{CO}$ (13 mL) under an atmosphere of air. The mixture became dark green after 10 min. 4-Ethynylbenzeneboronic acid pinacol ester (4.50 g, 19.7 mmol) was added, and the mixture was stirred rapidly for 2 h. The solvent was evaporated and the resulting yellow-green residue was washed with H_2O (50 mL), providing the yellow dialkyne ester S1 (1.90 g, 42%) as a white solid. $^1\text{H-NMR}$ (CDCl_3 , 300 MHz, 298 K) δ 7.65 (d, $J = 9.0$ Hz, 4H); 7.52 (d, $J = 9.0$ Hz, 4H); 1.34 (s, 24H). $^{13}\text{C-NMR}$ (CDCl_3 , 300 MHz) δ 135, 132, 125, 83, 75, 25. This spectrum matched that previously reported.

Synthesis of 1: A 20 mL scintillation vial was charged with the diboronate ester S1 (400 mg, 0.88 mmol) and NaIO_4 (400 mg, 2.0 mmol). The solids were dissolved in a THF:H₂O mixture (4:1, 6 mL) and stirred at rt for 12 h. 1M HCl (10 mL) was then added to the white suspension, which was stirred for another 12 h. The pale yellow-white suspension was diluted with H_2O (20 mL), and the solids recovered by filtration. The recovered solid was washed with an additional H_2O (20 mL) followed by hexanes (10 mL). The white solid was dried under vacuum to yield 233 mg (91%) of boronic acid 1. $^1\text{H-NMR}$ (DMSO-d_6 , 300 MHz) δ 8.26 (s, 4H); 7.82 (d, $J = 7.5$ Hz, 4H); 7.57 (d, $J = 7.5$ Hz, 4H). This spectrum matched that previously reported.

Synthesis of HHTP-DPB COF (Literature Conditions): Boronic acid 1 (20 mg, 0.069 mmol) and HHTP (7 mg, 0.022 mmol) were combined in a mixture of dioxane and mesitylene (1:1, 4 mL) and sonicated for 10 min. The light gray suspension was heated to 90 °C in an aluminum block for 72 h, and the resulting free-flowing tan powder was collected by filtration on a Hirsch funnel, washed with 1 mL anhydrous toluene and air-dried. The crude HHTP-DPB COF isolated after drying under vacuum for 12 h. Isolated yield 10 mg (71%).

Synthesis of HHTP-DPB COF (Homogenous Conditions): Boronic acid 1 (13 mg, 0.046 mmol) and MeOH (0.012 mL, 0.463 mmol) was dissolved mixture of dioxane / mesitylene (4:1, 4 mL). HHTP (10 mg, 0.031 mmol) was added and sonicated for 10 min, or until the HHTP is fully dissolved. The solution was filtered (0.45 µm PTFE) to remove any trace residual particulate into a 20 mL scintillation vial. The vial was heated to 90 °C for 20 h. After cooling to rt, the COF solid was filtered into a chemwipe with dry toluene and active using supercritical CO₂. Isolated yield 7 mg (65%).

Supercritical Activation: Crude COF powder was isolated into a chemwipe tied shut with copper wire, and placed into the super critical activation chamber. The chamber was filled with liquid CO₂ and allowed to sit for 5 min, and then half of the volume released. This was repeated six times or until the evacuated CO₂ no longer smelled of toluene. The liquid CO₂ was then heated to 40 °C at a constant volume and then the gas was slowly released.

Synthesis of COF-5 (Literature): 1,4-benzene diboronic acid (BDBA) (25 mg, 0.15 mmol), 2,3,6,7,10,11- hexahydroxytriphenylene [(HHTP) 16 mg, 0.050 mmol] and 1 mL of a 1:1 v:v solution of mesitylene:dioxane were added to a 20 mL scintillation vial. The mixture was sonicated for 10 min and then heated to 90 °C for 72 h. The reaction was filtered with anhydrous toluene and then dried under vacuum to yield a free flowing gray powder. Yield: 15 mg, 73 %

Synthesis of COF-5 (Homogenous Conditions): 1,4-benzene diboronic acid (115 mg, 0.694 mmol) and MeOH (0.175 mL, 6.938 mmol) was dissolved mixture of dioxane / mesitylene (4:1, 67 mL). HHTP (150 mg, 0.463 mmol) was added and sonicated for 10 min, or until the HHTP is fully dissolved. The solution was filtered (0.45 µm PTFE) to remove any trace residual particulate into a 150 mL round bottom flask. The flask was heated to 90 °C for 20 h. After cooling to rt, the COF solid was filtered with dry toluene and activated under vacuum.

Maximally Loading COF: A 10 mL test tube was charged with 5 mg of COF (either HHTP-DPB or COF-5) and then 1 mL of dry hexanes was added, followed by 1 mL of a 0.8 mg/mL solution 3 nm CdSe in hexanes. This solution was removed and refreshed every 24 h until the concentration of CdSe in solution did not change by UV-Vis measurement. Loaded COF samples were filtered with dry toluene and dried under vacuum at 50 °C for 12 h.

C. NMR Spectra

Figure A4.1: ^1H NMR of Compound S1

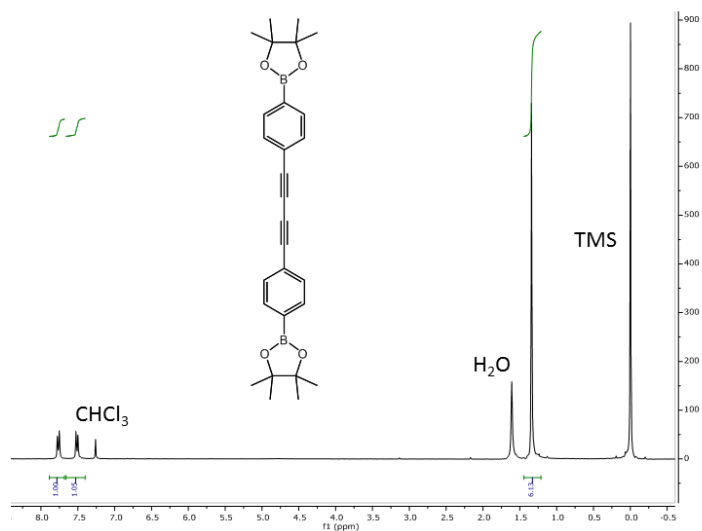
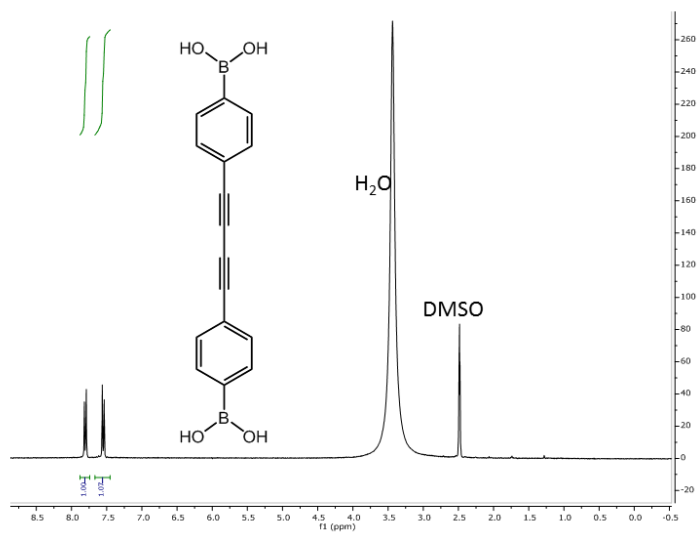
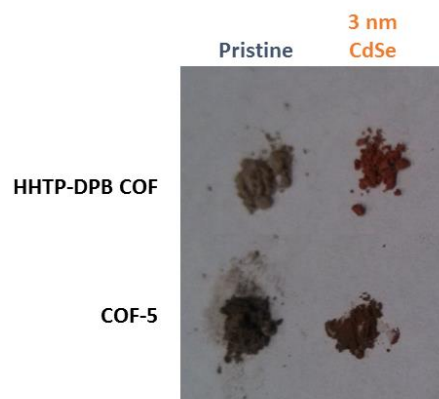


Figure A4.2: ^1H NMR of Compound 1



D. Photographs

Figure A4.3: Image of HHTP-DPB COF and COF-5 with and without CdSe nanocrystal loading



E. IR Spectra

Figure A4.4: IR Spectra of HHTP-DPB COF loaded with 3 nm CdSe Nanocrystals

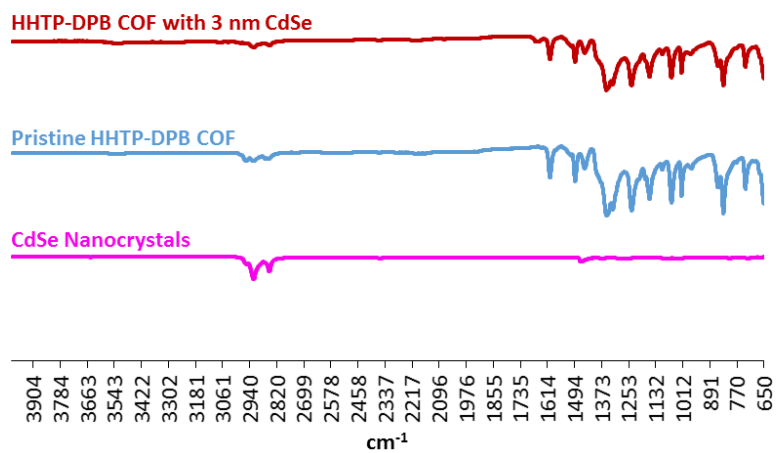
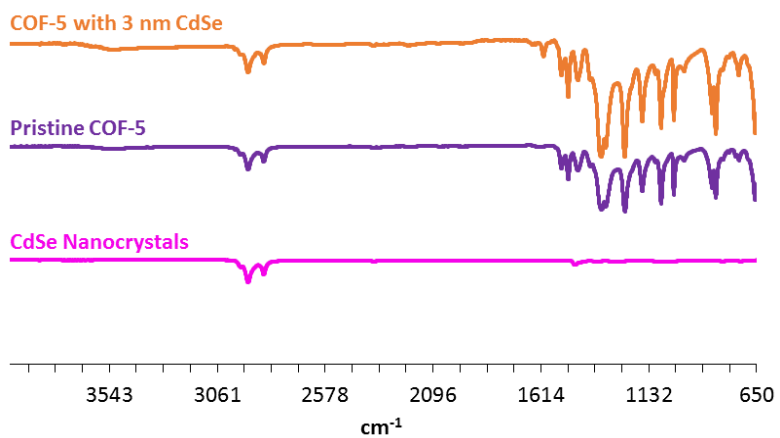
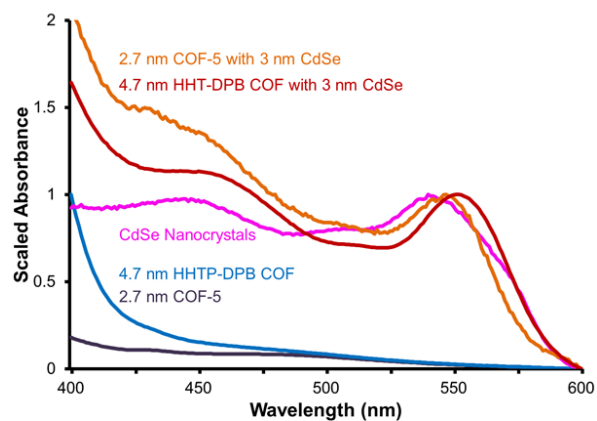


Figure A4.5: IR Spectra of COF-5 loaded with 3 nm CdSe Nanocrystals



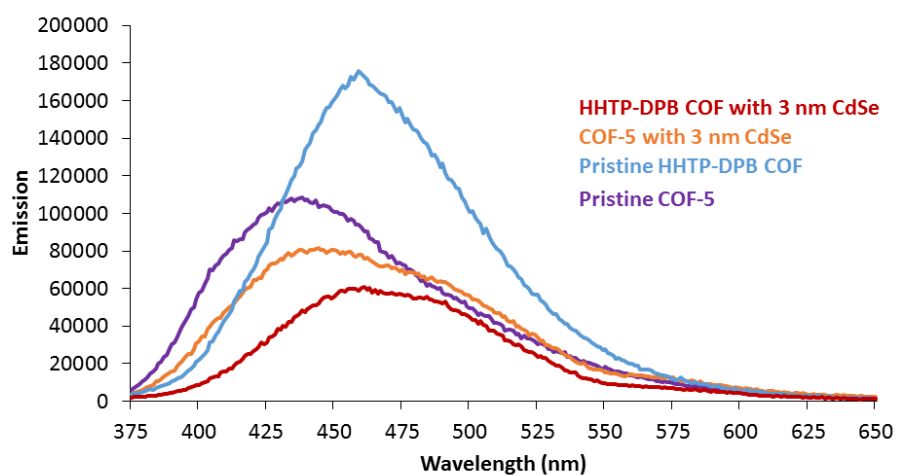
F. UV-Vis Spectra

Figure A4.6: UV-Vis spectra of HHTP-DPB COF and COF-5 powders with and without CdSe nanocrystals. CdSe nanocrystal spectra is of a drop cast film of the nanocrystals from hexanes



G. Fluorescence Spectra

Figure A4.6: Fluorescence emission spectra of HHTP-DPB COF and COF-5 powders with and without CdSe nanocrystals. $\lambda_{\text{ex}} = 350 \text{ nm}$



H. XRD Spectra

Figure A4.7: A) Powder x-ray diffraction of HHTP-DPB COF powder with and without CdSe nanocrystals B) PXRD of maximally loaded HHTP-DPB COF with CdSe showing the diffraction of the CdSe nanocrystals

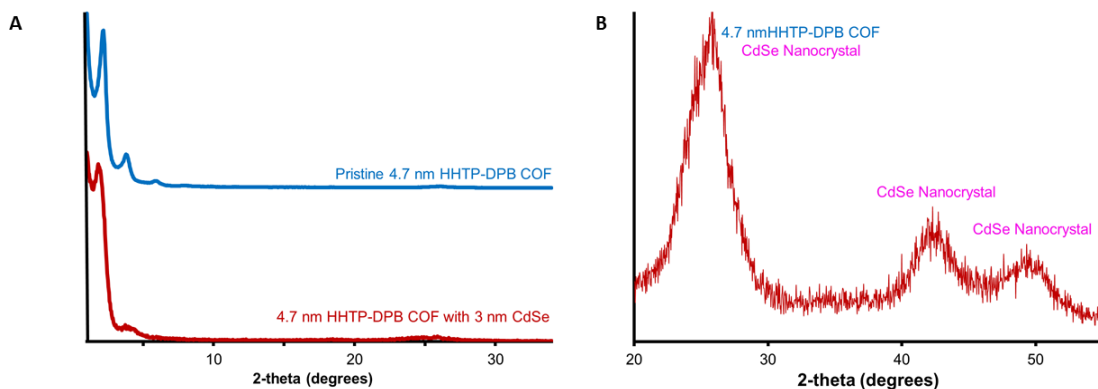


Figure A4.8: Powder x-ray diffraction of HHTP-DPB COF powder with and without CdSe nanocrystals showing different activation methods after CdSe Loading

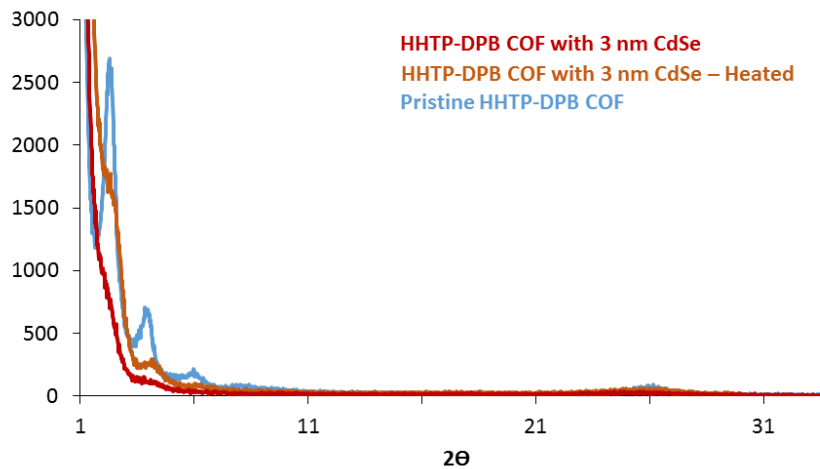
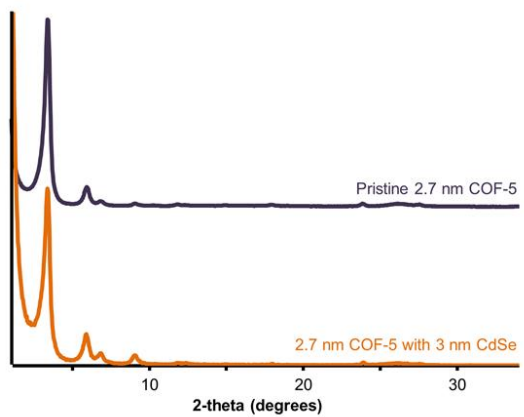
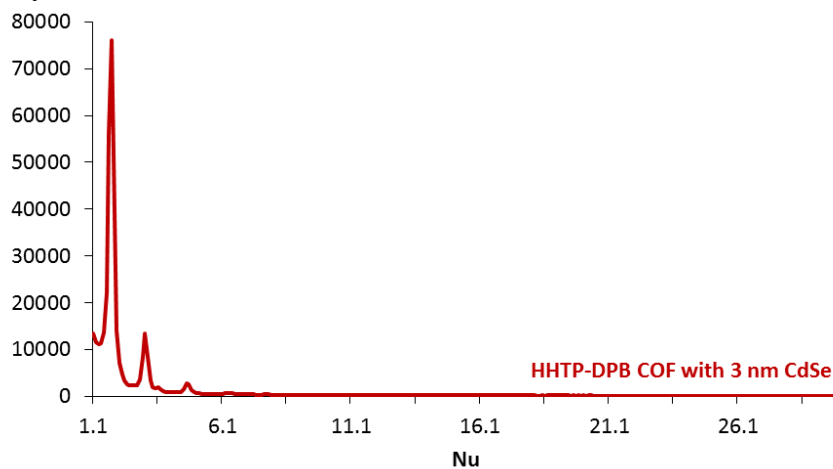


Figure A4.9: Powder x-ray diffraction of COF-5 powder with and without CdSe nanocrystals



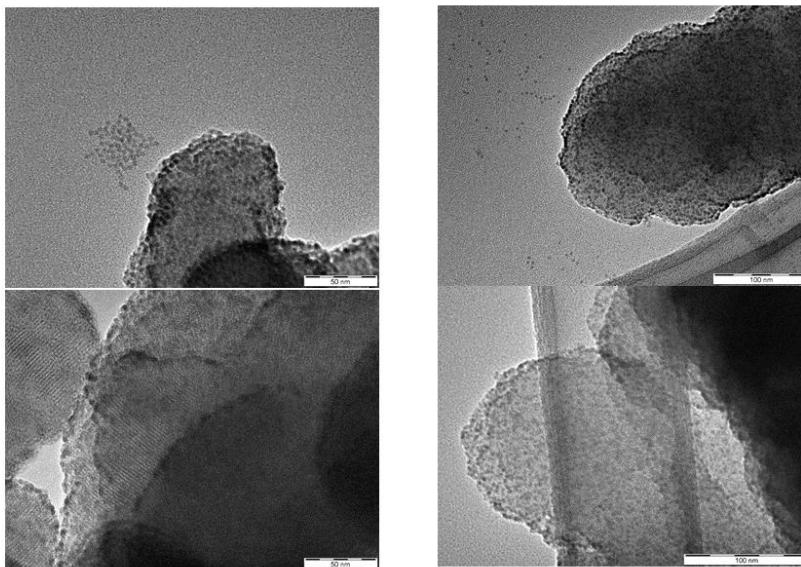
I. Synchrotron X-Ray Diffraction

Figure A4.10: Cross section of 2D GID of HHTP-DPB COF film exposed to CdSe nanocrystals



J. TEM Images

Figure A4.11: TEM image of HHTP-DPB COF powder loaded with CdSe nanocrystals



K. Surface Area Measurement

Figure A4.12 Nitrogen isotherm at 77 K of pristine HHTP-DPB COF (grown from homogenous conditions), and the same COF loaded with two different batches of 3 nm CdSe

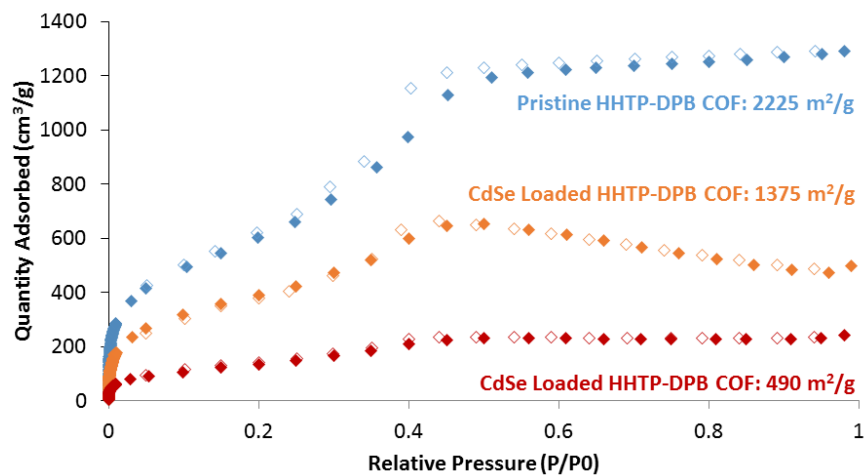


Figure A4.13: BET Plot for pristine HHTP-DPB COF in figure A4.12

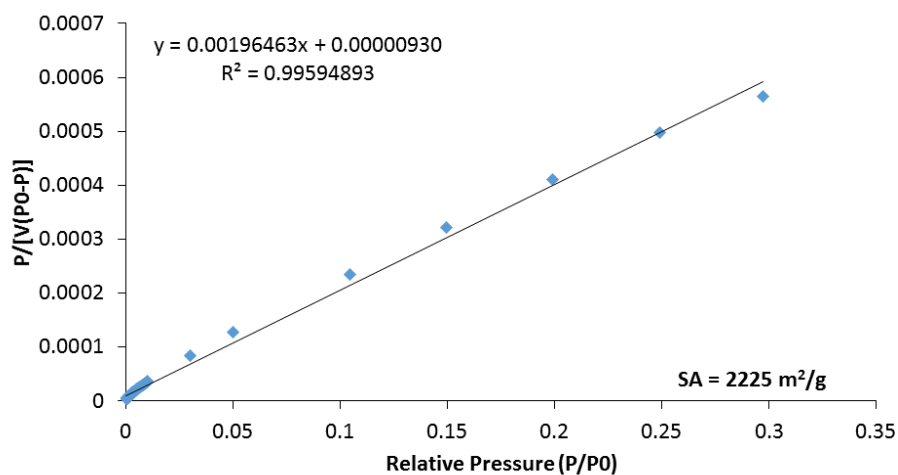


Figure A4.14: BET Plot for HHTP-DPB COF with 3 nm CdSe in figure A4.12 (orange trace)

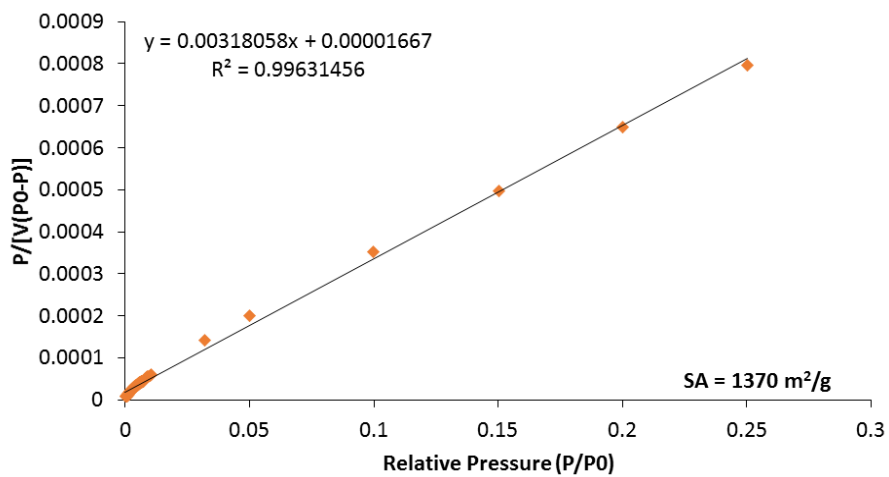


Figure A4.15: BET Plot for HHTP-DPB COF with 3 nm CdSe in figure A4.12 (red trace)

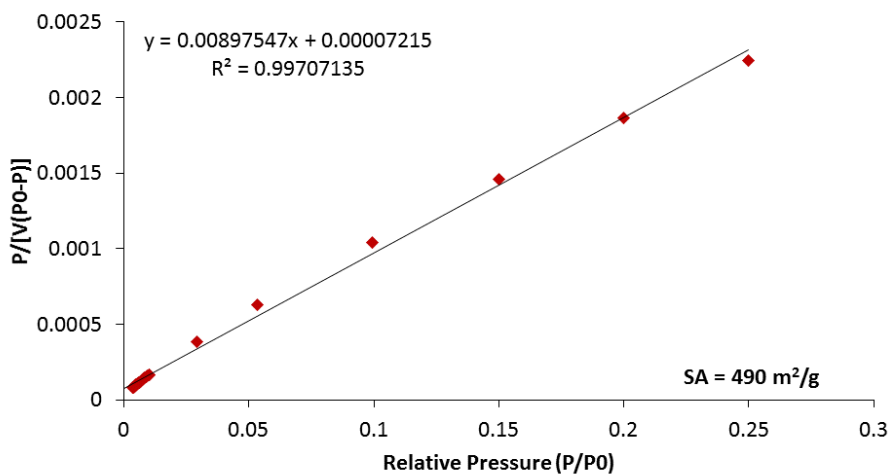


Figure A4.16: BET Plot for pristine HHTP-DPB COF in Figure 5.3A

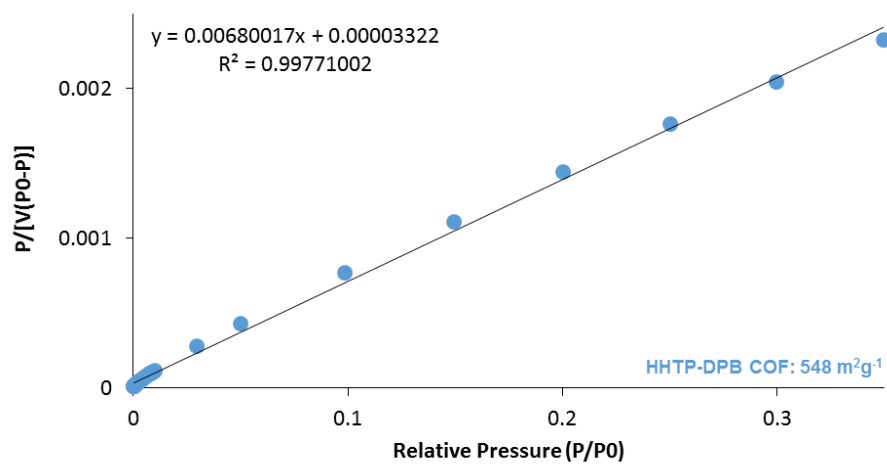
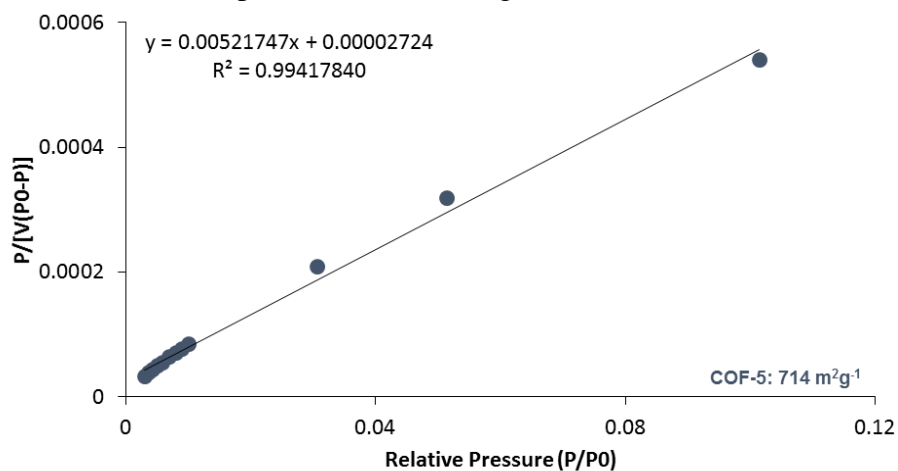


Figure A4.17: BET Plot for pristine COF-5 in Figure 5.3B



CHAPTER 6

HYDRAZONE-LINKED COF-43 INTERACTIONS WITH LI+

ABSTRACT: Here we report the loading of COF-43 with Li⁺ and H⁺ in a 1:1 ratio of M⁺ to hydrazone bond in the framework. Hydrazones have a long history of creating complexes with different metals, and COF-43 can also load larger M⁺ cations as well as some divalent species. These loading experiments lead to dramatic shifts in fluorescence emission, up to 100 nm, due to changes in the interlayer stacking. The metal loaded COF-43 can be utilized for benzylation and Sonogashira cross coupling reactions with increased moisture stability and modest recyclability.

Introduction: Since the discovery of boronate ester linked COFs in 2005¹, there has been a huge push to expand the types of linkers used to create these porous organic materials. COF-43 is one of three hydrazone linked COFs which is formed through the acid catalyzed condensation of a hydrazide with an aldehyde^{2,3}. The rate of dissolution of the linkage is pH dependent⁴ leading to its use in pharmaceuticals⁵⁻⁸ and drug delivery applications^{9,10}. Hydrazones have been known for many years to coordinate metal centers like Cu, Li, Rh¹¹⁻¹⁴ and even used for cyclization reactions¹⁵⁻¹⁸. In addition to containing this interesting chemical moiety, COF-43 has exhibited unique properties unseen in other COFs. COF-43 layers can be exfoliated from the bulk powder and the size and number of layers in the exfoliated material can be tuned depending on the exfoliation solvent¹⁹.

Other than exfoliation, there have been no successful methods to control COF morphology or particle size, though monomer truncation methods have been tried²⁰⁻²².

The ability to control particle size on these materials with well-defined nanoscale features would allow for implementation into electronic devices, filtration, and drug delivery. We attempted to synthesize COF-43 in an emulsion, and while it did not impart control on the macroscale, these experiments led serendipitously to finding that COF-43 has an affinity for Li^+ and other Lewis acid cations.

Discussion: The growth conditions and various properties of the hydrazone linked COF-43 have been well studied^{2,19}. The published growth condition for COF-43 has an organic layer containing the two monomers, and an aqueous acid layer, so it is a biphasic reaction (Figure 6.1). The acid is necessary to catalyze the condensation reaction which forms the COF-43 hydrazone linkers, thus it is easy to believe growth in an emulsion could control the particle size of the formed powder by limiting the reaction by the size of the droplets in the emulsion. Incorporating sodium dodecyl sulfate (SDS) as an emulsifying agent into the growth conditions, produced crystalline COF-43. However, as seen in Figure 6.2A, the resulting powder was bright yellow, instead of the very pale yellow of COF-43 produced under literature conditions. Furthermore, neither the particle size, nor crystallite size changed significantly under these growth conditions. Upon further exploration of COF-43 growth conditions, we found that crystalline COF could be produced under aqueous conditions, with or without the addition of SDS. Figure 6.2B illustrates the large shift in fluorescence emission from the COF that occurs when SDS is included in the growth conditions. Surprisingly, when COF-43 is synthesized without SDS (either as an emulsion, or aqueous), the resulting powder's emission is very similar to the emission from COF-43 made via literature conditions. It is only when grown in the presence of SDS, does

the emission change significantly.

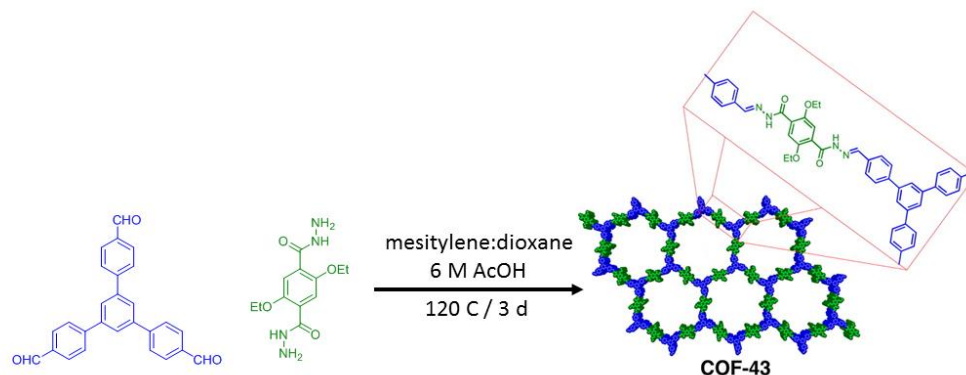


Figure 6.1: Solvothermal synthesis of COF-43 from tri-aldehyde (blue) and dihydrazide (green). Modified from reference 2

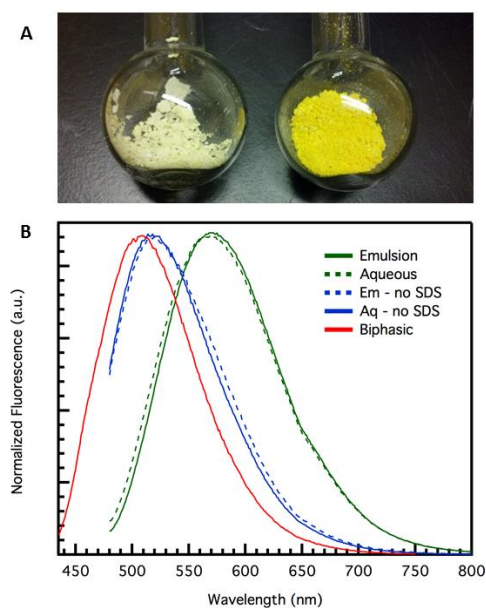


Figure 6.2: A) Photograph of COF-43 grown under literature conditions (left) and in the presence of SDS (right). B) Fluorescence emission of COF-43 under various growth conditions. Literature conditions (red), without SDS (red), with SDS (green)

To further understand this effect, we introduced COF-43 grown under literature conditions to solutions of SDS in THF to see if we could modulate the color change depending on the concentration of SDS in solution. We originally suspected

that it was the incorporation of the long alkyl chains from the SDS into the COF pores which affected the stacking of the material, leading to the significant color change that occurs when SDS is present during synthesis. During these trials, the age of the SDS solution produced significant differences in the change in fluorescence emission of the COF-43. Fresh solutions of SDS in THF did not induce a color change in the COF-43, but if the SDS solution was allowed to age for 24 hours, the COF-43 turned yellow upon the addition of the solution, which is seen in Figure 6.3A. To minimize quenching of the COF fluorescence, THF without stabilizers was used. To ensure the change in the color of the COF was not promoted by the development of peroxides in the solvent, various organic peroxides in solution were added to pristine COF-43 and significant color changes did not occur (Figure 6.3B). COF-43 does exhibit solvchromatic fluorescence emission, so the yellow color change seen with the addition of hydrogen peroxide is likely due to the water used in the peroxide solution.

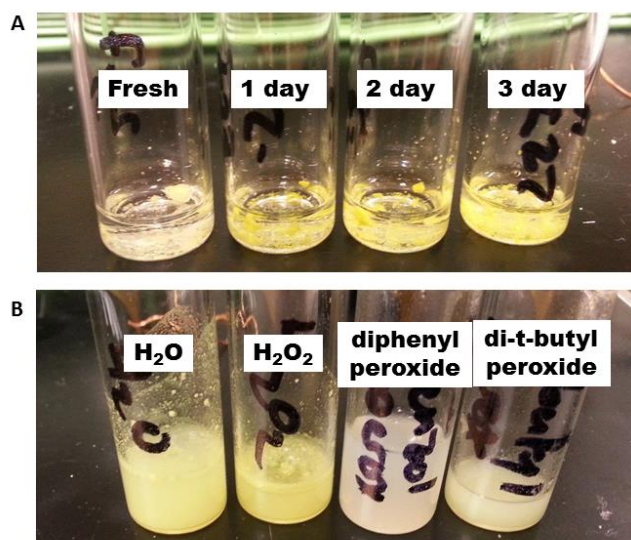


Figure 6.3: A) Photograph of COF-43 exposed to saturated solutions of SDS in THF which were allowed to age for different durations B) Photograph of COF-43 exposed to different peroxides in solution.

The first clue to unraveling the mechanism of the color change in the COF comes from the literature conditions. In the presence of the acetic acid catalyst, the COF is bright yellow, similar to the COF formed in the presence of SDS. It is only after washing the COF with THF to remove the acid, does the color fade to pale yellow. Addition of trichloroacetic acid (TCA) to COF synthesized without SDS also induces a significant color change, with the fluorescence emission shifting up to 100 nm. TCA was chosen for these experiments because it is solid at room temperature, which reduces concern about vapor phase contamination of other samples, which had been witnessed with trifluoroacetic acid as an additive. Also, the pH of TCA is low enough to produce color changes in the COF without digesting the powder. In a typical experiment, a known amount of TCA in solution was added to COF-43 and the solution allowed to evaporate at room temperature, leaving COF-43 loaded with a known amount of acid. Figure 3 shows the asymptotic change in fluorescence emission, leveling out at close to 1 equivalent of TCA per hydrazone. IR spectroscopy (Figure 6.5) of the TCA loaded COF-43 shows a weakening of the band corresponding to the C=N bond at 1650 cm^{-1} when compared to the carbonyl group at 1600 cm^{-1} . This finding suggests that the proton is association with the nitrogen, weakening the intensity of the C=N band without destroying the COF. However, the COF does not perform well as a pH sensor. Solutions with a pH =1 degrade the material, and aqueous solutions with pH between 4-9 only show a change in fluorescence due to the presence of water.

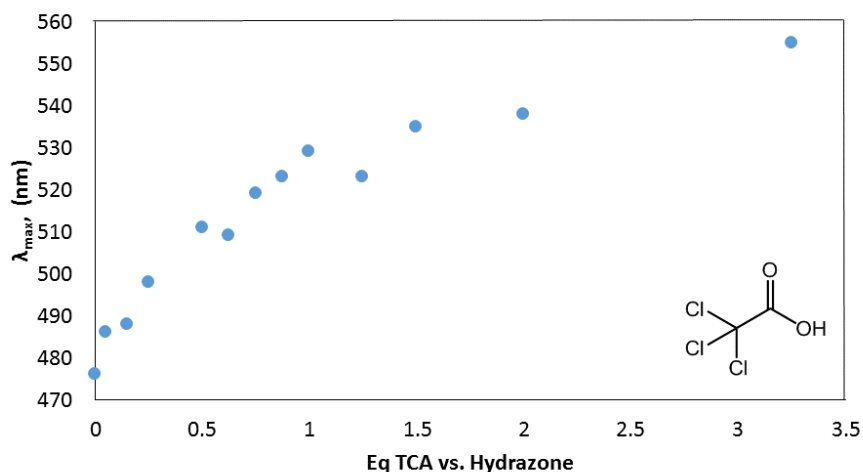


Figure 6.4: Plot of max fluorescence emission versus the equivalents of TCA added to COF-43. Structure of TCA in lower right corner

With the dramatic effects of TCA on COF-43, other cation sources were screened for similar effects on the COF emission. To maintain a similar stoichiometry for the proton – COF-43 interaction, various salts with the general formula MCl were tested. Exposing COF-43 to an excess of LiCl produced the largest change in fluorescence emission, perhaps due to the hardness of the cation. HCl degraded the COF, leading to its poor response, and the larger cations all produced similar responses, hovering around a shift of 18 nm (Figure 6.6). It is uncertain if the limited response of the larger cations is due to steric effects, or if the ions are too soft to coordinate with the hydrazone. The counterion for the Li also plays a huge role in the change in COF emission. A screening of Li salts shows LiCl and LiPF₆ both produce significant color changes (Figure 6.7). However, LiPF₆ can degrade to HF, which would make deconvolution the effect of Li⁺ from H⁺ difficult, so it was not used in future studies. Other anions, like ⁻OH and SO₄²⁻ do not produce large color changes, likely due to solubility restrictions. Other larger anions like Br⁻ and CF₃SO₃⁻ do not

have the same solubility concerns, but still only produce a 20 nm shift in emission. NBu₄PF₆ was tested to confirm that the PF₆⁻ anion did not contribute to the shifts in emission and to explore the effects of a softer cation.

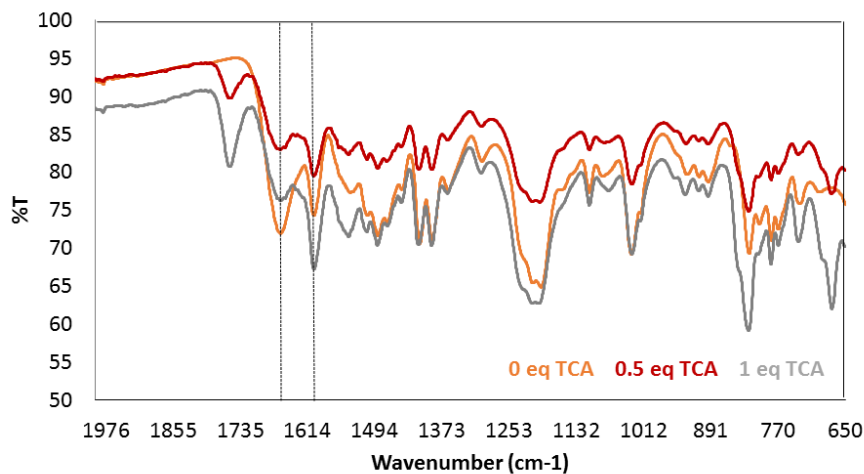


Figure 6.5: IR spectra of COF-43 exposed to difference equivalents of TCA. Dashed lines show the C=N bond at 1650 cm⁻¹ and the carbonyl peak at 1600 cm⁻¹. Growth of peak at 1750 cm⁻¹ from presence of TCA

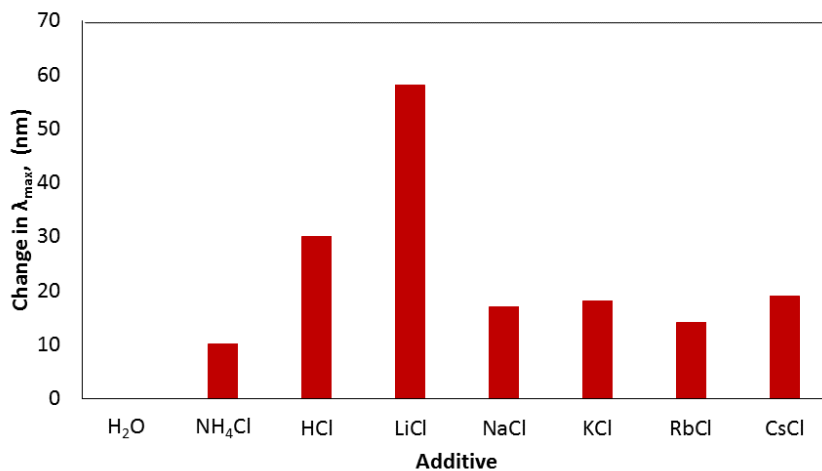


Figure 6.6: Change in maximum fluorescence emission of COF-43 exposed to excess additives

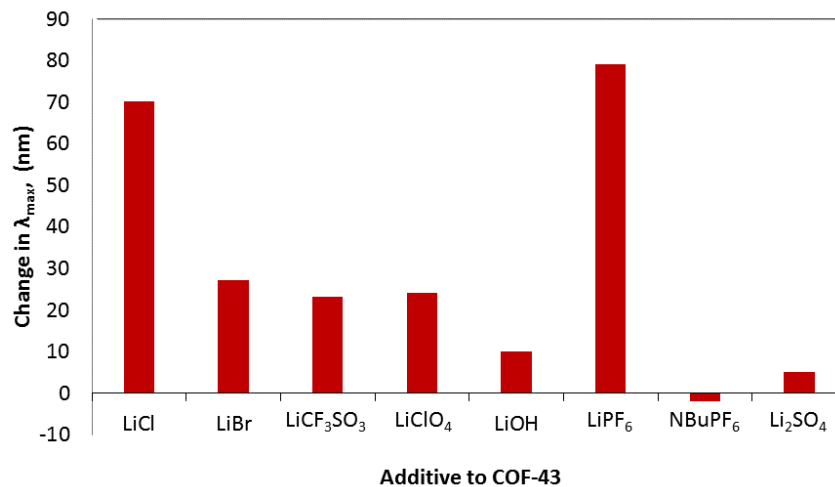


Figure 6.7: Change in maximum fluorescence emission of COF-43 exposed to excess Li additives

Further quantification of the change in emission of COF-43 with respect to the quantity of Li^+ loaded revealed an asymptotic curve which leveled out at nearly 1 equivalent of Li^+ per hydrazone, just like TCA, seen in Figure 6.8. The IR of the COF-43 loaded with LiCl shows a decrease in the intensity of the C=N band at 1650 cm^{-1} , showing the Li^+ interacts in a similar manner as H^+ (Figure SXX). ^7Li SSNMR also confirms the presence of Li in the loaded powder (Figure SXX). Surprisingly, significant color changes did not occur with the LiCl in solution, and it was only upon drying that the COF changed color.

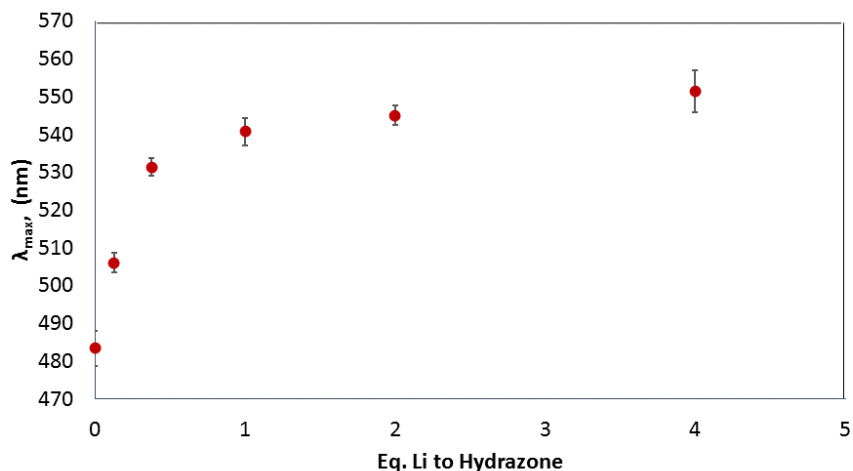


Figure 6.8: Maximum fluorescence emission of COF-43 exposed to different equivalents of LiCl

COF-43 is particularly sensitive to the addition of Li^+ . To test this sensitivity, solutions of 0.5 eq of Na^+ per hydrazone were made and then dosed with different concentrations of Li^+ and the results shown in Figure 6.9. The recovered powder still demonstrated the shift in fluorescence emission seen for solutions of just LiCl. When the reverse scenario was tested, varying the concentration of NaCl did not produce a significant color change, and the only shift seen is from the solvchromatic effects of water. This shows the enhanced sensitivity of COF-43 to Li^+ over other group 1 cations, which could be useful for future applications as a Li^+ concentrator, or Li^+ detector.

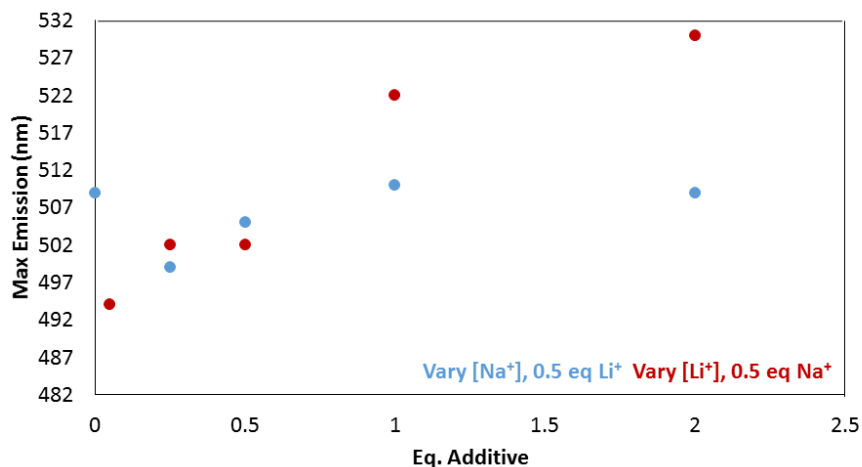


Figure 6.9: Plot of maximum fluorescence emission of COF-43 after exposing to solutions where the concentration of Li^+ is maintained and the concentration of Na^+ changes (blue), or where the concentration Na^+ is maintained and the concentration of

To understand the mechanism of this color change, a model compound (pictured at the top of Figure 6.10) which is similar to an edge of COF-43 hexagon was synthesized. This model compound has a very high molar absorptivity and its absorbance is between the COF-43 monomers and the bulk COF-43 powder. Solution based measurements of the model compound with up to 14 equivalents of Li^+ did not change absorbance or emission significantly. However, when those solutions were dried, with high Li^+ equivalents, the powder was yellow, instead of the as synthesized white. A plot of the color change versus equivalents of Li^+ showed an asymptotic behavior, with the peak occurring at 1 equivalent of Li^+ per hydrazone. Since the color change only occurs in the solid state, it implies that it is driven by changes associated with how the complexes stack with each other and is not strictly a binding phenomenon.

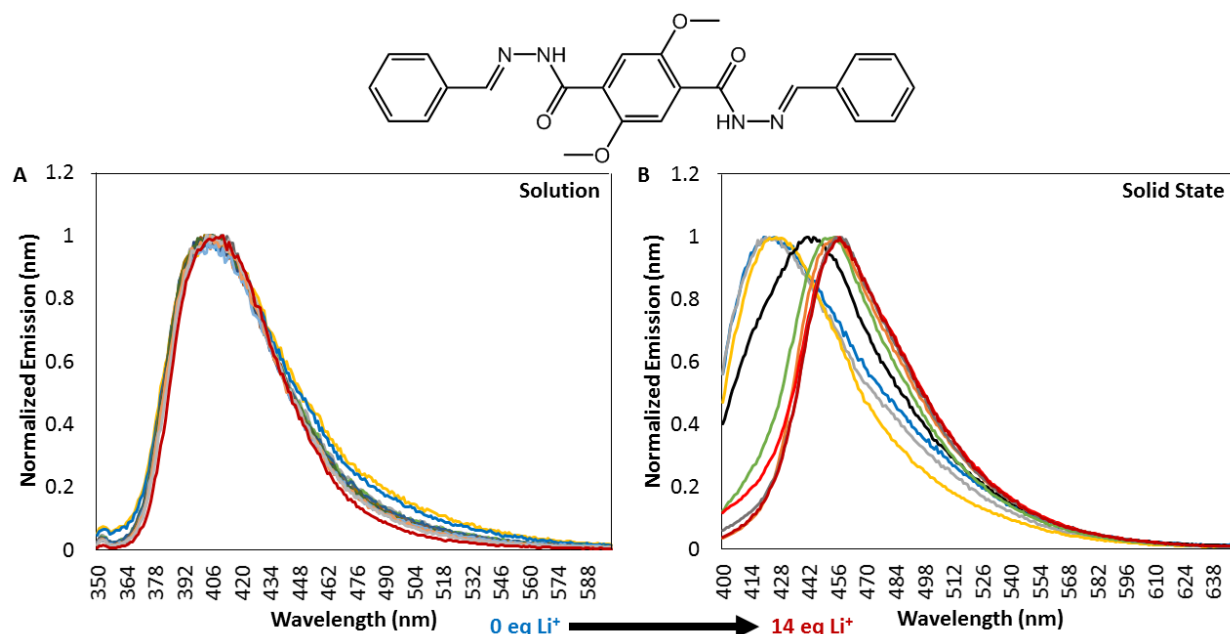


Figure 6.10: Top: Structure of model compound used for solution measurements. A) Fluorescence emission of model compound in solution with 0 (blue) to 14 eq of LiCl (red). B) Solid state fluorescence of samples in Figure 6.10A with the solid removed.

To further understand the fluorescence shifting effect seen for both the model compound and COF-43, soluble, exfoliated COF-43 was studied. COF-43 can be exfoliated in a variety of solvents, where soluble sheets are released from the COF and an amorphous powder remains¹⁹. Depending on the exfoliation solvent, the size of the sheets as well as their thickness (how many layers are stacked) varies. For this study the COF-43 was sonicated in either THF or dioxane for 10 min before filtering through a 0.5 μm filter. In previous reports, COF-43 exfoliated in dioxane was very thin, usually mono- or bi-layer, while COF-43 exfoliated in THF tended to be thicker, closer to 8 nm (about 25-30 layers)¹⁹. Similar to the model compound studies (Figure 6.10), in solution, the absorbance and emission of exfoliated COF-43 did not shift significantly with the addition of up to 8 eq Li^+ (Figure 6.11). Drying the solvent demonstrated the differences in the two exfoliation systems (Figure 6.12). The THF

exfoliated samples show a 20 nm shift in fluorescence emission while the dioxane exfoliated samples only show a 7 nm shift. Since the THF exfoliated samples are multilayer COF-43, there are more stacking interactions present before drying, which lead to a larger shift in fluorescence emission upon drying. With the single layer dioxane exfoliated COF-43, the random stacking upon drying does not allow for the color changing stacking interactions..

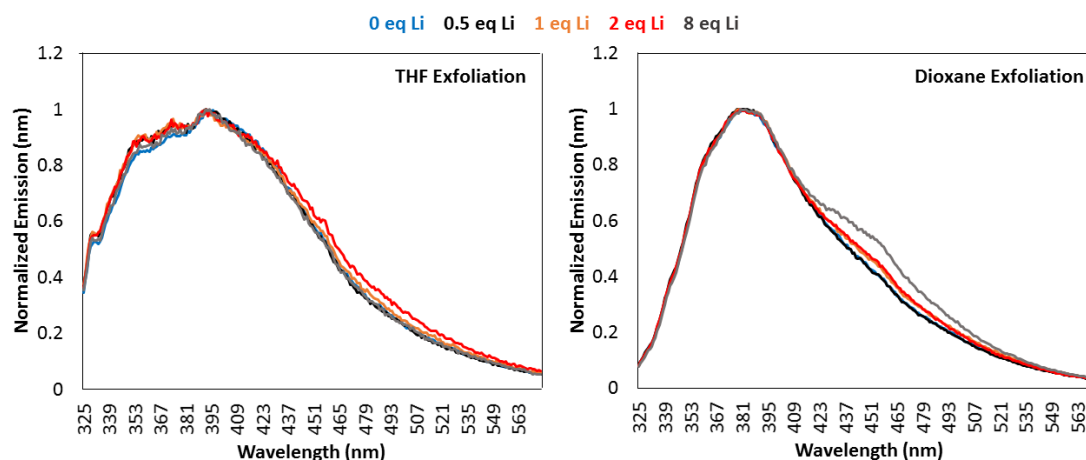


Figure 6.11: Fluorescence emission of soluble, exfoliated COF-43 in THF (left) or Dioxane (right) with 0 (blue) to 8 (grey) equivalents of Li^+ in solution

Inspired by the loading of M^+ metals into COF-43, catalytically active metals were also tested. There have been recent reports of various COFs used for catalytic applications due to their high surface area and regular pore geometry^{3,23,24}. Soaking COF-43 in MeCN solutions of both $\text{Cu}(\text{CF}_3\text{SO}_3)_2$ and $\text{Pd}(\text{PPh}_3)_2\text{Cl}_2$ yielded bright yellow COF-43 with a decreased C=N IR band, corresponding to an interaction with the metal cation. Surprisingly, when $\text{Cu}(\text{CF}_3\text{SO}_3)_2$ was added to the COF-43 powder

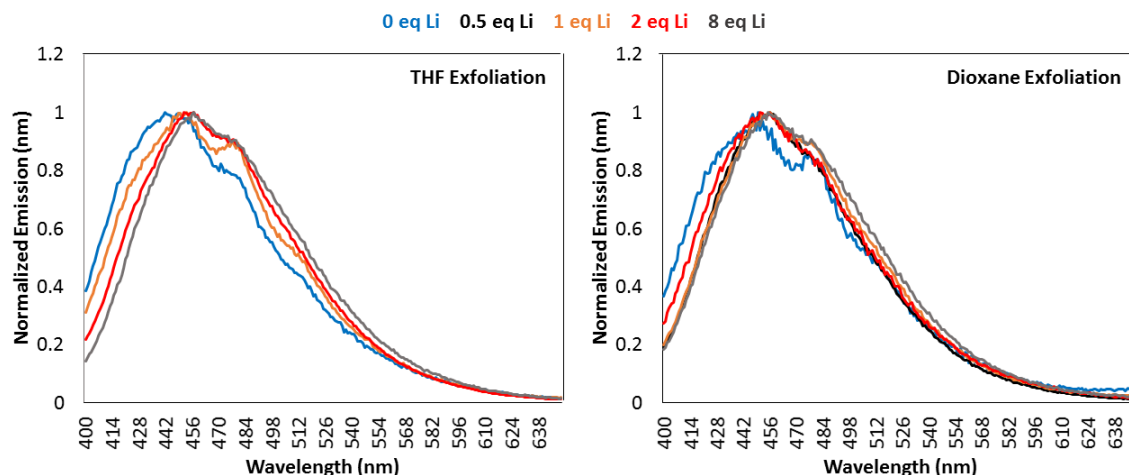


Figure 6.12: Fluorescence emission of the dried samples from Figure 6.11, with COF-43 exfoliated from THF (left) or Dioxane (right) with 0 (blue) to 8 (grey) equivalents in solution, the color change was instantaneous, instead of upon drying like the other systems investigated. This implies the interaction could be stronger, or the binding affects the interlayer interactions more significantly, which would be possible if the Cu^{2+} acts as a bridge between two COF layers. It is important to note that these metal loaded COFs are still catalytically active. $\text{Cu}@$ COF-43 can catalyze a benzylation reaction at the same rate as the homogenous catalyst and can be recycled once (Figures S19-S20). It is also moisture stable, and does not need to be stored in a dry-box, unlike the homogenous catalyst. $\text{Pd}@$ COF-43 catalyzes simple Sonogashira reactions without a decrease in rate, compared to the homogenous catalyst, and can also be recycled three times without a loss in productivity (Figure S21-S22). The pores of the metal loaded COF allows for facile diffusion of the reaction monomers, so the rate of the reaction is not diffusion limited. While the COF does not exhibit amazing levels of recyclability, the fact that these materials perform as well as the homogenous catalysts and can be recycled at least once, makes it worth noting in this thesis. This is

a step toward making heterogenous catalysts that are very active, recyclable, and easy to use.

Conclusion: The hydrazone linkage in COF-43 makes it an interesting candidate for metal loading which could lead to applications of loaded COF-43 in drug delivery.

When COF-43 is exposed to Li^+ or H^+ , up to a 100 nm change in fluorescence emission is seen. This large shift in emission stems from interlayer stacking interactions which are changed with the introduction of metal guests from solution. It is possible that larger cations are sterically limited and unable to cause large changes in COF-43 stacking which leads to smaller shifts in emission. COF-43 can also coordinate with divalent metals like Cu^{2+} and Pd^{2+} and the loaded COFs can be utilized for benzanulation and Sonogashira cross coupling reactions. While these catalysis do not outperform their homogenous counterparts, COF coordination also does not hinder the reaction progression.

REFERENCES

- (1) Côté, A. P.; Benin, A. I.; Ockwig, N. W.; O’Keeffe, M.; Matzger, A. J.; Yaghi, O. M. *Science* **2005**, *310* (5751), 1166–1170.
- (2) Uribe-Romo, F. J.; Doonan, C. J.; Furukawa, H.; Oisaki, K.; Yaghi, O. M. *J. Am. Chem. Soc.* **2011**, *133* (30), 11478–11481.
- (3) Stegbauer, L.; Schwinghammer, K.; Lotsch, B. V. *Chem. Sci.* **2014**, *5* (7), 2789–2793.
- (4) Kalia, J.; Raines, R. T. *Angew. Chem. Int. Ed.* **2008**, *47* (39), 7523–7526.
- (5) Mao, J.; Wang, Y.; Wan, B.; Kozikowski, A. P.; Franzblau, S. G. *ChemMedChem* **2007**, *2* (11), 1624–1630.
- (6) Andreani, A.; Burnelli, S.; Granaiola, M.; Leoni, A.; Locatelli, A.; Morigi, R.; Rambaldi, M.; Varoli, L.; Calonghi, N.; Cappadone, C.; Farruggia, G.; Zini, M.; Stefanelli, C.; Masotti, L.; Radin, N. S.; Shoemaker, R. H. *J. Med. Chem.* **2008**, *51* (4), 809–816.
- (7) Chimenti, F.; Maccioni, E.; Secci, D.; Bolasco, A.; Chimenti, P.; Granese, A.; Befani, O.; Turini, P.; Alcaro, S.; Ortuso, F.; Cardia, M. C.; Distinto, S. *J. Med. Chem.* **2007**, *50* (4), 707–712.
- (8) Vicini, P.; Incerti, M.; Doytchinova, I. A.; La Colla, P.; Busonera, B.; Loddo, R. *Eur. J. Med. Chem.* **2006**, *41* (5), 624–632.
- (9) Yoshida, T.; Lai, T. C.; Kwon, G. S.; Sako, K. *Expert Opin. Drug Deliv.* **2013**, *10* (11), 1497–1513.
- (10) West, K.; Otto, S. *Curr. Drug Discov. Technol.* **2005**, *2* (3), 123–160.
- (11) Banerjee, S.; Mondal, S.; Chakraborty, W.; Sen, S.; Gachhui, R.; Butcher, R. J.; Slawin, A. M. Z.; Mandal, C.; Mitra, S. *Polyhedron* **2009**, *28* (13), 2785–2793.
- (12) Barbazán, P.; Carballo, R.; Covelo, B.; Lodeiro, C.; Lima, J. C.; Vázquez-López, E. M. *Eur. J. Inorg. Chem.* **2008**, *2008* (17), 2713–2720.
- (13) Yang, Y.; Su, X.; Carroll, C. N.; Aprahamian, I. *Chem. Sci.* **2012**, *3* (2), 610–613.
- (14) Croteau, M. L.; Su, X.; Wilcox, D. E.; Aprahamian, I. *ChemPlusChem* **2014**, *79* (8), 1214–1224.
- (15) Sridharan, V.; Perumal, P. T.; Avendaño, C.; Menéndez, J. C. *Org. Biomol. Chem.* **2006**, *5* (9), 1351–1353.
- (16) Dang, T. T.; Dang, T. T.; Langer, P. *Tetrahedron Lett.* **2007**, *48* (20), 3591–3593.
- (17) Inamoto, K.; Katsuno, M.; Yoshino, T.; Arai, Y.; Hiroya, K.; Sakamoto, T. *Tetrahedron* **2007**, *63* (12), 2695–2711.
- (18) Ghavtadze, N.; Fröhlich, R.; Würthwein, E.-U. *Eur. J. Org. Chem.* **2008**, *2008* (21), 3656–3667.
- (19) Bunck, D. N.; Dichtel, W. R. *J. Am. Chem. Soc.* **2013**, *135* (40), 14952–14955.
- (20) Bunck, D. N.; Dichtel, W. R. *Angew. Chem. Int. Ed.* **2012**, *51* (8), 1885–1889.
- (21) Bunck, D. N.; Dichtel, W. R. *Chem. Commun.* **2013**, *49* (24), 2457–2459.
- (22) Brucks, S. D.; Bunck, D. N.; Dichtel, W. R. *Polymer* **2014**, *55* (1), 330–334.
- (23) Kamiya, K.; Kamai, R.; Hashimoto, K.; Nakanishi, S. *Nat. Commun.* **2014**, *5*.
- (24) Zhang, W.; Jiang, P.; Wang, Y.; Zhang, J.; Gao, Y.; Zhang, P. *RSC Adv.* **2014**, *4* (93), 51544–51547.

APPENDIX V

A. Materials. All reagents were purchased from commercial sources and used without further purification. CH₂Cl₂, PhMe, and MeOH were purchased from commercial sources and purified using a custom-built alumina-column based solvent purification system. Other solvents were purchased from commercial sources and used without further purification

Instrumentation. Infrared spectra were recorded on a Thermo Nicolet iS10 with a diamond ATR attachment and are uncorrected. Ultraviolet/visible/near infrared absorbance spectra were recorded on a Cary 5000 spectrophotometer with a Hg lamp.

Photoemission and excitation spectra were recorded on a Horiba Jobin Yvon Fluorolog-3 fluorescence spectrophotometer equipped with a 450 W Xe lamp, double excitation and double emission monochromators, a digital photon-counting photomultiplier and a secondary InGaAs detector for the NIR range. Correction for variations in lamp intensity over time and wavelength was achieved with a solid-state silicon photodiode as the reference. The spectra were further corrected for variations in photomultiplier response over wavelength and for the path difference between the sample and the reference by multiplication with emission correction curves generated on the instrument.

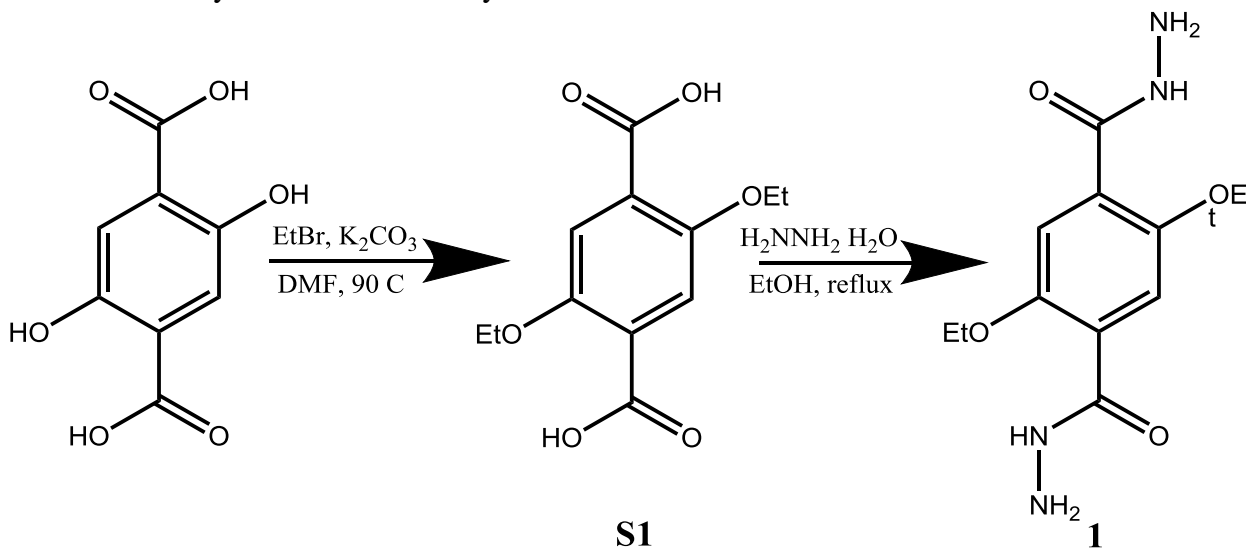
MALDI-TOF mass spectrometry was performed on a Waters MALDI micro MX MALDI-TOF mass spectrometer using positive ionization and a reflectron detector. MALDI samples were prepared by depositing the analyte dissolved in a saturated dithranol or tetracyanoquinodimethane solution onto a stainless steel sample plate. The plate was dried in air before loading it into the instrument. Calibration of the mass range was performed by addition of poly(ethylene-oxide) standards.

Gas chromatography/electron impact mass spectrometry was performed on an Agilent 6890N Network GC System with a JEOL JMS-GCmate II Mass Spectrometer (magnetic sector).

NMR spectra were recorded on a Varian 400 MHz, a Varian 500 MHz or a Bruker ARX 300 MHz spectrometer using a standard ¹H/X Z-PFG probe at ambient temperature with a 20 Hz sample spin rate.

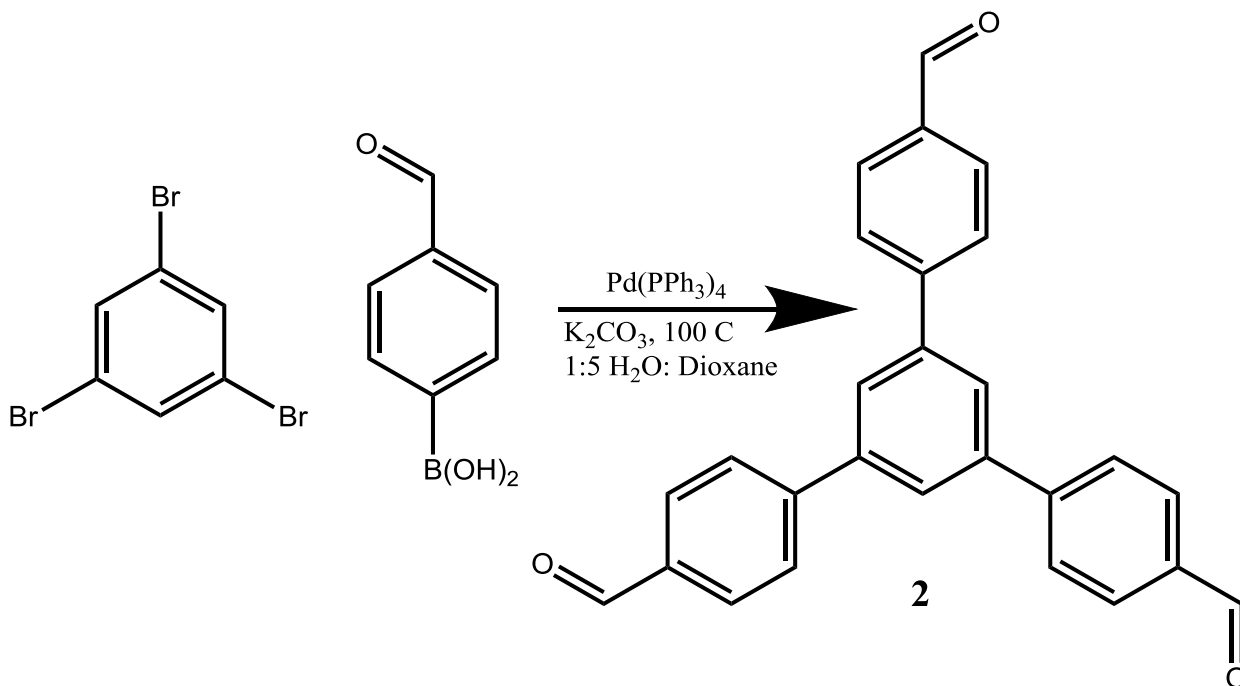
B. Synthetic Procedures

Scheme A5.1. Synthesis of linear dihydrazide **1**.



Synthesis of S1: Diethyl 2,5-dihydroxyterephthalate (4.0 g, 15.7 mmol) and potassium carbonate (10.0 g, 72.3 mmol) were placed in a dry 150 mL round bottom flask equipped with a stir bar, which was then sealed with a septum and purged with N₂. Dry DMF (80 mL) and bromoethane (2.8 mL, 37.8 mmol) were added by syringe. The reaction mixture was heated to 90 °C for 8.5 h. Upon full conversion, the reaction was cooled to rt and slowly quenched with aqueous HCl (1 M, 10 mL), and the resulting precipitate was isolated by vacuum filtration and dried under vacuum. The resulting diethyl 2,5-diethoxyterephthalate (4.41 g, 98%) was isolated as a white solid that required no further purification. ¹H NMR (300 MHz, CDCl₃) δ 7.35 (s, 2H), 4.36 (q, 4H), 4.07 (q, 4H), 1.43 (t, 6H), 1.39 (t, 6H). This spectrum matched that previously reported in 1.

Synthesis of 1: Diethyl 2,5-diethoxyterephthalate (4.5 g, 14.5 mmol) was dissolved in EtOH (58 mL) in a 150 mL round bottom flask equipped with a stir bar. Hydrazine Hydrate (8.5 mL, 174 mmol) was added slowly and the flask was then equipped with a condenser and heated to reflux for 15 h. The reaction was then cooled to rt and a white precipitate formed. The flask was then cooled further in the freezer for 3.5 h, and the white needles were isolated by vacuum filtration. Compound **1** was isolated as white needles (3.85 g, 94%). ¹H NMR (300 MHz, DMSO-d₆) δ 9.24 (t, 2H), 7.38 (s, 2H), 4.57 (d, 4H), 4.11 (q, 4H), 1.35 (t, 6H). This spectrum matched that previously reported in 1.



Synthesis of 2: Tribromobenzene (5.0 g, 15.9 mmol), 4-formylphenyl boronic acid (14.3 g, 95.3 mmol), potassium carbonate (13.2 g, 95.3 mmol), and palladium tetrakis(triphenyl phosphine) (0.92 g, 0.794 mmol) were added to a 300 mL round bottom flask equipped with a stir bar. The flask was evacuated and backfilled with N_2 three times. Dioxane (133 mL) and H_2O (27 mL) were mixed and then bubbled with N_2 for 10 min before adding to the reaction flask. The reaction mixture was then heated to 100 °C for 12 h. The reaction mixture was cooled to rt, after which a precipitate formed that was collected by filtration and washed with ethyl acetate. These isolated white solids is product 2 (3.83 g, 62%). $^1\text{H NMR}$ (400 MHz, CDCl_3) δ 10.11, (s, 3H), 8.02 (AA'BB', 6H), 7.91 (3H, s), 7.87 (AA'BB', 6H). This spectrum matched that previously reported in 1

Synthesis of COF-43. Dihydrazide 1 (37.0 mg, 0.131 mmol) and trialdehyde 2 (34.0 mg, 0.087 mmol) were sonicated in 2 mL mesitylene / dioxane (9:1 v/v) in a 4 mL vial until a fine suspension was obtained. The suspension was then transferred by pipet to a pre-scored 5 mL ampoule, 6 M acetic acid (0.2 mL) was added, and the whole mixture was flash frozen in N_2 (l) and flame sealed. The ampoule was put in an oven at 120 °C for 72 h, after which the ampoule was cooled to rt, opened, and the sample filtered with THF (6 mL), yielding COF-43 as an insoluble microcrystalline powder.

Metal Loading Procedure. In a typical loading, a stock solution of LiCl (0.0159 g, 3.75 mmol) in 1:4 MeOH:MeCN (25 mL) was created. COF-43 was weighed into a 20 mL vial, and the appropriate volume of LiCl solution was added via syringe. The solution was allowed to fully evaporate at room temperature.

COF-43 Exfoliated Procedure. COF-43 (10 mg) was added to a 20 mL vial. 5 mL of dioxane was then added and the sample was allowed to sonicate for 20 min. The solution was removed and then filtered through a 5 μm filter for solution based measurements. The isolated powder was dried under vacuum.

C. NMR Spectra

Figure A5.1: ¹H NMR of Compound S1

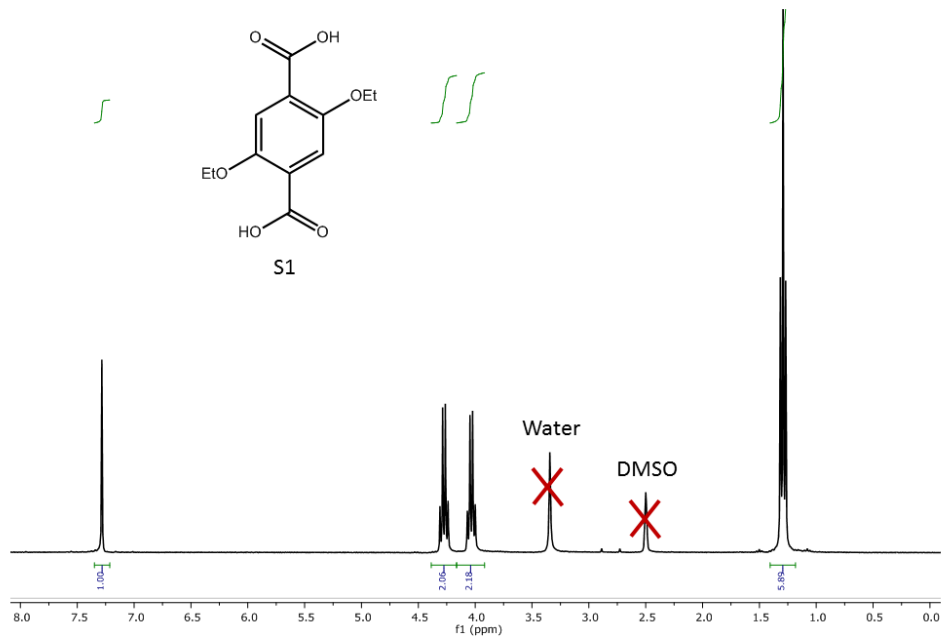
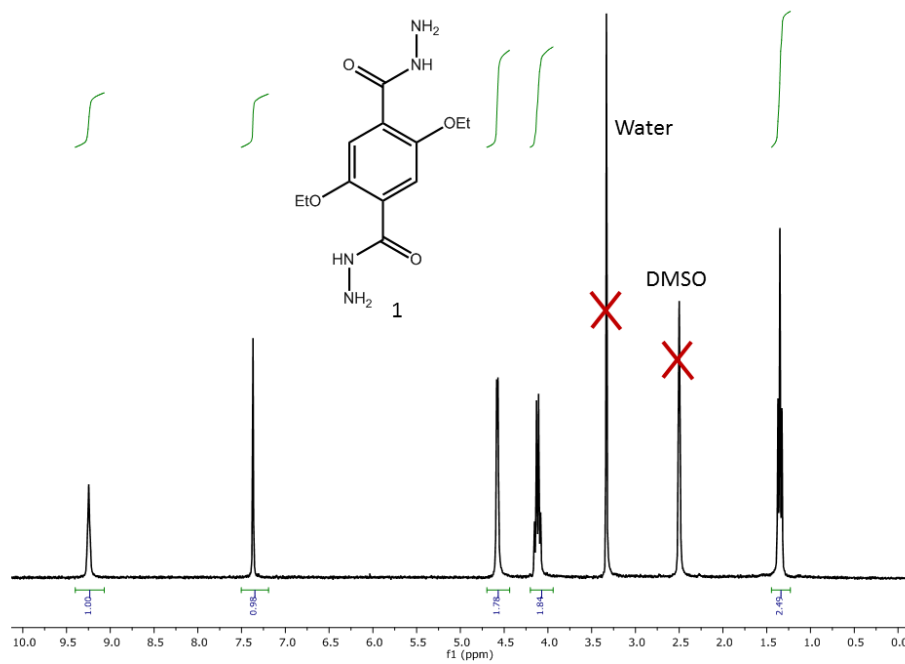
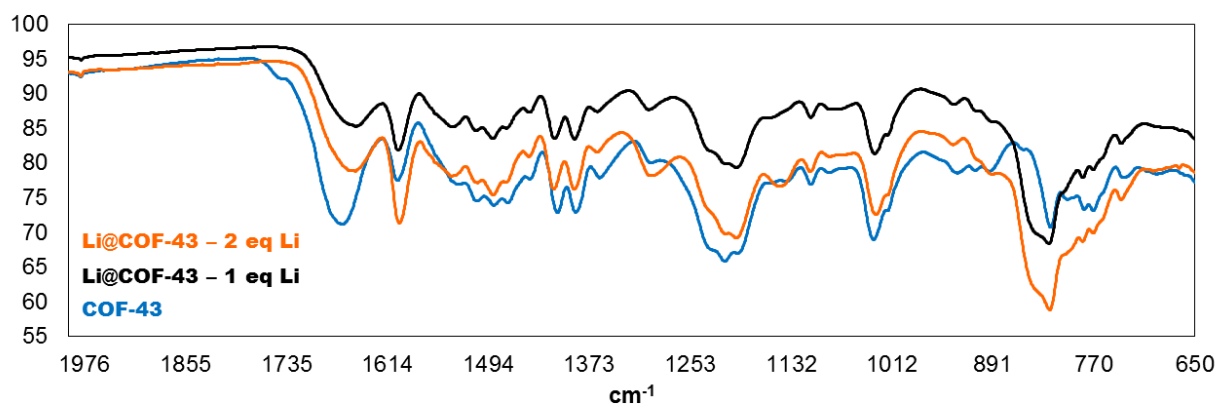


Figure A5.2: ¹H NMR of Compound 1



D. FTIR Spectra

Figure A5.5: IR Spectra of Li@COF-43



E. UV-Vis Spectra

Figure A5.6: Solid State UV-Vis Spectra of Li@COF-43

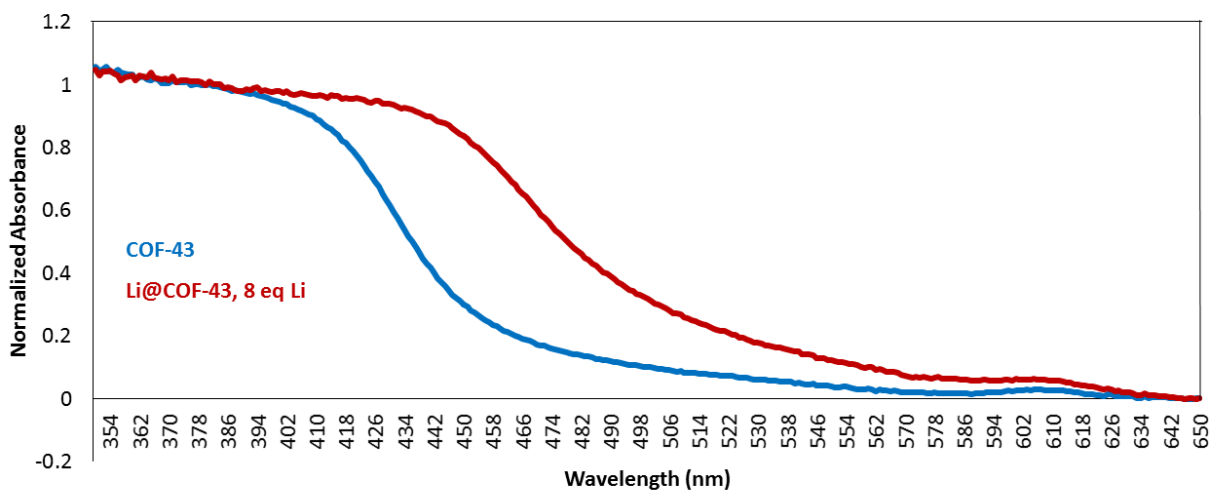


Figure A5.7: Solid State UV-Vis Spectra of H@COF-43

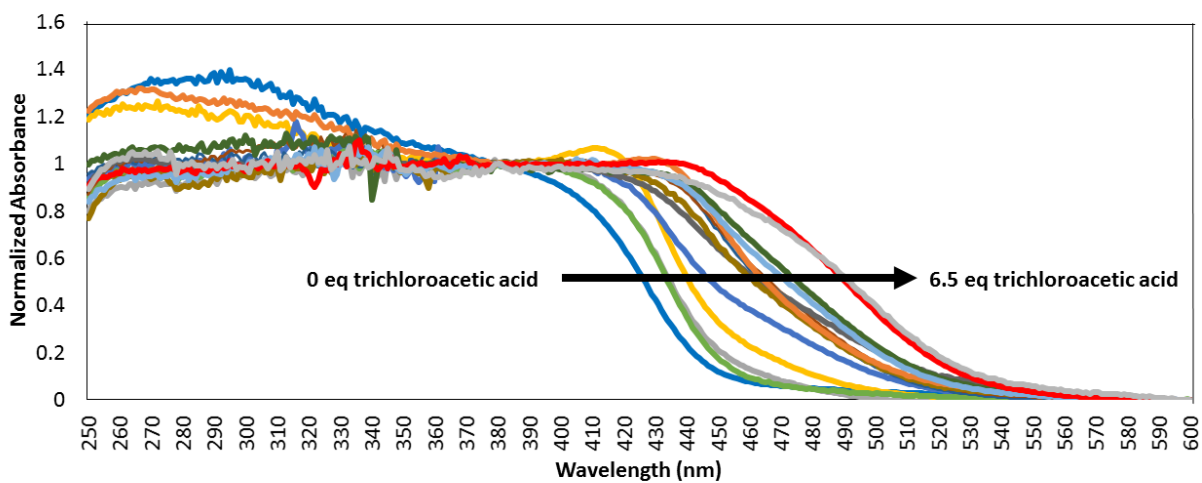


Figure A5.8: Solution UV-Vis Spectra of Li@ExfoliatedCOF-43

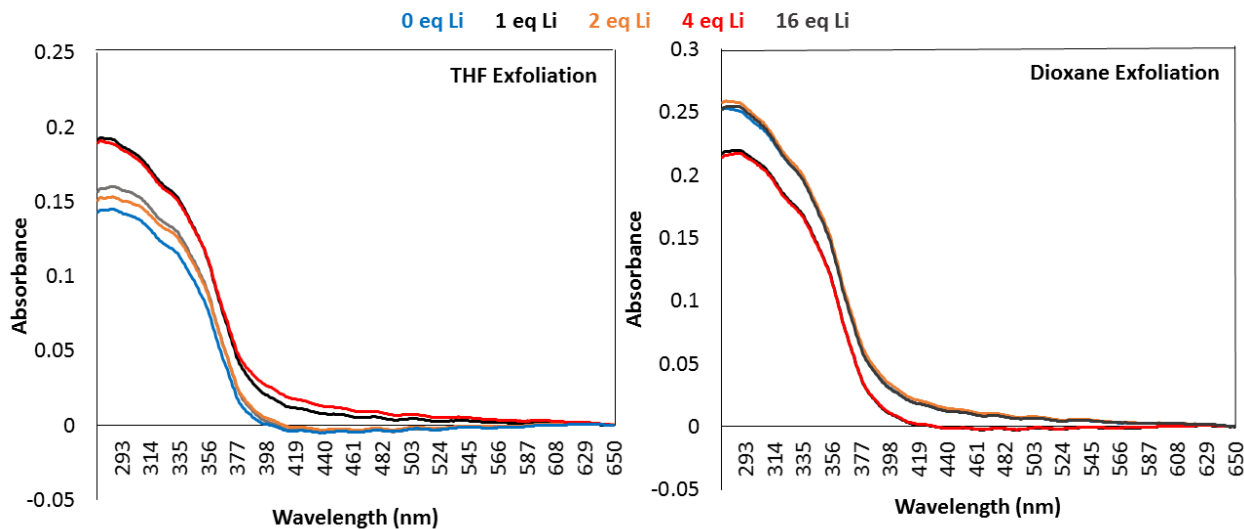


Figure A5.9: Solid UV-Vis Spectra of dried Li@ExfoliatedCOF-43

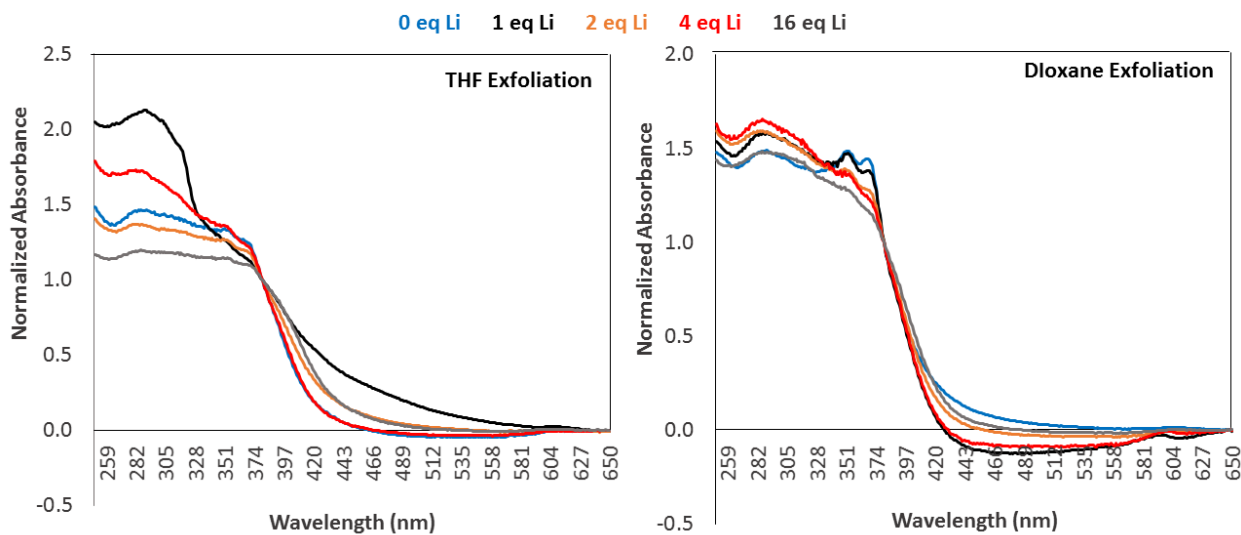


Figure A.10: Solid UV-Vis of exfoliated powder, Li@ExfoliatedCOF-43

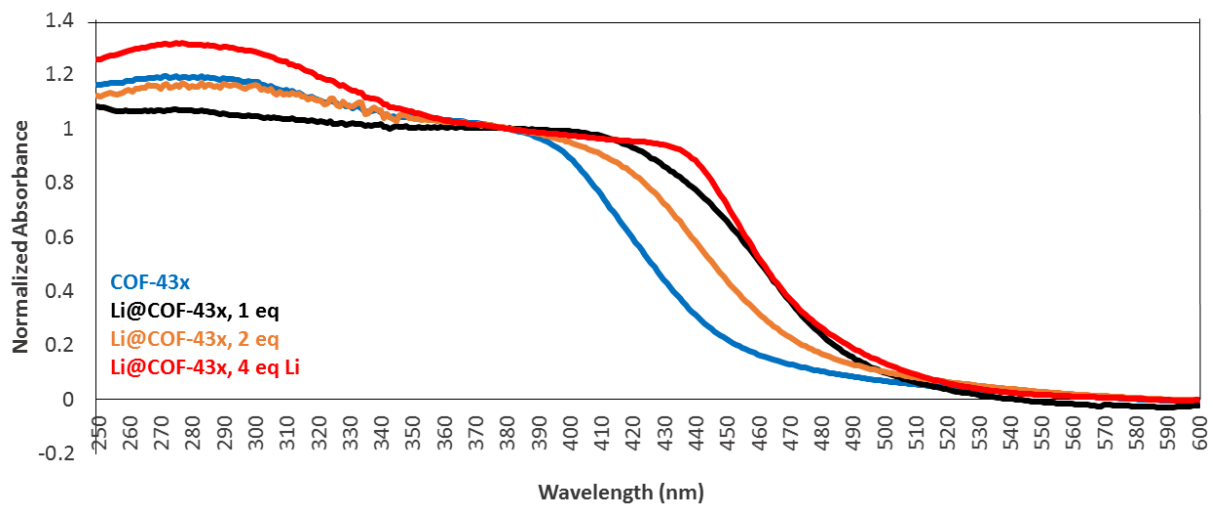


Figure A5.11: Solution UV-Vis Spectra of Li@ModelCompound

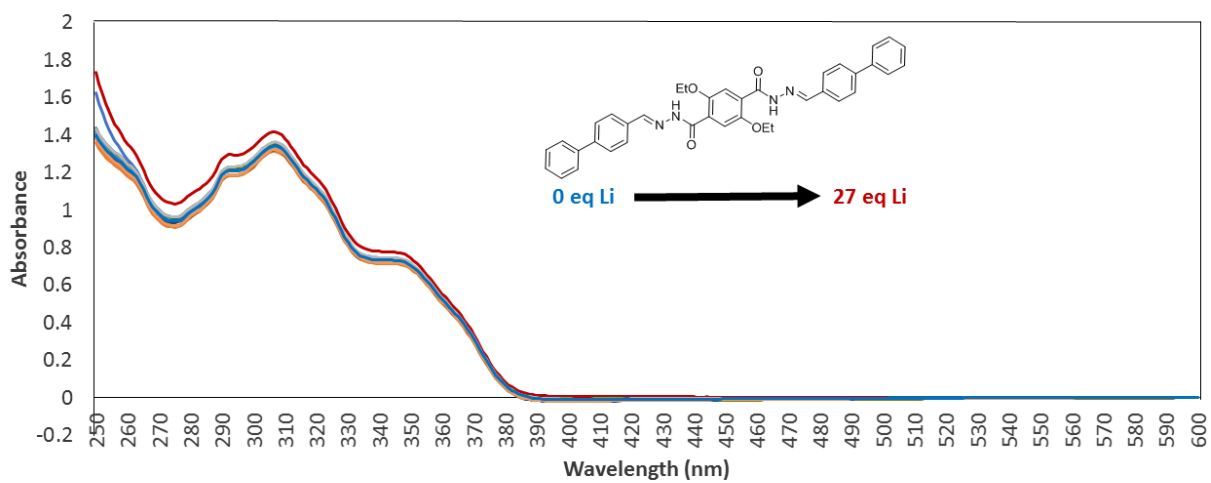
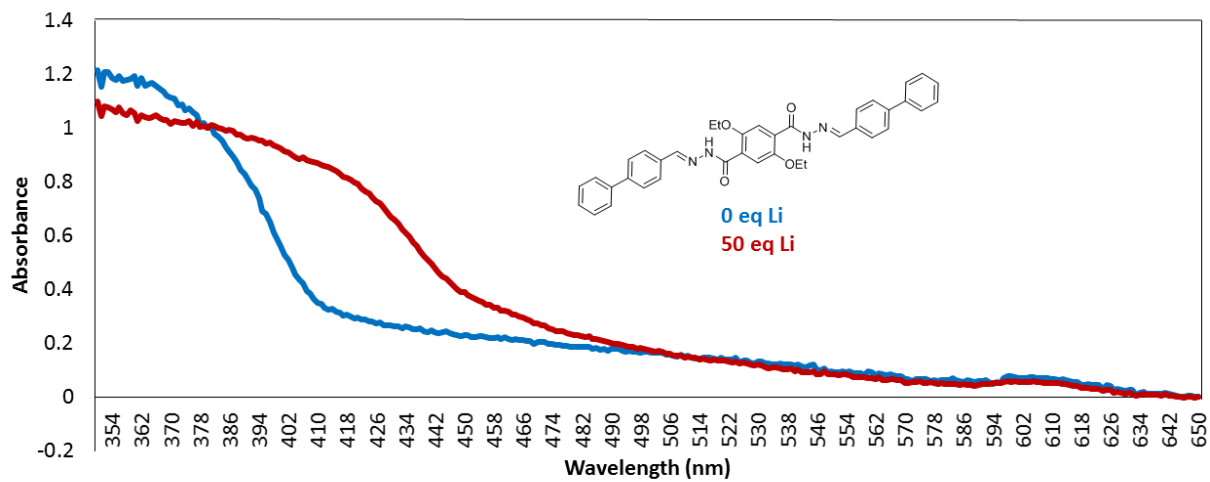


Figure A5.12: Solid UV-Vis Spectra of Li@ModelCompound



F. Fluorescence Spectra

Figure A5.13: Solid State Fluorescence spectra of Li@COF-43

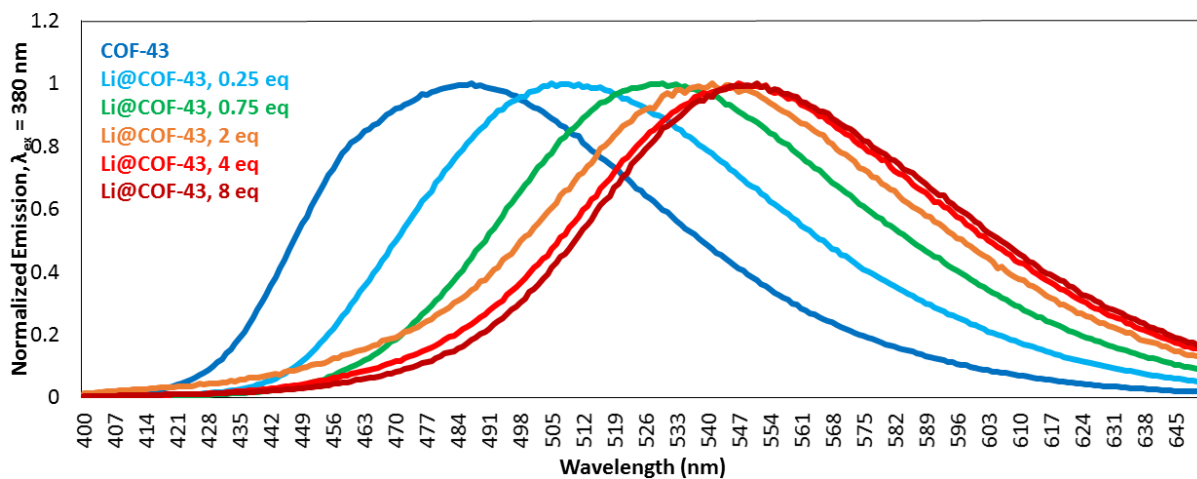


Figure A5.14: Solid State Fluorescence Spectra of H@COF-43

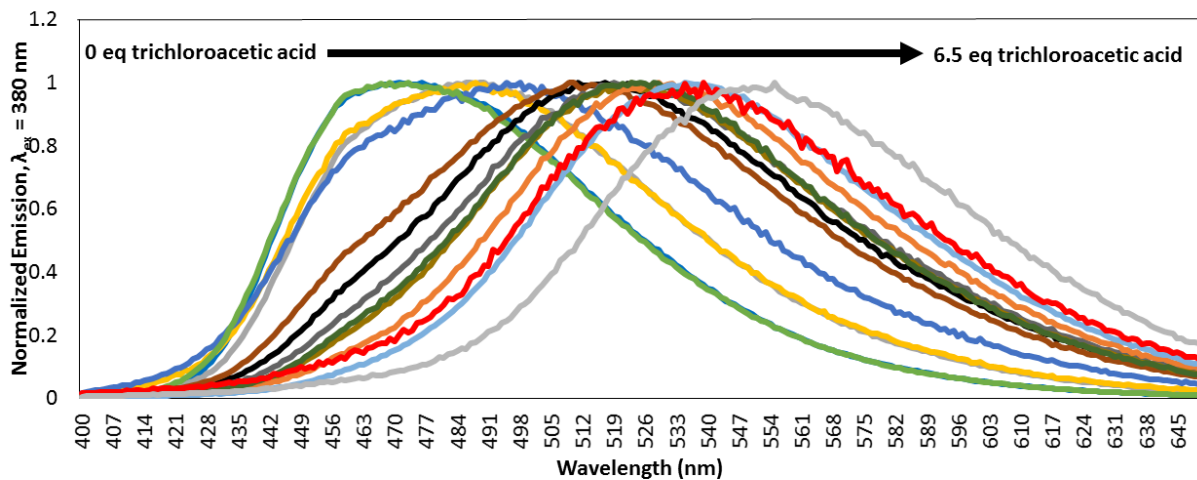
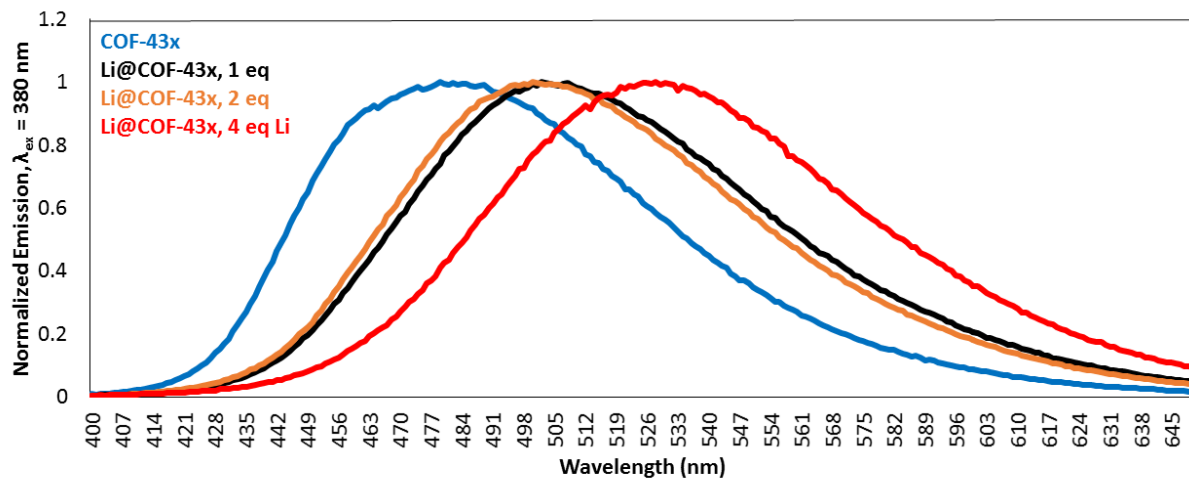
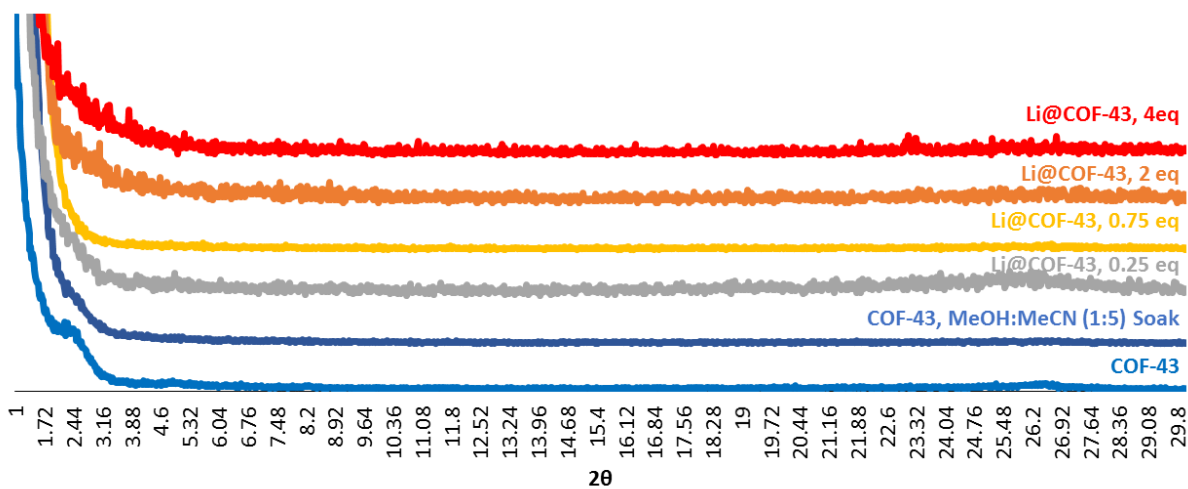


Figure A5.15: Solid Fluorescence Spectra of Insoluble Li@ExfoliatedCOF-43



G. XRD Spectra

Figure A5.16: Powder XRD of COF-43 loaded with different equivalents of LiCl



H. TEM Images

Figure A5.17: TEM Image of solvated exfoliated COF-43 with 2 eq. Li. COF-43 was exfoliated by sonicating sample in dioxane for 20 min. Diffraction pattern (left) from the selected area in the red circle from the image on the right

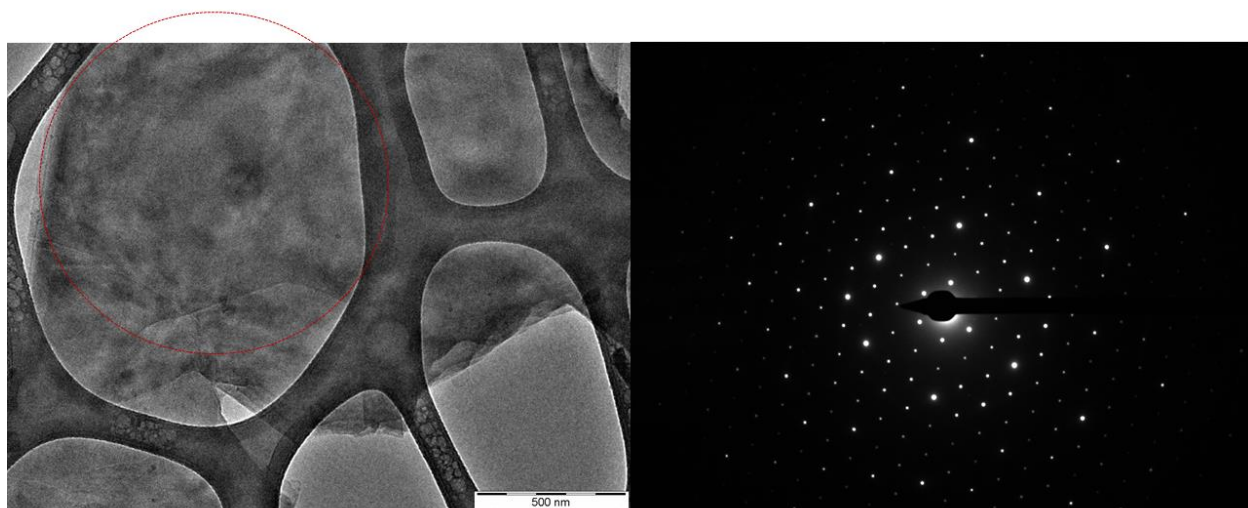
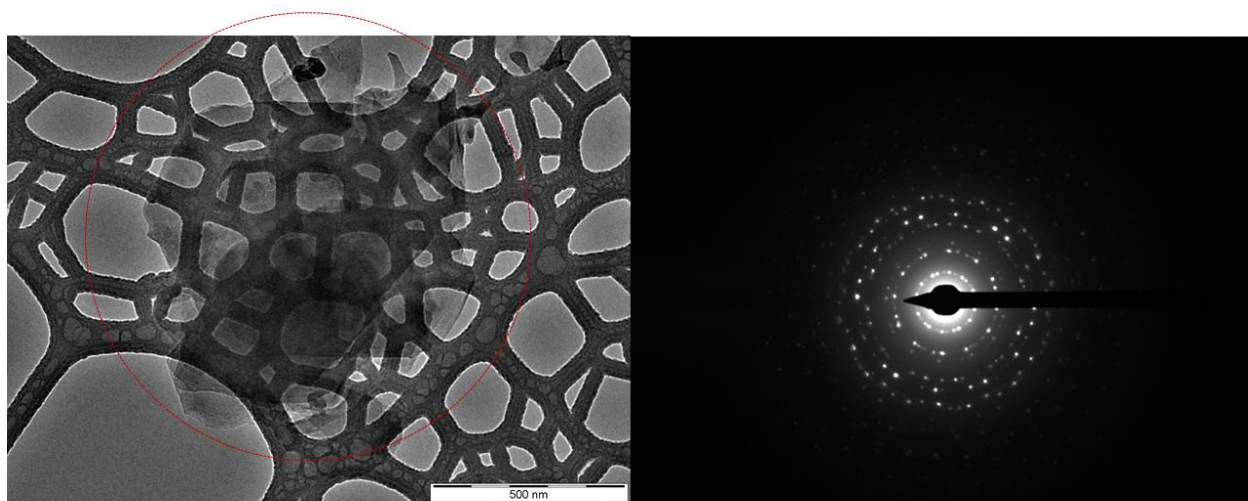
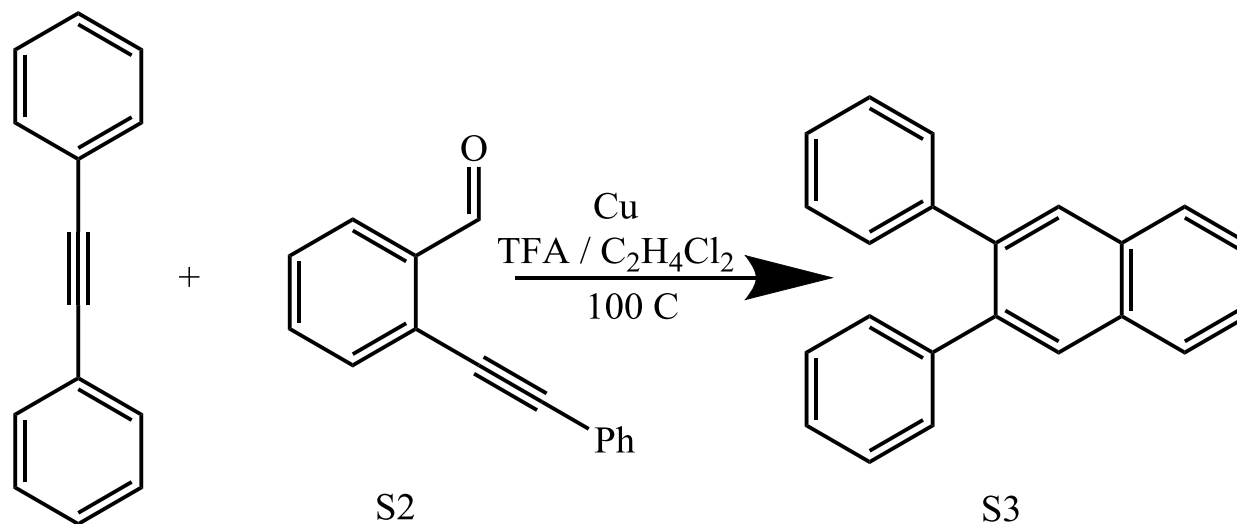


Figure A5.18: TEM Image of solvated exfoliated COF-43 with 2 eq. Li. COF-43 was exfoliated by sonicating sample in THF for 20 min. Diffraction pattern (left) from the selected area in the red circle from the image on the right



I. Benzannulation Reaction

Scheme A5.2: Benzanulation reaction



Copper catalyst (Cu(OTf)₂ (0.013 g, 0.036 mmol) for homogenous, Cu@COF-43 for heterogenous) was transferred to a round bottom flask and purged with N₂. In a separate vial, diphenyl acetylene (0.055 g, 0.309 mmol) and S2 (0.127 g, 0.617 mmol) were dissolved in C₂H₄Cl₂ (3 mL). This solution was added transferred to the reaction flask and placed in a 100 °C oil bath. CF₃CO₂H (0.024 mL, 1 equiv) was added using a micro syringe and the solution was refluxed. 0.1 mL aliquots were removed from solution, and washed with saturated aqueous NaHCO₃ (0.5 mL) and extracted with CH₂Cl₂ (0.5 mL). 0.1 mL of the extracted organic layer was diluted into an additional 1 mL CH₂Cl₂, and the formation of S3 was identified through GC-MS. This procedure was modified from 2.

Figure A5.19: Formation of benzanulated product comparing Cu@COF-43 and the homogenous catalyst $\text{Cu}(\text{CF}_3\text{SO}_3)_2$. Product formation determined by GCMS comparing to bromobenzene standard.

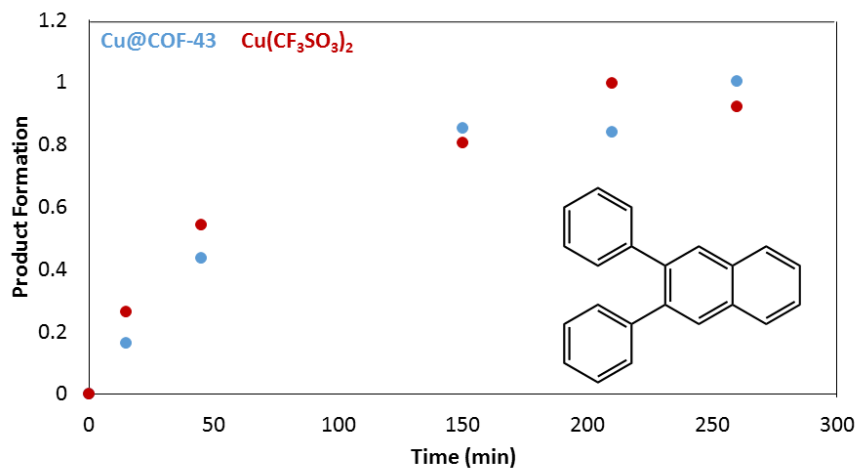
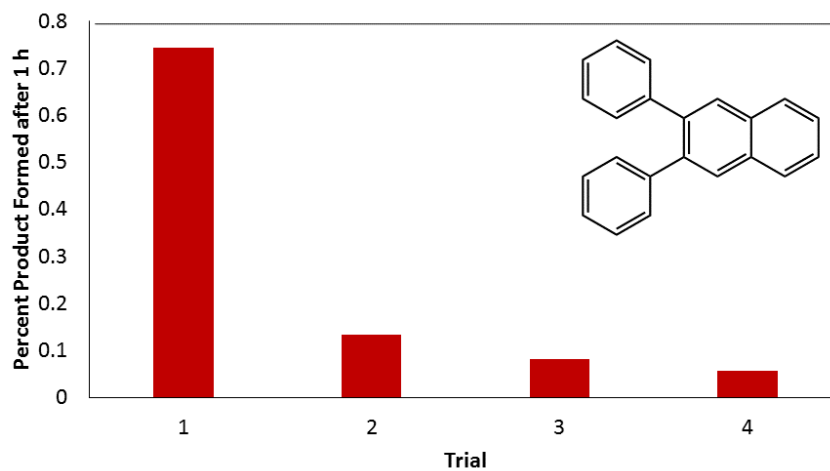
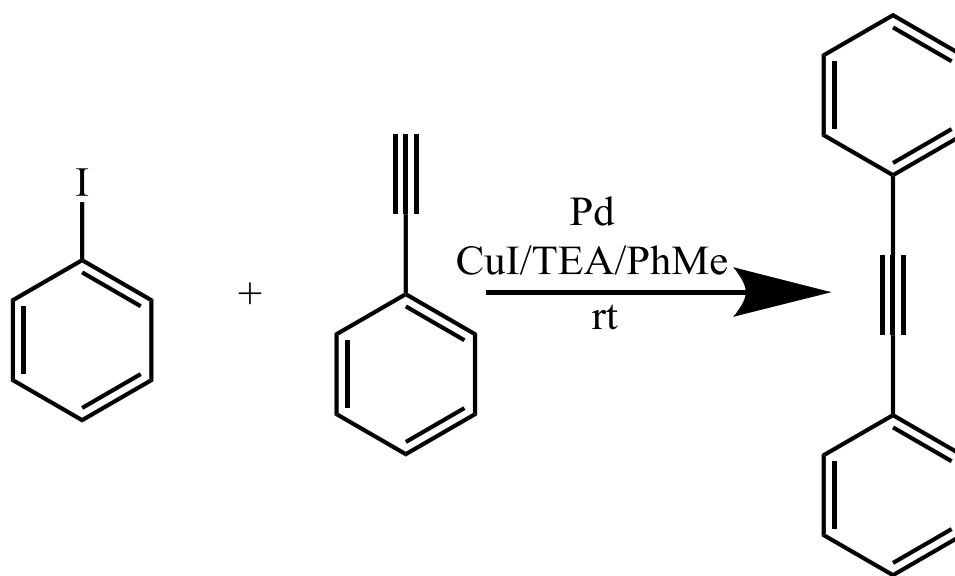


Figure A5.20: Recyclability of Cu@COF-43 looking at the amount of benzanulated product formed after 1 h of reaction.



J. Sonogashira Reaction

Scheme A5.3: Sonogashira Reaction



CuI (0.002 g, 0.009 mmol) and Pd source (Pd(PPh₃)₂Cl₂ (0.003 g, 0.005 mmol) for homogenous and Pd@COF-43 for heterogenous) were placed in a vial and put under vacuum and N₂ three times. Degassed toluene/trimethylamine (2:1) (3 mL) was added to the flask followed by Iodobenzene (0.047 g, 0.230 mmol) and phenylacetylene (0.029 g, 0.288 mmol) which were degassed separately through 3 freeze pump thaw cycles. Flask was allowed to react at room temperature with 0.1 mL aliquots were removed from solution, and washed with saturated aqueous NaHCO₃ (0.5 mL) and extracted with CH₂Cl₂ (0.5 mL). 0.1 mL of the extracted organic layer was diluted into an additional 1 mL CH₂Cl₂, and the formation of phenyl acetylene was identified through GC-MS.

Figure A5.21: Formation of alkyne coupled product comparing Pd@COF-43 and the homogenous catalyst Pd(PPh₃)₂Cl₂. Product formation determined by GCMS

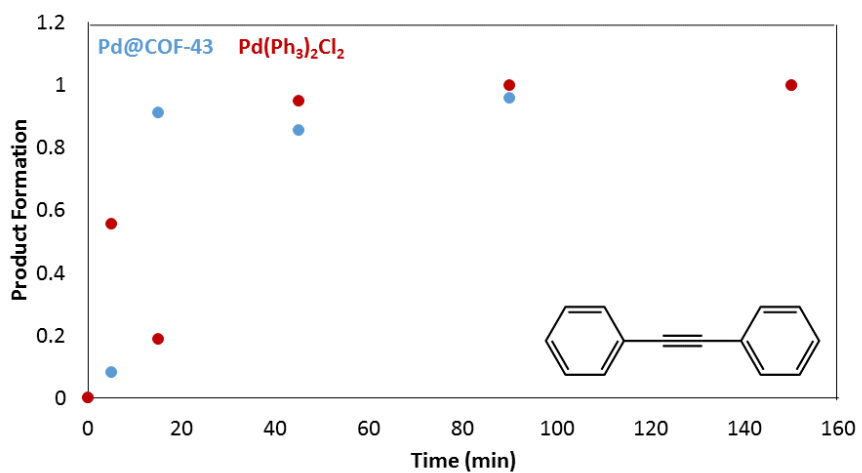


Figure A5.21: Recyclability of Pd@COF-43 looking at the amount of alkyne coupled product formed after 1 h of reaction.



K. References

- (1) Bunck, D. N.; Dichtel, W. R. *J. Am. Chem. Soc.* **2013**, *135* (40), 14952–14955.
- (2) Hein, S. J.; Arslan, H.; Keresztes, I.; Dichtel, W. R. *Org. Lett.* **2014**, *16* (17), 4416–4419.